Combination of a cold ion and cold molecular source

James M. Oldham

New College, University of Oxford

A thesis submitted for the degree of Doctor of Philosophy
Trinity Term, 2014

Combination of a cold ion and cold molecular source

James M. Oldham, New College, Trinity Term, 2014

A thesis submitted in partial fulfilment of the requirements for the degree of Doctor of Philosophy of the University of Oxford

Abstract

This thesis describes the combination of two sources of cold atomic or molecular species which can be used to study a wide range of ion-molecule reactions. The challenges in forming these species and in determining the fate of reactive events are explored throughout.

Reactions occur in a volume within a radio-frequency ion trap, in which ions have previously been cooled to sub-Kelvin temperatures. Ions are laser-cooled, with migration of ions slowed sufficiently to form a quasi-crystalline spheroidal structure, deemed a Coulomb crystal. Fluorescence emitted as a consequence of laser-cooling is detected; the subsequent fluorescence profiles are used to determine the number of ions in the crystal and, in combination with complementary simulations, the temperature of these ions. Motion imparted by trapping fields can be substantial and simulations are required to accurately determine collision energies. A beam of decelerated molecules is aimed at this stationary ion target. An ammonia seeded molecular beam enters a Stark decelerator, based on the original design of Meijer and co-workers. The decelerator uses time-varying electric fields to remove kinetic energy from the molecules, which exit at speeds down to 35 m/s. A fast-opening shutter and focussing elements are subsequently used to maximise the decelerated flux in the reaction volume while minimising undecelerated molecule transmission. Substantial fluxes of decelerated ammonia are obtained with narrow velocity distributions to provide a suitable source of reactant molecules.

Combination of these two techniques permits studies of reactions between atomic ions and decelerated molecules that can be entirely state-specific. Changes in the Coulomb crystal fluorescence profile denote changes in the ion identities, the rate of these changes can be used to obtain rate constants. Determination of rate constants is even possible despite the fact that neither reactant nor product ions are directly observed. This work has studied reactions between sympathetically cooled Xe^+ ions and guided ND_3 and has obtained data consistent with prior studies. Determination of reactive events is complicated if ion identities can change without affecting the fluorescence profile, or if multiple reaction channels are possible. A range of spectroscopic techniques are discussed and considered in regards to determining rate constants and product identities. Pulsed axial excitation of trapped ions can follow rapid changes in average ion weights and subtle changes for small crystals. Time-of-flight mass spectrometry is also demonstrated using the trapping electrodes and is suitable for discrimination of ions formed within the trap.

Acknowledgements

First, my sincerest thanks must go to my supervisor, Prof. Tim Softley, for all that he has done for me while I was part of his group – for taking me on to work on such an interesting project for my Part II year, for agreeing to let me continue in his group for my D. Phil., and for his unceasing advice, encouragement and understanding during that time. I'm especially grateful for his continued persistence while I was writing up; without it, there would have been no thesis to speak of.

I was very fortunate to be guided ably through my D. Phil. by Drs. Martin Bell, Alex Gingell and Stefan Willitsch. Stefan was the original inspiration for the Coulomb crystal simulations, always driving for a more sophisticated model. Alex, the guru of all things related to ion trapping, provided me with the platform to continue further Coulomb crystal experiments while teaching me all the tricks of the trade. Martin, in addition to being a general go-to in the event of any problems, instructed me in decelerator use, guided the progression of the combined apparatus, provided MATLAB expertise and more besides. The experiments performed in the lab were also aided by Lee Harper, Laura Pollum and Nabanita Deb, who all provided good humour and lightened the mood. Lee in particular was very patient in the optimisation of the decelerator, including our attempt to optimise by adjusting the vacuum chamber frames, an experience if nothing else!

Both the ion trap and the decelerator required their fair share of modifications and repairs over time and I am very grateful for the support of the mechanical and electrical workshops in the PTCL. In particular, Andy and Les from the mechanical workshop, and Kevin, Phil and John from the electrical workshop were all excellent in fulfilling my requests in the short timescales they had.

Thanks to all the other members of the Softley group over the years, especially Elin McCormack, Eric So, Sashi Ganeshalingam, Mark Ford, Will Doherty, Mark Detlefsen and Chris Rennick, for their friendship and for making life within the group much more enjoyable, and to Helen, Kat and Ali among others for achieving the same without. Thanks to Jamie, Nik and Tim for their help during my Part II year so that I could reach the start of my D. Phil.

Max deserves acknowledging for his assistance during the end stages of writing up, although the extent that he helped is debatable. Steph became a great help towards the end of writing up and during preparation for the viva, for which I'm very thankful.

Last, but certainly not least, I must thank my family for the love and support they have given, and especially my parents, Clive and Stephanie. Mum and Dad have always been a steady influence throughout my education and other endeavours, and have helped whenever needed, no matter what was asked of them. I am truly thankful for all that they have done and hope that they are proud.

Contents

Chapter 1

Introduction

The principal property of a given atomic or molecular species is the energy portioned into its various degrees-of-freedom. Of these, the translational energy of that species is both the easiest to comprehend and the easiest to have some element of control over. The Maxwell-Boltzmann distribution of a gaseous species provides that at an average ensemble temperature, T, the probability of a species in the ensemble having a particular speed ν will be

$$f(\nu) = \left(\frac{m}{2\pi k_B T}\right)^{3/2} 4\pi\nu^2 \exp\left(-\frac{m\nu^2}{2k_B T}\right). \tag{1.1}$$

It is thus clear that reducing the temperature and the range of velocities of a sample go hand in hand. The velocity considered in the expression above need not necessarily be velocity in the laboratory frame, and on occasion the centre-of-mass velocity of colliding partners is considered instead. However in many cases these frames are one and the same.

Outside of the laboratory, the Universe possesses a range of temperatures from 10^7 K in stellar interiors and in the warm-hot intergalactic medium to 30 K in most dark molecular clouds. Continued expansion of the Universe since recombination, the period approximately 300 000 years after the Big Bang when free protons and electrons combined to form neutral hydrogen atoms, has red-shifted the photons passing through the Universe at the time of recombination, so reducing the characteristic background temperature of the Universe to 2.7 K. In general this cosmic microwave background (CMB) radiation is pervasive and so effectively sets a lower temperature limit that will steadily decrease upon further expansion. However certain conditions can allow for lower temperatures to be reached in some dark molecular clouds, such as the Boomerang Nebula, with a temperature of approximately 1 K [1] possible by a combination of absorption of CMB photons and adiabatic expansion of the cloud. Somewhat closer to Earth, the atmospheric chemistry of Titan has generated great interest since the arrival of Cassini-Huygens in the Saturnian system in 2003, with atmospheric temperatures in the range of 70-100 K [2]. However, in the artificial environment of the laboratory, temperatures far closer to absolute zero can be achieved.

No discussion of low temperature molecules would be complete without some consideration of internal energies versus absolute energies. Pioneering experiments by Herschbach and Lee in the 1960s greatly advanced the use of pulsed molecular beams as a source of molecules suitable for investigations in the so-called collisionless regime. In using a free-jet expansion from a high pressure regime to a near-vacuum, adiabatic expansion of the gas results in the conversion of relative translational and internal energy into forward motion. This method has since proved invaluable in the field of chemical physics by enabling the creation of packets of molecules that are internally cold. However, the formation of an internally cold beam does not reduce the total energy of the system and so cannot be considered truly low-energy.

Research in cold chemistry and physics, where quantum effects start to dominate over classically expected properties, has grown significantly in the last thirty years. Notable advances in the field have included the demonstration of laser cooling of Na atoms in 1985 [3] and creation of Bose-Einstein Condensates of Li [4], Na [5], and Rb [6], all in 1995. As has been the case in other fields, both these advances used alkali atoms to reduce the complexity of these pioneering experiments.

Subsequent advancements of these methods for cooling atoms and molecules have allowed progression in two similar directions: the first, to investigate the properties of quantum systems at the lowest temperatures possible (in the ‘ultracold’ regime, $T < 1\ \mu$K); the second, to achieve suitable densities of atoms and molecules at low temperatures to permit investigation of chemical processes with relevance to a wide range of fields in physical chemistry.

As ever lower temperatures are accessed, it becomes less appropriate to describe atoms and molecules classically as particles. This is exemplified by studying the de Broglie equation, where the thermal de Broglie wavelength, Λ, for a thermal sample is given as

$$\Lambda = \frac{h}{(2\pi m k_{\mathrm{B}} T)^{1/2}} \tag{1.2}$$

where h is Planck's constant, m is the mass of the atom or molecule, k_{B} is Boltzmann's constant and T is the temperature. Using ammonia as an example molecule, at 300 K, $\Lambda = 24.4$ pm, at 1 K, $\Lambda = 423$ pm and at 1 μK, $\Lambda = 423$ nm. The N-H bond length is 101 pm – this is far greater than the de Broglie wavelength at 300 K and so the approximation of NH_3 as a classical particle is reasonably valid at high temperatures. However, at 1 μK the de Broglie wavelength is much larger than the bond length and so the molecule must be considered quantum mechanically. At 1 K an intermediate state occurs, with quantum effects affecting properties of the molecule but not necessarily dominating.

From this, another important quantity relevant to low temperature studies is the phase-space density, defined as $\rho = \Lambda^3 n$, where n is the density of the gas and Λ is the de Broglie wavelength. As ρ increases, the sample of molecules gets closer to quantum degeneracy, wherein new states of matter are formed from many-body interactions. For Bose Einstein condensation to occur, a phase-space density of $\rho > 2.612$ must be achieved [6]; it thus becomes evident that the atoms or molecules must not only be sufficiently cold, they must also be of a sufficient density to interact with each other. The final phase-space density that can be obtained by a particular technique can give an indication of magnitude that quantum effects will have on the system. Of course, quantum degeneracy can occur not only at low temperature extremes, but also at extremely high densities, for example neutron degeneracy in neutron stars.

1.1 Low temperature chemical dynamics

Collisions between molecules can either be elastic, where translational kinetic energy is maintained, or inelastic, where the translational kinetic energy changes. At ultralow temperatures, elastic and inelastic collisions are governed by different scattering rate laws [7]. In both cases, at the lowest energies only s-wave scattering can occur, with higher orbital angular momentum states energetically prohibited by the centrifugal barrier that arises as the two species approach. The dependence of the cross-sections of low-energy collisions upon the available energy were summarised by Eugene Wigner in the context of nuclear reactions, with a number of different threshold laws depending on the nature of the collision [8]; the laws derived by Wigner are also applicable for molecular collisions at sufficiently low energies. From these threshold laws, one can predict the scattering behaviours when only s-wave scattering is possible; the scattering cross-section for inelastic collisions is inversely proportional to $T^{1/2}$, whereas for elastic collisions the scattering cross-section becomes independent of temperature. The $T^{1/2}$ dependence can be rationalised by the interpretation that the scattering species will spend longer interacting with each other when at lower energies; the constant cross-section for elastic collisions arises due to quauntum reflection between the entrance and exit channels.

At higher temperatures, additional partial-wave scattering channels open when there is sufficient energy available to overcome the centrifugal barrier, such that reactive collisions can occur with non-zero orbital angular momentum. Scattering lengths can also be dramatically enhanced if the collision energy happens to be equal to a resonance between the species, for example a Feshbach resonance (when the collision energy is at the same energy as a bound state on a different potential energy surface) or a shape resonance (a quasibound state bounded by the centrifugal barrier). This can lead to a quite complex relationship between temperature and the collision cross-section in the intermediate-temperature range from 1 μK to 1 K, examples of which can be seen in Refs. [9, 10]. As temperatures increase further still, the scattering rates will become closer to that expected classically with scattering rates now broadly modelled using the Arrhenius equation.

The relative scattering rates for elastic and inelastic scattering are dependent not only on the identities of the scattering species but also the state of these species. When elastic scattering rates are sufficiently greater than inelastic scattering, an already cooled species could be used to sympathetically cool another species that cannot otherwise be cooled, as predicted in the case of *eg* Mg to cool NH [11]. The presence of electric or magnetic fields can also have a dramatic effect on scattering rates, as observed in the reaction of Rb with NH_3 [12], as well as the commonly used technique of Feshbach molecule creation [13].

In both cases, the long-range potential energy surface can have a significant effect on the scattering rates in a particular system. Studies by Clary and co-workers have shown a strong dependence on the radial exponent of the long-range potential [14].

In any event, the chemical reactions studied at low temperatures are restricted to a few classes. This is because the low energies of the reacting species will make any reaction with an activation energy present prohibitively slow, unless there is a significant contribution from quantum mechanical tunnelling through the barrier. A reduction in the reaction rate can even be observed due to the presence of a submerged barrier, for example in the reaction between Ca^+ and methyl halides [15, 16]. Thus, in the absence of tunnelling, any reaction studied must be barrierless. Classes of barrierless reactions include ion-molecule reactions (for example Ref. [17]), radical reactions (*eg* Ref. [18]) and atom-molecule reactions (*eg* Ref. [19]). Moreover, reactions can be induced after excitation, for example unimolecular decomposition and bimolecular reactions involving electronically excited molecules (*eg* Refs. [20, 21]).

1.2 Quantum information processing, Fundamental Model testing, and metrology

The exquisite control that can be achieved over cold atoms and molecules combined with the narrow transition linewidths that can be interrogated make these cold species ideal for studies of fundamental quantum systems, and for enhancing precision in measurements of fundamental constants.

The reduced linewidths that can be observed can be attributed to two factors. With the reduced motion of the coldest species, the spread in velocities in the direction of the interrogating radiation necessarily reduces. Consequently, Doppler broadening, defined as

$$\Delta\lambda = \sqrt{\frac{8k_bT\ln 2}{mc^2}}\lambda_0 \tag{1.3}$$

where $\Delta\lambda$ is the Doppler width for a central wavelength λ_0, will reduce as the temperature decreases. Furthermore, since the species travels so slowly through the spectroscopic cell, the interaction lifetime is also increased and so lifetime broadening becomes less significant, with the magnitude of the broadening inversely proportional to the interaction lifetime. This can particularly be the case when the cooled species are propelled upwards. These species experience the gravitational force and will continue to slow, providing a large integration time at the turning point. This technique is commonly used in atomic clocks, for example ^{87}Rb and ^{133}Cs atomic fountains [22]; experiments that can take advantage of this effect have also been theorised for molecules [23].

Such reductions in spectroscopic linewidths can enable more rigorous testing of fundamental models of quantum mechanics that can be difficult to achieve otherwise. A good example of this is seen in experiments searching for the electric dipole moment (EDM) of the electron. In the standard model of particle physics, the electron EDM is predicted to be non-zero but far smaller than can be experimentally detected at present. Measurement of a non-zero electron EDM larger than that suggested by the standard model would provide further evidence of the need for an extension to the standard model, for example by incorporation of supersymmetric particles into the model. The most precise measurements to date have used ThO molecules from a cryogenic buffer gas source, but have not yet discovered a non-zero electron EDM [24]. Alternate schemes that use a source of translationally cold YbF have also been devised [25] that could yield greater precision than prior measurements of the electron EDM in translationally hot YbF [26]. Cold molecular ions, such as HD^+ in the case of Schiller and co-workers [27], can also be used for tests of fundamental models, with 2-ppb accuracy possible in determination of vibrational energy levels of HD^+. At this level, effects of quantum electrodynamics can be compared with those calculated previously.

Pioneering studies by Wineland and co-workers have displayed the extent to which strings of ions can be manipulated while maintaining quantum coherence. Included in these studies is the ability to transfer motional entanglement to spin entanglement and vice-versa [28]. In addition, use of ultra-stable cavities has facilitated an Al^+ optical clock with an inaccuracy $< 1 \times 10^{-17}$ [29]. Experiments of a similar nature have been performed by Haroche and co-workers, primarily with ^{85}Rb atoms, in which cavity QED is used to produce entanglement between cavity photons and atomic spins, examples of which can be found in Refs. [30, 31]. For this work Wineland and Haroche were awarded the Nobel Prize in Physics in 2012.

1.3 Methods of cold molecule production

As the field of cold gas-phase science develops, new methods continue to be developed that both broaden the classes of species that can be cooled sufficiently, and further the cooling of these species. Production of cold molecules fall under two principal categories: cooling of a portion of a hot molecular sample (otherwise known as direct cooling), and formation of a cold molecule from a reservoir of cold atoms (indirect cooling). The relative simplicity of the structure of an atom can be regarded as a blessing and a curse, and the methods used for atoms and molecules vary accordingly. These two different classes of methods will thus be considered separately.

1.3.1 Indirect cooling

The simplicity of an atomic species means that there is a reduction in the difficulty in maintaining a population in a particular state, as required for laser cooling which is discussed further in chapter 2. The magnetic dipole moment of open-shell atoms also allows for magnetic trapping of the atoms. Reduction of the magnetic field can permit evaporative cooling, reducing the average temperature of an ensemble by removal of the hottest atoms.

These techniques have enabled preparation of a number of atomic species into a Bose-Einstein condensate (BEC), and similarities between BECs and Bardeen-Cooper-Schrieffer (BCS) states, such as those found in low temperature Type I superconductors, explored [32, 33]. Techniques of forming BECs have since developed further, and molecular BECs can be formed, including from Fermi degenerate gases [34].

Control of interactions between atoms also allows the formation of a range of exotic molecules. The first category of exotic molecules was alkali metal dimers, due to the ease of obtaining low-energy alkali atoms. These molecules were first created by photoassociation, in which two atoms, approaching each other on the ground potential energy surface (PES), are excited onto a higher-energy PES; the photon energy of the photoassociating laser is lower than the asymptotic energy difference between the two PESs to create a bound excited-state molecule. Initially, homonuclear dimers of cold Na atoms [35] and Rb atoms [36] were formed in 1993; since then, photoassociation of heteronuclear dimers has been seen, firstly for RbCs [37] in 2005. In addition, weakly-bound molecules can be created by careful adjustment of the potential interaction between the two atoms. The first demonstration of a so-called Feshbach molecule, created by adjustment of a magnetic field to form a weakly bound dimer, was of $^{87}Rb_2$ by Wieman and co-workers [38]. Denschlag and co-workers subsequently showed that the lifetime of these Feshbach molecules can be significantly increased by trapping the cold atoms in a three-dimensional optical lattice, reducing scattering rates between molecules [39]. This process is quite specific to alkali metal dimers, however, and a good deal of information about ground and excited level potential energies is required to create these dimers.

Due to the large interatomic distances for both photoassociated and Feshbach molecules upon formation, these molecules are often in a highly excited vibrational state. The application of stimulated Raman adiabatic passage (STIRAP) [40] to these cold molecules allows efficient transfer from these excited states into the ground vibrational state via an excited electronic state. This process was first demonstrated in 2008 for homonuclear Rb_2 [41] and heteronuclear KRb [42]. With the majority of molecules now in the ground rovibrational state, the inelastic scattering rate is significantly reduced and the molecule lifetime enhanced. This permits reactive scattering experiments to be performed as exemplified in reaction of ground-state KRb [43].

An extension of the properties used for creating these diatomics can be applied to the formation of so-called Efimov trimers. In these trimers it is customary to think of the molecule as created by a dimer and a single atom. The resulting principles, including that of the scattering cross-section, are then similar to those of a dimer formation [44]. However, Efimov trimers are formed by a purely quantum effect and would not be predicted to exist by simple bonding theory; the absence of one of the atoms would preclude bonding between the remaining two atoms [45].

Lasers can be used, in addition to cooling atoms and neutral species as described in chapter 2, as a method of restricting molecular motion. The ability to create standing wave fields in the presence of cold atoms can create a series of shallow traps for individual atoms or molecules – a so-called optical lattice. These lattices can be extended to three dimensions to form 3D arrays of atoms, or atoms can be confined in fewer dimensions to create strings or planes of cold atoms. In this way, and in combination with other methods of ultracold molecule formation, oriented reactions can be investigated, for example the bimolecular reaction of oriented KRb [46].

1.3.2 Direct cooling

Although molecules created from cold atoms have energies far lower than pre-existing molecules that have been cooled, the chemical variety of directly cooled molecules is much greater, in part due to the limited number of elements that can be cooled to sub-Kelvin temperatures and then used as molecular building blocks. Due to the great variety of properties that can be displayed by molecules, there are thus a large number of methods for directly cooling molecules, depending on the molecular property chosen.

The presence of a permanent dipole moment in molecules is used in many techniques, due to appreciable potentials that can arise from high electric or magnetic fields. An example of this is the use of a bent electrostatic quadrupole, initially demonstrated by Rempe and co-workers [47]. In this technique, the weak Stark potential in the quadrupole guides the slow portion of a Boltzmann distributed source around the bend, while faster molecules have sufficient energy to exceed the Stark potential and are lost. However, due to the initially warm source temperatures, a range of rotational states are present with different resulting Stark shifts. The rotational distribution that results can thus be non-thermal, although a characteristic temperature is often assigned [48]. In addition, little rotational cooling is seen when solely using this technique [49].

Another major source of cold molecules is from Stark deceleration, where time-dependent electric fields are used to convert kinetic energy into potential energy and so decelerate molecules. Discussed further in chapter 3, the importance of this technique, first demonstrated by Meijer and co-workers in 1999 [50], is profound. Analogous to this, Zeeman deceleration, instead using time-dependent magnetic fields [51] and AC Stark deceleration using optical [52] or microwave [53] fields are also possible.

In addition to cooling methods that involve repetition of an individual process which removes a fraction of the energy of a molecule each time, cold molecules can be made in a rather more dramatic fashion by collisions in crossed molecular beams, or momentum cancellation through photodissociation. In the former method, an atom in one beam can collide with a molecule of interest in the other beam. For a fraction of the molecules, the impulse experienced by the molecule is in the opposite direction to the initial velocity, so if the final state of the molecule is such that the impulse is equal in magnitude to the initial momentum then the velocity can be cancelled out. This was initially demonstrated by Chandler and co-workers to kinematically cool NO through collisions with Ar [54], and subsequently ND_3 [55]. Careful tuning of the photodissociation wavelength for a small molecule allows the recoil velocity of the fragments to be controlled; if the magnitude of the recoil velocity is equal to the magnitude of the velocity of the molecule prior to dissociation, a portion of fragments can thus formed with a velocity distribution centred around zero-velocity, which has been demonstrated for molecular [56] and atomic fragments [57].

Some techniques can be equally valid for a diverse range of atoms and molecules. The propensity for high vapour pressures of helium to be obtained at low temperatures allows a facile method for cooling atoms and molecules [58], independent of the requirement for a permanent dipole moment. The combination of a relatively high density of He atoms (on the order of 10^{15} cm^{-3} [59]) at low energies (typically ~ 5 K) ensures a high number of collisions with the species of interest, which collectively serve to thermalise the species to the temperature of the He atoms; this process is referred to as ‘buffer gas cooling’. Buffer gas cooling can also be extended to cooling ions, a reasonably common feature in ion mass spectrometry [60], as well as for studying reactions of trapped ions if they experience little driving motion [61]. In addition to being used as a stand-alone cold molecule source, combinations of a buffer-gas cooler with bent electrostatic quadrupoles [62] have been demonstrated. In contrast to bent quadrupoles with a room temperature beam source, buffer-gas cooled sources are internally cold as well as externally cold.

As well as being cooled by buffer gas, species can be cooled by seeding in a liquid helium nanodroplet [63]. In this technique, the He valve is cryogenically cooled; when open, the high pressure behind the valve combined with supersonic expansion causes the formation of droplets, commonly containing thousands of He atoms. The droplets then pass through a scattering chamber containing the species of interest, and can ‘pick-up’ one of these species. Due to the liquid nature of the droplet, a temperature of 0.38 K is achieved, with evaporation of helium atoms preventing rises in the droplet temperature. Using helium-3 results in a lower droplet temperature of 0.15 K [64]. Although often only one atom or molecule of spectroscopic interest is desired per droplet, when two or more species are added to a droplet, reactive scattering can occur [65], and spectroscopic measurements can be performed on exotic species [66]. Depending on the nature of the species picked up by the droplet, it may reside either on the surface or the centre of the droplet, with different properties observed [67].

Cold reactive collisions can also be investigated within an individual beam if sufficient reactive collisions occur. One method to achieve this is to use a specially shaped nozzle to ensure that molecules leave the nozzle with a uniform direction and speed, thus maintaining a high and uniform molecular density for up to a metre from the nozzle exit. This technique, deemed the CRESU technique when originally devised by Rowe *et al* [68], was first used for studies of ion-molecule reactions at low temperatures and expanded for neutral-neutral reactions by Sims *et al* [69], has allowed sensitive kinetics measurements to be made on a range of reactions of astrochemical interest. Although the molecules in the flow have only a low internal temperature, similar to that of a pulsed molecular beam, the density in the flow is sufficient for appreciable collisions between the molecules in the flow. Use of a liquid nitrogen cooled stagnation chamber and nozzle, to reduce the gas temperature prior to supersonic expansion, has allowed flow temperatures and collision energies down to 6 K to be achieved [70]. Pulsed versions of the CRESU system can also be used, principally by using a pulsed gas source prior to the nozzle [71]. Pulsed CRESU can reduce gas consumption rates for kinetics studies, although the flow temperatures obtained are generally higher for a given nozzle than using a continuous flow.

Combinations of cold molecule sources with more traditional spectroscopic and dynamical techniques can also allow advances in other areas that might not have been originally foreseen. An example of this is shown by Patterson *et al* in which a buffer gas cooled sample of 1,2-propanediol, an optically active molecule, is interrogated in a Fabry-Pérot microwave cavity [72]. The use of cold and translationally slow molecules with polarised microwave fields allows distinction of the two enantiomers by noting the phase of the subsequent free induction decay of the rotationally excited probed molecules.

1.4 Scope of this thesis

This thesis is concerned primarily with developments towards studying cold chemical collisions involving ions and molecules. One advance shown by this thesis is the combination of cold, state-selective sources of molecules and atomic ions to facilitate low collision energy scattering events with state selectivity in both reactants.

After introducing the general field of cold chemistry and physics here, chapter 2 provides a description of the methods used for trapping and cooling ions that are used both as reactants and as a probe for reaction events. The energy distribution of trapped ions is also considered, and the effects on scattering collision energies considered. Chapter 3 describes the second major component of the experimental setup, a method for decelerating neutral dipolar molecules. This is considered for deceleration of ammonia, with the aim of maximising energy resolution and molecular flux at the ion target.

Chapter 4 describes experimental techniques relevant to the combined experimental setup and an example reaction involving focussed ammonia molecules that have been examined with the new experimental setup, which is used to exemplify future reactions of interest. Chapter 5 examines both destructive and non-destructive methods that are used to identify trapped ions that could not otherwise be determined with conventional techniques.

Chapter 2

Trapping and cooling ions

A key component of the experiment described in this thesis is the source of cold ions. The theory behind trapping and cooling of individual ions is discussed, before ensembles of ions are considered. The method of laser cooling is described, with a focus on the cooling scheme for Ca^+ ions, and ensembles containing ions that cannot be laser cooled examined. The thermal properties of the ions are described, and the consequences on studying cold chemical reactions considered.

2.1 Ion trapping

Unlike cold neutral species, high densities of which can be maintained for several milliseconds without the need for trapping forces, ions of like charge strongly repel each other due to the Coulomb potential. External forces are thus required to contain an ensemble of ions at a suitable density for any reasonable amount of time. Ions are easily manipulated with electric fields, with substantial imparted forces achievable when using comparatively small voltages.

The electrostatic potential, ϕ, between charged electrodes is evaluated by solution of the Laplace equation,

$$\nabla^2\phi = 0, \tag{2.1}$$

which, when written in Cartesian co-ordinates in three dimensions, leads to the partial differential equation

$$\left[\frac{\partial^2}{\partial x^2} + \frac{\partial^2}{\partial y^2} + \frac{\partial^2}{\partial z^2}\right] \phi = 0. \tag{2.2}$$

The obvious result from this is that at no point in space can there be a potential minimum in all directions, and thus no trapping is possible when solely using static voltages to create a static potential, as stated in Earnshaw's theorem [73]. This problem can be overcome by combining electric fields with magnetic fields, as achieved in a Penning trap [74, 75], or by using time-varying voltages to create a varying potential. This second technique is used in a range of trap geometries which are collectively named Paul traps after Wolfgang Paul. Both types of traps are commonly used; for this Hans Dehmelt, designer of the first Penning trap, and Paul were awarded the Nobel Prize in Physics in 1989.

Two main categories of Paul traps exist: spherical Paul traps, based upon the original design by Paul and Steinwedel [76], and linear Paul traps. The principal difference between these is the fact that a spherical Paul trap uses oscillating voltages for confinement in all directions. There is thus a single point in space at the centre of the trap where there is no oscillation in the potential. A linear Paul trap however uses static voltages in one direction and so has no oscillating potential along the principal axis of symmetry in the trap. Since an oscillating potential induces an oscillation in the motion of an ion, with a greater oscillation in the potential inducing more motion, a linear trap is thus desirable for cooling a large number of ions. In addition, linear traps provide easier optical access and are less challenging to construct, since cylindrical electrodes are commonly used as opposed to the hyperbolic electrodes required for a spherical trap.

Linear Paul traps are themselves split into a number of categories depending on the number of trapping electrode stacks: the most common varieties are the quadrupole, octupole and 22-pole traps, with the trap order given by the number of electrode

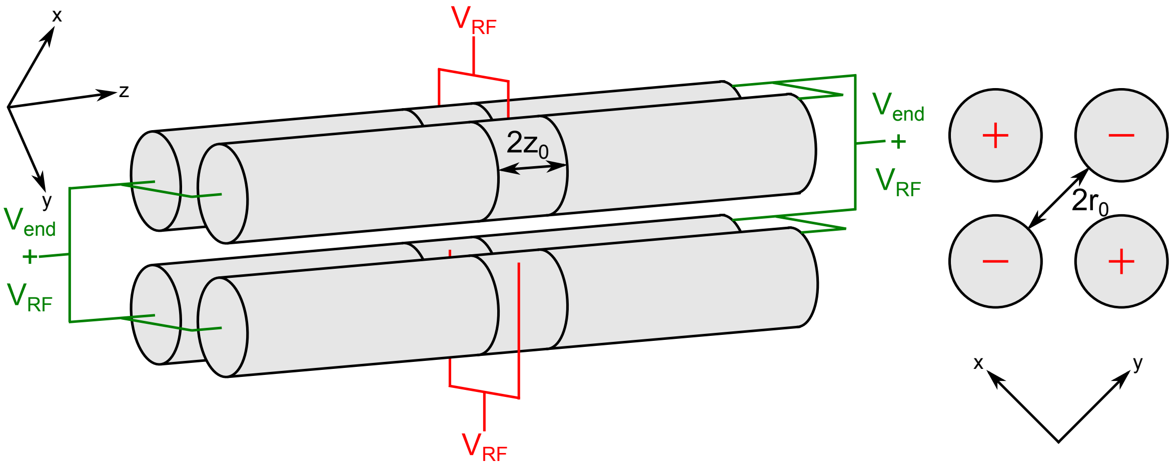

Figure 2.1: Voltages applied to the ion trap (left), designated V_{RF} for the RF voltage and V_{end} for the end-cap voltage. Phase of the RF voltage applied to each electrode rod (right).

stacks. This chapter is predominantly concerned with the linear quadrupole trap; higher-order traps are briefly discussed at the end of the chapter.

A linear Paul trap typically uses segmented electrode stacks, as described below, or distinct electrodes to carry different voltages [77]. When using segmented electrodes, two kinds of voltages are selectively applied to each electrode, as seen in figure 2.1: an oscillating voltage that alternates in sign on adjacent electrode rods, applied to all electrodes; and a static voltage applied to the first and last segments of each stack. These trapping voltages are respectively referred to as the radial and axial (or end-cap) trapping voltages. The overall trapping potential is thus equal to the sum of the potentials due to these voltages

$$\phi_{\mathrm{trap}}(x, y, z, t) = \phi_{\mathrm{RF}}(x, y, t) + \phi_{\mathrm{end}}(x, y, z). \tag{2.3}$$

The axial trapping potential can be expressed by a Taylor expansion around the trap centre, with the potential at the trap centre defined to be zero. At small distances from the axial symmetry plane of the trap, the only significant term in the expansion is proportional to the square of the axial displacement of the ion. The linear term in the expansion is assumed equal to zero due to the trap symmetry normal to the principal axis when equal voltages are applied to each end-cap, while higher-order terms are assumed to be negligible compared to the quadratic term at the displacements considered (< 1 mm from the trap centre). The axial potential is thus

$$\phi_{\text{end}}(x, y, z) = \frac{\kappa V_{\text{end}}}{z_0^2}\left(z^2 - \frac{(x^2 + y^2)}{2}\right) \tag{2.4}$$

where V_{end} is the end-cap voltage and $2z_0$ is the distance between first and last electrodes in each rod. κ is the proportionality constant required for the potential to match the harmonic approximation. The repulsive terms in x and y are required to satisfy the Laplace equation, and are equal in magnitude due to radial symmetry in the trap.

The radial trapping potential is dependent on the trap order, which depends on the number of electrode rods; the following discussion concentrates on a quadrupole trap, while the case for a general linear trap is described in Ref. [78]. For a linear quadrupole trap, at small displacements from the trap axis the radial potential can again be approximated as a harmonic potential. The instantaneous potential is given as

$$\phi_{\text{RF}}(x, y, t) = \frac{V_{\text{RF}}}{2}\left(\frac{x^2 - y^2}{r_0^2}\right)\cos\left(\Omega_{\text{RF}} t\right) \tag{2.5}$$

where V_{RF} and Ω_{RF} are respectively the amplitude and frequency of the radio-frequency (RF) voltage, $2r_0$ is the minimum distance between diagonally opposite electrodes. From this, it is clear that if only static voltages are applied no trapping is possible; ions could only remain in the trap if they are completely stationary and sitting on the saddle point of the potential, along the trap axis. However, rapid oscillation of the radial voltages to consecutively create saddle points in orthogonal directions effectively creates an overall trapping potential. This radial trapping potential is additionally sufficient to overcome the radial repulsive terms that arises from the axial trapping potential and the Coulomb repulsion between like-charged ions to allow trapping of many ions.

Combination of the axial and radial potentials gives the overall instantaneous trapping potential

$$\phi_{\text{trap}} = \frac{V_{\text{RF}}}{2}\left(\frac{x^2 - y^2}{r_0^2}\right)\cos\left(\Omega_{\text{RF}}t\right) + \frac{\kappa V_{\text{end}}}{z_0^2}\left(z^2 - \frac{x^2 + y^2}{2}\right). \tag{2.6}$$

This potential can now be incorporated into the equations of motion for a trapped ion. As motion in each dimension is independent of motion in other dimensions in a quadrupole trap, three independent equations of motion can be obtained. Since

$$\begin{aligned}
\boldsymbol{F} = m\boldsymbol{a} = -Q\nabla\phi, && (2.7)\\
\Rightarrow \ddot{x} + \left(\frac{QV_{\text{RF}}}{mr_0^2}\cos\left(\Omega_{\text{RF}}t\right) - \frac{\kappa QV_{\text{end}}}{mz_0^2}\right)x = 0 && (2.8)\\
\ddot{y} + \left(-\frac{QV_{\text{RF}}}{mr_0^2}\cos\left(\Omega_{\text{RF}}t\right) - \frac{\kappa QV_{\text{end}}}{mz_0^2}\right)y = 0 && (2.9)\\
\ddot{z} + \left(\frac{2\kappa QV_{\text{end}}}{mz_0^2}\right)z = 0. && (2.10)
\end{aligned}$$

where Q and m are the charge and mass respectively of the ion under consideration.

These equations are all of the family of the Mathieu differential equations, which have the general form [79]

$$\frac{d^2u}{d\zeta^2} + \left(a - 2q\cos 2\zeta\right)u = 0. \tag{2.11}$$

Equations 2.8 to 2.10 are transformed into this general form using the substitutions

$$\begin{aligned}
a_x = a_y = -\frac{\kappa QV_{\text{end}}}{m\Omega_{\text{RF}}^2 z_0^2}; \quad a_z = -2a_x && (2.12)\\
q_x = -q_y = \frac{QV_{\text{RF}}}{m\Omega_{\text{RF}}^2 r_0^2}; \qquad q_z = 0 && (2.13)\\
\zeta = \frac{\Omega_{\text{RF}}t}{2} && (2.14)
\end{aligned}$$

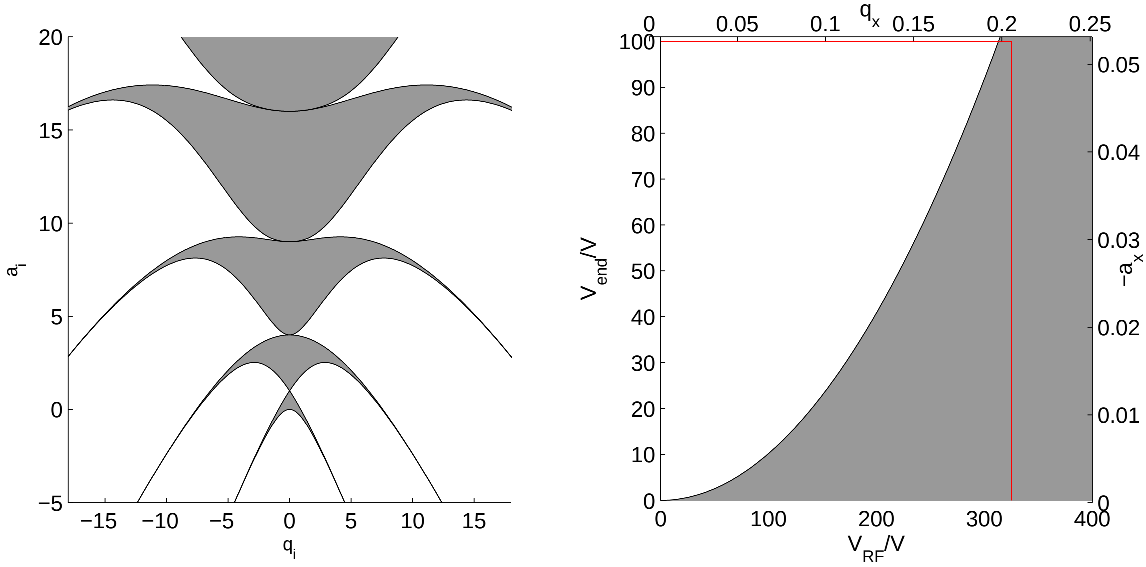

Figure 2.2: Regions of stability (shaded) for the linear quadrupole trap that correspond to periodic solutions of equation 2.11, using generalised Mathieu parameters (left) and by multiplication of the a_i and q_i parameters by the scaling factors for the Oxford ion trap (right). Limitations of experimental voltages are shown in red.

where a_i and q_i are the relevant substitutions for each dimension. Solution of the Mathieu equation gives periodic or non-periodic solutions dependent of the values given to a_i and q_i, which are seen in figure 2.2, the regions being bounded by the eigenfunctions of the Mathieu equation. Periodic solutions obtained correspond to a stable ion trajectory inside the trap, and hence the ion is trapped, whereas non-periodic solutions lead to rapid ejection of an ion from the trap.

Although many regions of stable trajectories are evident, most are inaccessible due to the fact that a_x and a_y must both be negative since a_z must be positive to ensure periodic solutions are obtained when a_z in equation 2.12 is substituted into the equation of motion along the z-axis, equation 2.10. Still other regions are discounted due to the high voltages required to access these regions, to give just one stability region of interest. Given the experimental limits of 325 V for the RF voltage and 100 V for the endcap voltage, for calcium ions trapped by a RF field with a frequency of 3.80 MHz this gives maximum Mathieu parameters of $a_x \approx -0.053$ and $q_x \approx 0.21$;

the range of voltages suitable for trapping within this range are shown on the right of figure 2.2.

From consideration of stable a_i and q_i it is clear that a suitable oscillation frequency is crucial to obtaining suitable Mathieu parameters and thus to ion trapping. If the oscillations are too rapid, the impulse applied to an ion during each cycle will be too small, and the resulting potential too shallow, to contain the ion. Conversely if the oscillations persist for too long, an ion will collide with an electrode before the RF voltages change sign. This effect can also be demonstrated mechanically, albeit more simply with a rotating potential as opposed to a oscillating potential.

Between these two unstable conditions lie an intermediate range of frequencies, for which the RF phase changes sufficiently rapidly for the ions to experience forces that lead to a stable trapped trajectory. When averaged over an RF cycle, the time-dependent forces lead to a radial trapping potential, which is also sufficiently deep to overcome the repulsion between ions in the trap. The derivation of the time-averaged 'pseudopotential' from the oscillating potential is shown rigorously in Ref. [78], and can be expressed as

$$V^*(R_0) = \frac{Q^2 E_0^2}{4m\Omega_{\mathrm{RF}}^2} + Q\Phi_s \tag{2.15}$$

where V^* is the time-averaged potential, R_0 is the average position of an ion in an RF cycle, E_0 is the amplitude of the oscillating electric field, and Φ_s is any electrostatic potential present. Assuming a zero-to-peak RF voltage of 150 V, and an RF frequency of 3.8 MHz, the trapping depth for a $^{40}\mathrm{Ca}^+$ ion is 7.6 eV. The trapping depth arising from this pseudopotential is not only sufficient to trap an individual ion, it exceeds the repulsion between two ions, and so more than one ion can be trapped, with the ion separation dependent on the depth of the pseudopotential. A large number of ions trapped together will form a spheroidal cloud, minimising the collective potential energy; the properties of these clouds are described further in section 2.4. With an ensemble of ions trapped, they are now ready to be cooled.

2.2 Laser cooling

Trapped ion densities on the order of 10^8-10^9 cm^{-3} are feasible using modest trapping voltages as above, with ensembles of ions numbering from 1 to 10^5 commonly encountered. This ensemble is now well suited for being cooled. For higher-order traps with a large, flat potential, trapped ions are contained in a relatively large volume; for these ions buffer gas cooling is a well-suited technique, and can reduce ion temperatures down to the range of several kelvins [61]. However, for quadrupole RF traps, the ions are confined to a cylindrical volume with a radius of tens-hundreds of microns. In this circumstance, for certain atomic ions, laser cooling provides a cooling technique to bring ions to millikelvin temperatures that is relatively simple to implement.

The technique of laser cooling was developed in the mid-1980s by several groups, including that of Chu[1] and co-workers [3], with initial laser cooling studies performed on alkali metal atoms, which all have a simple electronic structure at low energies. The processes that were developed for these atoms are equally relevant to the isoelectronic group 2 monocations, of which calcium is used in our experiment.

The process of laser cooling is conceptually simple to understand. Since a photon with wavelength λ has a momentum $p = h/\lambda$, absorption of a photon by an ion will affect the ion's momentum by that amount while electronically exciting the ion. After some period of time a photon shall be emitted from the excited ion, which will again affect the ion momentum by an amount equivalent to the photon momentum. Upon multiple absorption and emission cycles, a net force is experienced by the atom as photons are emitted near-isotropically[2] while the absorbed photons, coming from a laser beam, all have momentum vectors pointing in the same direction. The unidirectionality of the resultant force is achieved by detuning of the cooling laser to

---

[1] Chu, along with C. Cohen-Tannoudji and W. Philips were awarded the 1997 Nobel Prize in Physics for laser cooling.

[2] The presence of electric and magnetic fields cause a deviation from isotropic emission of the photon, but this is a minor effect.

lower frequencies and the Doppler shift induced by ion motion relative to the laser propagation, as described below.

Since the electronic transitions considered have a finite lifetime, the photon scattering rate, γ_p, for an atom can be written as [80]

$$\gamma_p = \frac{s_0\gamma/2}{1 + s_0 + (2\delta/\gamma)^2} \tag{2.16}$$

where δ is the laser detuning from the transition frequency, γ is the spontaneous decay rate of the excited state and s_0 is the on-resonance saturation parameter, given as

$$s_0 = \frac{2|\Omega|^2}{\gamma^2} = \frac{I}{I_s} \tag{2.17}$$

where Ω is the Rabi frequency, which corresponds to the coupling strength between the atom and the laser field, I is the intensity of the laser field and I_s is the transition saturation intensity. For a large ensemble of ions, this assumes a steady-state has been achieved, such that the rates of photon absorption and emission are equal.

If the detuning is zero, then maximum photon absorption occurs for stationary atoms, with equal probabilities of photon absorption for atoms moving with a given speed either towards or away from the laser propagation. However, if the frequency of the laser is decreased slightly[3], the maximum photon absorption occurs for atoms moving towards the laser, due to Doppler-shifting of the photon energies.

The force upon a stationary atom will be equal to the photon momentum multiplied by the scattering rate, *ie*

$$\begin{aligned} F &= (h/\lambda)\gamma_p \qquad (2.18)\\ &= \frac{(h/\lambda)s_0\gamma/2}{1 + s_0 + (2\delta/\gamma)^2} \qquad (2.19) \end{aligned}$$

---

[3] A process commonly known as red-shifting.

which, for non-stationary ions, must be modified to incorporate Doppler-shifting to give

$$F = \frac{(h/\lambda)s_0\gamma/2}{1 + s_0 + [2(\delta - \omega_D)/\gamma]^2} \tag{2.20}$$

where ω_D is the Doppler shift due to the ion motion, which is given as $2\pi\nu/\lambda$ when the ion has a velocity ν. From this, a laser that is sufficiently red detuned will only exert an appreciable force on atoms moving in the opposite direction to the laser direction. There is thus an impulse against the motion of the atom, retarding the motion of the atom in the direction of the laser. Due to this continual retarding force, laser cooling has also been referred to as ‘optical molasses’ when acting in all directions.

When the ions are still hot, laser cooling is most rapid when the product of the photon absorption rate and momentum transfer per photon is maximised. It is thus beneficial to maximise the laser powers when initially cooling ions. Once the ions have reached low temperatures, the minimum obtainable temperature is a function of the laser detuning and the laser power, which are adjusted in light of this.

A key difference in the implementation of laser cooling for atoms and ions is the number of laser beams required to efficiently cool the desired species. Since atomic species only interact very weakly with each other and with external trapping fields, each atom can be considered independent of the other atoms. Thus, the atoms must be cooled in each dimension, and from both directions in each dimension, to remove the kinetic energy in each dimension; a total of six mutually perpendicular beams. However, for ions, fewer lasers are needed since the ions interact strongly with each other and remain trapped, even when the ions possess large amounts of kinetic energy.

For large ion ensembles, a laser beam in a single dimension is sufficient, since the Coulomb force between ions effectively couples the radial and axial components of the ions’ thermal motion in the trap. A reduction of the axial thermal energy will thus also reduce the radial thermal energy until the two have equilibrated. This process continues until motion in all directions is reduced to sub-Kelvin temperatures. For linear traps, axial cooling is most efficient, since there is no RF-heating in the axial direction to modulate axial velocities. Laser cooling from just one direction in this dimension is also feasible, since hot ions will oscillate back and forth in the trap, so will spend approximately half the time travelling in a suitable direction to be cooled.

For small ensembles of a few ions, and in particular single ions, an additional laser beam perpendicular to the primary cooling laser is beneficial to reduce radial motion which may not be as efficiently coupled as in a large ensemble. The reduced efficiency in cooling transverse motion is particularly evident for single ions, where there is significant smearing of the fluorescence profile if only an axial laser is used.

The discussion above assumes that there are only two relevant energy levels, and transitions only occur between these two levels. This assumption is only valid for a few atomic species, such as Na, Be^+ and Mg^+. However, the two-level model can still be used in a modified form for more complicated systems if the number of accessible energy levels is small and significant populations can be maintained in the two relevant energy levels. If this is satisfied, a closed cooling cycle is said to occur. For certain ions and neutral atoms with a closed cooling cycle, laser cooling involving more than two levels still provides an efficient means of reducing the temperature of selected ions to the millikelvin regime without much added complexity. All group 2 monocations fall into this category, with particular emphasis in this thesis given to laser cooling of $^{40}Ca^+$. Minimising the range of accessible levels is important to reduce the number of lasers required to restore population to the cooling transition.

The singly charged calcium cation has an argon-like electron core, and a valence electron in the 4s orbital. The lowest electronically excited states occur when the valence electron is excited to either the 4p or the 3d orbital; these states are both split by spin-orbit coupling into two J-levels. Since an atom possesses no rotational or vibrational motion, the energy levels of calcium depend solely upon the electronic configuration, giving a simple set of low-lying energy levels, shown in figure 2.3, which

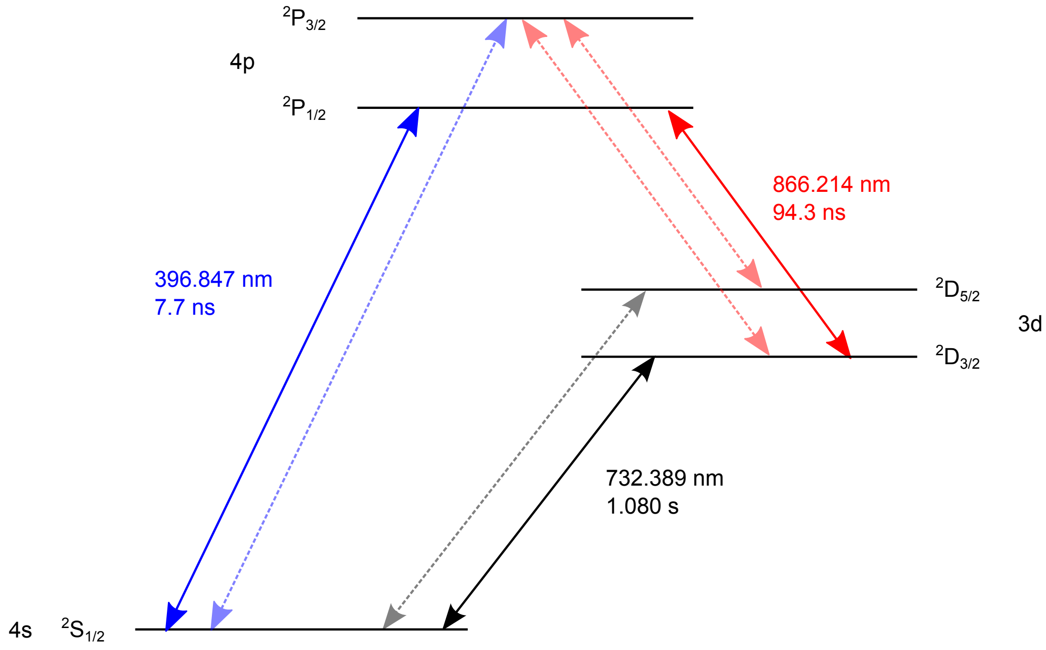

Figure 2.3: Low level electronic states of the Ca^+ ion, and associated wavelengths for $^{40}Ca^+$. Transitions relevant to our laser cooling scheme are denoted by solid lines, transitions in schemes used elsewhere by dashed lines. Transition wavelengths and decay lifetimes from Ref. [81].

becomes a closed cycle with a small number of lasers.

A consequence of using calcium as the laser-cooled ion is that the 3d level is lower than the lowest unoccupied 4p level, a case that also similarly arises with heavier group II cations and the neutral group I analogues. For both magnesium and beryllium ions, the 3d orbital is at significantly higher energies than the lowest unoccupied p orbital (ca 35,000 cm^{-1} and 65,000 cm^{-1} respectively). Thus the cooling cycle is closed for both of these ions when using just one cooling laser, at a wavelength of 313 nm for $^9Be^+$ [82] and 280 nm for $^{24}Mg^+$ [83]. However, Ca^+ ions in the 4p $^2P_{1/2}$ state can relax to the 3d $^2D_{3/2}$ state in addition to returning to the 4s $^2S_{1/2}$ state. Both transitions are fully allowed, and so the relaxation rate and resultant branching probabilities are determined by the Einstein A coefficients. In this case, 7.5% of the 4p $^2P_{1/2}$ population relaxes to the 3d $^2D_{3/2}$ state. Ions in the 3d $^2D_{3/2}$ state are metastable with no dipole-allowed transition to the 4s $^2S_{1/2}$ state. If the ions are not removed from this state, the metastable population would rapidly increase and laser cooling would cease. Thus a second laser is required to transfer the population from the 3d $^2\mathrm{D}_{3/2}$ state back to the 4p $^2\mathrm{P}_{1/2}$ state. The added complexity of requiring a second laser to cool Ca^+ is somewhat compensated by the fact that the transition wavelengths can now be accessed using the fundamental output of cw-diode lasers.

The efficiency of laser cooling is principally governed by two factors: the power of the cooling laser (in future discussion, the “cooling laser” will in general be referring to the 397 nm laser, since this drives the main cooling transition) and the detuning of the cooling laser from the electronic transition. Optimal cooling is achieved when $\delta = -\gamma/2$, which in the case of $^{40}\mathrm{Ca}^+$ is equal to a red detuning of ~ 65 MHz.

The minimum achievable temperature when laser cooling is the so-called Doppler limit, T_D, related to the linewidth of the cooling transition. In determining this limit, the cooling rate derived from equation 2.20 and the heating rate due to recoil of the ions after photon emission must be equal so that the ions reach an equilibrium energy that is non-zero. T_D is derived in Ref. [80] and given as

$$T_D = \frac{\hbar\gamma}{2k_B}. \tag{2.21}$$

For Ca^+ with $\gamma \sim 2\pi \times 20.7$ MHz, this is approximately 500 μK. Since 3D crystals are used in these experiments, the ions shall experience some RF-heating so that this temperature is not achieved in practice. Ion energies can be further reduced by use of sideband-cooling techniques [84], by which the Doppler temperature is reduced due to narrower transitions.

A useful consequence of the laser cooling process arises when one wishes to detect the cooled species. Due to the continuous driving of the laser cooling transition, the cooled ions regularly fluoresce, with large photon fluxes in all directions. Use of focussing optics and a CCD camera permit position-sensitive fluorescence profiles to be recorded. The resulting profiles obtained have excellent signal to noise, with images obtained on timescales on the order of one second. Overall fluorescence intensities from an ion ensemble can also be detected with a photo-multiplier tube (EMI 9558A) which can be used to determine excited state populations at various detunings of both the 397 nm and 866 nm lasers [16]. As will be seen later, the fluorescence profiles obtained are important in determining thermal properties of the ions, and in deducing rates of reactions involving trapped ions when profiles are regularly obtained. Temporal changes in the fluorescence can also be detected that can then be used to identify trapped ions, as described further in chapter 5.

As noted by Alex Gingell [85], reactive lifetimes of calcium ions are strongly dependent on the populations of the excited states, since each state will contribute a different amount of energy to a reaction event. The state populations are in turn determined by the laser detunings and powers. This is also seen in reactive experiments with Mg^+ [86], although elucidation of the relative populations is simpler with a two-level system. This state-dependent lifetime can also be observed experimentally, when monitoring the loss of ions due to background reactions. However, this is not relevant for the work presented in this thesis since studied reactions involve sympathetically cooled ions.

Since the advent of laser cooling, more sophisticated cooling schemes have been devised to reduce the temperature of the ions below the Doppler limit. Sideband cooling [87, 88] uses a Raman transition for the main cooling transition, as opposed to a dipole-allowed transition as described above, in the case of Ca^+ this is commonly the $3\mathrm{d}\,{}^2\mathrm{D}_{5/2} \leftarrow 4\mathrm{s}\,{}^2\mathrm{S}_{1/2}$ transition at 729 nm. The reduced transition linewidth permits a lower temperature limit, since there is a lesser Doppler width associated with the transition, which permits cooling of a narrower range of ion velocities. The cooling cycle is subsequently closed with lasers pumping the $4\mathrm{p}\,{}^2\mathrm{P}_{3/2} \leftarrow 3\mathrm{d}\,{}^2\mathrm{D}_{5/2}$ and $4\mathrm{p}\,{}^2\mathrm{P}_{1/2} \leftarrow 3\mathrm{d}\,{}^2\mathrm{D}_{3/2}$ transitions. Wineland and co-workers have used this technique to cool ions into their ground motional level, permitting measurements of entanglement induced in the ions. Other methods of further cooling past the Doppler limit are not considered here, but are discussed in Ref. [80].

2.2.1 Sympathetic cooling of non-laser cooled ions

Although recent developments have shown the ability to laser cool certain molecules [89, 90, 91], it is in general extremely challenging to cool a vast majority of molecular species since there is no closed cooling cycle available. A number of neutral molecules, including SrF [89] and TlF [92] have shown potential for cooling due to favourable diagonal Franck-Condon factors; the greatest success so far has come from cooling of SrF, a pseudo-closed cycle with 3 lasers is possible, and a magnetic field of a few Gauss is sufficient to de-stabilise dark hyperfine states. Molecular ions, *eg* BH^+ and AlH^+ have also been considered for laser cooling [91]. Coupling of the molecules to a cavity-mode to allow cavity-assisted laser cooling has also been theoretically investigated [93]. Methods have been explored for cooling the rovibrational motion of molecules in contrast to translational motion [94, 95]. In general though, laser cooling of molecular ions is extremely difficult, and cannot generally be easily applied to one molecule from another.

Fortunately, ions that cannot be laser cooled can still be sympathetically cooled when co-trapped with a laser cooled species. This is due to the fact that the laser cooled (LC) and sympathetically cooled (SC) ions interact via the Coulomb force. In this case, an LC ion that can be assumed to be initially stationary will be imparted with momentum from an SC ion when they interact. Due to the conservation of momentum, the SC atom will also experience a change in momentum. Since any momentum imparted to the LC ion will be transferred to the radiation field, the SC ion continuously loses energy in a trap potential modified by the Coulomb repulsion of the LC ion, so that LC ions act a heat sink for other ions.

Sympathetic cooling is most effective when masses of the LC and SC ions are closely matched. This is particularly the case when the ions reach their equilibrium positions, since the depth of the trap pseudopotential is mass-dependent. Simulations performed by Schiller and Lämmerzahl suggest mass ratios of 0.33-8 (a mass range of 13-320 u when ^{40}Ca^{+} is the LC ion) for effective sympathetic cooling below 10 K [96] and of 0.8-1.8 (32-72 u) for co-crystallisation [97]. Although SC ions cannot be directly imaged as they do not fluoresce, the presence of these ions modifies the potential for LC ions so that their presence can be inferred from fluorescence profiles. LC components of bi-component crystals can show a regular structure when the number of SC ions outnumber LC ions by a factor of ten.

It should be noted that although cooling the translational motion of an SC ion is quite efficient, internal motion of the ion is in general not altered [98, 99] since the trap frequencies are significantly different from rotational transition frequencies, which results in poor coupling. Schemes that can be used to cool internal motion include those of Drewsen and co-workers in which a Raman transition is used to reduce the rotational energy of a single MgH^{+} molecular ion, with the transition frequency chosen so that population is transferred from the $J = 2$ to $J = 0$ state without the reverse transition possible [94, 100]. An extension of this technique has been theoretically investigated by Deb *et al* for the molecular ions HCl^{+} and DCl^{+} and neutral molecules LiH and CsH [101]. A similar cooling scheme involving two cooling lasers can also cool HD^{+} to its rovibrational ground state [102].

Since the rotational distribution of SC ions is found to equal a thermal distribution, a reduction in the number of rotational states present can also be achieved by use of a cryogenically cooled trap. This reduces both the overall and peak intensity, and the energy of the peak intensity, of the black-body radiation (BBR) until the rotational distribution equilibrates again.

Sympathetic cooling of the translational energy of a hot ion by an already cold

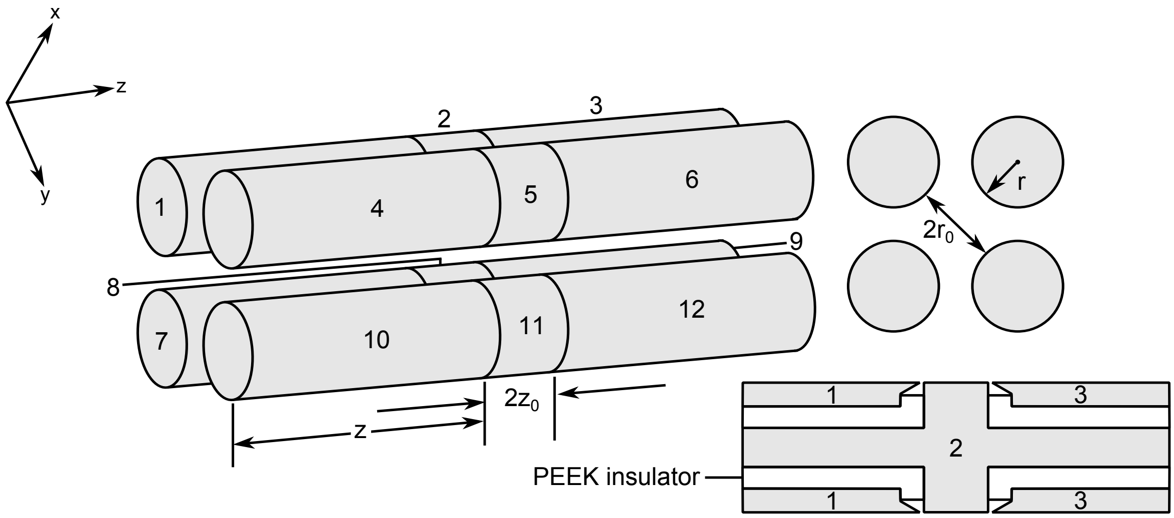

Figure 2.4: Critical trap dimensions, as given in Table 2.1, electrode labels, and simplified cut-through of an electrode stack.

ion is particularly efficient when compared to neutral species due to the near-isotropic nature of the potential between the ions at distances relevant to these experiments. This can be compared to the generally anisotropic nature of potentials between atoms and molecules, through which high inelastic scattering rates generally preclude the use of sympathetic cooling [103]. Collisions between atoms and trapped ions have also shown some promise in sympathetically cooling of the internal modes of a molecular ion, as exemplified by Hudson and co-workers when cooling $BaCl^+$ with ultracold calcium atoms [104].

2.3 Experimental setup

A true quadrupole can only be realised by using hyperbolic electrodes [105]. However, construction difficulties as well as the requirement for optical access to the trap centre perpendicular to the trap axis demands an alternate electrode design. Cylindrical electrodes are suitable alternatives since electrode profiles will be similar for hyperbolic and cylindrical electrodes near to the trap axis, although higher-order terms will be

Parameter		
Electrode radius	r	4 mm
Minimum distance of electrode from trap centre	r_0	3.5 mm
Length of central electrodes	$2z_0$	5.5 mm
Length of endcap electrodes	z	20 mm
RF frequency	Ω_{RF}	3.8 MHz
RF voltage	V_{RF}	50-300 V
Endcap voltage	V_{end}	0-50 V
Harmonicity constant	κ	0.095

Table 2.1: Dimensions and operating parameters of trapping electrodes.

necessarily present in the radial potential, which can become significant at large radial distances. The ratio between electrode radius and electrode-trap minimum distance is chosen such that a quadrupolar field is most truly approximated [106]. This occurs when $r/r_0 \approx 1.148$, and the parameters chosen are such that the electrodes are machined with high precision while minimising the deviation from this value.

Each electrode cylinder is constructed of a similar design, with the electrode core exposed in part to act as the central electrode, as shown in the cut-through of an electrode in figure 2.4. The end-cap electrodes slide onto the recessed core to maintain a constant stack diameter. Insulators are used to prevent contact between individual electrodes. The end-cap electrodes are secured using threaded connectors on both ends of the stack. With this electrode design, access to the centre of the ion trap is maximised with connections to the trap power supplies located at the ends of each electrode stack.

Trapping voltages are applied through wires connected to the individual electrodes. A square-wave output from a function generator with 1 V amplitude and frequency equal to Ω_{RF} is fed to a resonant circuit built in-house, creating a sinusoidal resonant signal. Two DC power supplies, one fixed at 25 V and one with variable output, are used to produce a DC signal at V_{RF}, which is then modulated by the output of the resonant circuit; adjustment of V_{RF} is achieved by varying the magnitude of the

Electrodes	Voltage range / V	Purpose
1,3,4,6,7,9,10,12	0–100	Variation of V_{end}
1,4,7,10	0–10	Variation of axial minimum position
3,6,9,12	0–10	
1,2,3	-5–5	Variation of radial minimum position
4,5,6	-5–5	
4,5,6,7,8,9	0–10	Removal of x-y degeneracy in radial potential

Table 2.2: Controllable voltages from the quadrupole tuning box, electrode labels correspond to those in figure 2.4.

variable output. Small (typically < 20 kHz/day) changes in the square-wave frequency are made to ensure the circuit remains on resonance, the resonant frequency of which can be affected by temperature and charge deposition on electrodes. This ensures the RF voltage transmitted to the electrodes is as close to sinusoidal as possible.

Static voltages for each electrode are controlled with a quadrupole tuning box built in-house. Six independent voltage controllers can be adjusted, with each controller providing a desired fixed voltage to specific electrodes, as seen in table 2.2. The voltages for each electrode are combined and applied constantly to the resonant circuit for that electrode, enabling a shift in the zero-level of the RF voltages, while leaving the RF phase and amplitude unchanged. These tunable voltages provide the ability to vary the endcap voltages, as well as manipulation of the position of the trapping minimum, a crucial ability when searching for ion fluorescence and when minimising RF-heating.

An effusive beam of calcium atoms is formed by heating grated calcium filings in a resistively-heated, hollow stainless steel tube, capped at one end. This calcium oven is visually aligned to the centre of the ion trap by viewing the reflection of the 397 nm laser on an optical fibre, positioned at the trap centre, through the tube. Prior to loading calcium in the trap, the oven is heated for a period of time to degas the filings. This degassing period is typically approximately 2 hours after exposure of the oven to atmospheric pressure, and 5 minutes at the beginning of each day if kept under UHV conditions. Once degassed, a current of 10-16 A is passed through the oven, with greater currents heating the oven more and producing a greater calcium flux.

A metal plate is located 3 cm from the oven aperture; a hole with dimensions 2 mm x 1 mm is drilled into this plate to collimate the atomic beam and reduce calcium deposition on the trap electrodes, which can induce modifications of the trap potential. A rotating shutter is placed prior to the skimmer to selectively block the calcium beam. This allows the oven heating current to be applied constantly, so reducing the time required to heat the oven when a new crystal is required and giving a more stable beam flux, while reducing background collisions of calcium atoms with trapped ions when not ionising.

Those atoms that reach the trap centre are ionised in a non-resonant 2-photon process by the variable-wavelength radiation from a frequency-doubled or -tripled dye laser (Sirah Lasertechnik GmbH, Cobra) pumped by 532 nm radiation from a pulsed Nd:YAG laser (Continuum Inc, Surelite III-10) which is focussed by a spherical biconvex lens, $f = 25$ cm. Although the wavelength for calcium ionisation is not the determining factor for the wavelength range that the dye laser is used for, the wavelength is varied to some extent to minimise ionisation of background species simultaneously with ionisation of calcium. Unlike ionisation by electron bombardment [107], formation of doubly-charged ions is quite unfavoured by laser ionisation due to the requirement of a 3 or 4-photon[4] non-resonant process in creation of Ca^{2+}. Resonant ionisation of calcium for trap loading has been demonstrated by Drewsen and co-workers [108, 109], proceeding via the 4s5p state of calcium. Since the linewidth used is narrow compared to the isotopic separation, ions can be formed with isotope selectivity, which is beneficial for few ion experiments. However, as ^{40}Ca is the most abundant isotope by far (97%), and other abundant isotopes are heavier and can be easily cleaned from the

---

[4] At 317 nm, 4 photons are required to ionise Ca^{+}; at 248 nm, 3 photons are required.

crystal (see section 4.3.2) if required, non-resonant ionisation is a suitable technique for our needs.

Laser cooling is achieved using cw-diode lasers (Toptica Photonics AG, DL-100) at relevant wavelengths to the desired laser cooling transitions and focussed by a biconvex lens, $f = 60$ cm. The optical setup can be seen in figure 2.5. A piece of optical fibre, fixed to a UHV compatible translation stage and used solely for initial alignment of the cooling lasers, is positioned so that the tip of the fibre is in the centre of the trap. The lasers are then aligned to the optical fibre by maximising the intensity of the reflection of the laser beam off the tip of the fibre. The intensity of this reflected light is detected by eye when the vacuum chamber is open, or by use of the CCD camera used when performing experiments.

The two beams are initially aligned with no lenses in the beampaths. The lenses are then alternately placed back into the beampath and each beam is aligned so that it reflects off the fibre through both lenses. The ionisation laser is generally not aligned to the fibre, since the high energy photons ablate the surface of the fibre onto the trap electrodes, which affects the position of the RF minimum and stability of trapped crystals. Instead it is aligned outside the chamber to coincide with the beampaths of the cooling lasers. Once the lasers are aligned, the optical fibre plays no further part in the experiments and is withdrawn from the trap vicinity.

Cooling laser wavelengths are continuously monitored using a Fabry-Perot interferometer (HighFinesse GmbH, WSU-30). The laser wavelengths are measured to a precision of 5 MHz, equivalent to a precision of 3 fm for the wavelength of the blue cooling laser. Laser wavelengths can additionally be controlled by use of a negative feedback loop, controlled by a custom LabView script [85], to ensure constant laser detuning during an experiment. The tendency of the wavemeter to be affected by changing external conditions means that there is usually a slow drift in the measured frequency of the atomic transitions (upto 20 MHz per day). To maintain consistent

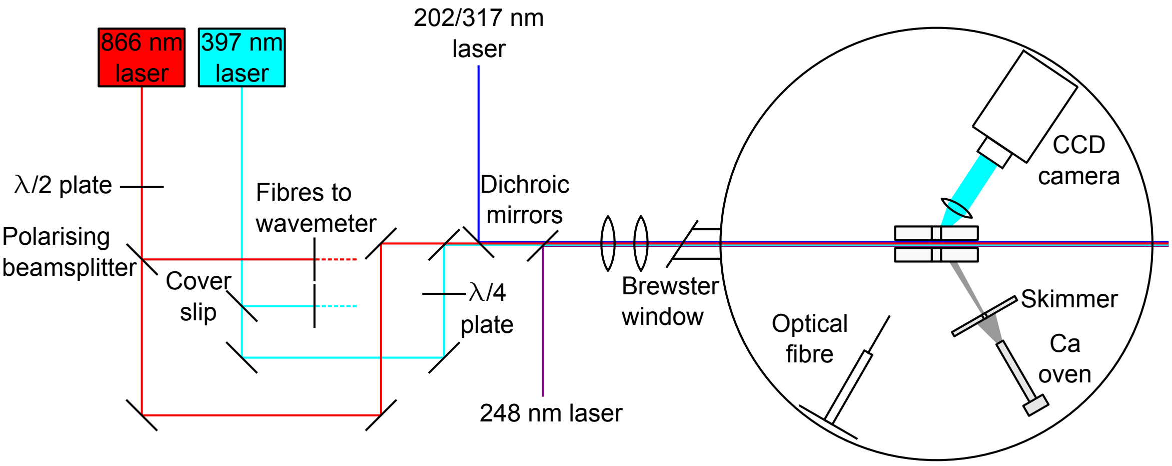

Figure 2.5: Optical setup of ion trap apparatus. The CCD camera is mounted above the ion trap, outside the vacuum chamber.

laser detunings, it is thus necessary to note the measured transition frequencies regularly. For the blue laser, the transition frequency is the frequency at which a crystal melts; for the red laser, the transition frequency is the frequency at which ion fluorescence is maximised [85].

Detection of ion fluorescence is limited by optical access to the trap, with a minimum electrode separation of 2.6 mm at a distance of 5.3 mm from the trap centre. Thus 7.8% of the fluorescence is expected to escape from a particular electrode gap without being scattered. Ion fluorescence is focussed by an x10 Nikon objective lens and travels along a variable length telescope to an intensified CCD camera.

The ion trap and oven are kept under ultra-high vacuum (UHV) conditions to minimise heating of the ions from collisions with background molecules; background pressures $< 10^{-9}$ mbar are typically required. The trap is contained in a cylindrical vacuum chamber with an inner diameter of 30 cm, which is pumped by a turbomolecular pump (Leybold Turbovac 361), in turn backed up by a rotary pump. A foreline trap placed between the turbo and rotary pumps prevents pump oil vapours from entering the chamber under typical conditions, although was insufficient when the rotary pump suffered a catastrophic failure.

Initial pumping down of the chamber rapidly brings the chamber pressure to below 10^{-7} mbar, followed by a further gradual decrease, typically due to slow desorption of water from the chamber walls. This decrease can be hastened by baking the chamber; a typical baking cycle involves heating the chamber to 150-180 °C for two or three days before allowing it to cool. The chamber pressure after baking is typically low 10^{-9} mbar, which can be reduced further by use of a titanium sublimation pump. A thin metal shield is placed between the trap and the sublimation pump to prevent deposition of titanium on the trap electrodes.

2.4 Coulomb crystals

Since the only trappable species are cations, the complete ensemble may be described as a one component plasma (OCP). In contrast to plasmas consisting of positive and negative charges, OCPs are comparatively simple to characterise, with the structural properties of an OCP depending principally on the parameter Γ, given as

$$\Gamma = \frac{E_{\text{pot}}}{E_{\text{kin}}} = \frac{Q^2}{4\pi\varepsilon_0 a_{\text{ws}} k_B T} \tag{2.22}$$

where Q is the charge of the trapped ion species, and a_{ws}, the Wigner-Seitz radius, is equal to $\sqrt[3]{n_0}$, with n_0 denoting the ion density. Infinitely large OCPs adopt a liquid-like state when $\Gamma > 2$ [110] and solid-like crystalline structures when $\Gamma > 170$ [111], although phase-transitions are less well defined than for conventional phases of matter. The solid-like structures formed are termed Coulomb or Wigner crystals. Since the ratio of kinetic and potential energies is relevant here, a Coulomb crystal can be formed in any scheme in which the kinetic energy is sufficiently reduced. However, even when a crystalline structure is adopted, there is significant ion migration through the crystal, which will reduce as Γ increases.

Coulomb crystals formed in this experiment typically have inter-ionic distances of

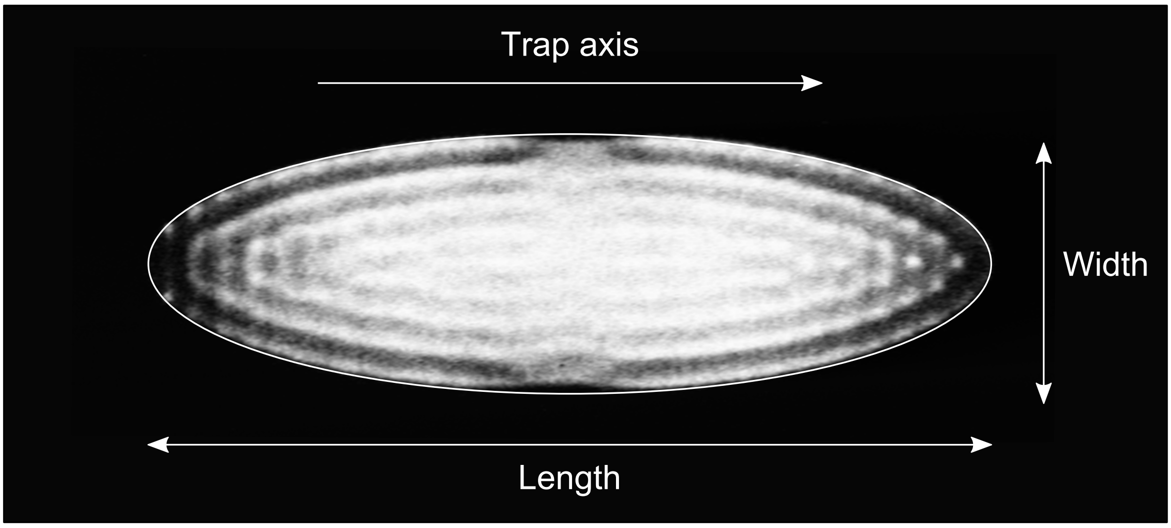

Figure 2.6: Greyscale fluorescence profile of a Coulomb crystal. The presence of a few sympathetically cooled ions can be inferred from the deviation of the profile from the fitted ellipse at the maximum crystal width.

approximately 10-20 microns, dependent on the trapping voltages applied. Coulomb crystals formed experimentally in ion traps can range in size from 2 to approximately 10^5 ions. For smaller crystals, surface effects dominate over bulk effects and cause a shell-like structure to pervade throughout the crystal. For large ensembles of ions, a body-centred cubic lattice arrangement is adopted in the centre as surface effects become less significant [112]. However, the surface of the crystal still has a shell-like structure, which persists for several Wigner-Seitz radii into the crystal [113]. For crystals considered in this thesis, there are typically five shells or fewer present, so structures are approximated in the small crystal regime.

When the ions in the crystal are laser cooled, they will continuously fluoresce, allowing the crystal to be observed. Due to the optical setup described above, there is a fairly narrow focal plane of $\sim 10\ \mu$m thickness from which the fluorescence is observed. The resulting fluorescence profile is thus of a slice through the 3D crystal as seen in figure 2.6; the CCD camera is on a vertical translation mount to ensure the focal plane passes through the central slice of the crystal. The size of the crystal can be determined by calibration of the camera – imaging of the optical fibre, that has a

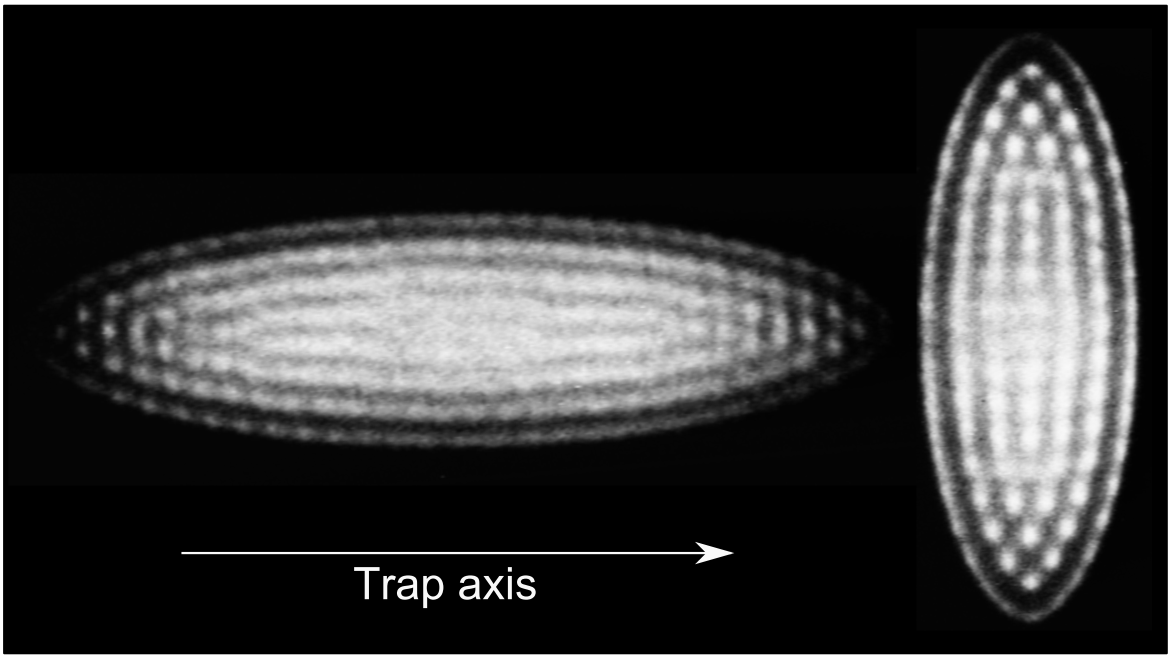

Figure 2.7: Fluorescence profiles of prolate (left) and oblate (right) crystals, with apparently similar structures.

known diameter of 400 μm, is used as a ruler as it passes through the same plane.

Due to the radially symmetric nature of the pseudopotential from equation 2.15, the trapped crystals will have cylindrical symmetry if they are centred around the RF minimum, which is the case if there is no static potential. Utilisation of this fact with a suitable image slice of the Coulomb crystal allows the determination of the crystal volume. When this volume measurement is combined with a measurement of a_{ws} the number of fluorescing ions in a crystal can be determined.

An important parameter for Coulomb crystals is the aspect ratio, α, the ratio between axial and radial dimensions of the crystal, defined as in figure 2.6 and determined by curvature of the axial and radial trapping potentials. At extreme aspect ratios, strings and discs of ions can be formed. However, between these two extremes a range of spheroidal crystals can be made. When viewing Coulomb crystals experimentally, it is important to consider the orientation of the imaging apparatus relative to the ion trap. Since the fluorescence profiles obtained display only a thin slice of the crystal, prolate and oblate crystals with similar semi-major and semi-minor axes will have apparently similar structures in the focal plane, as seen in figure 2.7, but will have different thermal properties, as discussed later.

2.4.1 Multicomponent crystals

The one component plasma described above involves cations with equal charge and mass. However, the model can be extended to permit an ensemble of cations with different masses to be trapped together. As discussed in section 2.2.1, any molecular ions trapped with a laser cooled species will also be cooled, and will co-condense with the laser cooled species, a process first seen by Wineland and co-workers in a Penning trap [114]. The exact form of the resulting crystal is dependent on the relative mass-to-charge ratios of the ions, as well as the trapping parameters described previously for a single-component crystal.

When considering the structure of a bicomponent crystal, it is useful to first consider the differences in hypothetical crystals with one type of ion. The first item of note is the relative position of ions in the Coulomb crystal. As given in equation 2.15, the radial pseudopotential experienced by an ion is

$$V^*(R_0) = \frac{Q^2 E_0^2}{4m\Omega_{\mathrm{RF}}^2}. \tag{2.23}$$

An ion with a greater mass-to-charge ratio therefore experiences a shallower pseudopotential. In contrast to a trapping depth of 7.6 eV for $^{40}\mathrm{Ca}^+$ when $V_{\mathrm{RF}} = 150$ V, a trapped $^{132}\mathrm{Xe}^+$ ion will experience a trapping depth of 2.3 eV. Assuming a constant endcap voltage, the balance between the forces for an ensemble of heavier ions will lead to a crystal with a greater average radial distance. In addition, since the axial potential is independent of ion mass, the greater radial displacement will also lead to a corresponding decrease in the axial displacement. Both these factors lead to a change in the aspect ratio of the crystal.

In a 3D ion ensemble of two or more types of ions, a spatial segregation is seen between species due to the mass-dependent potential. Lighter ions experience a deeper trapping potential than heavier ions, as shown in figure 2.8 for the case of Ca^+ and Xe^+, and move to the centre of the trap so that the overall potential energy is minimised. The heavier ions then surround the lighter ions, at greater radial distances. Moreover, there is a separation between the species, equivalent to

$$\frac{r_1}{r_2} \approx \sqrt{\frac{m_1/Q_1}{m_2/Q_2}} \tag{2.24}$$

where r_1 is the outer radius of the subensemble with lower mass-to-charge ratio, and r_2 is the inner radius of the subensemble with greater mass-to-charge ratio [115, 116]. This is due to the fact that as the mass of the heavy ion increases, it experiences an increasingly shallow potential, *eg* for Xe^+ in figure 2.8, while the lighter ions are confined in the centre of the trap, and so the heavy ion is found at ever greater radial distances.

If the SC ion is heavier than the LC ion, the mass of the SC species has an effect on the structure of the fluorescence profile for the LC species in a bicomponent crystal. When the SC ion is much heavier than the LC ion, the distance between the different species is large and there is a negligible change to the structure and fluorescence profile of the LC component compared to a single component crystal. When the masses are similar, the segregation is small and the presence of the heavier ions radially confines the lighter ions further, so that the fluorescence profile assumes a capped-cylindrical shape, of greater length than if the heavy ions are absent. This can be observed in simulated images in figure 2.10.

Since the SC ions are not excited by the cooling lasers, they do not fluoresce and so cannot be directly detected (an exception to this was shown by Drewsen and co-workers when working with bicomponent crystals of $^{24}Mg^+$ and $^{40}Ca^+$, which can both be laser cooled [117]). However, the effect of the SC ions on the shape of the LC ensemble means that their presence can be inferred. When solely using experimental images, only a limited amount of qualitative information can be obtained about the non laser cooled species. For example, the SC ion mass can only be denoted as either heavier or lighter than $^{40}Ca^+$ depending on the position of the dark ions; further identification requires either mass spectrometry of the crystal, which is discussed in chapter 5, or deduction of the identity from thermodynamic and kinetic considerations.

2.5 Manipulation of trapped ions

Alteration of the trapping potential will lead to an imbalance between the trapping and repulsive Coulomb forces that each trapped ion will experience. This equilibrium is regained when the ions move to balance these forces, which changes the size and shape of the crystal. Since the ions are highly fluxional, this process occurs on a more rapid timescale than can be observed experimentally. The above equations assume that there is no static force shifting the ions away from the RF minimum of the trap, or from the minimum of the axial well expected from the axial voltages. However, charge deposition on electrodes and changes of the RF voltages supplied due to heating of the trap and trapping electronics may cause the trap potential minimum to be in a distinct position to the RF minimum and gradually drift.

If the two minima do not overlap the ions will be hotter, due to RF-heating as explained in section 2.6.1. The fluorescence profiles will also be less clearly defined since excess motion can occur in the observation plane, and deceptive, asymmetric fluorescence profiles can occur if more than one ion species is present. This asymmetry is again due to the mass-dependent pseudopotential; a small static voltage in one direction shall displace the trap minimum further for a heavier ion, as can be seen in

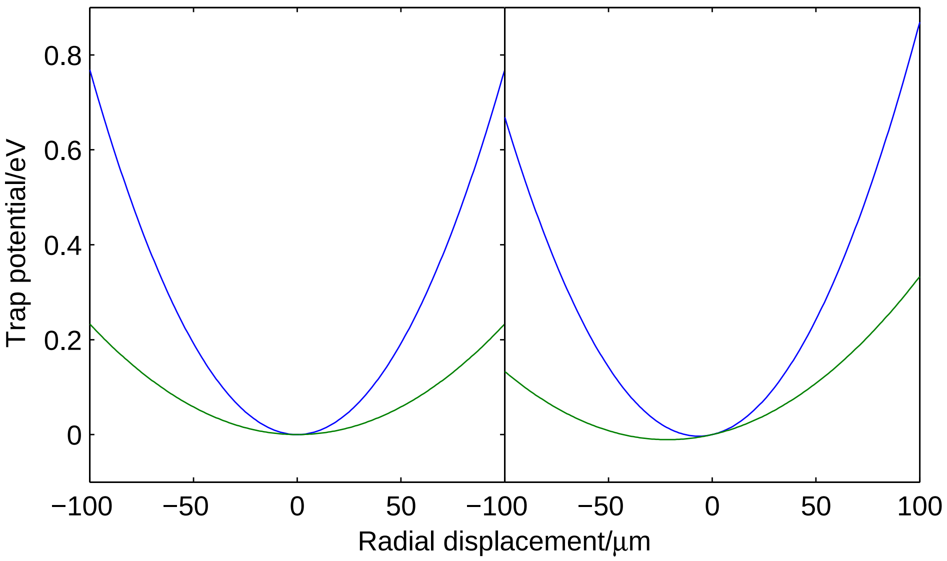

Figure 2.8: Pseudopotentials for ^{40}Ca$^+$ (blue) and ^{132}Xe$^+$ (green) when the RF minimum coincides with trap axis (left) and when a 1 V static radial offset is applied (right).

figure 2.8.

Coulomb crystals are kept in the RF minimum by application of small static voltages on selected electrodes. Changes of these static voltages on the order of 0.1 V per day are required to ensure crystals remain at the RF minimum, although these changes are often erratic due to the unpredictable nature of charge deposition and desorption.

As well as minimising RF-heating imparted to ions, radial optimisation of crystals is particularly important when imaging bicomponent crystals and when investigating chemical reactions. As described previously, heavier ions move to the crystal edges. If the crystal is well centred, the potential minimum will be in the same position for both calcium and heavier ions and both types of ion will be equally distributed around the trap minimum. Applying a static voltage to move the crystal from the RF minimum means the pseudopotential minima for different ion species no longer overlap, as seen in figure 2.8. The lowest energy configuration of the crystal now becomes one where the heavier ions are preferentially found on one side of the crystal. This also deforms the calcium component to a certain extent, causing a 'banana' shaped fluorescence profile [15]. Since species numbers are determined via the 2D fluorescence profile with the assumption of cylindrical symmetry of dark ions around the calcium component, the crystal must have this symmetry to obtain accurate ion numbers.

Ionisation of the non-fluorescing isotopes of Ca along with formation of $^{40}\mathrm{Ca}^{+}$ has a beneficial effect in producing a small number of heavier ions that allow optimisation of the crystal position before performing any further experiments. The crystal is determined to be in the RF minimum when the lengths of the flattened sides are equal and maximised. The dark ions formed can then be removed by q-cleaning (section 4.3.2).

Maintenance of the axial minimum is also periodically checked. Although no additional heating occurs when the crystal is axially offset, it can prove problematic in keeping the crystal in sight of the camera when regular changes in aspect ratios are required, since changes in the axial trapping voltage are needed and thus the position of the effective axial minimum can change if offset.

2.6 Simulation of Coulomb crystals

As described previously, Coulomb crystals are observed experimentally by imaging ion fluorescence. Details about the crystal can be deduced from these fluorescence profiles, such as ion numbers and the density of the fluorescing species. However, many other characteristics cannot be obtained solely from these images, including ion temperatures [118], and the number of dark ions present. One method that can be used to determine these parameters is to simulate the trapped ions.

A molecular dynamics (MD) approach is used in simulation of the Coulomb crystals. A pre-existing MD simulation program, ProtoMol, which was designed by Izaguire and co-workers [119, 120], is adapted to fully simulate the Coulomb crystals, including the time-dependent nature of trapping electrodes. An alternative to performing simulations involving a time-dependent radial potential is to instead use the radial pseudopotential in the force model. Differences are seen in the structure of the crystal depending on the radial potential used [121].

The force model used in the simulation for an individual ion is expressed as

$$\boldsymbol{F}_{\mathrm{tot}} = \boldsymbol{F}_{\mathrm{trap}} + \boldsymbol{F}_{\mathrm{ion}} + \boldsymbol{F}_{\mathrm{cool}} + \boldsymbol{F}_{\mathrm{heat}} \tag{2.25}$$

where $\boldsymbol{F}_{\mathrm{trap}}$ describes the trapping potential, $\boldsymbol{F}_{\mathrm{ion}}$ describes the Coulomb potential between ions, $\boldsymbol{F}_{\mathrm{cool}}$ describes the laser cooling force and $\boldsymbol{F}_{\mathrm{heat}}$ describes the various heating processes. These forces are all evaluated individually for each ion then summed together. One can conceptually split the various forces into two categories: $\boldsymbol{F}_{\mathrm{trap}}$ and $\boldsymbol{F}_{\mathrm{ion}}$ define the spatial equilibrium, whereas $\boldsymbol{F}_{\mathrm{cool}}$ and $\boldsymbol{F}_{\mathrm{heat}}$ define the temperature equilibrium. The simulations are run using a velocity-Verlet algorithm [122] to determine the intermediate ion positions and velocities.

A range of possible trapping potentials are developed and used depending on the crystal properties that one wishes to investigate. The most common potential used is a time-dependent analytical potential, derived from equation 2.6, with the forces of the form

$$\boldsymbol{F}_{\mathrm{trap}} = \frac{QV_{\mathrm{RF}}}{r_0^2}(\boldsymbol{x} - \boldsymbol{y})\cos(\Omega_{\mathrm{RF}}t) + \frac{Q\kappa V_{\mathrm{end}}}{z_0^2}\left[2\boldsymbol{z} - (\boldsymbol{x} + \boldsymbol{y})\right]. \tag{2.26}$$

A full numerical potential can also be used, with the numerical potential obtained by modelling the ion trap electrodes in SIMION 8.0, a charged particle optics simulation program [123], and solving the Laplace equation. This provides forces with 0.1 mm grid spacing, with forces between these points obtained by linear interpolation. However, for the size of crystals of interest, there is a negligible difference between using the analytical and numerical potentials, with deviations between the harmonic analytical potentials used and the numerical potential apparent at radial displacements of > 1 mm. Due to the vastly increased run time of simulations using the numerical potential, its use is disfavoured in comparison to the analytical potential.

A key factor in using the time-dependent potential is the length of the timestep used in the simulation. Since thermal ion motion is slow in comparison to the oscillation of the potential, the step-length will thus be limited by Ω_{RF}, with several timesteps needed to smoothly model the oscillating potential. The timesteps can be of any length within this constraint; it is not necessary to have an integral number of timesteps per RF cycle. However, determination of ion energies exclusive of RF-induced motion is significantly easier if an integer number is used. A value of 30 timesteps per RF period is chosen to balance accuracy of the time-dependent potential with the running time of the simulation, with little change having been found when the number of steps per period exceeds 20 [124]. Given an experimental Ω_{RF} of 3.8 MHz, the timestep length chosen is thus ~ 8.8 ns.

Another method that can be used to simulate the trapping force is to instead use the time-independent pseudopotential. The advantage to using this potential is that there is no longer any time-dependency, and so the timestep can now be much greater than in the fully time-dependent potential, when the timestep must be sufficiently short to smoothly model the changing potential. The maximum timestep duration is determined by the change in potential experienced by the individual ions over the timestep. Assuming an ion velocity of 5 m/s, which corresponds to the most probable velocity in a Maxwell-Boltzmann distribution for calcium at 60 mK, an ion moves 1 μm in 200 ns. This compares to an minimum ionic separation of 10 μm, so a 200 ns timestep is deemed sufficiently accurate for obtaining general information about the crystal composition and structure. Using this potential is particularly useful for monitoring migration of ions through a crystal. For a pseudopotential, the force model used is

$$\boldsymbol{F}_{\mathrm{trap}} = \omega_r^2(\boldsymbol{x} + \boldsymbol{y}) + \omega_z^2\boldsymbol{z} \tag{2.27}$$

where ω_r^2 and ω_z^2 are the radial and axial harmonic frequencies respectively and are defined as [125]

$$\begin{aligned} \omega_z^2 &= \kappa Q V_{\mathrm{end}}, && (2.28) \\ \omega_r^2 &= \frac{Q^2 V_{\mathrm{RF}}^2}{4 m r_0^4 \Omega_{\mathrm{RF}}^2} - \frac{\kappa Q V_{\mathrm{end}}}{2}. && (2.29) \end{aligned}$$

Both the pseudo and time-dependent potentials can be used in the creation of simulated fluorescence profiles. However, to properly characterise the total energy distributions of a crystal, the time-dependent forces must be used.

The forces arising from the ion interaction are treated according to the Coulomb equation, this is repulsive as all ions are cations; the force on the jth ion by other ions in the crystal is

$$\boldsymbol{F}_{\mathrm{ion},j} = \sum_{i=1, i \neq j}^{N} \frac{Q_i Q_j}{4\pi\varepsilon_0 r_{ij}^2} \hat{\boldsymbol{r}}_{ij} \qquad (2.30)$$

where $\boldsymbol{r}_{ij}$ is the distance between two ions in the direction of the force on the jth ion.

The Coulomb interaction is evaluated directly between every ion at every stage. Algorithms are built into ProtoMol to evaluate electrostatic forces faster, for example MultiGrid and mesh-based Ewald methods [119]. However, these algorithms are typically more efficient for sample sizes of 2×10^4 or more ions, and so are not used in our simulations. In addition, all ions are treated as point particles: at an ion separation of 10 μm, the repulsive Coulomb force between two ions is 2.31×10^{-18} N, whereas assuming a dipole moment of 1 D for a molecular ion, the ion-dipole interaction is 9.61×10^{-24} N, this is thus a good approximation to the complete electrostatic interaction between ions.

Laser cooling is simulated in one of two ways. The first is to use the radiative force as given in equation 2.20. The force model is simplified if one assumes that counter-propagating lasers are used, so that the overall force $\boldsymbol{F}_{\mathrm{cool}} = \boldsymbol{F}_{+} + \boldsymbol{F}_{-}$, where $\boldsymbol{F}_{\pm}$ refer to the forces from the counter-propagating lasers. $\boldsymbol{F}_{\pm}$ is defined from equation

2.20, *ie*

$$\boldsymbol{F}_{\pm} = \frac{(h/\lambda)s_0\gamma/2}{1 + s_0 + \left[2(\delta \mp |\omega_D|)/\gamma\right]^2}, \tag{2.31}$$

and $\boldsymbol{F}_{\text{cool}}$ obtained from the sum of these terms,

$$\boldsymbol{F}_{\text{cool}} = \frac{8\pi h \delta s_0 \dot{z}}{\lambda^2\gamma\left[1 + s_0 + (2\delta/\gamma)^2\right]^2}, \tag{2.32}$$

where terms including ω_D in the denominator are neglected assuming $\dot{z}$ is sufficiently small. Except for $\dot{z}$, the terms in $\boldsymbol{F}_{\text{cool}}$ are all constant and so can be simplified to the form used in the force model,

$$\boldsymbol{F}_{\text{cool}} = -\beta\dot{z}, \tag{2.33}$$

where β is a cooling factor, with an assumed value of $\beta/m_{\text{Ca}} = 860\ \text{s}^{-1}$.

Another method is to apply a thermostat to the system, artificially removing the energy from the system. The thermostat typically used in this case is a Berendsen thermostat [126]. The thermostat can be adjusted to vary the proportion of kinetic energy removed at each stage. This method can be useful if the ions are not initially in their equilibrium positions, and there is a large amount of excess energy that must be removed.

To counteract the laser cooling force such that experimentally realistic temperatures are obtained in the simulation, a stochastic heating force is also added, *ie*

$$\boldsymbol{F}_{\text{heat}} = k_{\text{heat}} * R \tag{2.34}$$

where R is a random Gaussian function in 3 dimensions. k_{heat} is arbitrarily defined to obtain the desired crystal secular temperature. This force covers unpredictable stochastic events such as collisions of the ions with background gas molecules, trap imperfections, and any excess RF-heating.

Alternatively, if simulations are desired at a given temperature without consider-

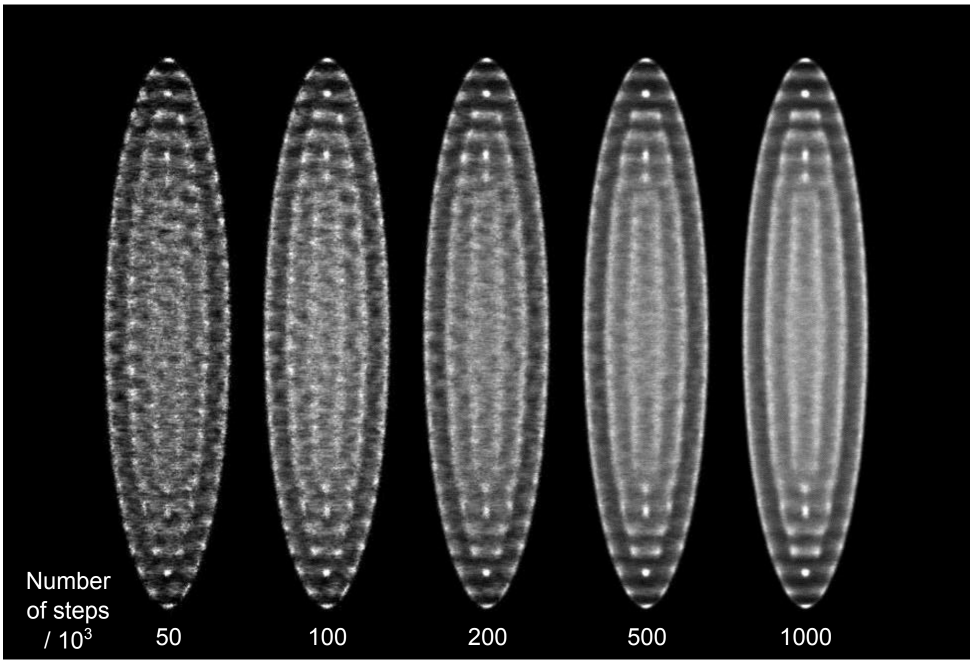

Figure 2.9: Simulated images of a 500 Ca^+crystal when varying timestep ranges that ion positions are averaged over.

ation of the magnitude of cooling forces applied, one possible option is to artificially set the secular temperature of the ions, then perform the simulation in the absence of heating and cooling forces. To achieve this one must first obtain the RF-averaged ion positions for a crystal approaching 0 K (typically < 1 μK) using an artificial cooling model before adjusting the ion temperatures. The advantage of this method is that ions can be rapidly cooled into equilibrium positions, reducing the amount of time required to simulate a crystal at a given temperature.

Simulated images are obtained from the output of the MD simulations for comparison with experimental images. Instantaneous visualisation of the crystal at given timesteps is achieved using VMD, developed by the University of Indiana [127]. This is useful for obtaining qualitative information about crystal shapes while performing a simulation and for monitoring motion of ions through a crystal. However, only limited information can be obtained that relates to experimental images since temporal distributions of the ions are not considered.

Images that replicate experimental fluorescence profiles are obtained by recording the ion positions at each timestep in the simulation after a certain time to allow the crystal to equilibrate. The ion positions are then sampled for approximately 5×10^5 timesteps, equivalent to 4 ms of simulated time. This is small compared to the time that ion fluorescence is collected in the experimental images (typically several tens-hundreds ms), but is found to be an adequate compromise between replication of experimental images with simulated images and simulation run time. Moreover, little difference is seen between simulated images with this many timesteps and ones with more steps included, as seen in figure 2.9.

Once the ion positions are obtained, 2D sliced probability density images of the ions are created, with each slice corresponding to ions at a specific distance from the focal plane, nominally the centre of the crystal. A Gaussian blur is applied to sliced images that are not in the focal plane, with greater blurring for slices that are further from the plane. These slices are then summed together to give a simulated image to compare with experimentally obtained images.

By comparison of experimental images to images obtained from a range of simulations with differing conditions, the properties of the crystal can be determined. Of most importance are the number of ions in the crystal, which can also be deduced from measurement of the crystal volume, and the energies of these ions. For pure calcium crystals, the crystal size and aspect ratio, and the inter-shell spacing are used for comparison and are used to calibrate the output of the simulations.

When studying bi-component crystals, it is also possible to estimate the number of dark ions present if the dark ion identity is known by obtaining the similar profiles of the fluorescing component, in spite of there being no experimental image of the dark ions. The accuracy that can be obtained when counting dark ions is dependent on the identity of the dark ion, with a greater accuracy for ions close in mass to $^{40}\mathrm{Ca}^+$. This can be easily shown with two crystals both containing an equal number of calcium ions

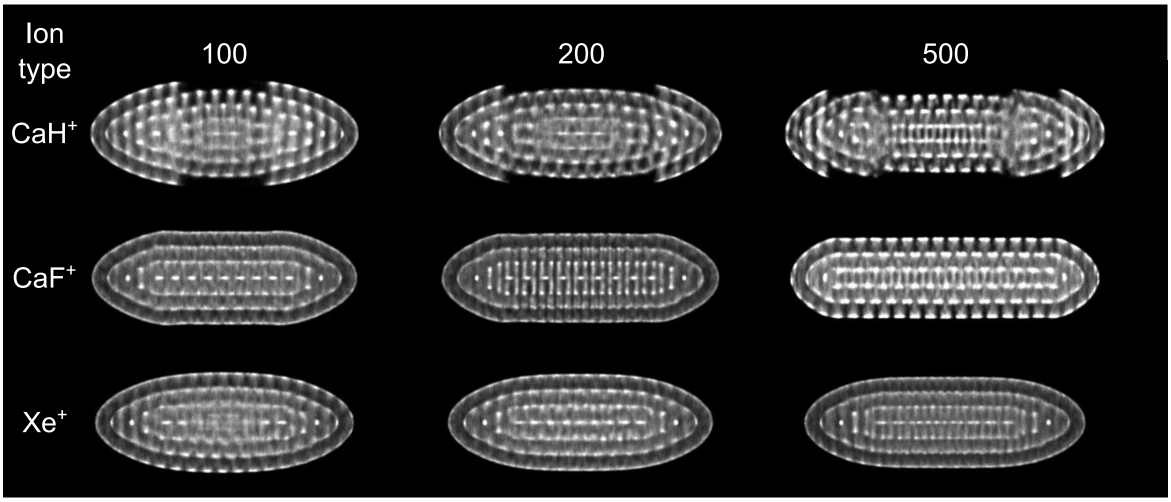

Figure 2.10: Bicomponent crystals and the effect of the number and identity of sympathetically cooled ions on fluorescence profiles of crystals containing a 500 Ca^+ core.

and dark, heavy ions. As seen in figure 2.10, when the ions are similar in mass, the spacing between crystal segments is small because of the similar radial potentials for each ion. Adding further dark ions in this case has a significant effect on the profile of the calcium segment, and thus the fluorescence profile. For far heavier ions the dark ions are much further away from the calcium core. Addition of further heavy ions has a less significant effect on the Ca^+ portion, due both to this increased separation, and the greater number of heavy ions that can be positioned in similar radial and axial displacements when at greater distances.

For light ($m/z < 40$) ions, the situation is reversed. In this case, the number of light ions can be estimated by determining the diameter of the dark core. When comparing experimental and simulated images, the two parameters that are typically beneficial for assigning ion numbers are the diameter of the dark core, and the axial distance between the two furthest fluorescing points. For lighter ions, the difference in mass between the light ion and calcium is of less importance, since the calcium ions are repelled a similar amount from the trap axis, as seen in equation 2.24. If the identity of the ion is unknown, some error in the ion number can arise since there will be a different axial length for the dark core while maintaining the same core width for

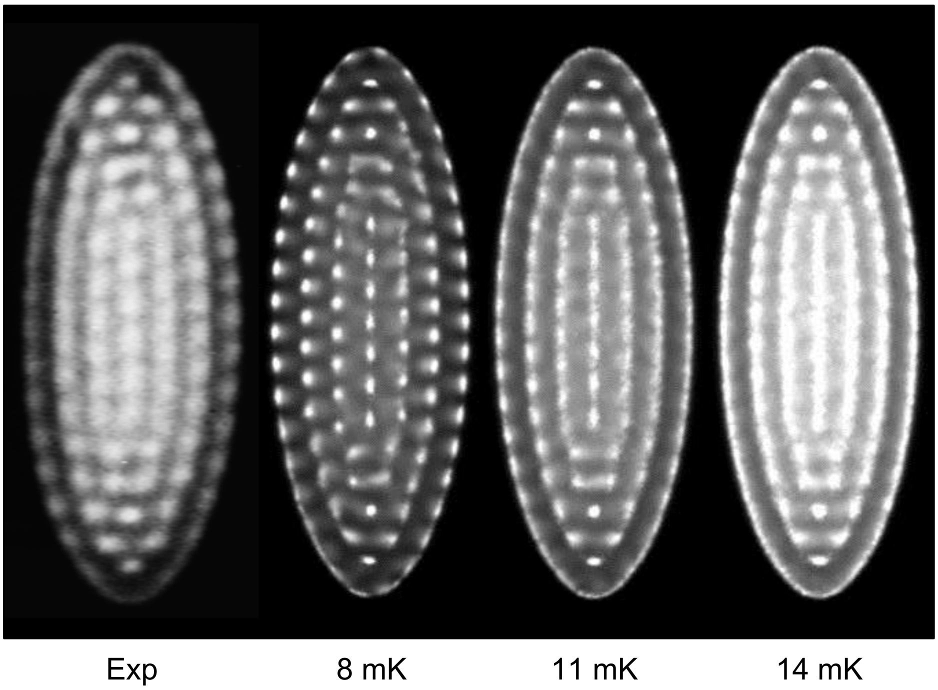

Figure 2.11: A fluorescence profile of a 460 Ca^+ crystal, with simulated images at various secular temperatures. For this crystal, closest agreement is observed for 11-14 mK.

different ions.

In addition to the size and aspect ratio of the crystal, the simulated images provide information on the experimental secular energies of the ions, primarily from the size of the individual fluorescence 'spots' in the images and the extent that individual spots can be resolved in the image. The size of the resolved spots is determined both by the distance between ions, and the temperature of the ions. The distance between ions is in turn dictated by the RF voltage; a lower RF voltage reduces the ion density, which results in a flatter potential around the equilibrium point of an ion since the curvature of the potential is predominantly due to Coulomb repulsion with other ions. An ion at a given temperature will thus be able to move further around this point and a larger spot will appear in the fluorescence profile. Likewise, for a given RF voltage, ions at a higher temperature will move further around their individual potential well and the spots will appear larger. In addition there is increased migration of ions through the crystal at higher temperatures which results in increased fluorescence between the spots, as seen in figure 2.11.

2.6.1 Ion energies and the feasibility of temperature assignment

As touched upon earlier, the motion of an ion can be split into two components: random thermal motion of the ions and ordered motion driven by the oscillating radial trapping potential. The thermal motion can be approximated as the change in the position of an ion from one point in an RF cycle to the next, such that RF-induced motion is not included, and is referred to as secular motion. Over the course of an RF cycle, an ion with a secular energy corresponding to 10 mK would travel approximately 500 nm, so will only experience a slight change in the pseudopotential during this time. Meanwhile, an ion with a radial displacement of 50 μm oscillates from RF-induced motion with an amplitude of $\sim$ 5 μm. This disparity means that the secular and ordered motion can be treated separately.

The fact that the two types of motion can be separated means that one can thus obtain energies of the ions excluding and including the driven motion, respectively denoted as the secular energy, E_{sec} and effective energy, E_{eff}. These are calculated as

$$E_{\text{sec}} = \frac{1}{2N}\sum_{i=1}^{N} m_i \langle \boldsymbol{v}_i \rangle^2, \tag{2.35}$$

$$E_{\text{eff}} = \frac{1}{2N}\sum_{i=1}^{N} m_i \langle v_i^2 \rangle \tag{2.36}$$

where in both cases the averaged term in the expressions is defined as the cycle-averaged value, *ie*

$$\langle x \rangle = \frac{1}{h}\sum_{s=1}^{h} x \tag{2.37}$$

where h is the number of timesteps in the cycle. Since $\boldsymbol{v}_i$ is a vector quantity with

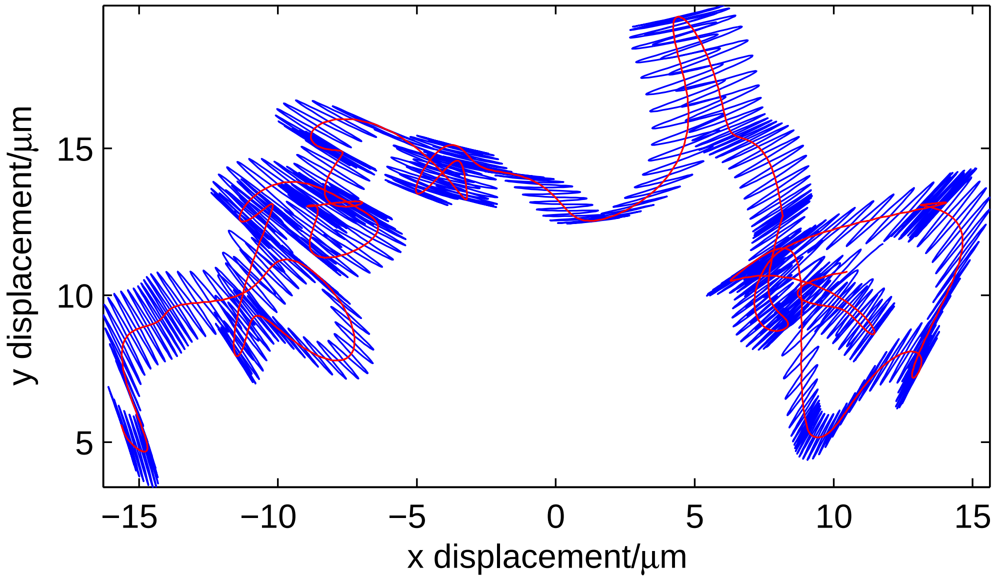

Figure 2.12: Trajectory of a trapped ion in a Coulomb crystal over 10 μs, with motion including RF-ordered motion (blue) and excluding ordered motion (red). During this period of time, the ion travelled 1870 μm and 130 μm respectively.

a component that oscillates over the course of one RF cycle, the RF motion that this component equates to thus sums to zero for calculation of E_{sec} to leave only the average residual thermal motion. However, this is maintained in calculation of E_{eff} due to averaging of the speed of an ion, in which the summation of the RF motion no longer disappears. The difference between these two types of motion can be observed in figure 2.12, with secular motion appearing as a lower-frequency and longer-range motion than ordered motion. Although independent and discussed further, it should be noted here that ordered motion is position-dependent and over the course of an RF cycle will be the cause of the majority of the ion motion.

2.6.2 Secular energy

The magnitude of the secular motion of ions in a crystal corresponds to the typical temperature assigned to a given crystal, and unlike the ordered motion, is directly reduced by laser cooling. For a given crystal, the secular temperature assigned is found to be similar throughout the crystal. From simulations of Coulomb crystals, it is observed that the distribution of secular energies closely matches the Maxwell-Boltzmann distribution.

Assigning a secular temperature to crystals is achieved by comparison of experimental fluorescence profiles with simulated images obtained from simulations with various secular energies, as seen in figure 2.11. As the secular temperature of a crystal increases, the ions possess more random motion, and so move further from the equilibrium positions in their individual potential wells formed by surrounding ions. This increased motion ‘smears’ out the fluorescence of the ion. For large crystals a visual comparison is made, whereby definition of shells and individual ions within the fluorescence profile are used as markers for maximum and minimum secular temperatures in the crystals. In the evaluation of ion temperatures in a large crystal, it is important to ensure the crystal is positioned in the RF minimum and that the imaging focal plane passes through the centre of the crystal. If these conditions are not achieved, defocussing of individual ions will increase the apparent temperature of the ions, while RF-induced motion of ions in the focal plane, which is entirely perpendicular to the plane when optimised correctly, will instead have a component parallel to the plane, which shall disperse the fluorescence more.

Assigning a secular temperature is simpler if ion strings are considered instead of three-dimensional crystals. In this case, one can compare the full-width half-maximum of the fluorescence spots of each ion with those obtained by simulation. In this fashion, one can also obtain the defocussing that occurs upon moving the crystal out of the focal plane.

When viewing experimental images, there is no observable change in secular temperature from changes in V_{RF} or V_{end}. However, due to different ion densities upon changes in V_{RF}, fluorescence profiles of individual resolvable ions will have different

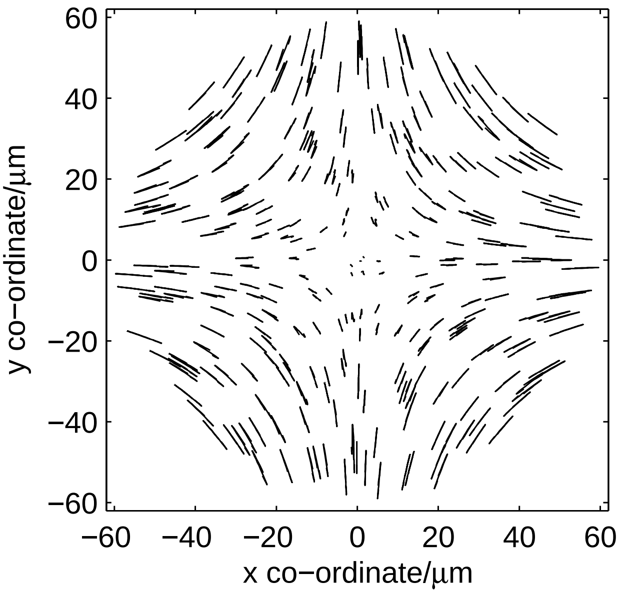

Figure 2.13: Radial projection of a 300 ion crystal, showing motion of ions over one RF cycle. Electrodes are in the direction of $x = 0$ and $y = 0$, imaging optics in the direction of $y = x$.

FWHMs, even with the same secular temperature, due to tighter confinement of individual ions.

2.6.3 Effective energy

As seen in the trapping potential, any off-axis ion is subject to forces from the oscillating electric field. Thus, with the exception of ion strings positioned in the RF minimum, driven motion resulting from the oscillating RF potential, termed micromotion, is the cause of the vast majority of an ion's motion[5]. Thus it is vital to know the energies of ions in a crystal if one wishes to obtain energy-dependent reaction rates. As might be expected from the nature of the potential, the magnitude of the driving force imparted upon an ion is proportional to the distance from the trap axis, and

---

[5] The energy contributions of secular and micromotion are roughly equal for an ion at a distance of 5 μm from the trap axis.

thus the micromotion is also proportional to this displacement. The direction of the force also varies according to the position of the ion, as seen in figure 2.13. For the purposes of solely considering the effective energy of a crystal, the direction of an ion motion is unimportant, although it is again considered in section 2.7.

From equations 2.8 and 2.9 we see that the overall radial force experienced by an individual ion is

$$\boldsymbol{F}_{\mathrm{RF}}(x,y,t) = \frac{QV_{\mathrm{RF}}}{r_0^2}\left(\boldsymbol{x}-\boldsymbol{y}\right)\cos(\Omega_{\mathrm{RF}}t) \tag{2.38}$$

and thus the magnitude of the force is

$$\begin{aligned} |F_{\mathrm{RF}}|(x,y,t) &= \frac{QV_{\mathrm{RF}}}{r_0^2}\sqrt{x^2+y^2}\cos(\Omega_{\mathrm{RF}}t) && (2.39)\\ &= \frac{QV_{\mathrm{RF}}}{r_0^2}r\cos(\Omega_{\mathrm{RF}}t) && (2.40)\end{aligned}$$

where r is the radial displacement of the ion. Since

$$\boldsymbol{v}(x,y,t) = \frac{1}{m}\int \boldsymbol{F}_{\mathrm{RF}}dt = \frac{QV_{\mathrm{RF}}}{\Omega_{\mathrm{RF}}mr_0^2}\left(\boldsymbol{x}-\boldsymbol{y}\right)\sin(\Omega_{\mathrm{RF}}t) \tag{2.41}$$

thus the instantaneous energy is

$$E = \frac{1}{2}mv^2 = \frac{Q^2V_{\mathrm{RF}}^2}{\Omega_{\mathrm{RF}}^2mr_0^4}r^2\sin^2(\Omega_{\mathrm{RF}}t) \tag{2.42}$$

and the average energy in an RF cycle will be

$$\begin{aligned} E_{\mathrm{ave}} &= \frac{1}{2\pi/\Omega_{\mathrm{RF}}}\int_0^{2\pi/\Omega_{\mathrm{RF}}} Edt && (2.43)\\ &= \frac{Q^2V_{\mathrm{RF}}^2}{2\pi\Omega_{\mathrm{RF}}mr_0^4}r^2\int_0^{2\pi/\Omega_{\mathrm{RF}}}\sin^2(\Omega_{\mathrm{RF}}t)dt && (2.44)\\ &= \frac{Q^2V_{\mathrm{RF}}^2}{2\pi\Omega_{\mathrm{RF}}mr_0^4}r^2\left[\frac{1}{2}\left(t-\frac{1}{2\Omega_{\mathrm{RF}}}\sin(2\Omega_{\mathrm{RF}}t)\right)\right]_0^{2\pi/\Omega_{\mathrm{RF}}} && (2.45)\\ &= \frac{Q^2V_{\mathrm{RF}}^2}{2\Omega_{\mathrm{RF}}^2mr_0^4}r^2. && (2.46)\end{aligned}$$

Thus the energy of an ion is dependent on a number of factors. Due to the slow migration of an individual ion throughout a crystal, its energy will vary over time as well.

Naturally, one wishes to consider the overall energy of ions in a Coulomb crystal involved in a reaction. This is effectively achieved by integrating the average energies of all ions in a crystal. One finds that there is a natural dependence between the crystal properties, *eg* size, aspect ratio and density, and the average ion energy. However, also of note is the distribution of energies, which will also be briefly explored.

For a given crystal, the distribution of secular energies closely resembles a Maxwell-Boltzmann distribution, and so it is reasonable to assign a secular temperature to the whole crystal. However, the distribution of effective energies does not resemble a Maxwell-Boltzmann distribution and so cannot have a characteristic temperature assigned. For convenience and to facilitate comparison with the secular temperature, an average effective energy can be provided in kelvin units, but the energy distribution must be used to determine collision energy distributions.

Dependence of E_{eff} on trap parameters

There are many ways that the average energy of a crystal can be altered, through tuning of trapping parameters. These will all serve to alter the average distance of an ion from the trap axis.

Changing the number of ions, n, in a crystal effects an obvious change in E_{eff}. Assuming the crystal to be a prolate spheroid with minor-axis $2a$ and major-axis $2b$, such that the major-axis is parallel with the trap axis, the average radial displacement, $\bar{r}$, is $3\pi a/16$. Any change in n shall change the crystal volume proportionately, while the aspect ratio remains the same in the absence of any changes in trapping voltages. The axis lengths, and $\bar{r}$, will thus be proportional to $n^{1/3}$. With E_{eff} proportional to r^2, the ion energy at this average radial position will thus be proportional to $n^{2/3}$.

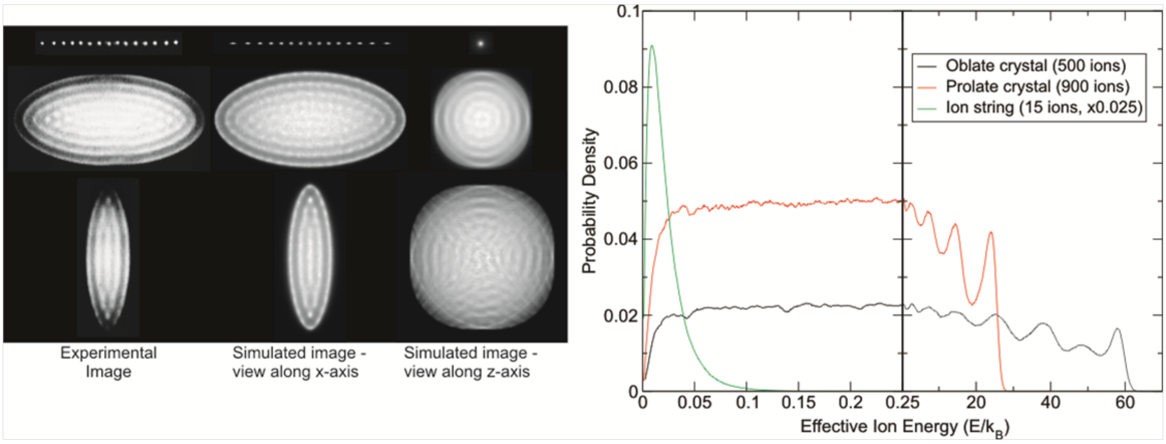

Figure 2.14: Experimental and simulated images (left) and corresponding energy distributions (right) of Coulomb crystals with different aspect ratios. Note the change in scale for ion energies.

Changing the endcap voltage at a constant V_{RF} principally serves to change the aspect ratio of the crystal. Reducing the endcap voltage reduces the axial trapping depth and repulsive radial force. This serves to decrease the aspect ratio of the crystal and, for a given crystal with a fixed number of ions, reduce the radial displacement of each ion. This in turn will reduce the average kinetic energy of the crystal. This effect is seen in figure 2.14.

Adjusting the RF voltage has a more complex effect, since the magnitude of micromotion is itself dependent on $\mathrm{V_{RF}}$. The key differences in crystal structure when increasing the $\mathrm{V_{RF}}$ are a decrease in a_{ws} and a decrease in the aspect ratio. When combined, these serve to reduce the average radial displacement of each ion. The exact effect on the average energy is complicated, and dependent on the exact values used for the trapping parameters.

Effect of secular temperature

As previously discussed, the secular and driven motion can be adiabatically separated. However, the magnitude of the secular motion can have an effect on the distribution of total ion energies. Two principal effects are seen: temperature changes when the crystal remains crystalline, and when it has melted. At low temperatures while still crystalline, the crystal volume, and thus Wigner-Seitz radius, varies by only a small amount due to increased motion of the outer shell ions. There is consequently little change in the average energy of the crystal. The principal effect that occurs is that the plasma coupling parameter (equation 2.22) has now reduced, and as such ion motion through the crystal increases. This serves to 'fill' the voids between shells, creating a more uniform distribution.

A greater effect is seen at higher temperatures, when the crystal is at a high enough secular temperature to melt. There is now a significant increase in the Wigner-Seitz radius and thus the volume of the ion cloud correspondingly increases. Thus the average radial co-ordinate can be expected to increase as the cube root of a_{ws} and the average energy will increase. However, in the region of temperature that is experimentally investigated ($T_{\mathrm{sec}} < 50$ mK), there is no significant change in a_{ws} and so the secular temperature has little effect in determination of the total energy distribution.

2.6.4 Energies of multicomponent crystals

With a range of chemical reactions sought, it is evident that more than one ionic reactant will be used. Equation 2.46 shows the mass dependence of the average ion energy, with heavier ions at a given radius possessing a lower total energy, which can be observed in figure 2.15. However, because of the mass-dependent radial potential, the average radius for a cloud of heavier ions will also be greater. The latter effect is more significant, which results in an increase in the average ion energy for heavier ions.

This effect becomes more complicated since, for reactions involving a sympathetically cooled ion as a reactant, the reactant ions will either be radially confined or repelled, depending on their mass. This affects the radial distribution of the SC ion,

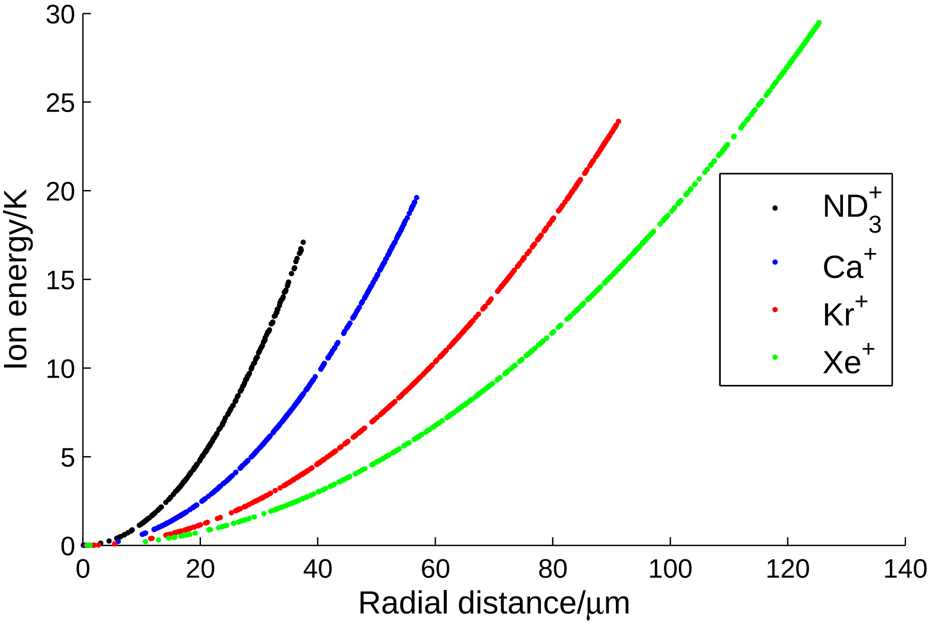

Figure 2.15: Simulated energies for ions in 500-ion crystals of ions relevant to this thesis. For each crystal, $V_{\mathrm{RF}} = 150$ V, $V_{\mathrm{end}} = 4.8$ V and $T_{\mathrm{sec}} = 10$ mK.

so affecting the energy distribution. This can be seen in figure 2.16, which compares energy distributions for calcium ions with a range of other ions in bi-component crystals. In these examples, the principal difference is observed between reactant ions heavier and lighter than calcium. In the case of lighter ions, for example ND_3^+, the distribution resembles the low-energy part of a corresponding calcium distribution while the converse is true for heavier ions such as Kr^+ and Xe^+. In the case of the heavier ions, there is a slight increase in E_{eff} due to separation between the crystal components, which becomes more significant as the SC ion mass increases further.

As well as a change in the effective energy of SC ions due to the time-dependent trapping potential, the SC ions will also be at a higher secular temperature than the LC ions. The degree to which the secular energy of SC ions is reduced is related to the ratio of the masses of the LC and SC ions, as discussed in section 2.2.1. For the trapped ions relevant to this thesis, Xe^+ ions in particular will be quite separated from Ca^+ ions and so cooling will be less efficient than for lighter ions. The secular temperature of Xe^+ is

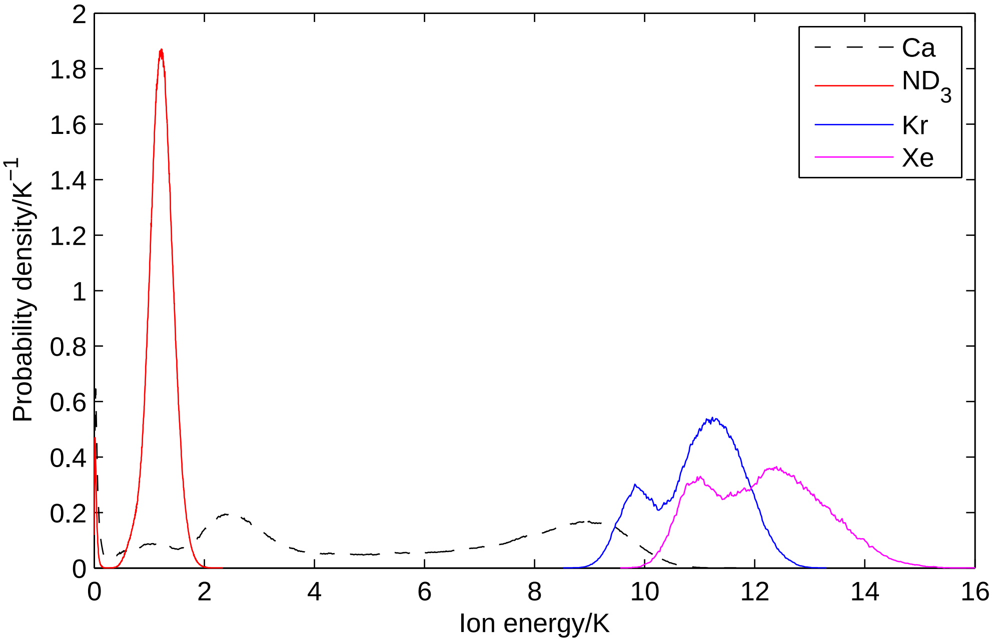

Figure 2.16: Effective energy distributions for sympathetically cooled ions in a crystal of 200 Ca$^+$ and 100 sympathetically cooled ions, with a 300 Ca$^+$ crystal for comparison.

thus possibly too high to permit these ions to crystallise, although they will still be at a sufficiently low secular temperature that the secular energy can be neglected when considering the total energy of the ions, since the driven motion will still dominate.

2.7 Considerations for reactive collision energies

Although the absolute energy of the trapped ions is of some interest, when one is concerned with reactions of these ions the key item of interest is the distribution of collision energies between the ions and the neutral molecular species. Work by Gerlich and co-workers has suggested that the masses of the species are important in determining the collision energy, and that comparatively low collision temperatures can be achieved even with one species moving rapidly if a stationary target is heavy compared to the moving species [128].

In determining collision energy distributions, a transformation from the laboratory

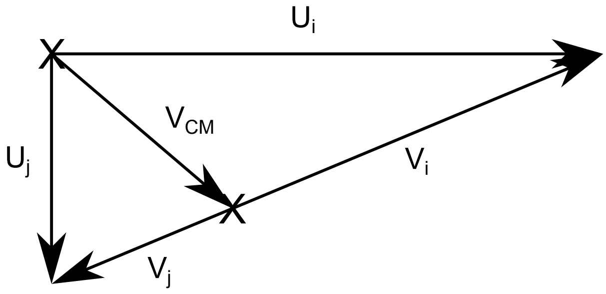

Figure 2.17: Newton diagram for collisions. In this example, velocities of the ion and molecule are orthogonal, a case that occurs when molecules are travelling along the trap axis, or when molecules travelling perpendicular to the trap axis scatter with ions in the symmetry plane perpendicular to the molecule's motion.

frame to the centre-of-mass frame is required since only the relative motion of the reactants contributes to the energy available to the reaction, as denoted in the Newton diagram in figure 2.17. Upon performing this transformation, the laboratory velocities of each species, u_i and u_j, are converted to reduced velocities, v_i and v_j, by the formulae

$$v_i = \frac{v_{\mathrm{rel}} m_j}{M}, \tag{2.47}$$

$$v_j = -\frac{v_{\mathrm{rel}} m_i}{M} \tag{2.48}$$

where $v_{\mathrm{rel}} = u_i - u_j$ and $M = m_i + m_j$. The collision energy will thus be

$$E_{\mathrm{coll}} = \frac{1}{2}\left(m_i v_i^2 + m_j v_j^2\right) \tag{2.49}$$

$$= \frac{1}{2}\mu v_{\mathrm{rel}}^2 \tag{2.50}$$

where μ is the reduced mass, $m_i m_j/(m_i + m_j)$. If the velocity of j is vastly slower than the velocity of i then $v_{\mathrm{rel}} = u_i - u_j \approx u_i$ and the centre-of-mass velocities approximate as

$$v_i \approx \frac{m_j}{M} u_i, \tag{2.51}$$

$$v_j \approx -\frac{m_i}{M} u_i \tag{2.52}$$

and the collision energy is

$$E_{\text{coll}} \approx \frac{1}{2}\mu u_i^2. \tag{2.53}$$

The width of the collision energy distribution in this case is thus minimised if the travelling species has a narrow velocity distribution. The output from a Stark decelerator, as will be discussed in chapter 3, is particularly good in terms of the energy resolution of the decelerated molecules, and so the width of the collision energy distribution will be minimised. This approximation can be appropriate either if ion strings or very small crystals are used, such that the ion energies are vanishing, or when the molecules are from a room temperature distribution and so have a much greater energy than trapped ions.

A difference in the collision energy distributions can be observed depending on the direction of the molecular beam with respect to the trap axes. Prior work by Bell *et al* [16, 49] used an electrostatic guide as a source of cold molecules, with the guided molecular beam travelling parallel to the trap axis, whereas a decelerated molecular beam described in this experimental setup travels perpendicular to the trap axis, passing between the trap electrodes. Since the micromotion is contained in the plane perpendicular to the trap axis, the ion motion will thus be perpendicular to the molecular motion from an axial molecular source, and shall always increase the collision energy.

For a molecular source perpendicular to the trap axis, the combination of molecular energy and ion micromotion is more complex, due to the different angles between molecular and ion motion. In some cases, the collision energy between an ion and molecule can be reduced if the RF phase moves the ion in the same direction as the molecule. However, the predominant effect is broadening of the collision energy distribution relative to the ion energy distribution. This broadening is reduced for smaller crystals and so these are best suited for reaction studies that require high energy-resolution.

2.8 Energy distributions for higher-order linear RF traps

Thus far the motion of a trapped ion has only been considered for a quadrupole trap. Multipole traps are discussed extensively by Gerlich [78], the effect of the number of trapping electrodes on the ion energies will be considered briefly here.

Multipole traps are of a similar configuration to quadrupole traps, in that adjacent electrodes will possess RF voltages of opposite signs at any given time. As with the quadrupole trap, the multipole-expansion is exact if electrodes are hyperbolic, although at sufficiently small radial distances from the trap centre, the multipole expansion can be curtailed after the first non-zero term if cylindrical electrodes of the correct diameter are used. The primary difference in the radial trapping potential for the various multipoles traps is the order of the radial-dependence of the potential. Whereas in the quadrupole trap the time-dependent potential has an r^2 dependence, for a trap with $2n$ electrodes, the radial time-dependent potential instead has an r^n dependence while the axial potential remains harmonic. The magnitude of the radial driving force is therefore proportional to r^{n-1}.

This change in the trapping potential has key differences both upon ion energy distributions and on plasma structures. A brief discussion of the expected structures in hexapoles and octupoles follows.

2.8.1 Hexapole traps

Ions in a hexapole trap experience a quadratic radial trapping force due to the decreased angular spacing of the electrodes. Since the other forces present in the trap remain the same, this creates a somewhat more complicated effective radial potential than the harmonic potential seen for a quadrupole trap. This situation is also observed with other higher-order traps.

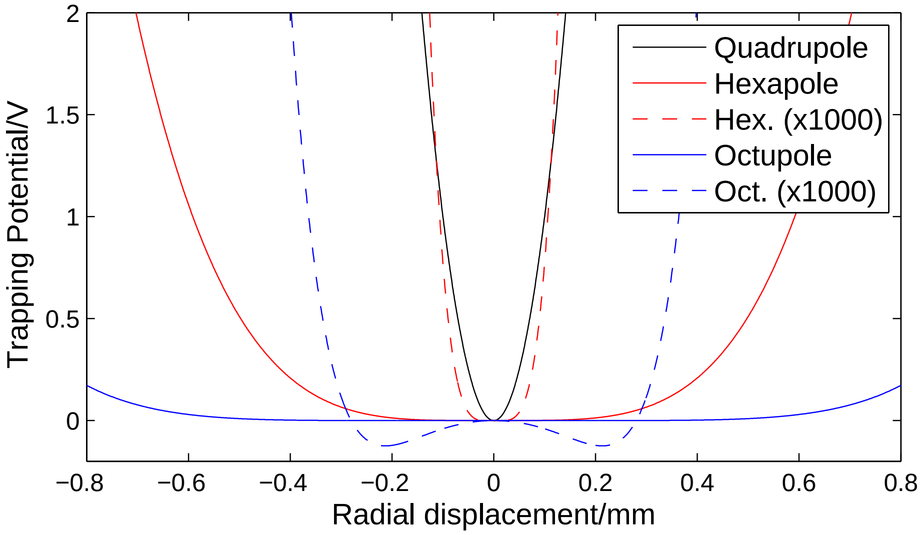

Figure 2.18: Trapping potential for quadrupole, hexapole and octupole traps. Although not visible, the hexapole potential has a potential minimum of 0.5 μV at $r = 15$ μm.

One obstruction to using a hexapole trap is the experimental access available. Unlike in the quadrupole and octupole traps, there are no two access points perpendicular to each other and the trap axis, which would further complicate the experimental setup.

One consequence of using a higher-order trap is that the radial co-ordinates can no longer be considered separately as with a quadrupole trap [78] and motion in the x- and y-axes are coupled due to electrodes of a particular polarity no longer all being in a particular symmetry plane. However, from the time-dependent potential, a time-independent pseudopotential can still be obtained, with cylindrical symmetry maintained. For a hexapole trap,

$$\phi_{\mathrm{psd}}(r) = \frac{9Q^2V_{\mathrm{RF}}^2}{4mr_0^6\Omega_{\mathrm{RF}}^2}r^4. \tag{2.54}$$

Since the axial trapping potential still maintains the form of that in the quadrupole trap, namely

$$\phi_{\mathrm{end}}(x,y,z) = \frac{\kappa V_{\mathrm{end}}}{z_0^2}\left(z^2 - \frac{x^2+y^2}{2}\right) \tag{2.55}$$

it is thus clear that the overall radial potential encountered by an ion will be dominated by the repulsive term arising from axial trapping at small radial displacements, and conversely dominated by the RF trapping force at large radial displacements. The radial potential minimum is found at the point which these two forces balance.

If the potential is plotted as a function of the radial displacement as seen in figure 2.18, we see that the time-dependent potential for a hexapole trap appears relatively flat. When including the repulsive radial force from the static end-cap voltage, the radial potential minimum is no longer located at the trap axis as per the quadrupole trap, but at a certain distance where the repulsive and trapping forces balance.

2.8.2 Octupole traps

Somewhat more beneficial than hexapole traps are octupole traps, as used in studies by Okada and co-workers [129]. Similar to hexapole traps, the presence of a repulsive radial force of quadratic order, combined with a trapping force of higher order creates a local maximum along the trap axis. The radial pseudopotential for an octupole is

$$\phi_{\text{psd}}(r) = \frac{4Q^2V_{\text{RF}}^2}{mr_0^8\Omega_{\text{RF}}^2}r^6 \tag{2.56}$$

which, when combined with the static repulsive potential due to axial forces, again creates a trapping potential with an off-axis minimum. Due to the higher-order trapping potential, there is a greater area where the potential is ‘flat’. When compared to a hexapole, the potential minimum is both at a greater displacement and deeper with respect to the potential at the trap axis.

2.8.3 Comparison of ion energies in low-order traps

As with ions in a quadrupole trap, motion of ions in a hexapole or octupole trap can be separated into secular motion and micromotion. The adiabatic approximation is valid for these traps, and also holds for traps with up to 30 RF electrodes [78].

To aid comparison between quadrupole traps and those of higher-order, most trap parameters have been chosen to replicate those in table 2.1. The only necessary parameter that would need to change experimentally is the electrode radius, which for these simulations is assumed to be the required value for each trap assuming $r_0 = 3.5$ mm.

As observed by Okada and co-workers, the flat radial potential in octupole traps means that Coulomb repulsion between ions forms ionic rings and tubes [129]. Similar structures are observed in a hexapole trap, although the tubes formed are longer and with a smaller radius, with multiple shells formed with few ions. It should be noted that the ions do not necessarily reside in the radial minimum as in figure 2.18, since repulsion from other ions will push the ions further from the trap center.

From the profiles shown in figure 2.19, it can be observed that in a higher order trap, there is less of an increase in the average energy when the crystal size is increased. However, when using similar endcap voltages for different traps, a slightly narrower energy distribution for the trapped ions is observed for lower order traps. Given these factors, collision energy distributions with a higher order trap will be less dependent on the number of ions, which can be useful if this varies between experimental cycles. There are thus potential advantages to studying reactions with higher order traps. Due to the shallower trapping in higher order traps, the endcap voltage used could be further reduced, which would narrow the energy range further as the repulsive force dominates at small radial displacements.

However, there would be complications in observing the progress of a reaction. Due to the large diameter of the ion rings, there would be very few ions that could be in the imaging focal plane at any given time. It would thus be more difficult to monitor reactions from fluorescence images. The increased diameter of the ring will also mean a much greater laser beam width is required, so that a correspondingly greater laser

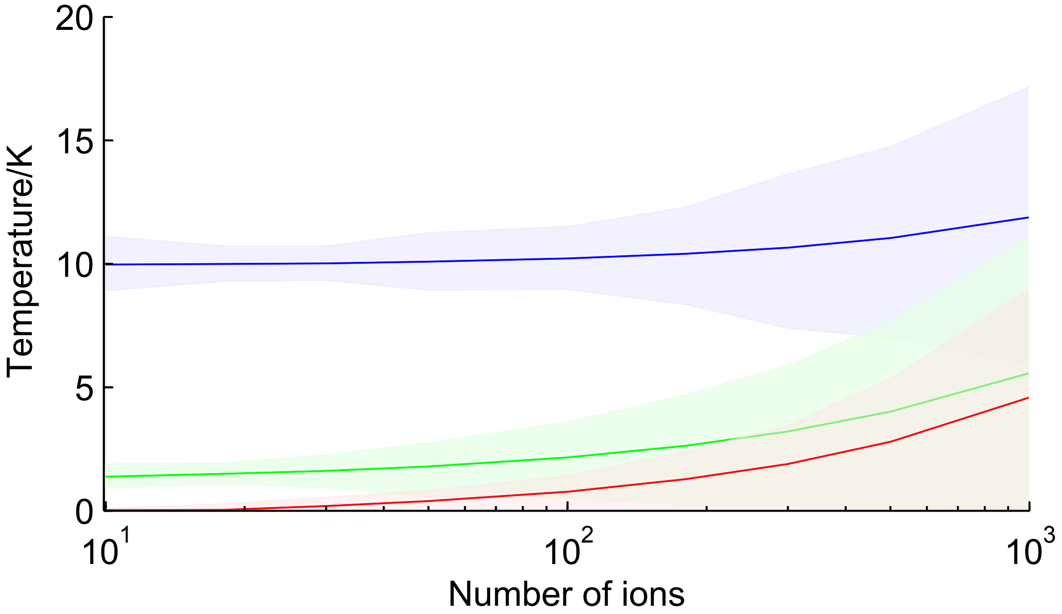

Figure 2.19: Energy ranges for crystals in quadrupole (red), hexapole (green) and octupole (blue) traps, $V_{\mathrm{RF}} = 150$ V, $V_{\mathrm{end}} = 0.3$ V. Solid lines denote average energies.

power to give the same intensity at the crystal. The increased radius also means that there will be less of a change in the images during the course of a reaction, so any reactions would need to be investigated in combination with mass spectrometric methods as in chapter 5. In light of these considerations, future reactions shall be studied using the quadrupole trap as described above.

2.9 Conclusions

This chapter has discussed the theory behind trapping and cooling ions, and the experimental considerations required. When sufficiently cooled, the ions form a solid-like structure that is suitable for observation. The trapped ions are a suitable species for studying low-energy collisions, and are thus used as a 'target' for decelerated molecular beams that are described in the next chapter. Simulations are also required to complement experimental data, and a method for simulating this ions has been discussed. Crystal features that are derived from the simulations include the number of dark ions that cannot be observed otherwise and the temperature of ions in the crystal.

The simulations also show an important property of the ions in the crystal, namely the thermal distributions that arise from RF-induced motion of the ions. For a quadrupole trap, the size and shape of crystal, determined by the trapping voltages, strongly influence the width of the distributions. From the profiles shown for higher order traps, it can be observed that in a higher order trap, there is both a narrower energy distribution for the trapped ions, and there is less of an increase in the average energy when the crystal size is increased. There are thus potential advantages to studying reactions with higher order traps. However, there would be complications in observing the progress of a reaction. For the trapped ions in a quadrupole, the range of energies is of consequence when considering collision energy distributions during reactions with other cold species.

Chapter 3

Deceleration of molecular packets

The focus of chapter 2 is the requirement of using RF electric fields to trap ions and the resulting implications for the ion energies that can be attained. However, the advantages are also manifest in that the trapping depth of several eV attained when using modest voltages allows a trapping lifetime that can extend to several hours, or even days under ideal conditions. Hence the ions contained make an ideal ‘target’ for a cold molecular flux, as has been utilised previously when using a bent electrostatic quadrupole guide as a continuous source [16, 49]. However, the guided molecules in these experiments were rotationally hot, with limited flexibility in translational temperature. A natural progression is to replace the source of molecules with one that is rotationally cold, and that has a translational temperature that is both adjustable over a large energy range and can reach comparable temperatures to the quadrupole guide. Both of these features can be realised with a Stark decelerator, which forms the basis of this chapter. The general principles of Stark deceleration are discussed, as are the adaptations needed to the system to make it compatible with the existing ion-trap setup and maximise the sensitivity for future reactions. Understanding the characteristics of the decelerator are a necessary precursor of reaction studies involving decelerated molecules, which are discussed later in chapter 4.

3.1 Need for Stark deceleration

A molecular beam formed by supersonic expansion from a valve has low rotational and internal translational energy[1]. However, the beam possesses a high translational energy in the laboratory frame, indeed, with speeds greater than that of a Maxwell-Boltzmann distribution of the gas at room temperature since the molecules' rotational and translational kinetic energy has been predominantly converted into longitudinal motion [130]. Depending on the identity of the principal component of the beam, beam velocities of 250-2000 m/s are observed. Since the beam speed is dependent on the average molecular weight in the beam, by seeding a small amount of the molecule of interest in a noble gas the average weight, and beam velocity, can be altered.

The crossed molecular beam experiment has been a major tool in the field of reaction dynamics, since it can bring together packets of molecules with carefully defined collision energies. However, the crossed molecular beam technique is generally inapplicable to the low energy ($\ll 0.5$ eV) regime due to the high velocity of the beams, and there is a range of collision energies since the molecules in the beam still have a velocity spread of several tens of m/s. This can be mitigated to an extent by reducing the angle between the crossed beams, resulting in a lower beam velocities in the centre-of-mass frame and correspondingly smaller collision energies, and by minimising the velocity spread in the beams. The ultimate limit of this is demonstrated by Narevicius and co-workers, who achieve collision energies down to 10 mK when using a bent magnetic quadrupole to guide one molecular beam, merging it with another [131].

Velocities of molecular beams can also be reduced by cooling the molecular beam source, but at the cost of a lower seeding percentage, and thus reduced densities, of the molecules of interest in the beam to prevent clustering within the beam. Mechanical methods for reducing beam velocities by having a non-stationary source have been

---

[1] The vibrational energy is typically not low, but is close to the temperature of the backing gas due to poor conversion between vibrational and translational energy.

Species	Stages used	Minimum velocity achieved (m/s)	References
CO* ($a^3\Pi_1$)	63	100	[50]
ND_3	130	35	[133], this work
LiH* (X, J=1)	100	53	[134]
H_2CO	143	26	[135]
OH	69	323	[136]
NH* ($a^1\Delta$)	130	330	[137]
SO_2	326	53	[138]
YbF	87	276	[139]

Table 3.1: Stark decelerated species and minimum achieved velocities.

investigated by Herschbach and co-workers [132] with achieved beam speeds of 35 m/s. However, the rotational distribution of the beam resembles that of a beam from a stationary valve.

Since the groundbreaking experiments by Stern and Gerlach in 1922 [140], many techniques have been developed to alter the momentum of neutral particles using electric or magnetic fields [141]. The first attempt to reduce the energy of molecules in a beam was by Wharton and co-workers [142] among others, but these attempts were unsuccessful at the time. The first practical demonstration of deceleration of neutral species by electric fields was achieved by Meijer and co-workers when decelerating a beam of CO* [50], and has been extended to many other species since that time, examples of which are seen in table 3.1.

3.2 The ammonia molecule

Ammonia is an oblate symmetric top with C_{3v} symmetry, the rovibronic structure of which is extremely well studied [143, 144]. The low lying vibrational structure of the ammonia molecule is a classic example of a double-well oscillator, as shown in figure 3.1, that arises due to a non-zero barrier to inversion of the ammonia molecule through the trigonal planar configuration. If the wells are considered in isolation,

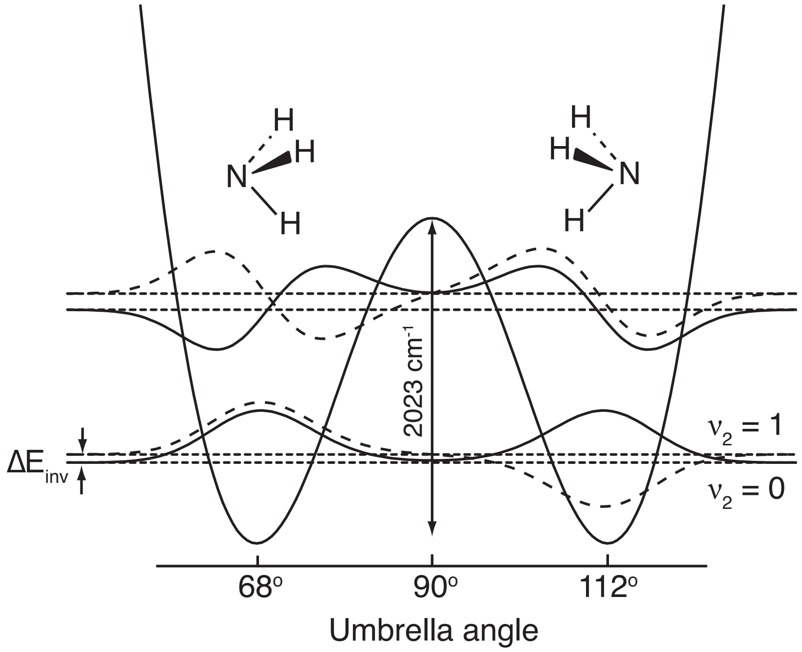

Figure 3.1: Low lying vibrational energy levels of NH_3.

excitations correspond to excitation of the umbrella vibrational mode, ν_2. However, as wavefunctions confined to only one of the wells are not eigenfunctions of the molecular Hamiltonian, a superposition of the states in each well is taken, to give a symmetric and antisymmetric vibrational state. The energy splitting between each pair of vibrational states is determined by the tunnelling rate between the non-stationary states in the two wells, which is itself dependent on the height and width of the barrier to inversion. For ammonia, the local maximum between the two wells resides 2023 cm^{-1} above the well minima, which is sufficiently low for an appreciable tunnelling rate. This circumstance can be compared to the vibrational structure of *eg* PH_3 or CH_3F, wherein no tunnelling occurs due to the much higher inversion barriers (11,000 cm^{-1} for PH_3). With no inversion the symmetric and antisymmetric states seen are degenerate. However, where there is an appreciable tunnelling rate, such as in ammonia, the inversion splitting, ΔE_{inv}, is now significant.

Assuming that the Born-Oppenheimer approximation is valid, nuclear and electronic motions are considered independent of one another and so the energy difference between the inversion barrier and the potential well minima is invariant for the various isotopologues of a given molecule, to a very good approximation. However, due to the different reduced mass of each isotopologue, the vibrational constants shall differ and so there will be differences in the relative barrier height, between a given vibrational level in one of the single wells and the inversion maximum. This is exemplified by the isotopologues of ammonia, of which NH_3 and ND_3 are of most interest to the work in this thesis. Due to the greater reduced mass of the N-D bond relative to that the N-H bond, energy gaps between adjacent vibrational states are correspondingly smaller and the ground vibrational state will thus be lower in energy relative to the barrier. This increased barrier height from the ground vibrational state in ND_3 reduces the tunnelling rate and so also decreases the inversion splitting between states to 0.053 cm^{-1} for ND_3 from 0.79 cm^{-1} in the case of NH_3.

Ammonia is present in para ($K \neq 3i$) and ortho ($K = 3i$) forms, where K is the rotational quantum number about the principal symmetry axis and i is an integer. The spin statistics of the proton and deuteron dictate that there is a weighting between ortho and para states of 2:1 for NH_3 and 11:8 for ND_3 [145]. Upon supersonic expansion, rotational cooling reduces the population of the excited rotational states, but there is no conversion between the different spin states on the timescale of the experiment. The lowest para state, with $|J, K\rangle = |1, 1\rangle$, is thus a predominant species present in the molecular beam. Since the ortho species present in the beam, the $|J, K\rangle = |0, 0\rangle$ and $|1, 0\rangle$ states, experience no first-order Stark effect, only the $|J, K\rangle = |1, 1\rangle$ state shall be considered in the interaction of ammonia with electric fields.

The relative populations of the low-lying rotational states can also give an indication of the internal temperature of the molecular beam. Determination of the molecular beam temperature, and all subsequent detection of ammonia, occurs through detection of the ionised species. Ammonia is ionised in a [2+1] REMPI process via the $\tilde{B}(v = 5)$

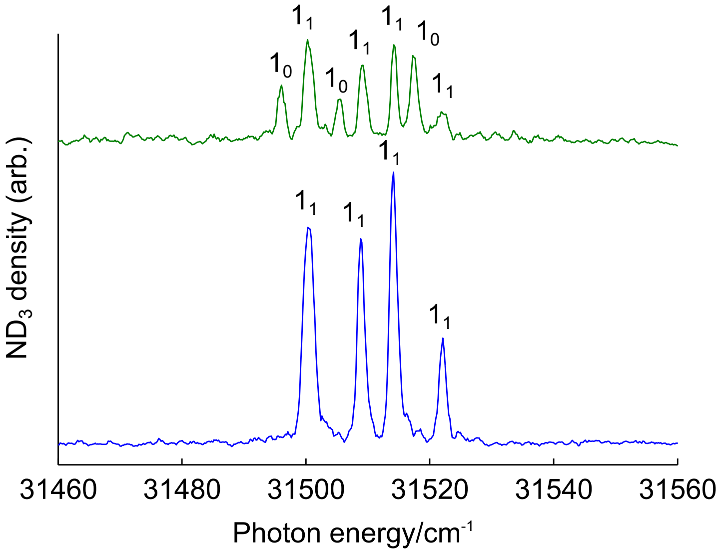

Figure 3.2: [2+1] REMPI spectra of ND$_3$ states present in the molecular beam in the absence of (top) and with (bottom) deceleration fields. Transitions are denoted by the J_K quantum numbers of the ground-state levels.

state at approximately 63,000 cm^{-1}; a spectrum taken around this transition is shown in figure 3.2, from which significant population of the various $J = 0$ and $J = 1$ states is observed. Fitting of the spectrum obtained with PGOPHER [146] yields an internal beam temperature of 5 K.

3.2.1 Stark effect in ammonia

In an electric field, molecules are subject to the Stark effect. The magnitude of this effect is given as

$$
\begin{aligned}
U_{\text{stark}} &= -\vec{\mu} \cdot \vec{E} && (3.1)\\
&= -|\vec{\mu}||\vec{E}| \cos\theta && (3.2)\\
&= -|\vec{\mu}||\vec{E}| \frac{MK}{J(J+1)} && (3.3)
\end{aligned}
$$

where $\vec{\mu}$ is the dipole moment of the molecule, $\vec{E}$ is the electric field, θ is the angle between $\vec{\mu}$ and $\vec{E}$, J is the total rotational quantum number, M is the space-fixed rotational quantum number and K is the molecule-fixed rotational quantum number about the principal axis of symmetry in the molecule. In high electric-fields, M and K are no longer good quantum numbers individually and are instead expressed as the product MK. Equations 3.2 and 3.3 are equivalent since the $MK/J(J+1)$ term in equation 3.3 is the expectation value of $\cos\theta$ in equation 3.2.

In the case of ammonia, the Stark effect is modified by the addition of another quantum number to signify the inversion state [147]. The resulting Stark energy experienced by an ammonia molecule with inversion splitting ΔU_{inv} is

$$U_{\mathrm{stark}} = \pm\sqrt{\left(\frac{\Delta U_{\mathrm{inv}}}{2}\right)^2 + \left(|\vec{\mu}||\vec{E}|\frac{MK}{J(J+1)}\right)^2} \mp \frac{\Delta U_{\mathrm{inv}}}{2}. \tag{3.4}$$

If higher-order perturbation effects are neglected, then at high electric fields the E-field dependent term dominates over the inversion splitting dependent terms, and approaches that seen in equation 3.3. However, at lower electric fields, the magnitude of the Stark shift at a given E-field is affected by the magnitude of the inversion splitting. This accounts for the most significant difference seen in the Stark maps for the $|J = 1\rangle$ state of NH_3 and ND_3. For both species the inversion splitting causes the Stark effect to become quadratic at sufficiently low electric fields. Since there is a greater inversion splitting for NH_3 at zero electric field, the non-linear effects persist to higher electric fields for NH_3, and so the Stark energy increases more slowly as the electric field increases. As seen in figure 3.3, the increase in Stark energy from zero electric field to 10^5 V cm^{-1} is 1.15 cm^{-1} for ND_3, which compares to 0.9 cm^{-1} for NH_3. This effect is by no means exclusive to the $J = 1$ rotational states; higher rotational levels present in the supersonic expansion due to non-zero internal molecular temperatures also undergo similar effects, and low-field seeking states of the $J = 2$ and $J = 3$ states have been experimentally observed after deceleration [148].

The Stark potential that can be achieved with relatively modest high voltages

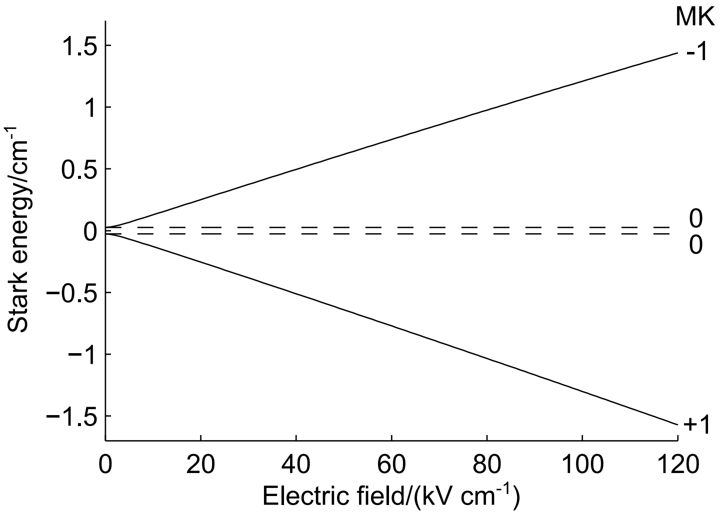

Figure 3.3: The Stark effect for ND_3.

has already been used in this lab [85, 147] to velocity-select a cold fraction of a room-temperature effusive beam that passes through a bent quadrupole. Application of high voltages to the electrodes forms a potential minimum for low-field seeking molecules, which is only shallow enough to guide low velocity molecules around the bend and in the direction of a Coulomb crystal. Since static voltages are used for this technique, a continuous source of molecules into the quadrupole can be used, ensuring a continuous cold molecule flux at the crystal. In contrast to this, the deceleration method described below uses time-dependent electric fields and so must be used with a pulsed molecular source.

3.3 Stark deceleration of ammonia

As seen in figure 3.3, the interaction of an electric field with a polar molecule lifts the degeneracy of the MK rotational quantum number and imparts a Stark energy on the molecule. For those states where the product MK is negative, the dipole moment can be thought of as aligned in the opposite direction to the electric field and so an increasing electric field will increase the Stark energy, such that these molecules

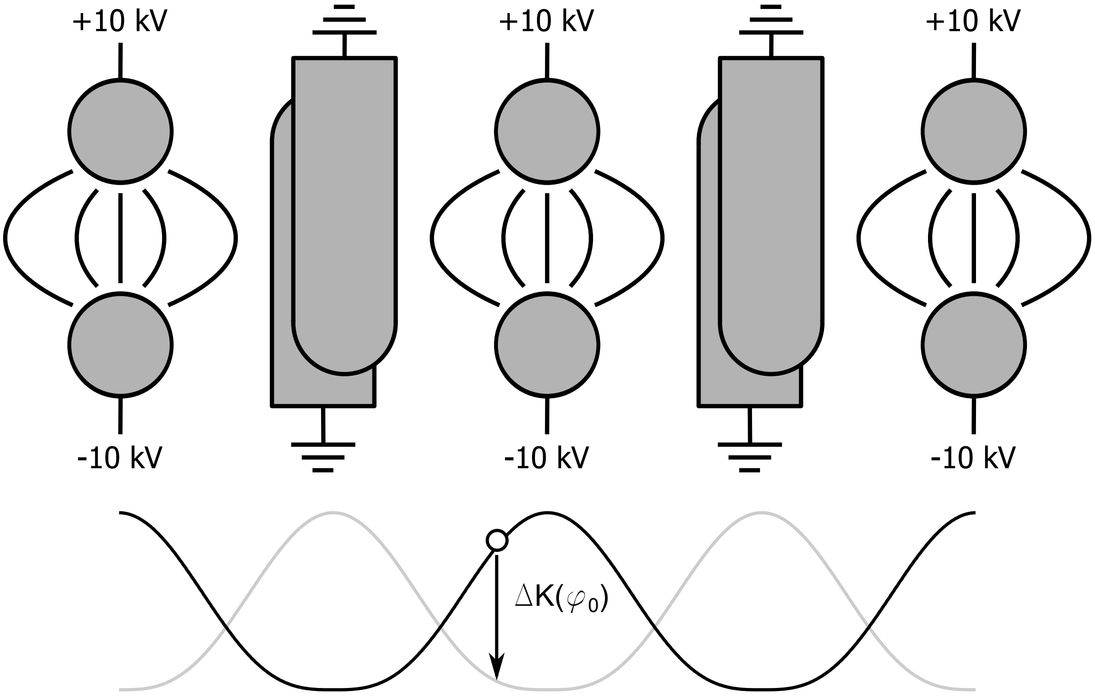

Figure 3.4: Schematic of an ammonia molecule travelling through a decelerator stage, and the potential energy experienced by the molecule.

experience a force towards regions of low electric fields (and are referred to as low field seeking states, lfs). Other states which have the product MK positive will conversely experience a decrease in Stark energy and hence experience a force to regions of high electric fields (high field seeking states, hfs).

The Oxford Stark decelerator consists of 131 pairs of spherically-capped cylindrical electrodes. At a given time, high voltages are applied to alternate electrode pairs, with one of the electrodes in the pair held at a voltage of typically +10 kV and the other at typically -10 kV. This creates a peak electric field between electrodes of 100 kV cm^{-1}. As a molecule approaches the electrode pair, it experiences an increase in the electric field. Lfs molecules will thus experience an increase in the Stark energy, and the kinetic energy must likewise decrease. If only static voltages are applied to the electrodes then the reverse occurs after the molecule moves past the pair of electrodes and there will be no overall change in the trajectory or kinetic energy of the molecule. However, if the voltage is switched off rapidly enough, the electric field will reduce while the molecule is effectively stationary. The molecule will thus lose its Stark energy due to the reduced electric field, but without regaining the kinetic energy, and so will experience an overall deceleration. The magnitude of this deceleration, on the order of 1 cm^{-1} loss of kinetic energy, is small compared to the initial kinetic energy of ~ 120 cm^{-1} of the molecule; thus, the process of conversion of kinetic to potential energy, followed by loss of the potential energy must be repeated many times for a substantial deceleration to be observed. This can be achieved if the same high voltage is applied to the next pair of electrodes while the first pair is grounded. The cumulative effect of removing 1 cm^{-1} of kinetic energy per electrode pair (henceforth referred to as a decelerator stage) can bring the molecules very close to a standstill. This process can be seen in figure 3.4.

The magnitude of kinetic energy loss and velocity change imparted at each decelerator stage is dependent on the timing of the voltage switch. At this stage it is apt to define the deceleration phase angle, ϕ, which denotes the position of a molecule at which the voltages are switched. A phase angle of 0 is defined as halfway between two sets of electrodes and a phase length equivalent to twice the separation between adjacent deceleration stages. The phase angle dictates the amount of potential energy gained at each stage and thus the eventual deceleration. The phase angle chosen also determines the relative proportion of molecules from a molecular beam that can be decelerated.

When considering the trajectory of a molecule through the decelerator, it is simplest to first consider a synchronous molecule, one defined with an initial position and velocity such that it retains a constant phase angle through the decelerator, defined as ϕ_0, and thus follows the same potential through each stage. This is most easily considered with a phase angle of 0: in this circumstance, the molecule is always exactly halfway between subsequent electrode pairs upon switching. A synchronous molecule will experience equal decelerating and accelerating impulses over the course of a switching cycle, and thus will experience identical forces over the course of subsequent switching cycles. Similarly, for other phase angles, the synchronous molecule will be found at a position where the electric field magnitudes are the same from one stage to the next. However, since it now experiences an average decelerating force, it thus experiences a removal of kinetic energy that is equal for all stages. One can also note that a phase angle less than 0 will result in acceleration of the synchronous molecule.

The kinetic energy loss per deceleration stage, $\Delta K(\phi_0)$, can be expressed as a Fourier series [149] which gives

$$\Delta K(\phi_0) = 2a_1 \sin(\phi_0) + 2a_3 \sin(3\phi_0) + \dots \tag{3.5}$$

of which reduction of the RHS to the first term is a reasonable approximation. Of note is the fact that there is a diminishing increase in energy loss as ϕ increases.

The treatment of synchronous molecules has been dealt with extensively, and is explained in the work of Bethlem [149] and van de Meerakker [150] following similar treatments of synchronous ions in particle accelerators, as described in Ref. [151]. The treatment of synchronous molecules leads to two important points: the approximation of the numerous spatially-fixed switching potentials to a single potential that travels along the decelerator and applies a constant retardation force to the synchronous molecule, and the concept of phase-space stability, whereby certain non-synchronous molecules remain on stable trajectories through the decelerator by remaining in the travelling potential. It is at this point relevant to mention that the deceleration process is conservative – only a section of the phase-space distribution of the molecular beam that enters the decelerator is able to be slowed. As such, Stark deceleration is subject to the Liouville theorem that states that phase-space density cannot increase during a conservative process.

When converted to a travelling potential, the average force experienced by a molecule close to the synchronous point over one decelerator stage is

$$\bar{F}(\phi_0 + \Delta\phi) \approx -\frac{\Delta K(\phi_0 + \Delta\phi)}{L} \tag{3.6}$$

where $\bar{F}$ is the average force experienced over a decelerator stage, and $\Delta\phi$ is the phase difference from that of the synchronous molecule. Incorporating equation 3.5 into equation 3.6 gives

$$\begin{aligned}
\bar{F}(\phi_0 + \Delta\phi) &\approx -\frac{2a_1 \sin(\phi_0 + \Delta\phi)}{L} && (3.7)\\
&\approx -\frac{2a_1(\sin\phi_0 \cos\Delta\phi + \sin\Delta\phi \cos\phi_0)}{L} && (3.8)\\
&\approx -\frac{2a_1(\sin\phi_0 + \Delta\phi \cos\phi_0)}{L} && (3.9)\\
&\approx \bar{F}(\phi_0) - \frac{2a_1 \Delta\phi \cos\phi_0}{L} && (3.10)
\end{aligned}$$

when assuming $\cos\Delta\phi \approx 1$ and $\sin\Delta\phi \approx \Delta\phi$ for small $\Delta\phi$. The difference between the average force applied a non-synchronous molecule and a synchronous molecule is therefore linearly proportional to $\Delta\phi$. A non-synchronous molecule will thus oscillate around the synchronous point with a frequency equal $\sqrt{2a_1 \cos\phi_0/mL}$, where m is the mass of the decelerated molecule. This is explained by the deceleration experienced by the non-synchronous molecule over a number of stages. If initially ahead of the synchronous molecule, it will experience a greater increase in Stark energy before the voltage switch and thus a greater retarding force. The molecule will thus travel backwards with respect to the synchronous molecule. When behind the synchronous molecule it will conversely experience a smaller retarding force and travel forward with respect to the synchronous molecule. This oscillation in both the position and velocity with respect to the synchronous molecule equates to a rotation of the non-synchronous molecule around the synchronous molecule in phase-space. The range of initial molecular positions and velocities that lead to stable trajectories through the

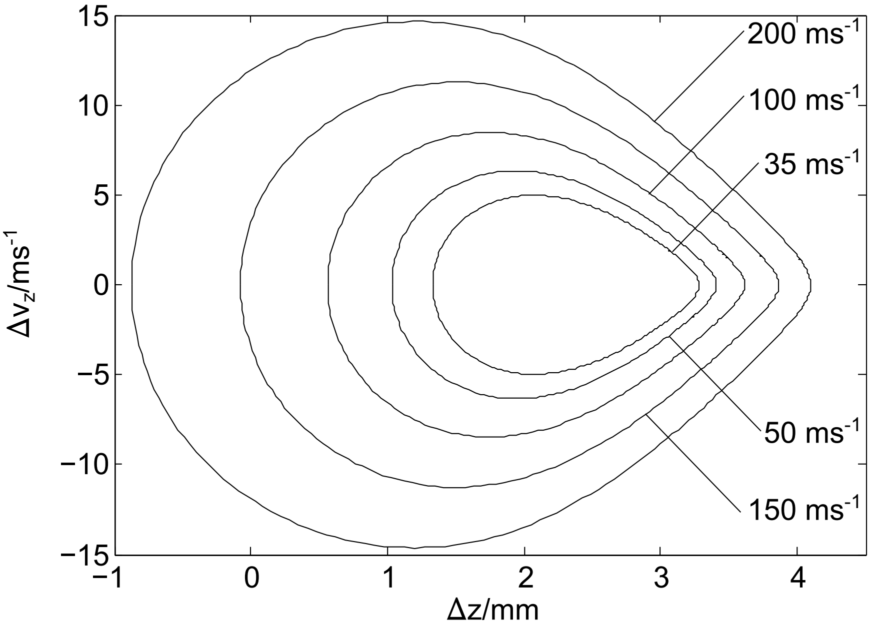

Figure 3.5: Separatrices at various phase angles, from a one-dimensional decelerator model. Final velocities for ammonia molecules are also given for each phase angle, assuming an initial beam velocity of 385 m/s.

decelerator form a six-dimensional volume known as the separatrix.

Upon increasing the phase angle, a range of effects are seen, both for the synchronous molecule and the molecular packet. Firstly, the synchronous molecule will be further advanced in the deceleration stage when switching voltages, so experiencing a greater deceleration for each stage. This is equivalent to experiencing a continually steeper gradient in the travelling potential. While the synchronous molecule shall have a portion of its kinetic energy removed at each electrode stage and will still remain at a fixed position in the travelling potential, non-synchronous molecules will again oscillate around the synchronous position. However, the range of stable trajectories is reduced and the separatrix has a smaller volume, as seen in figure 3.5. This continues until the separatrix reaches zero volume when $\phi = 90°$.

The effect of the phase angle on the final velocity is seen in figure 3.6. As the phase angle increases, there is a corresponding increase in the kinetic energy removed. Since the velocities of the molecules are quadratically proportional to their kinetic

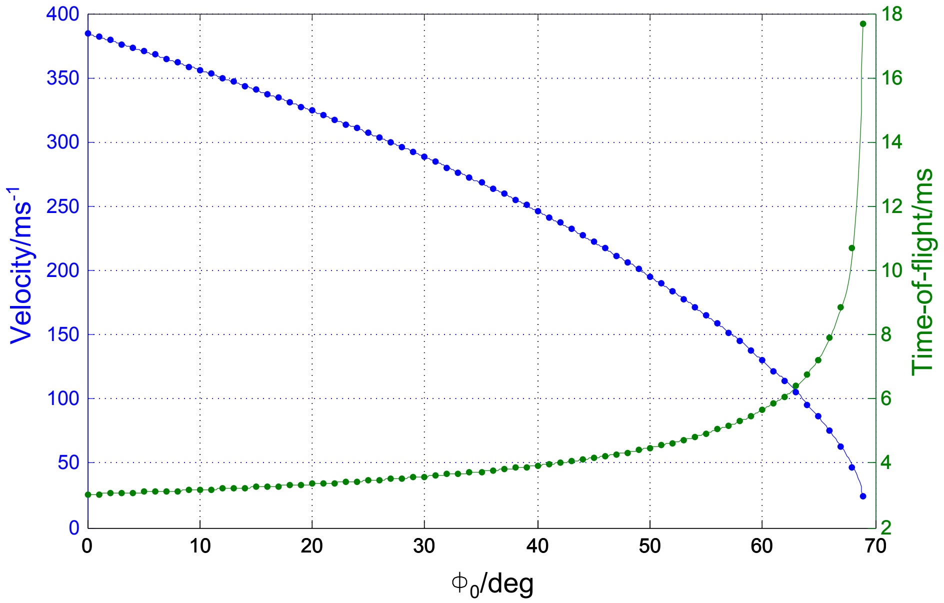

Figure 3.6: Plot of final velocities as a function of decelerator phase angle (blue) and arrival time of the packet at the ionisation region (green).

energy, there is thus a non-linear effect on the final velocities, with the final velocities decreasing slowly at first, and then more rapidly until a point may be theoretically reached where all the kinetic energy is removed. As the phase angle increases, the decelerated peak arrives later in the ionisation region, that being the centre of the ion trap in this experiment.

Transverse motion of the molecules must also be considered since, although the beam is collimated by the skimmer before the decelerator, there is still sufficient transverse motion present to significantly reduce the density of molecules that can reach the ionisation region. However, this is neatly dealt with by the decelerator stages, since regions of highest electric field will be close to the electrodes, reducing slightly on the symmetry axis of the decelerator. The lfs molecules will thus experience a transverse restoring force if they are not on the decelerator axis.

In common with particle accelerators, using a 1D trajectory model of molecules passing through the decelerator gives separatrices with distinct cut-offs between stable and unstable trajectories. However, experimental evidence from both particle accelerators and Stark decelerators [152] shows that this is not the case, with sections inside the separatrix void of molecules. Thus a 3D model is required to accurately model phase-stability in a decelerator. Regions that are stable according to the 1D model but found to be unstable with the 3D model can generally be described by coupling between the transverse and longitudinal forces.

A simple way to increase the molecular density after the decelerator is thus to ensure the separatrix is uniformly filled. This can be achieved by use of a genuine travelling potential well, such as that used in the ring decelerator of Meijer and co-workers [153, 154]. In this a number of potential wells are formed with a peak to peak distance of several electrode distances. The potential then moves by smooth voltage changes on each electrode. As the potential now varies smoothly, the coupling between longitudinal and transverse motion is reduced. Alternatively, one can use the third harmonic of the deceleration, such that only one in three decelerator stages are decelerating, while the other two merely guide the beam [155]. In both cases the coupling between longitudinal and transverse motion is broken to allow complete filling of the separatrix. However, more sophisticated electronics are required for the ring decelerator, and a longer decelerator is needed when using the third harmonic technique to attain a specific deceleration. To maximise the deceleration of ammonia and the velocity range that can be accessed, we use the decelerator in the conventional fashion.

3.3.1 Occupation of multiple wells

Recent developments in the field of pulsed valve design now allow certain valves to operate with sufficiently fast opening times that the length of the gas pulse is shorter than the separation between decelerator stages, *eg* Jordan valves with pulse widths of 25 μs or piezoelectric cantilever valves with pulse widths of ≈ 10 μs [156], so that only one travelling potential is filled. However, for the purposes of studying cold ion-

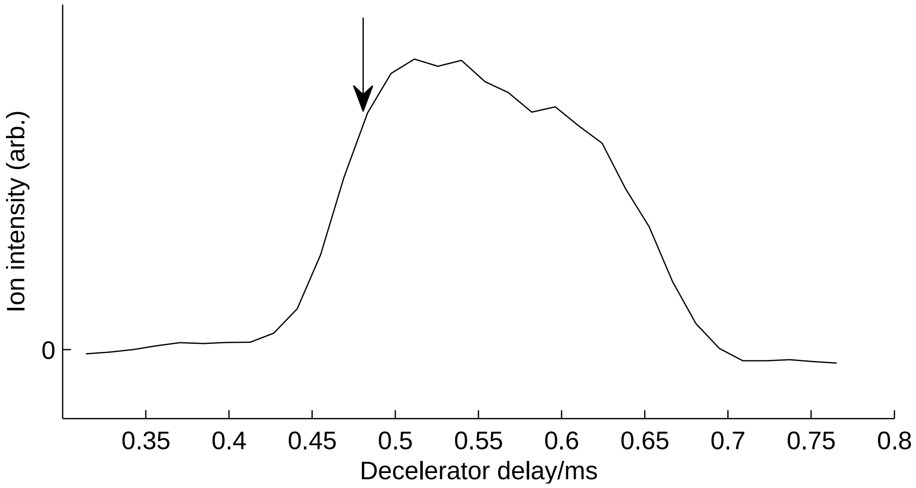

Figure 3.7: Ion intensity as a function of delay time between pulsed valve and initial decelerator charge. Decelerator operated at $\phi = 60^\circ$, $v_{\text{final}} = 133$ m s^{-1}. The arrow depicts the decelerator delay chosen for subsequent experiments, reducing the occupancy of advanced wells.

molecule reactions, we wish to maximise the flux of decelerated molecules, which can be achieved when using a pulsed solenoid valve with a longer opening time.

The temporal width of the pulsed molecular beam from the solenoid valve used is approximately 150 μs, which is principally determined by the minimum duration that a voltage must be applied to the solenoid for the valve to fully open. If an initial beam speed of 385 m/s is assumed, a pulse so formed from the valve shall have a length of approximately 6 cm along the longitudinal axis. Alternate pairs of electrodes are all charged simultaneously, and so travelling potential wells both in front of and behind the potential well considered in the previous section (the ‘principal’ well) also exist and can be filled to some extent. The general deceleration principles described above apply equally to these additional wells, although the timing sequence for deceleration can affect the phase-space acceptance and final velocities of these packets. These effects are summarised for potential wells filled in front of and behind the principal well.

If the additional filled well is in front of the principal well, these molecules shall initially experience a timing sequence identical to those molecules of the main well.

The phase-space acceptance for this advanced well will be equal in terms of the velocity component to the main well while the translational acceptance will be shifted forward by 11 mm. At the end of the decelerator, molecules in the advanced well will exit the decelerator before the final two deceleration sequences. Thus these molecules will leave the decelerator with greater kinetic energy than those in the main well. Molecules trapped in wells still further ahead encounter even fewer deceleration stages and exit the decelerator even faster.

Conversely, the potential well behind the principal well will only come into existence when the principal well has travelled through two deceleration stages. The phase-space acceptance of this trailing well is thus equal to the phase-space distribution of stable molecules in the principal well after two decelerator stages, *ie* a synchronous molecule in this well will have a lower velocity. Similar to the advanced well, the trailing well will also have the translational acceptance shifted back by 11 mm relative to the principal well. At the end of the decelerator, the molecules in the trailing well are still travelling through the decelerator when the molecules in the principal well have now left the decelerator. If the decelerator timing sequence terminates once the principal well has completed its journey through the decelerator, these trailing molecules now travel freely for the final two stages of the decelerator as well as the distance to the focussing elements. There would be a decrease in the density as the packet disperses for a greater distance than the principal well. However if the decelerator timing sequence has additional stages added of equal duration to the last deceleration cycle, the trailing molecules will be bunched through the final stages, while maintaining a similar phase-space distribution to the principal packet.

It is obviously desirable to maintain as narrow a velocity distribution as possible at the end of the decelerator, while maximising the flux of decelerated molecules that arrive at the detection region. When considering both of these train packet requirements, it is preferable to operate the decelerator such that the ‘principal’ packet is

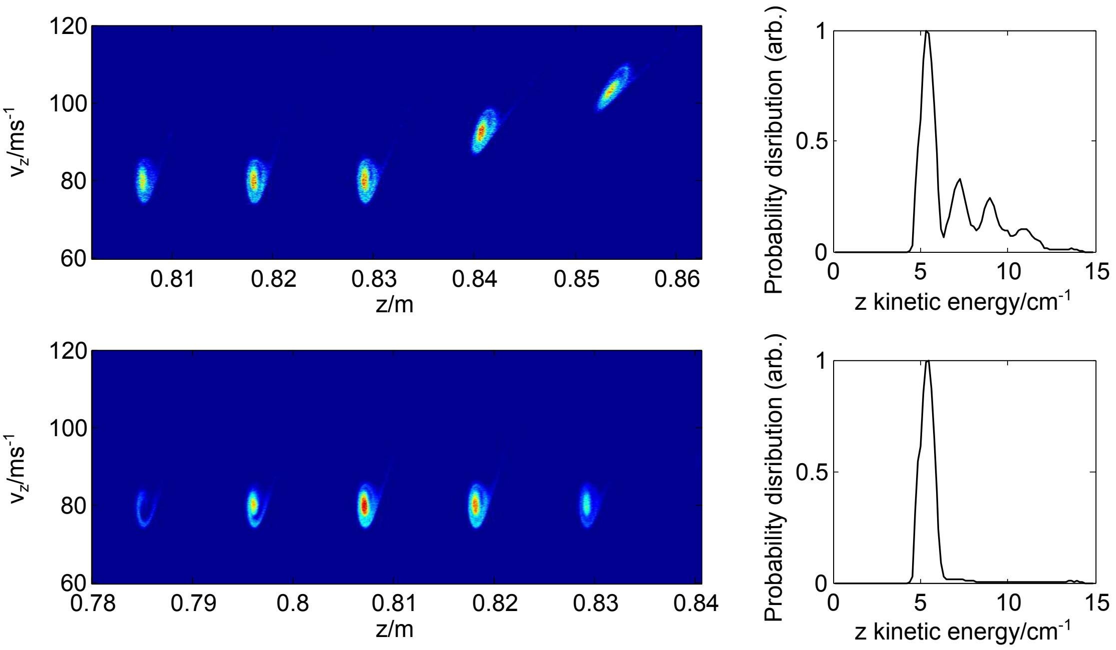

Figure 3.8: Simulated phase-space diagram of multiple packets at the end of the decelerator, with the main packet in the centre of the train (top) and leading the train (bottom). Kinetic energy distributions of the two trains show a much narrower peak when the main packet leads the train [157].

filled by molecules at the leading edge of the molecular beam, which requires the decelerator sequence to start typically 0.45-0.5 ms after the valve opens. As seen at the bottom of figure 3.8, this ensures that all packets with appreciable population trail the ‘principal’ packet and so exit the decelerator with similar velocities. When operating the decelerator in this fashion, occupation of multiple wells becomes less of a problem in achieving narrow energy distributions, while allowing a greater flux of decelerated molecules at the ion trap.

3.4 Experimental setup

The Oxford Stark Decelerator is shown schematically in figure 3.9 and is based upon the design of the original Stark decelerator constructed by Meijer and co-workers [158]. The decelerator apparatus is principally contained in two differentially pumped vac-

Component	Dimension	Size/mm
Hexapole 1	Length	60 mm
Decelerator	Electrode radius	1.5 mm
	Gap between electrodes	2 mm
	Distance between adjacent pairs (Centre-to-centre)	5.5 mm
Hexapole 2	Length	60 mm
Buncher	Electrode radius	3 mm
	Gap between electrodes	4 mm
	Distance between adjacent pairs (Centre-to-centre)	11 mm
Hexapole 3	Length	70 mm
	Hexapole-trap gap	25 mm

Table 3.2: Dimensions of the decelerator used in the work of this thesis.

uum chambers, with the final part leading into the trap chamber. A pulsed molecular valve (General Valve, series 99) is used to create a temporally short packet of molecules. A gas mixture with a 5 bar stagnation pressure of 10% ND_3 seeded in Xe is used as the source of the molecular beam. These conditions give an average molecular beam speed of 385 m/s when it enters the decelerator.

The valve is surrounded by a copper jacket to allow for some control of the beam velocity by changing the temperature of the valve – the temperature of the jacket itself is controlled by a liquid-nitrogen cooled gas flow through the jacket. The valve temperature can be reduced to 200 K; reducing the temperature further risks condensation of ammonia in the valve. The advantages of cooling the valve are evident; 35% of the initial energy of the beam is removed, such that the average speed is now 315 m/s. A lower phase angle is thus required to achieve a certain final velocity. However, operating the valve at reduced temperature requires a lower percentage of ND_3 in the backing gas mixture to prevent clustering of the molecules, which results in a subsequent reduction in the density of decelerated molecules. Thus in practice, the valve is operated at room temperature, with a room temperature air flow passing through the copper jacket to maintain a stable valve temperature. The valve is mounted on

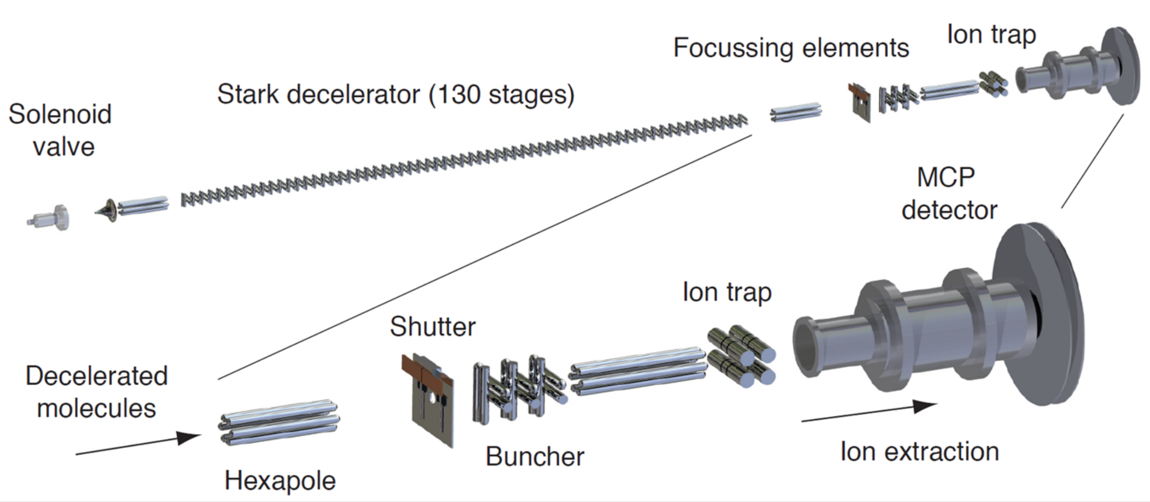

Figure 3.9: Schematic of the decelerator setup [157].

translation stages and can also be moved in all directions when under vacuum; the valve position is optimised prior to deceleration experiments.

The packet passes through a skimmer with an aperture of 1.5 mm at a distance of ~ 30 mm from the valve nozzle, before entering the decelerator chamber. As well as collimating the beam, the skimmer is attached to a differential pumping stage between the source and decelerator chambers. When in operation, the source chamber has typical pressures of 0.5-1.5$\times10^{-5}$ mbar whereas the decelerator chamber maintains a pressure of 3-5$\times10^{-8}$ mbar. When the valve is not in operation, these pressures reduce to $< 5 \times 10^{-7}$ mbar and $< 1 \times 10^{-8}$ mbar respectively. The valve assembly is mounted on a translation stage to ensure alignment of the valve, skimmer and decelerator.

The packet travels in free flight for 40 mm before entering the first electrostatic hexapole. The packet is transversely focussed, although the effect is minor due to the high velocity of the beam prior to deceleration. It then travels in free flight again before reaching the decelerator. Molecules contained in the separatrix are now decelerated according to the timing sequence chosen. After leaving the decelerator, the decelerated packets are collimated by a second hexapole positioned 10 mm after the final decelerator stage. A fast-opening (750 μs opening time) shutter is located after the second hexapole to selectively allow transmission of decelerated molecules only. The decelerated molecules can then be longitudinally focussed as desired using several bunching elements, and transversely focussed into the ion trap using a final hexapole.

After passing the high voltage stages, the decelerated molecules can interact with trapped ions if studying ion-molecule reactions (as will be discussed in chapter 4). If the decelerator is to be used in isolation, relative ammonia densities can be quantified at the ion trap region. Decelerated molecules are ionised with a Sirah pulsed dye laser at 317 nm, in a [2+1]-REMPI process via the $\tilde{B}(v = 5)$ state. The laser is focused 20 cm from the trap centre by a bi-convex lens, with a focal length $f = 30$ cm. By employing the ion-trap electrodes as the repeller and extraction electrodes of a Wiley-McLaren time-of-flight spectrometer, the ions are directed towards a set of microchannel plates and detected. The Wiley-McLaren spectrometer is fully characterised in chapter 5 but at this stage it is sufficient to note that ammonia densities recorded are those in the centre of the ion trap and so will be equivalent to those experienced when ions are trapped.

The voltages applied to the decelerator and focussing elements are supplied by two high voltage power supplies (Spellman High Voltage Electronics Corp, SL300). Alternate electrodes of the same voltage are held in electrical contact by a square rod travelling the length of the decelerator, which also ensures the colinearity of these electrodes. While two electrode rows are held at high voltage, the other two rows are grounded. High-voltage switches (Behlke Electronic GmbH, HTS-150 PGSM) are used to allow for rapid switching between high-voltage and ground. Switch timings are determined by a MATLAB script that performs a one-dimensional trajectory calculation of a synchronous particle travelling through the decelerator at a given initial velocity and decelerator phase angle, an example of which is shown in figure 3.10. A bias voltage of +100 V is applied to electrode rows 1 and 2 to prevent the occurrence

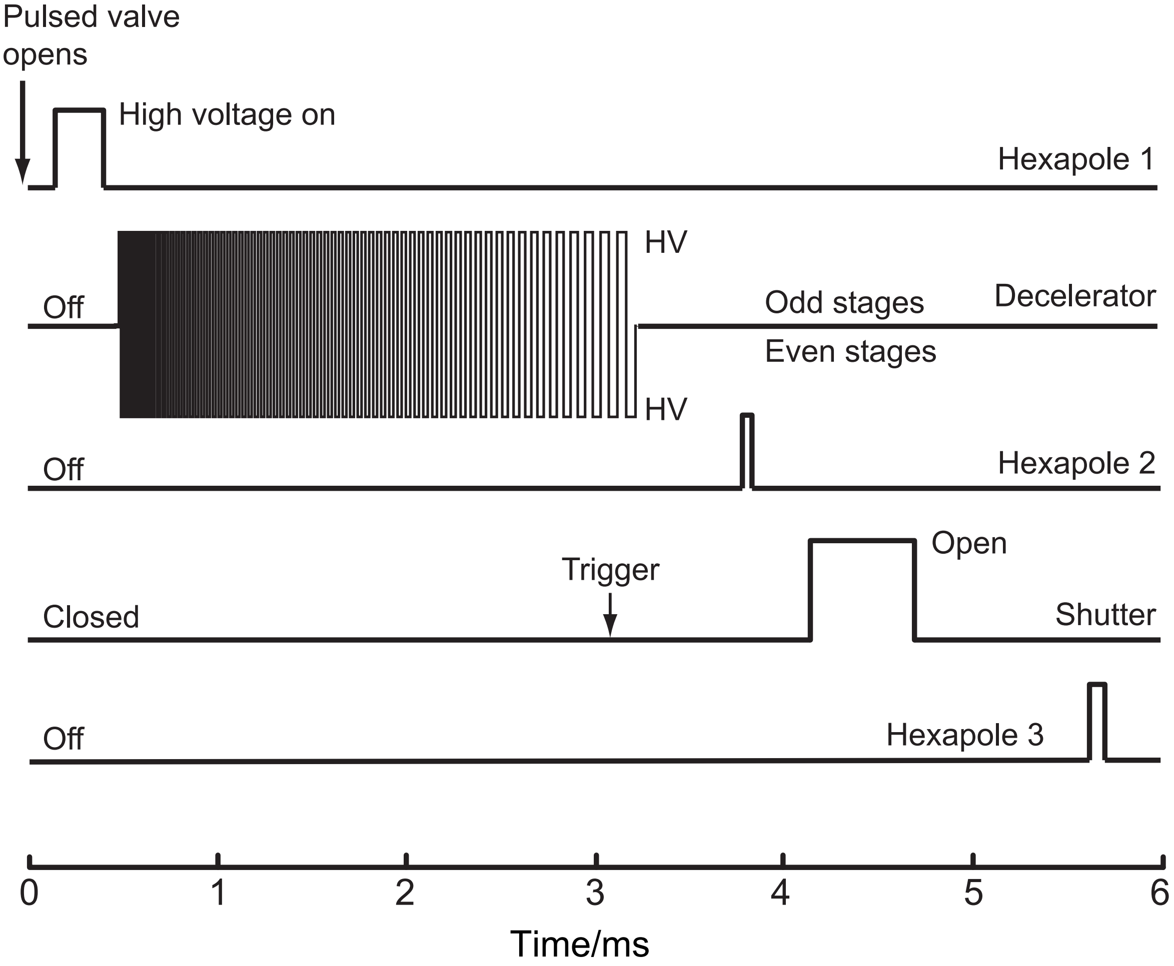

Figure 3.10: Example timing sequence employed for a typical pulse sequence for deceleration of ND_3 and subsequent separation and focussing of decelerated ND_3.

of a zero electric field along the beam axis when the molecules are travelling between the decelerator and other electrodes. This voltage thereby minimises the possibility of Majorana oscillations, which can reduce or negate the effectiveness of the bunching or focussing stages as well as reducing the state purity of the decelerated beam.

Crucial to the density of detected molecules is alignment of the electrode stages relative to each other. A misalignment results in poor phase-space matching for the respective elements and the density of decelerated molecules will significantly decrease. Two methods are used to ensure correct alignment. Firstly, a theodolite[2] is positioned along the beamline, and the alignment checked by use of the variable focus. This allows rough (≈0.2 mm) alignment of the bunching elements with respect to the decelerator. Subsequently, alignment tools are attached to the decelerator and hexapole with a pinhole drilled through the centre of the tools to confirm alignment of the stages using an attenuated helium-neon laser. Finally, the laser is aligned through the decelerator assembly when in the vacuum chamber to confirm alignment of the decelerator, bunching elements and hexapoles with the skimmer and ion trap/time-of-flight apparatus.

After any occasion when the chamber has been brought to atmospheric pressure, the decelerator electrodes need to be conditioned to minimise the possibility of a electric discharge while the decelerator is in operation, which could have catastrophic effects on the electronics involved. These discharges can occur due to imperfections on the electrode surfaces; when a discharge occurs, the immediate area of the electrode surrounding the discharge melts, reducing the surface roughness. The electrodes are conditioned by applying static voltages one pair of electrodes at a time while monitoring the current drawn by the electrodes, which should be zero in the absence of any ill effects. The current is limited to reduce the energy of any discharges and prevent damage to the electrodes. The voltage is increased by 500 V every 10 minutes if

---

[2] An instrument, commonly used in surveying, that has a telescopic sight with a variable focus.

no discharge is observed, to a final voltage of 12.5 kV. This process is then repeated with the other electrode pair. If discharges are observed, a stable voltage is placed on the decelerator until the discharges no longer appear. This can take an appreciable amount of time.

3.5 Utilisation of a fast opening shutter

When discussing the decelerator it is of course necessary not to forget the context in which the decelerator is being used, *ie* as a source of cold molecules that react with a stationary target. The discussion above has considered changing the magnitude of the velocity vectors for the decelerated molecules, but not the direction. Indeed, it is implicit in the phase stability argument that the overall direction does not change, otherwise there would be no decelerated molecules at all. Molecules that pass through the decelerator shall travel in largely the same direction, so that both decelerated and undecelerated molecules shall reach the ion trap, albeit at different times.

This evidently presents a challenge in investigating low energy ion-molecule reactions, since there will be a significant number of reaction events due to undecelerated molecules if they can also reach the ion trap. Since the undecelerated molecular flux is additionally an order of magnitude or more larger than the decelerated flux, any sensitivity to cold reactions will vanish. Thus there is an imperative to ensure that only cold molecules may reach the trap.

Two classes of methods can be used to overcome this issue. One can initially align the decelerator to a location outside the ion trap and then direct the cold molecules toward the ion trap after the decelerator, or one can align the decelerator to the centre of the ion trap and ensure the hot molecules cannot reach the trap.

Meijer and co-workers have previously demonstrated an electrostatic mirror [159] by using a plane of electrodes, alternately grounded and charged, held at an angle

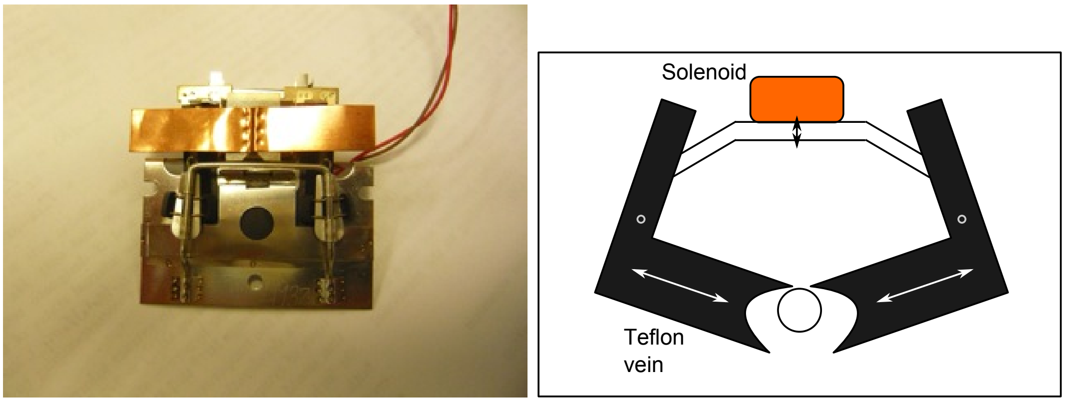

Figure 3.11: Picture and simplified schematic of the mechanical shutter used in the deceleration experiments.

to the incoming beam. Another way that could be used to direct molecules would be to use a bent electrostatic guide – however, there would be difficulties in guiding faster molecules toward the trap, since the potential well is relatively shallow. Previous guiding of ammonia by a bent quadrupole has revealed only molecules with a longitudinal velocity of less than 50 m/s will be guided [160] effectively so that the variety of energies possible form the decelerator is limited. There is additionally the possibility of a mismatch in phase-space acceptance between the two devices, which would reduce the decelerated molecular density further.

It is also economical to use the vacuum chambers that were used when the two experiments operated in isolation. This limits the extent to which the decelerated beam can be directed in relation to the position of the ion trap since there are limited ports on the trap vacuum chamber that can be combined with the decelerator chamber.

Considering this, a technique is thus required to ensure hot molecules do not reach the vicinity of the trapped ions despite travelling towards the ion trap. One potential method is to move the ions to a region of the trap where they are protected from the incoming molecular beam. This is possible by altering the voltages applied to each end-cap of the trap. Because the trap voltages can be altered rapidly, it should be possible to move the ion crystal on the order of a millimetre, where it could be shielded from the molecular beam with a skimmer placed near the ion trap. The disadvantage to this method is that the molecular beam is quite diffuse in the region before the ion trap, and so using a skimmer would reduce the density of decelerated molecules[3].

The method chosen to selectively transmit cold molecules is to use a fast-opening shutter. The opening time of the shutter is thus chosen such that the hot molecules are blocked and no longer remain in the beamline while the cold molecules are transmitted, allowing the desired effect to be achieved.

A fast-opening UHV compatible laser shutter (Vincent Associates, Uniblitz LS6TF) is found to be suitable for the described need. The shutter consists of a 6 mm aperture so that all decelerated molecules can pass through when the shutter is fully open. An aperture of this size is beneficial since the decelerated packets disperse after exiting the final stage of the decelerator due to non-zero transverse velocities. This shutter, shown in figure 3.11, consists of two Teflon-coated veins that are attached to a metal strip. By pulsing a voltage through a solenoid, the strip is pulled down and the veins are pulled apart to expose the aperture, thus opening the shutter for the duration that a voltage is applied. A copper heat sink is in thermal contact with the solenoid to permit 10 Hz operation of the shutter in UHV conditions.

A rise time (characterised as 10-90% transmission) of 400 μs is observed when both veins are operational. The lifetime of the shutter is given as approximately 10 million opening cycles, during which time the Teflon is progressively worn away from the veins. The veins are observed to be susceptible to cracking, which can completely halt motion of the veins past each other. Removal of a cracked vein such that the shutter operates with only one vein permits continued use of the same shutter assembly with the shutter still completely closed when required. In this case the shutter now has an increased opening time of 750 μs, still sufficient for selective transmission of decelerated

---

[3] Although the decelerated packet has a small cross-section at the trap centre, its cross-section is considerably larger at the location of a hypothetical skimmer due to the tight focussing of the beam in the final hexapole.

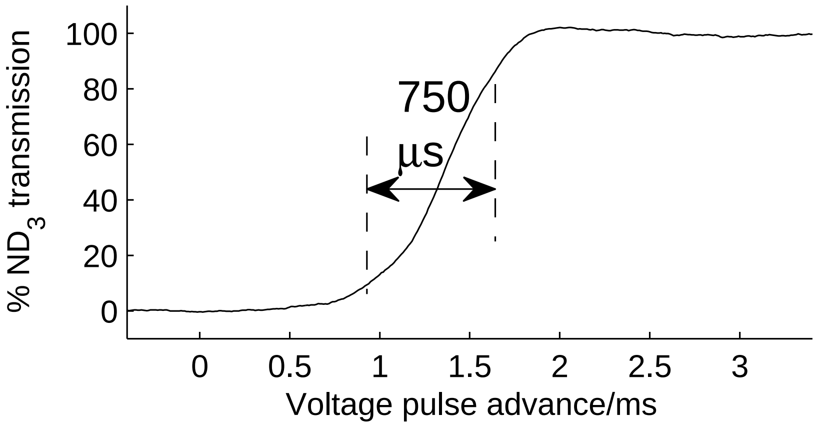

Figure 3.12: Operation of the mechanical shutter, the opening edge of the shutter shown. The voltage pulse advance is defined as the time the shutter trigger signal (from figure 3.10) is sent relative to the expected arrival of the molecular packet at the shutter.

molecules.

The position of the shutter is important for maintenance of background vacuum conditions in the trap chamber. The shutter is fixed to a metal plate to create a differential pumping stage between the decelerator and trap chambers, so that transmission of blocked molecules is minimised. Since this stage is located fairly close to the decelerator, this increases the importance of the shutter opening speed. When decelerating molecules to 100 m/s, a separation of approximately 2 ms is seen in the arrival times of the two principal peaks at the ion trap. However, the temporal separation at the shutter is only 800 μs. Although a greater time resolution is possible by having the shutter closer to the ion trap, the hot molecules would no longer be restricted to the decelerator chamber, and thus could indirectly reach the ion trap and enhance the rate of background reactions.

Due to the position of the shutter in the decelerator assembly, there is no access to the shutter *in situ*; the entire decelerator must therefore be removed from the vacuum chamber if the shutter requires repair or replacement. Removal of the decelerator is a quite arduous process, and care must be taken not to misalign any of the elec-

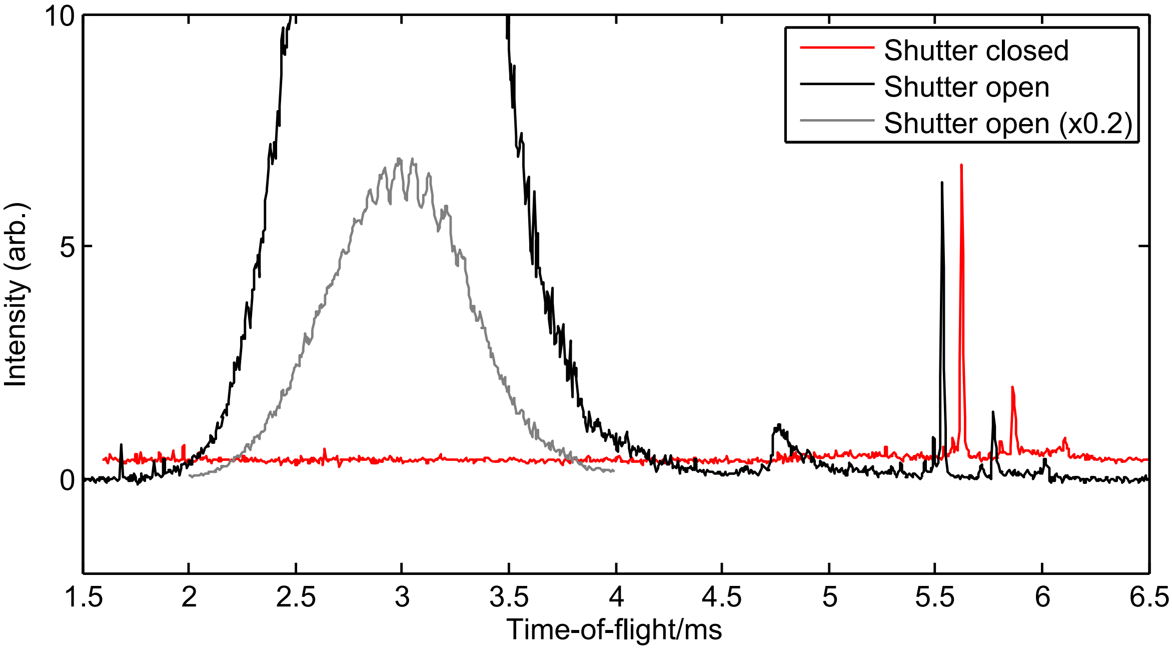

Figure 3.13: Time-of-flight scans for a beam decelerated to 100 m/s with the fast opening shutter open for passage of all molecules and closed, except for the passage of decelerated molecules. T-o-f scan while shutters closed is shifted upwards and delayed by 0.1 ms due to overlap with t-o-f scan while shutter open.

trodes. Access to the shutter when the decelerator is out of the chamber is still highly restricted, and replacement is not trivial. Since the shutter is quite fragile, there is also the potential for damage when replacing or repairing a shutter. It is thus chosen to continue using a shutter when only one vein is in operation, since the shutter performance is only diminished by a small amount.

Use of the shutter located between the second hexapole and the buncher allows unit transmission of cold molecules while fully blocking undecelerated molecules at velocities up to 100 m/s. Figure 3.13 presents this for a beam decelerated to 100 m/s. Above this velocity the shutter is still useful – a decelerated peak can still be obtained if the opening time is delayed sufficiently to block the hot molecules. This is achieved at the expense of transmission probability for decelerated molecules if the opening time is delayed. In this case, the shutter is still opening when the leading edge of the decelerated packet arrives, so that molecules on the outer edge of the packet are

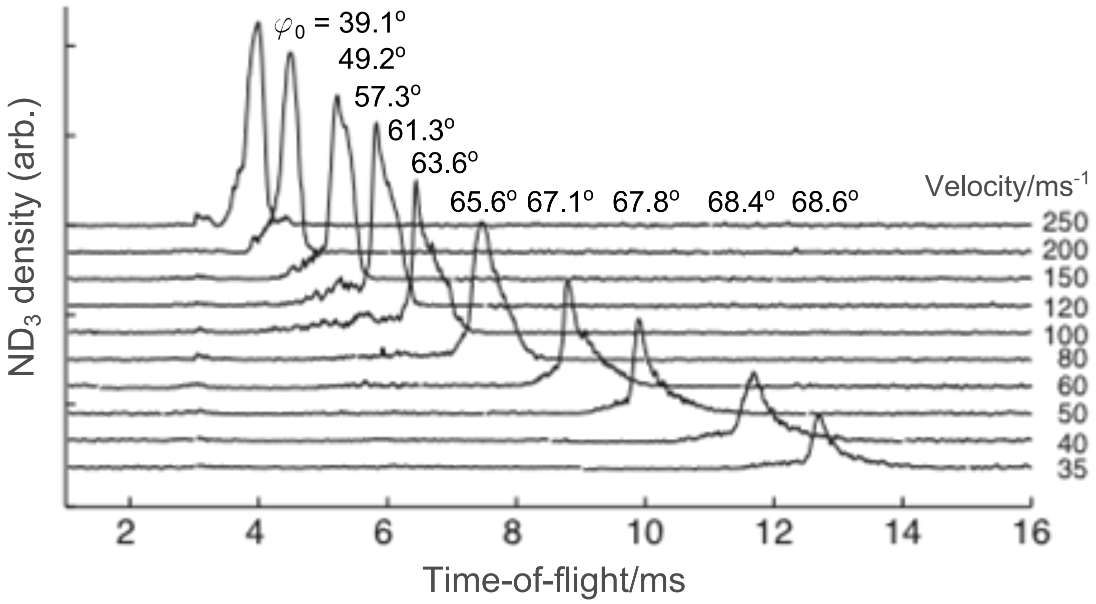

Figure 3.14: Time-of-flight spectra of decelerated peaks after blockage of the undecelerated beam, with final velocities of the decelerated peak.

deflected out of the beam.

At higher velocities still, the slow tail of the main beam is no longer distinct from the decelerated peak, due in part to elongation of the tail of the main beam. The shutter can be used to block the majority of the undecelerated molecules such that with decelerated velocities of 250 m/s, 75% of the transmitted molecules are from the decelerated packets. For studies of molecules with high velocities, a lighter seed gas can be used. This will increase the initial beam speed and increase the delay of the decelerated packets, although there is a corresponding reduction in the density of decelerated molecules due to the increased phase angle required.

Elimination of the hot molecules by the shutter from the molecular beamline as it passes into the ion trap chamber allows examination of the decelerated molecules without the need to consider adverse effects from the hot molecules. This is first evident when considering the time of the decelerated peak with respect to the predictions from computer simulations. Figure 3.14 exhibits experimental time-of-flight spectra, the arrival times of which can be compared with the theoretical predictions in figure 3.6. Good agreement is seen.

3.6 Focussing of decelerated molecules

The distance between the final deceleration stage and the ion trap is constrained by the size of mounting assembly for the decelerator. Since the opening in the ion trap chamber is smaller than the decelerator, a reducing nipple is placed between the two chambers, in which focussing elements are placed to adjust the parameters of the molecular packet after deceleration.

3.6.1 Maximising reactant flux at ion trap

The flux of decelerated molecules that arrives at the centre of the ion trap and can interact with the Coulomb crystal is key to the sensitivity of the reaction experiments. Since the cross-section of the Coulomb crystal perpendicular to the longitudinal axis is less than 1 mm^2 the flux will be proportional to the density of decelerated species in the centre of the packet. As the packets of molecules leave the decelerator they begin to diverge due to a small but non-zero transverse velocity spread. With a distance between the end of the decelerator and ion trap of 30 cm, the molecular flux density is an order of magnitude less than at the end of the decelerator if the molecules experience free flight. Reduction of the decelerator-trap distance results in less dissipation of the flux. However, this is not possible when using existing vacuum chambers and so electrostatic focussing hexapoles are used instead, similar to those used previously by Heiner *et al* [161], which are seen in the lower part of figure 3.9.

The electrostatic hexapole has been shown to be an effective device in focussing molecules with a first-order Stark effect. In regions of the hexapole close to the axis of symmetry, the electric field is proportional to the square of the distance from the

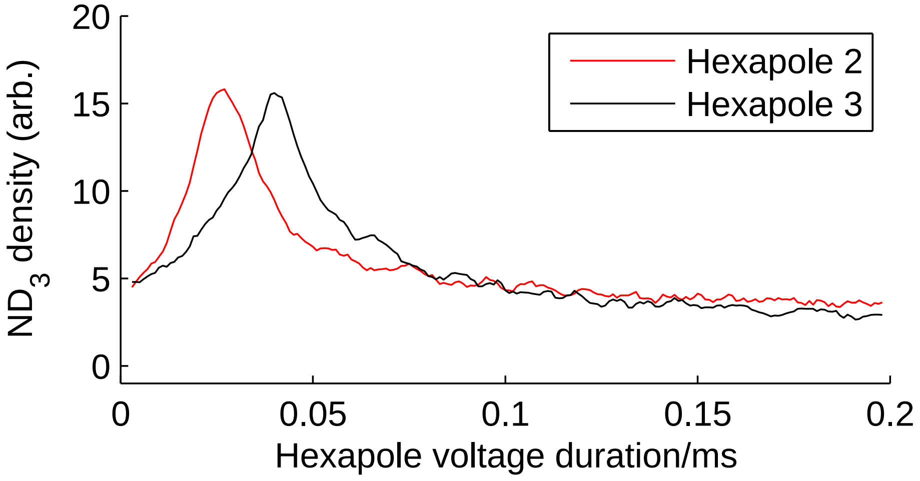

Figure 3.15: Variation of ND_3 density based upon the effective lengths of the two hexapoles. For each scan the duration of the voltage pulse for the hexapole not being scanned is chosen to give the maximum signal intensity.

symmetry axis. For molecules with a first-order Stark effect, they will experience a quadratically increasing Stark potential, which will impart a force linearly proportional to the distance from the symmetry axis and directed towards the axis. The molecules can thus be refocussed to a volume equal to the original volume when leaving the decelerator. Since the Stark effect in ammonia is non-linear for low electric fields, this creates an aberration such that the molecules originally near the symmetry axis experience weaker focussing [162].

Two hexapoles are used to increase the molecular flux. The first hexapole, immediately after the decelerator, collimates the packets transversely. Some transverse expansion of the packet occurs due to the distance travelled between the final decelerator stage and the start of the voltage pulse upon the hexapole, but further dispersal as the packets travel through the shutter and bunching elements is prevented. The expansion of the packet is beneficial since fewer molecules will be in a region of low electric field when being focussed by either of the hexapoles, so a smaller aberration shall occur.

The second hexapole, immediately before the ion trap, then focusses the collimated packets tightly into the ion trap. Although the hexapoles have length of 50 and 70 mm respectively, the effective hexapole length that the molecules experience is significantly shorter than this as voltages are pulsed through the hexapoles for a fixed duration, on the order of tens of microseconds.

Variation of the duration that the hexapoles are charged effectively alters the focal length of the hexapoles. A variable focal length can also be achieved by keeping the hexapoles charged at all times but varying the voltages applied. For simplicity, the hexapoles are kept in electrical contact with the decelerator electrodes, and so are charged using the same power supplies with a constant voltage of ± 10 kV. Variation of the duration of the voltage pulse is beneficial since a high voltage is always used, reducing the volume where non-linear focussing effects will be present for a desired focal length of the hexapole. Use of a voltage pulse allows the position of the focussing to be altered as well as the magnitude of focussing by changing the timing of the pulse. This is of greatest benefit for the final hexapole where the greatest signal intensity is achieved when applying the voltage pulse whilst the packet is near the end of the hexapole. Since the distance to the ion trap is reduced, the voltage pulse is correspondingly longer to more tightly focus the packet to the centre of the ion trap. To prevent loss of ND_3 from the $MK = -1$ state due to hyperfine depolarisation, a bias voltage of + 100 V is applied constantly, so that field-free conditions do not arise throughout the focussing elements when the focussing voltages are off.

The combined effect of the two hexapoles on an individual decelerated packet is seen in figure 3.15. When only one hexapole is used and the other hexapole has no voltages applied to it there is some enhancement of the molecular density as they reach the ion trap, but using both in combination allows a far greater enhancement, of approximately a factor of four. The density decreases past the optimal focussing time as the packets are now getting overfocussed, reducing the density of the packet when it reaches the ion trap.

The situation becomes more complex when multiple packets are considered. Assuming no bunching forces are present, the molecular packets will spread and will eventually form a continuous packet of molecules. Thus it is impossible to optimally focus the entire ensemble of decelerated molecules using the voltage pulse technique, as the focal distance will be constant whereas the distance of the molecules from the ion trap will vary significantly. In this case a time-of-flight scan is taken with no hexapole voltages present. The arrival time of the peak ion intensity is noted and the voltage durations for the hexapoles are optimised for this portion of the packet. This method is additionally useful for reducing the intensities of satellite peaks seen in the time-of-flight spectrum when longitudinal focussing is desired, as described in the next section.

3.6.2 Longitudinal focussing

Due to the non-zero spread in longitudinal velocities of decelerated molecules, the phase-space distribution of the molecules will stretch spatially over the course of travelling from the end of the decelerator to the ion trap. It is thus desirable to rotate the phase-space distribution such that the velocity distribution is narrowed further or the spatial distribution is compacted again, as shown in figure 3.16. Due to Liouville's theorem, the phase-space density cannot be compressed and so narrowing the spread in one dimension of phase-space will increase the spread in another dimension; however, this is often an acceptable consequence.

Longitudinal focussing is achieved by pairs of electrodes of a similar design to those found in the decelerator, but with the dimensions doubled. This follows the bunching design of Heiner *et al* [161, 163]. Instead of there being one set of electrodes held at high voltage at any given time as is seen when molecules pass through the decelerator, voltages are applied for specific durations (between 20 and 70 μs per element) as molecules pass through the bunching elements. Assuming the synchronous molecule

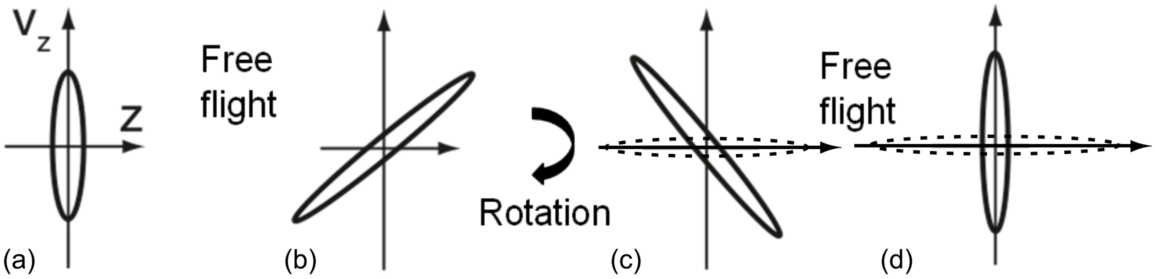

Figure 3.16: Schematic phase-space distributions of the decelerated packet throughout the bunching elements for spatial focussing (solid) and velocity focussing (dashed). Velocity focussing requires less bunching since a smaller rotation of the phase-space distribution is required.

is passing through a grounded stage, and hence exactly between two charged stages at the middle of the voltage pulse, the overall velocity of the packet will be unchanged. However, since molecules that are travelling faster after exiting the decelerator will have moved further, they will experience an increasing electric field over the course of the voltage pulse, thus decelerating slightly. Conversely, initially slower molecules will be accelerated. Combined, this serves to rotate the phase-space distribution of the molecular packet [147]. The phase-space distributions obtained when bunching are not uniformly rotated, due to non-harmonic effects, especially at long bunching times, and due to the non-linear Stark shift at low electric fields, similar to that seen in the hexapole focussing.

Due to the phase-space distribution at the end of the decelerator, shown in figure 3.16(a), a phase-space distribution at the start of the buncher similar to that in figure 3.16(b) is obtained. A small rotation of the phase-space distribution is required to give the distribution at the end of the buncher (figure 3.16(c)) that ensures velocity focussing at the ionisation region (figure 3.16(d)), while a larger rotation is needed for spatial focussing, since the fast molecules must be slowed down to such an extent that the other slower molecules can catch up. The effect of varying the duration of the voltage pulses on the resulting time-of-flight profiles is shown in figure 3.17. In

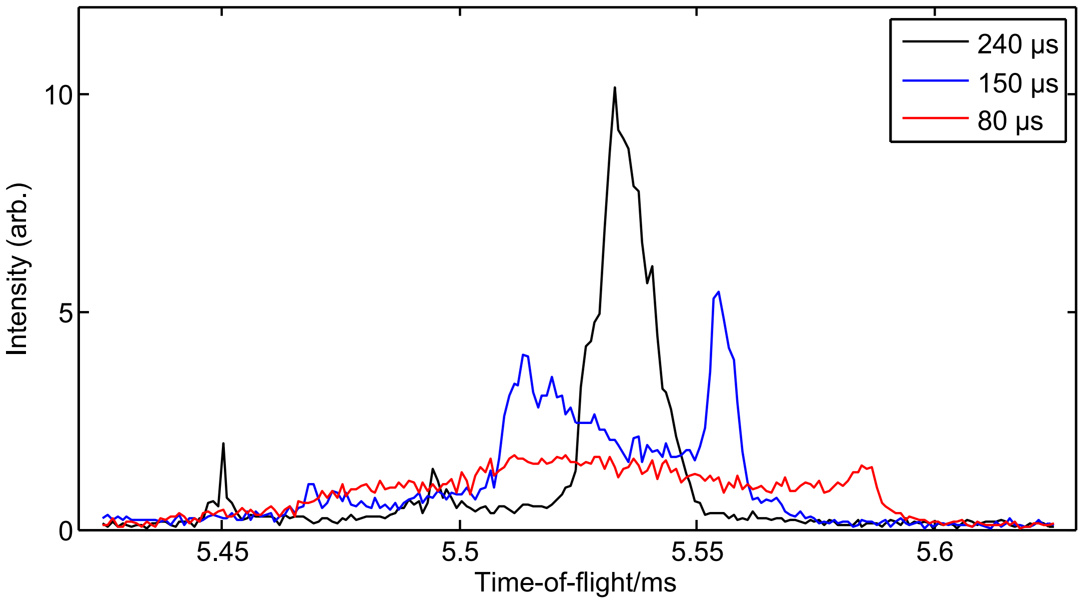

Figure 3.17: Decelerated signal at various bunching times, including those for spatial-focussing (black) and velocity-focussing (red).

this case, for a decelerated packet with final velocity of 100 m/s, a bunching time of 80 μs corresponds to velocity focussing, and results in a broad peak; in contrast, a bunching time of 240 μs corresponds to spatial focussing, with a sharp peak observed, at the expense of a lower velocity resolution.

There are, however, limitations to the use of longitudinal focussing in its current form, both at higher and lower velocities. For higher velocities, due to the distance between bunching electrodes of 11 mm, there is a maximum duration for the voltage pulses, dependent on the speed of the decelerated packet, given as $\tau_{\max} = 1.1 \times 10^{-2}/v_{\text{dec}}$. However, the phase-space distribution of molecules decelerated at a lower phase angle requires a greater rotation, since there is a greater spread in velocities exiting the decelerator due to the larger acceptance volume. At a certain final velocity (130 m/s for spatial bunching) the bunching times required for spatial focussing are greater than $\tau_{\max}$ and so the required bunching cannot be fully achieved. Since spatial bunching requires longer voltage pulse durations than velocity bunching, this limitation is thus seen most readily in this case. Addition of further bunching

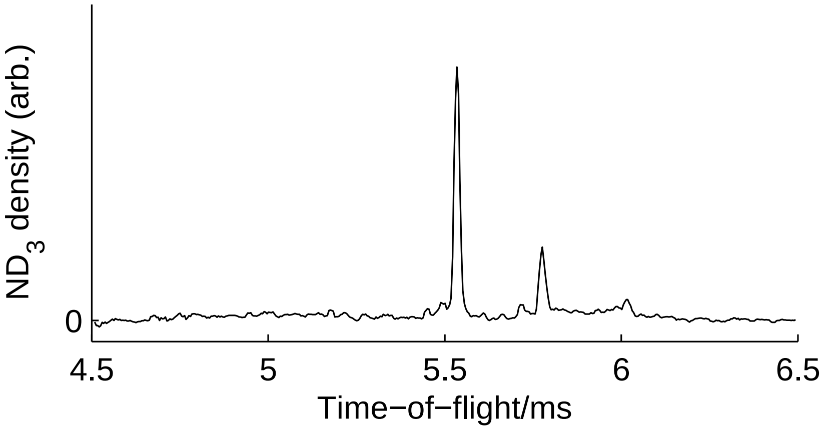

Figure 3.18: Multiple spatially focussed beams arising from multiple decelerated packets, when using a spatial bunching scheme.

stages permits a greater overall bunching time, and hence a greater rotation of the phase-space distribution, which can be used for spatial bunching of faster packets.

At final velocities below 60 m/s, bunching becomes inefficient with the current electrode setup since the molecules are transversely overfocussed due to the time spent by the packet experiencing a set of static forces. Thus, while the longitudinal phase-space distribution is rotated according to requirements, the transverse density is significantly reduced. This problem can be ameliorated by using bunching stages analogous to those of a ring decelerator [164].

The above treatment has considered how a single packet is bunched, the number and duration of voltage pulses are chosen to optimise the desired rotation of the phase-space distribution for this packet. However, multiple packets leave the decelerator and some of these packets shall experience some of the bunching forces that are principally for the main packet. This is seen in time-of-flight profiles as a series of sharp peaks, as seen in figure 3.18. If velocity focussing is desired, there is no effort made in confining the packets spatially, and thus, since they have spread and merged together by the bunching stages, there will be only one broad peak. Since additional packets may not experience as much bunching as the main packet, there may be some reduction in the magnitude of spatial focussing achieved for these satellite peaks. In addition, the separation between packets is 11 mm, which is equal to the bunching stage separation. Thus only alternate packets shall experience bunching effects. Effects of the bunching stages on the different packets in the train can be examined by delaying the voltage pulses such that bunching occurs for the trailing peaks instead of the main peak.

The impact of the buncher and hexapoles on additional packets are numerous. Notably, the desired bunching will only occur for the central packet, while others will be focussed to a lesser extent. This can have detrimental effects on the energy resolution that can be achieved. This is particularly the case if the principal well is in the middle of a pulse train. The leading well has a significantly different velocity and so can experience an anti-bunching effect.

3.7 Optimisation of a decelerated peak

The process of obtaining a decelerated packet suitable for collision experiments involves optimisation of several components. Many have been described above, but the process will be repeated here. Many initial steps may be skipped if repeating deceleration experiments from day to day.

It is first desirable to confirm the alignment of the ionising laser with the centre of the trap. This is achieved by ensuring the ionisation beam overlaps with the cooling lasers. Although it is possible to use the optical fibre in the alignment process as described on page 35, great care must be taken if attempting this since extended exposure of the fibre to the pulsed laser beam results in ablation of the fibre onto the trap electrodes, which can temporarily affect the position of the trap minimum.

The position of the pulsed valve must now be optimised. Although the skimmer is fixed in its optimal position with respect to the decelerator while the assembly is recombined, removal and reattachment of the valve assembly results in a small change in position of the valve which cannot be determined until under vacuum. Optimisation of the valve position is performed without any voltages applied to the decelerator, and the shutter open for its maximum duration (approximately 8 ms) centred around the expected time of arrival. Confirmation that the laser is of the desired wavelength can be obtained prior to this by leaking ammonia into the trap chamber via the leak valve. It is also desirable to optimise the laser firing time relative to the valve opening time to maximise the sensitivity to which the optimal valve position can be found. Since the detected signal will still be quite weak, an integration time of ~ 10 s is used before moving the valve assembly a small amount.

Once this is accomplished, the decelerator can be tested. It is at first beneficial to operate the decelerator in the bunching mode, *ie* $\phi_0 = 0$. The observed time-of-flight spectrum will show an enhancement in ion signal over the entire spectrum due to transverse focussing that now occurs. However there is further enhancement at that time for which the initial velocity has been entered into the timing scheme, with a minor relative depletion either side of this enhancement. If the beam velocity as entered for the timing scheme is correct, the enhanced peak should appear in the centre of the distribution; if not this velocity is changed to compensate.

Further optimisation of the decelerator while in the guiding configuration is difficult since the guided and unguided molecules arrive simultaneously at the ion trap. One should then change the timing sequence so that the decelerated peak is distinct from the main peak while a sufficiently large density of decelerated molecules is present to be detected without the aid of the focussing elements after the decelerator. Suitable values are phase angles ranging from 40 - 60 degrees and a decelerator start time 0.5 ms after valve opening. A broad peak should now be visible, although it will be of low intensity. If no decelerated signal can be seen, the voltage pulses for the second and third hexapoles may be added to the timing sequence to transversely focus the packet and increase the density.

After acquisition of a decelerated signal, it is now desirable to choose the start time of the deceleration sequence with respect to the valve opening time, which can vary slightly from day to day depending on the stagnation pressure and seeding percentage of the gas, and the longitudinal position of the valve, to ensure the principal well filled is at the front of the train. A scan is performed, scanning the on-time of the decelerator, and the chosen on-time is that where the signal intensity is 90% of the maximum value on the rising edge of the signal. The rising edge is steep enough to ensure that occupation of leading wells is negligible in this case. At this stage the beam should now be optimised through the decelerator and the subsequent elements can now be considered.

It is now desirable to optimise the opening time of the shutter, which can vary slightly as the shutter ages, or more substantially if only one vane is in operation. For this, it is first beneficial to configure the bunching elements to a spatial-focussing mode, which allows a precise determination for the shutter trigger time at which the ion signal starts to decrease. It is often desirable to have the shutter open as late as possible while maximising the ion density since molecules arriving before the main peak are often adversely affected if any bunching takes place.

The optimal hexapole times should now be confirmed. This is an iterative process in that the pulse duration on one hexapole is kept constant while it is varied on the second. As the optimal value is reached for one hexapole, this time is retained while the pulse duration for the other hexapole is varied. The optimal intensity is normally obtained after two iterations for each hexapole.

Finally, to get a decelerated sample with minimum velocity spread, the bunching time must be reduced such that velocity focussing occurs. Although the peak signal intensity reduces, the integrated intensity remains the same. After performing these steps, energy distributions that should be obtained are displayed in figure 3.19 for the final velocities shown in figure 3.14.

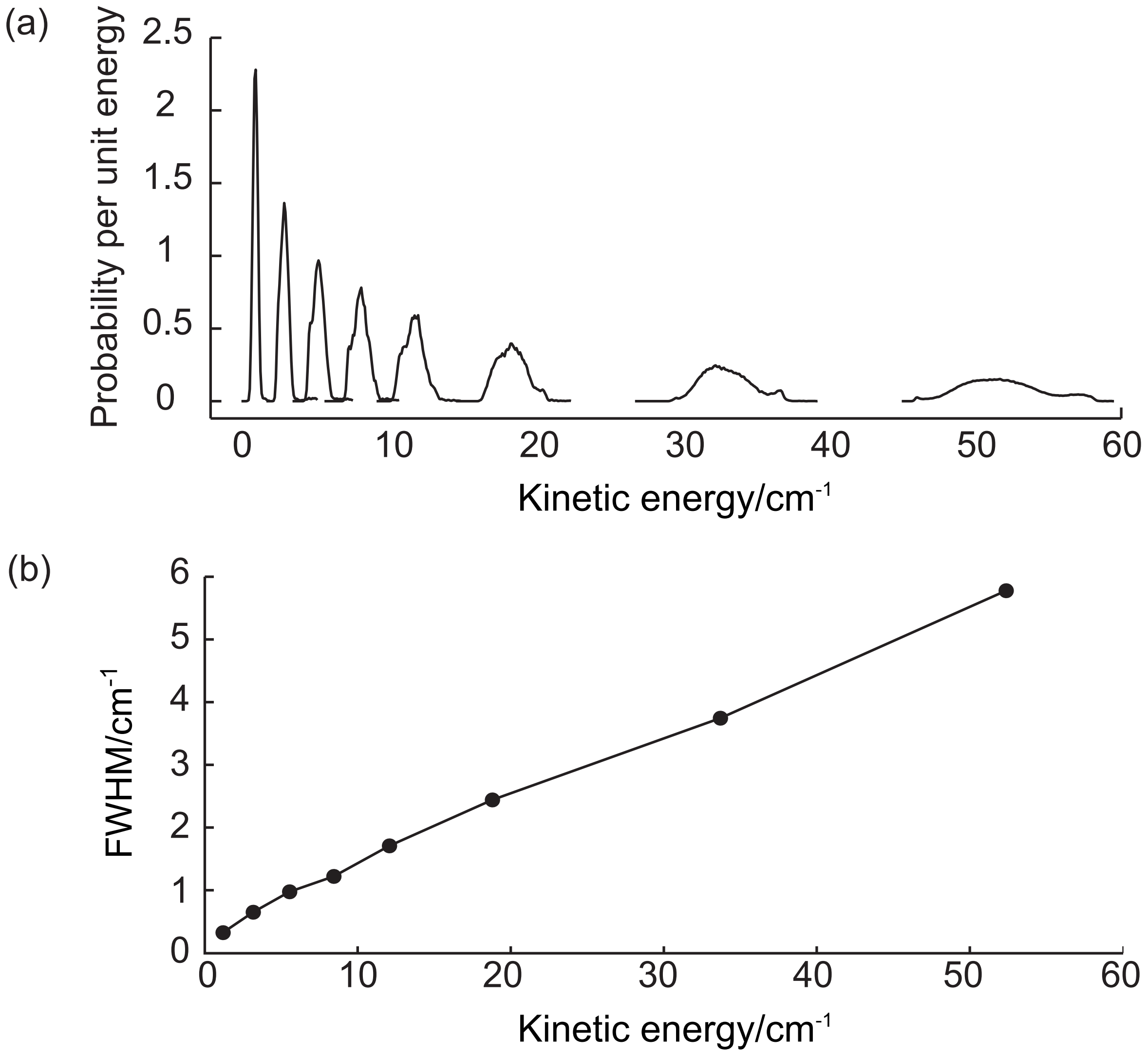

Figure 3.19: (a) Energy probabilities for a range of decelerated peaks. (b) Corresponding peak widths.

3.8 Other deceleration methods

As seen in table 3.1 and as discussed, only species with a sufficiently large Stark effect and with lfs states that persist to high electric fields can be decelerated efficiently. Methods for which Stark deceleration as described above are unsuitable are briefly described below.

3.8.1 Alternate Gradient deceleration

The requirement for lfs states presents challenges with large molecules, which have no lfs states at high electric fields due to higher-order effects in the Stark Hamiltonian [165]. Additionally, the ground state of any molecule is a hfs state, thus there is always a finite lifetime to lfs molecules remaining in that state. It is therefore desirable to be able to decelerate hfs states and thus an adaptation of the decelerator technique used for lfs states is used [166].

The conventional approach to deceleration of hfs molecules is alternate gradient (AG) deceleration. In this technique, pairs of cylindrical electrodes of opposite polarity are placed along the beam propagation axis, as seen in Ref. [165]. In contrast to the electrodes in a conventional decelerator, the electrodes in an AG decelerator run parallel to the beam direction, with the electric field remaining roughly equal along the length of the electrodes. The electrode voltages are raised while the molecules are passing between the electrodes in a pair. In this way the electrodes can be charged without altering the longitudinal potential. Deceleration of the beam thus occurs in the region after the electrodes, when the molecules move into a region of lower electric fields.

An additional challenge occurs when decelerating hfs molecules – that of focussing the beam. Due to the highest electric fields occurring at the electrode surfaces, hfs molecules will be diverted from a sinusoidal path through the decelerator. This defocussing of the packet is avoided by alternating the position of the electrodes relative to the beam, in a similar fashion to a conventional decelerator. The overall effect of the electrode orientation over many pairs is a net focussing. This is despite the fact that, for a given distance from the axis of symmetry, the defocussing force is larger than the focussing force. The net focussing arises due to the fact that molecules will generally be far from the axis when between focussing electrodes and experience a large force in that plane, while they are closer to the axis when between defocussing electrodes, and so will experience a smaller force.

3.8.2 Zeeman deceleration

The fundamental requirement for a species to be Stark decelerated is the presence of a permanent electric dipole moment. This immediately eliminates atoms as suitable species, as well as any molecules with a $\mathrm{D_{nh}}$ symmetry. However, most atoms in their ground electronic state have one or more unpaired electrons, and thus they have a permanent magnetic dipole moment. The same can also be said for paramagnetic molecules, such as triplet oxygen, and excited noble gas atoms, such as Ne^* [167].

Just as a Stark decelerator uses varying electric fields to remove energy, Zeeman decelerators use magnetic fields, with open cylindrical electromagnets typically used. The cylindrical symmetry of the magnetic fields from these magnets reduces the problems with transverse loss, since there is transverse focussing at each position off the decelerator axis.

The bulk of the early studies of Zeeman deceleration concentrated on hydrogen atoms and molecules. Due to their comparatively low mass, fewer deceleration stages are required to decelerate the atoms by a given amount, with seven electrodes in the first decelerator [168], increasing to twelve stages for subsequent decelerators. One challenge to using electromagnets such as these is the requirement to pass a large current through them, which can affect the effectiveness of the magnets by heating them if in the absence of a suitable cooling system.

3.8.3 Deceleration using EM radiation

The original method of Stark deceleration uses electrodes to create the high electric fields. However, electric fields of similar magnitudes can be created by use of a suitably intense source of electromagnetic radiation. In these examples, deceleration of molecules occurs due to the AC Stark effect [169] as opposed to the DC Stark effect described for the conventional and AG decelerators.

In the method of optical deceleration, intense electric fields are created by focussing a powerful laser beam. By careful positioning of the laser with respect to the molecular beam, a portion of the beam will intersect the laser beam when initially fired, and will experience a change in potential energy [170]. When the laser beam, typically at 1064 nm, is far-off-resonant, the molecules are all in a high-field seeking state, with the magnitude of the Stark effect being proportional to the laser intensity and, for this case, the polarisability of the decelerated molecule. Since there are only hfs molecules present, timing the laser pulse so that molecules are passing through the centre of the beam as the laser pulse begins ensures that the molecules will move to a lower laser intensity region, and thus lower electric field, resulting in an increase in the Stark energy and a corresponding decrease in the kinetic energy. When using this method, a range of molecules can be decelerated, *eg* benzene [52] and NO [171].

A recent development has been to use microwave fields in a resonant cylindrical cavity to provide a decelerative force for high field seeking ammonia [172]. Careful choice of the cavity size permits excitation of the $TE_{1,1,12}$ mode, giving 12 stationary E-field maxima along the length of the cavity. For ammonia, multiple states can be decelerated, depending on the microwave frequency relative to the inversion transition frequency [173]. As with optical deceleration, use of the AC Stark effect means the deceleration is experienced by hfs molecules. A continuous microwave field in the cavity permits transverse focussing of the hfs molecules, while using time-dependent microwave fields additionally allows control of longitudinal motion. Controlling the times that the microwave field is switched on gives an analogous switching sequence to the high voltages used on the decelerator above, and bunching, deceleration and acceleration of a packet of molecules has been demonstrated.

3.9 Conclusions

In this chapter the configuration of the Oxford Stark decelerator has been characterised in the context of exploring future reactions with trapped ions. Optimisation of the conditions for a variety of final beam velocities have been achieved, and with the installation of a shutter after the decelerator, separation of the decelerated molecules from residual hot molecules is possible. The creation of a beam with a controllable average energy and narrow energy resolution provides a useful source of molecules for cold ion-molecule reactions, which are discussed in the next chapter.

Chapter 4

Reactions of molecules with cold ions

The previous two chapters have described the two major components of the combined reaction apparatus: the ion trap and the Stark decelerator. In this chapter the combined system is considered and reactions of Xe^+ and guided ND_3 molecules are investigated. These provide a useful study for future work that will utilise decelerated ND_3 for exploration of low-energy ion-molecule reactions.

4.1 Ion-molecule reactions

Ion-molecule reactions are a major source of chemical transformations in the Universe, with the formation of complex molecules in interstellar clouds proceeding through many different ion-molecule reactions [174], of which a large fraction is expected to occur on the surfaces of interstellar dust particles. In combination with the extremely low densities (< 100 particles cm^{-3}) in these clouds, the regular formation of ions from the interaction of molecules with radiation and cosmic rays ensures an appreciable proportion of species present are ions. In particular, the H_3^+ ion, first observed by Thomson in 1912 [175], can be formed by ionisation of H_2, followed by reaction with another H_2 molecule [176].

The temperatures of predominantly neutral clouds are typically in the range of 10-100 K. The experiments described in this chapter between guided ND_3 and Xe^+ are at temperatures ($\sim$ 170 K) slightly higher than the upper limits of this range, but further studies including decelerated ND_3 could probe the entirety of this temperature range.

The potential energy surface between an ion and a neutral molecule is principally composed of ion-dipole (if the molecule is polar) and ion-induced dipole terms [177]

$$V(R,\theta) = -\frac{|\vec{\mu}|Q\cos\theta}{R^2} - \frac{q^2\alpha}{2R^4} \tag{4.1}$$

wherein $\vec{\mu}$ is the permanent electric dipole moment of the molecule, $\vec{R}$ is the distance between the centres-of-mass of the ion and neutral molecule, and θ is the angle between $\vec{R}$ and $\vec{\mu}$.

The average-dipole orientation (ADO) theory, initially developed by Su and Bowers in the 1970s [178, 179, 180], can be used to provide estimates of rate constants for ion-molecule reactions. This theory takes into account the fact that, although the dipole of the molecule isn't 'locked in' and pointing at the ion (such that $\theta = 0°$), there is a greater propensity for the dipole to be pointing towards the ion than away. This factor effects a marginally more attractive potential between the species. Notably, the reaction rates obtained using ADO theory are significantly enhanced relative to the rates predicted from Langevin theory.

4.2 Crystal stability with decelerator fields

In most situations, the ion trap can be considered a Faraday cage, such that external electric fields have little effect on the stability of Coulomb crystals. This is particularly useful when arranging the wires from the chamber feedthrough to the trap electrodes where consideration is only needed for optical access to the trap and a clear path between the oven and trap centre.

However, in contrast to a true Faraday cage, the ion trap is not completely enclosed, with gaps between the electrode stacks along the length of the trap and at the ends of the stacks. Thus a sufficiently large electric field external to the trap can penetrate into the volume enclosed by the electrodes and have a significant impact on the equilibrium position of the trapped ions. This has been used constructively by Schiller and co-workers, who employ an extraction electrode external to the trap to selectively remove ions [181]. However this effect can also reduce crystal stability, which is observed when decelerator electric fields from the final hexapole can penetrate into the trap.

Application of static voltages to the decelerator electrodes has no apparent effect on crystal stability, or on the position of the crystal according to the CCD images obtained, so it is reasonable to deduce that any reduction in crystal stability when time-dependent voltages are used is due to some form of excitation of the crystal from the switching voltages. This can be rationalised by excitation of one of the motional frequencies of the crystal. For $^{40}\mathrm{Ca}^+$ in our trap, the effective radial and axial trapping frequencies are $\sim$ 500 and $\sim$ 100 kHz respectively, whereas the switching frequencies for the decelerator are typically between 3 and 40 kHz; since the switching frequencies are lower than the trapping frequencies, they are unlikely to be the cause of the excitation.

While the decelerator is in switching mode, a ringing artefact is observed when switching voltages are applied to the decelerator, where the applied voltage oscillates about the desired voltage. The frequency of this oscillation is on the order of a MHz, and so it is suspected that this ringing causes excitation of the one of the crystal radial modes, heating the crystal sufficiently to Doppler shift the ions from the laser cooling transition. Ringing artefacts appear to persist for several tens of microseconds after the voltages are switched; it is thus theorised that at higher phase angles, when voltages are applied to the decelerator for a greater overall time, the crystal experiences a greater period of excitation and thus is heated up more, which causes a crystal to melt at lower decelerator voltages.

The most significant crystal heating is observed when no shielding is present between the hexapole and trap; when time-dependent voltages are used, the crystal melts at all phase angles before the typical operating voltages of ±10 kV are reached. Destabilisation of the crystal is least severe when the decelerator is operating at a phase angle of 0°; heating of the crystal is noticeable at $V_{\text{dec}} = 5$ kV, while crystal melting occurs at ~ 8 kV. As ϕ increases, the crystal melts at lower V_{dec}, with melting at ~ 5 kV when $\phi = 60°$.

A small grounded metal plate is thus mounted to the trap base and positioned between the trap and hexapole. A 1 cm diameter hole in the plate is covered with a grounded mesh (85% transmission) to reduce penetration of the decelerator fields and crystal heating while allowing through the decelerated flux. With this plate in place, crystals are now stable to above 10 kV at guiding phase angles, $\phi = 0°$. For phase-angles where the decelerated peak is distinct from the main molecular beam, *ie* $\phi > 50°$, crystals show normal stability up to ~ 6 kV, and melt below 8 kV. At these voltages the ammonia molecules are decelerated less, while using greater phase angles both reduces the molecular flux and the V_{dec} at which the crystal will melt. Thus for the purposes of this thesis, reactions between xenon ions and ammonia molecules from the decelerator will consist of guided ammonia with no deceleration. Since ammonia travels in the beam at 385 m/s, and Xe^+ ions have an average energy of 12 K, this leads to an average collision energy of ~ 13 meV.

4.3 Components of a reactive experiment

There are several distinct phases to perform when obtaining rate constants for reactions involving ions in a Coulomb crystal, of which some are additionally necessary when using dark ions as a reactant. These are discussed below and experimental considerations explored.

4.3.1 Formation of a calcium crystal

Firstly, a calcium crystal must be loaded into the trap, before sympathetically cooled ions are loaded and cooled. RF voltages are typically reduced to 100 V while loading. By doing this, if the ionisation laser is slightly misaligned from the trap axis there is less additional kinetic energy obtained by the ions upon moving to the trap centre. In addition, this allows a more facile crystallisation of the ions once they have been cooled due to the reduced potential energy of the system, allowing crystallisation at higher ion temperatures. Crystallisation may be observed immediately if ions are formed close to the trap minimum, in which case the crystal growth can be observed while calcium is ionised, or, if not, can be seen once the ions' kinetic energy is sufficiently reduced.

While loading ions into the trap, the power of the 397 nm laser at the trap is maximised ($P_{397,\mathrm{max}} \approx 900\ \mu$W) and the laser detunings reduced to hasten crystallisation; the detuning of the 866 nm laser is reduced to zero, but since the crystal is more sensitive to the 397 nm laser detuning [85], a small detuning of 20-30 fm from the atomic transition is maintained for this laser to prevent loss of the crystal. These steps also serve to increase the amount of fluorescence if it is difficult to observe the ion cloud. Once crystallisation has occurred and the ions appear cool, the 397 nm laser power is reduced to $P_{397} \approx 200\ \mu$W and the 397 nm detuning is increased to 60 fm to reduce the equilibrium temperature of the ions; no changes are made to the 866 nm laser power throughout the experiment, with $P_{866} \approx 5$ mW.

On occasion, there may be no fluorescence observed after ionisation. This can typically be attributed to a shift in position of the RF minimum with respect to the cooling lasers, which can occur after large charge depositions on the electrodes. In the event of this happening, the tuning voltages are adjusted to shift the position of the trap minimum and the ion cloud to the position of the cooling lasers, which is confirmed when fluorescence is observed. Although fluorescence is now seen, the ions may be hot due to mismatch between the RF and trapping minima. The tuning voltages are thus adjusted to bring the minima closer together, and the beampaths of the cooling lasers realigned to maintain fluorescence from the ion cloud, until the RF and trapping minima overlap once more. Overlap of the minima is confirmed once a symmetric structure is seen in the fluorescence profile – symmetry perpendicular to the imaging plane can be established by adjusting the static voltages to lift or lower the crystal from the imaging plane.

There can occasionally be no ion fluorescence observed if an incorrect laser frequency is measured by the wavemeter, which principally occurs due to temperature variations of the wavemeter or in the laboratory. If the loss in fluorescence is instantaneous, it is normally due to the blue detuning decreasing sufficiently to melt the crystal. In this case, the 397 nm laser can be further red-shifted until fluorescence is observed. Otherwise, the 397 nm laser may need to be shifted in either direction to restore fluorescence. The 4p←3d transition has a broader absorption profile due to power broadening from the 866 nm laser, so the 866 nm laser frequency can be fixed to a known suitable value.

4.3.2 Cleaning Coulomb crystals

A common difficulty encountered when one wishes to investigate chemical reactions involving Coulomb crystals is the presence of undesirable ions. If they are present then they may react preferentially with the neutral reactant, or affect the sensitivity of ion counting. These may be formed contemporaneously while forming another ionic species[1] or by the steady reaction of a crystal with background gases while conditions

---

[1] An example is the non-isotope selective ionisation of calcium, such that the 3% abundance of other non-fluorescing isotopes will always be present. Other ions may be formed, generally at higher

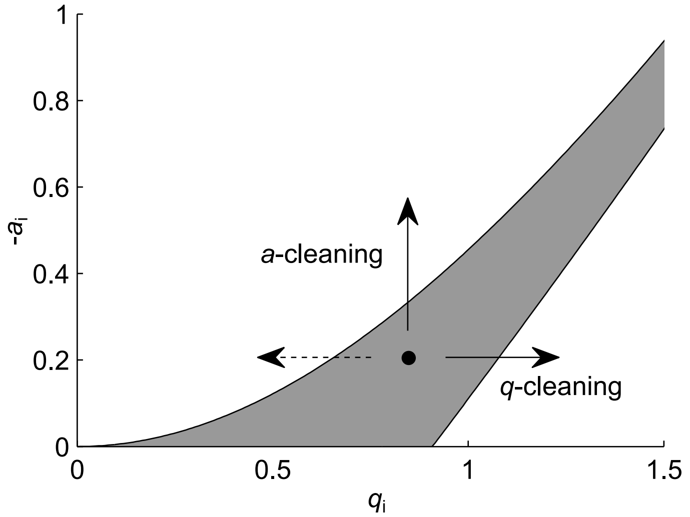

Figure 4.1: Mathieu plot for stable trapping, and changes in Mathieu parameters to clean crystal of unwanted ions.

are being prepared for reaction studies. However, the mass-dependent nature of zones of stability of ions in a trap, discussed in section 2.1, can be used to our advantage to remove these ions. Two related methods of crystal cleaning are achieved by increasing either the endcap voltage or by increasing the RF voltage, seen in figure 4.1. Since these actions serve to increase the a- and q-parameters respectively, they are thus commonly known as a- or q-cleaning. The cleaning method chosen is dependent on the mass of the ion that one wishes to remove.

a-cleaning

a-cleaning is suitable for removing heavier ions and can be visualised conceptually by noting that heavier ions have a shallower radial trapping depth due to the mass-dependent nature of the pseudopotential. As such, when the endcap voltage is increased, the repulsive radial forces, from equation 2.4, overcome the trapping forces at lower endcap voltages for heavy ions. Practically, a-cleaning is simply achieved by increasing the endcap voltage to a point whereby the heavier ions are no longer

---

rates at greater laser frequencies.

trapped while the calcium ions remain trapped. This process is quite efficient at removing heavy ions from a crystal while maintaining trapped $^{40}\mathrm{Ca}^+$ as the ion crystal retains its structure throughout the process and remains laser cooled, since the voltage increase is relatively slow (< 10 V s^{-1}). At typical operating conditions with V_{RF} = 150 V, there is still a significant difference (2.5 V) in critical endcap voltages for calcium-40 and calcium-44, the second most abundant isotope of calcium. Thus this method can be consistently used to remove heavy ions.

Although a-cleaning can also be performed by reduction of V_{RF}, this is generally more challenging to control since the volume of the laser cooled species increases. The proportion of ions in the focal region decreases and thus the overall fluorescence intensity drops to such a level at the required V_{RF} that it is very difficult to distinguish when the crystal has been cleaned of the heavier ions. This, combined with the shallower radial potential for all ions at low V_{RF} can result in a greater background loss rate of the ion of interest.

q-cleaning

In contrast to a-cleaning, q-cleaning is suitable for removal of lighter ions. In this case, the RF voltage is increased until the lighter ions are now in an unstable zone of the Mathieu diagram (figure 2.2). These ions now experience exponential RF-heating, eventually getting ejected from the trap.

This process is in general less efficient than a-cleaning. This is in part due to the trapping voltages that can be experimentally reached, with a maximum RF voltage of approximately 300 V, such that only ions with mass-to-charge ratios below 25 are ejected. At these voltages, the deviation of the trapping voltage from a sinusoidal oscillation also starts to become significant which will cause additional RF-heating of all ions.

It is also observed that as V_{RF} increases, the OCP coupling parameter, as given in equation 2.22, increases, since the ions are closer together and the potential energy increases. However, loss of crystallisation at high trapping voltages generally leads to loss of a large fraction of Ca^+ due to greater repulsion between the ions when closer together. To prevent this, the cooling lasers are detuned further from the atomic transitions at the regular trapping voltages so that the crystal melts. V_{RF} is then increased to remove the light ions, before being reduced to recrystallise the ions. The loss of Ca^+ is greatly reduced when the crystal is melted at low V_{RF} before cleaning, this process can be repeated several times if light ions accumulate over time.

With a pure calcium crystal obtained, it can either be used directly for a reaction, or reactant ions can be loaded, in this case either Kr^+ or Xe^+.

4.3.3 Loading of noble gas cations

At the low collision energies considered in this experiment, no reaction is predicted to be possible between ND_3 and Ca^+. To confirm this prediction, ND_3 is admitted into the trap chamber at reasonably high pressures; no change in the crystal is observed due to reactions. A different reactant ion is thus required to study reactions with decelerated ND_3. Performing this experiment was necessary to confirm that Ca^+ would be an inert spectator ion in any reactive experiments subsequently performed.

Reaction of any decelerated species with Ca^+ would also require deconvolution of the relative contributions from ground and excited states of Ca^+ to any measured reaction rate. It is instead desirable to use an ionic reactant that will exist in a single state, in addition to the previous requirement that it can react with decelerated ND_3. Noble gas ions are thus chosen for these experiments, since these ions possess no rotational or vibrational motion. In a reaction with decelerated molecules, when only a single state of the decelerated molecule can reach the trap, there would thus be quantum state selectivity of the reactants. Both xenon and krypton have been used as the noble gas.

Xenon ions

Xenon ions can be loaded into the crystal in one of two ways: xenon gas can be admitted to the trap chamber via the leak valve attached to the chamber and ionised in the region of the crystal, or it can be used as the seed gas for a molecular beam that passes through the decelerator such that a fraction of the Xe atoms subsequently pass through the trap.

Ionisation from the leaked source is the simpler technique of the two. Xenon gas at a backing pressure typically of 1.5 bar is leaked into the trap chamber through a leak valve until a chamber pressure of between 2×10^{-9} and 1×10^{-8} mbar is measured on the ion gauge. A calibration factor of 0.4 is required to give accurate absolute pressures for Xe; this indicates actual Xe pressures of 8×10^{-10} and 2.5×10^{-9} mbar. The actual pressure is chosen such that the desired number of ions are formed after admission of the ionising laser for approximately 10 s; this allows for reasonable reproducibility in loaded ion numbers while minimising ionisation of background molecules. The leak valve is then closed and the chamber pressure rapidly drops to below 10^{-9} mbar. Depending on the number of Xe^+ and the rate at which they are formed, some heating of calcium ions can be observed, as seen in figure 4.2. The crystal is thus left a short time to reach its equilibrium temperature again.

Ionisation from the molecular beam is a similar process to that seen from a leaked source, with the pulsed general valve used in deceleration experiments used as a source of Xe. A stagnation pressure of 5 bar is used to minimise the valve opening time. Xe is the seed gas of any gas mixtures used in deceleration experiments and will comprise >95% of any mixture, it thus makes little difference to the ionisation rate whether pure Xe or a Xe/ND_3 mixture is used. Although the beam travels the length of the decelerator, no effect is experienced by Xe if the decelerator is charged since it only possesses a second-order Stark effect. Upon entering the ion trap chamber the xenon passes between the trap electrodes before getting ionised. When ionising from this

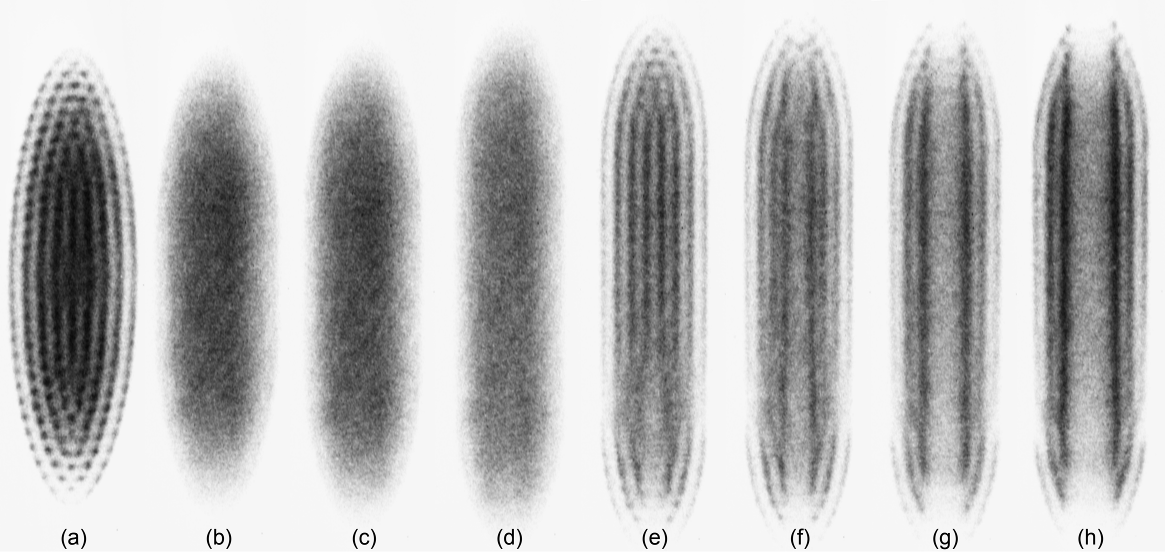

Figure 4.2: Progression of fluorescence profiles during a reaction sequence. (a) Pure $^{40}Ca^+$ crystal after loading and cleaning of crystal, (b-e) Loading of Xe^+ into crystal, (e-h) charge transfer between Xe^+ and ND_3, resulting in formation of dark core.

source, it is necessary to change the opening time of the shutter to compensate for the earlier arrival of Xe at the trap relative to decelerated ND_3.

Regardless of the loading method used, Xe is ionised via a [2+1]-REMPI transition at 249.6 nm, initially exciting to the $5s^2 5p^5 6p\ ^2[1/2]_1$ state. This wavelength is obtained from the doubled output of a dye laser (Sirah Lasertechnik GmbH, Cobra), pumped from the 355 nm frequency-tripled output of an Nd:YAG laser (Continuum Inc, Surelite III-10). Since there is no timing relevant to ionisation of gas leaked into the chamber, this method of Xe^+ production is often preferable at first to optimise the wavelength of the ionisation laser. Subsequently, ionisation from a beam is preferred since less heating will occur from collisions of background gas with trapped ions.

When the ionisation laser is tuned to the transition, the ionisation rate from the xenon beam can be quite rapid – if the rate is large enough, the introduction of kinetic energy imparted by introducing many Xe^+ ions will exceed the amount that can be removed by the cooling lasers and can melt the crystal. If this is observed the ionisation laser wavelength is detuned away from the transition, reducing the ionisation rate, until the crystal persists while loading. Ionisation of Xe via other intermediate states was attempted with appreciable laser intensities accessible in the range of 205-209 nm. However, no ionisation signal was observed. [2+1]-REMPI is again possible at certain wavelengths in this region, however the Rydberg electron in these intermediate states is excited to orbitals with $n \geq 11$, with the efficiency of excitation scaling as $1/n^3$.

Although determining the optimal ionisation wavelength is possible while observing the ion loading rate into the crystal, the process is simpler and much more rapid when using the ion ejection apparatus, described in chapter 5.

Krypton ions

Krypton can be ionised in a similar fashion to xenon, albeit using different ionisation wavelengths. In this case a [2+1]-REMPI transition is again used with excitation via the $4s^2 4p^5 5p$ state – although many transitions are accessible, the transition to the $^2[1/2]_0$ state gives the greatest ionisation signal. This requires a laser wavelength of 202.3 nm, obtained from the frequency-tripled output of a dye laser, which is pumped by the 532 nm output of a frequency-doubled Nd:YAG laser.

The ultimate wavelength chosen is in part also chosen by observation of the rate of background ion formation. This is observed principally when considering the ionisation of krypton, for which a similar [2+1]-REMPI transition at 204.2 nm, via the $^2[3/2]_2$ state can be more appropriate if there is a higher ionisation rate of background gases at the former wavelength. Due to the lower laser powers available at these wavelengths compared to the wavelengths used for xenon ionisation, krypton ionisation is generally a more gradual process, and often performed at the peak of the transition wavelength.

4.3.4 Background losses of reactant ions

In addition to the desired reactions, for example with ND_3, background reactions may occur as a result of the noble gas ions reacting with background molecules. These

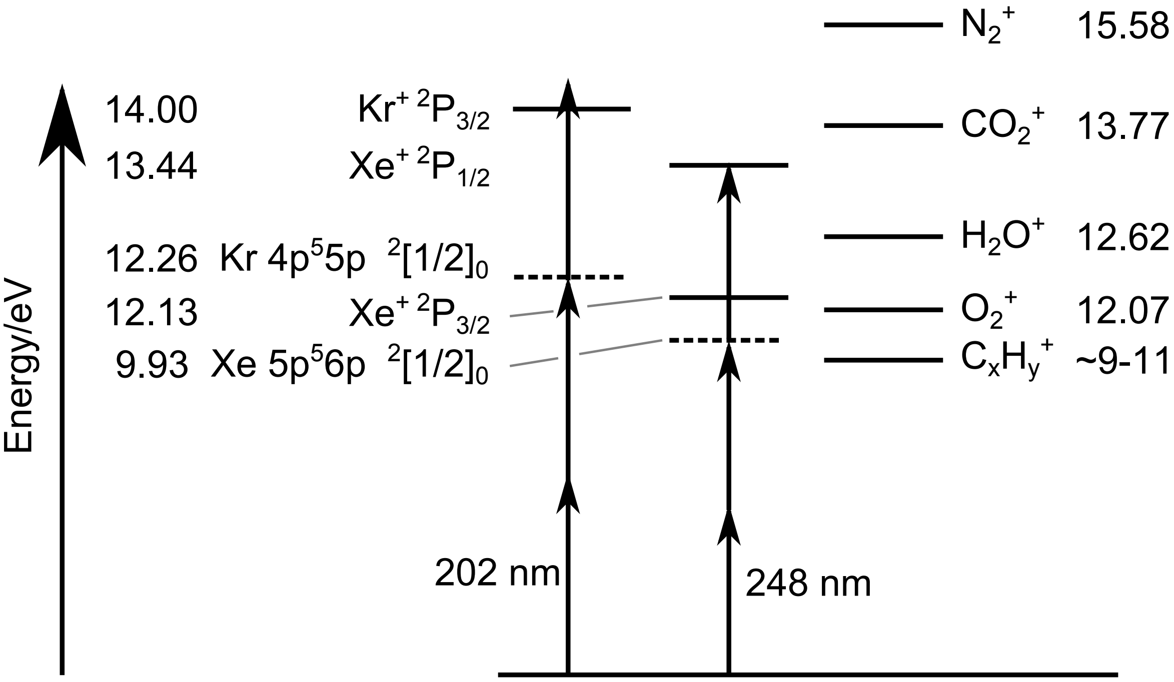

Figure 4.3: Energies of noble gas ions of interest and of selected background ions. Atomic level energies from Ref. [182], molecular ionisation energies from Ref. [183]. $C_xH_y^+$ refers to the range of ionisation energies for hydrocarbons present in the chamber from pump oil vapours.

principally occur due to charge-transfer reactions, with the possibility of these reactions occurring considered by study of ionisation energies, which can be observed in figure 4.3. Due to the low kinetic energies of the ions, it is assumed that only exoergic reactions can take place.

From this it is clearly seen that xenon is a desirable reactant to use, since charge exchange between ground-state Xe^+ and water is endoergic by 0.5 eV, whereas with Kr^+ and water it is exoergic. Ionisation of Xe at the wavelength used results in approximately 22% of the Xe^+ formed initially being in the higher-energy $^2P_{1/2}$ state [184], for which charge-transfer with water is energetically allowed. Although the $^2P_{1/2} - ^2P_{3/2}$ transition is electric dipole-forbidden, the lifetime of the upper state is 48 ms [185] due to an Einstein coefficient $A_m = 21$ s^{-1} for the magnetic dipole transition of Xe^+. It can thus be assumed that there is complete relaxation into the ground ionic state before there is an opportunity for reaction of any ions with background water.

For both Xe^+ and Kr^+, the ionisation energies of various hydrocarbon pump oil vapour molecules are lower than those of the noble gas atom. Although these hydrocarbons are usually prevented from reaching the vacuum chamber by use of a foreline trap, those that are present likely entered the chamber after a breakdown of the rotary pump that overwhelmed the trap. Thus there is an unavoidable background charge-transfer reaction, although this can be compensated for by comparison of reactions in the presence and absence of ammonia in the chamber. The presence of hydrocarbons in the chamber is seen when taking a background mass spectrum using a residual gas analyser attached to the chamber.

One background reaction channel that can be eliminated is the reaction of Ca^+ with ammonia. Previous studies have shown no charge-exchange reaction between the two [49], as to be expected since the ionisation potential of Ca, 6.11 eV, is lower than that of ND_3, 10.7 eV. In addition, no reactive events, such as formation of CaH^+, are observed. To confirm this, ND_3 was admitted into the ion trap chamber in the presence of a pure calcium crystal – after 30 minutes there was no formation of a dark core or loss of Ca^+ above that observed for background loss.

4.4 Reaction of ammonia with xenon ions

Due to the high mass and relatively low ionisation energy of the xenon atom compared to other noble gases, Xe^+ is a common propellant in ion propulsion thrusters in which the impulse is obtained by acceleration of the xenon ion through an electric field, combined with the conservation of momentum. The high impulse per unit mass of these thrusters compared to conventional chemical thrusters (albeit at the expense of a much lower thrust) has meant that xenon ion thrusters are used increasingly often on a range of space missions from low-Earth orbit to the asteroid belt [186, 187, 188]. Reactions of Xe^+ have thus been of interest to the ion thruster community to maximise efficiency of such engines, particularly for those missions that operate in orbits where the Earth's atmospheric density is still appreciable.

In this experiment, reaction of ammonia with Xe^+ follows the pathway expected of that for a simple charge-exchange process. A range of other reaction pathways are possible for the Xe^+-NH_3 system, albeit with endoergicities of > 1 eV. Only the charge-exchange pathway is exoergic and previous studies using guided ion-beams have observed that for collision energies below 5 eV, only the charge-exchange pathway is followed [189]. Thus at thermal energies and below we can be confident that any reaction involving Xe^+ and ND_3 will be a charge-exchange reaction. This is the case for reaction experiments involving guided ND_3 and cold Xe^+ as the average collision energy is 13 meV.

Work by Alge and co-workers studying the reaction of NH_3 with $Xe^+(^2P_{3/2})$ and $Xe^+(^2P_{1/2})$ in a selected-ion flow tube (SIFT) obtained rate coefficients of 8.3×10^{-10} and 1.8×10^{-10} cm^3 s^{-1} at 300 K for the $^2P_{3/2}$ and the $^2P_{1/2}$ states respectively [190]. The rate constant predicted by ADO theory is 1.66×10^{-9} cm^3 s^{-1} – the observed rates for the $^2P_{3/2}$ and the $^2P_{1/2}$ states are thus a factor of two and ten less respectively than that predicted. Reaction studies using a guided ion-beam [189] have shown temperature-dependent cross-sections broadly at values predicted by ADO theory [178], with an $E_T^{-1/2}$ dependence, although only hyperthermal conditions were studied.

Assuming ADO theory still holds at the conditions that are used in this experiment, a rate constant of $\sim 2.2 \times 10^{-9}$ cm^3 s^{-1} would be expected at collision energies between guided ND_3 and cold Xe^+, as is the case for experiments described in this thesis, and a rate constant of $\sim 1.2 \times 10^{-8}$ cm^3 s^{-1} would be expected for an average collision energy of 5 K, which would correspond to the collision energy between decelerated ND_3 and cold Xe^+ in future reactions. Since the decay of the $Xe^+(^2P_{1/2})$ state to the $Xe^+(^2P_{3/2})$ state is rapid compared to the rate of reactive events, we can only obtain

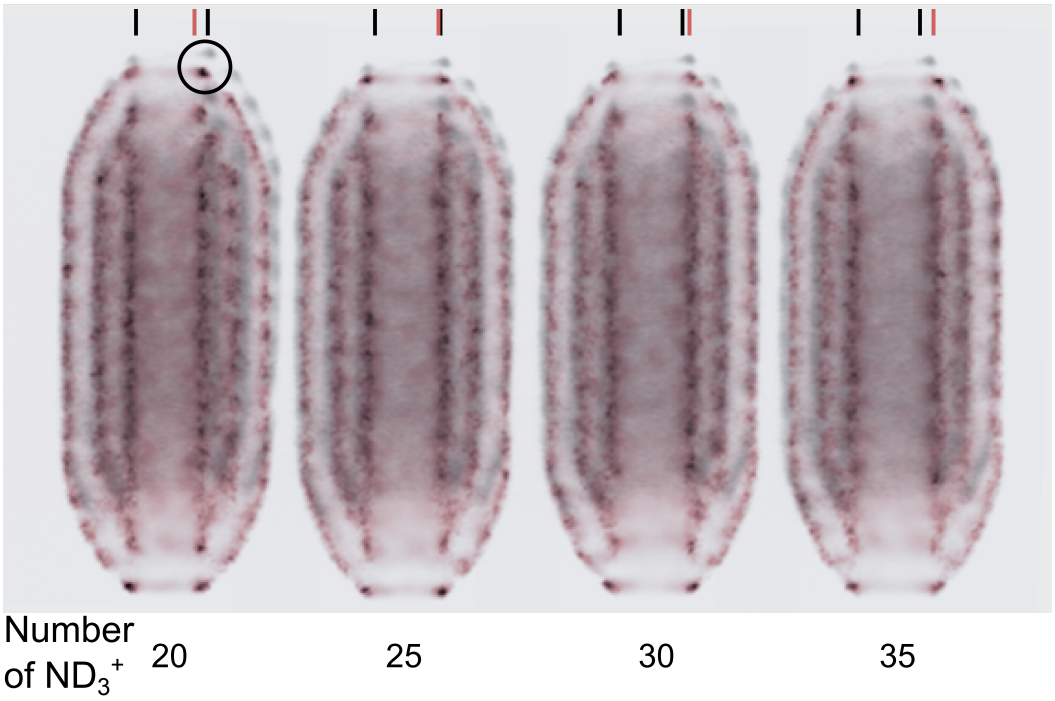

Figure 4.4: Comparison of simulated images (shaded pink) and an experimental image of a Coulomb crystal with a light core (shaded grey), in determination of the size of the core, solid lines denote the edge of the core. Comparison between core sizes in each image is easiest for the isolated ions next to the core, circled for the first image. The best fit for this crystal contains 350 Ca^+, 27 ND_3^+ and $\sim$ 150 OCS^+.

a rate constant for the ground state ${}^2P_{3/2}$ ion.

4.5 Modelling formation rates of light ions

Due to the small number of light ions formed during a reaction cycle, it is important to accurately determine the number of ions in the dark core. This can be achieved by simulation of crystals to achieve a simulated image that matches the experimental fluorescence profile or by determining the volume of the dark core from experimental images.

Matching experimental and simulated images is most beneficial when there are too few light ions to form a core that extends through the length of the crystal, where the length of the core is compared instead. Once the core passes through the entire crystal, simulations can then be used to compare core diameters of crystals with varying numbers of light ions. This procedure is generally applicable for any reaction in which light ions are formed. Prior to reaction studies of Xe^+ with ND_3, the suitability of this technique for modelling light ion formation was examined when studying the reaction between OCS^+ with ND_3 [49, 85], an example of matching a crystal containing OCS^+ and ND_3 is shown in figure 4.4. This method has also been used by Willitsch and co-workers in the state-selective charge-transfer of vibrationally-excited N_2^+ with Ar [191], where the core volume decreases during the reaction.

The comparison of experimental and simulated images allows the number of light ions to be determined with an error of ± 1 ion for up to ~ 25 ions, and with an error of ± 2 ions for up to 60 ions. In the case of a small number of reactant ions having been formed, this method is most useful to determine the product ion dependence on time. However, this method is quite labour-intensive due to the number of simulations that need to be performed to accurately determine the light ion number.

For reactions where significant numbers of reactant and product ions can be formed, the number accuracy that can be obtained from comparison of simulated and experimental images matches that of core volume measurement. This facilitates much more rapid analysis of fluorescence images.

In this case, where a large enough dark core is present, the diameter of the core can be determined by finding the radial points either side of the trap axis with maximised fluorescence intensity (as shown in figure 4.5 for a simulated fluorescence profile). From this distance, the Wigner-Seitz radius must be subtracted to give the outer diameter of the light ion core. Assuming a constant core diameter[2] and cylindrical symmetry of the core, the volume of the core can be approximated assuming the core length is equal to the calcium part.

If there is a non-uniform core-diameter, which can arise if there is sufficient radi-

---

[2] This is observed experimentally for Ca cores when Ca^+ is the lightest component of the crystal and is a small part of the crystal, for example when most Ca^+ has reacted.

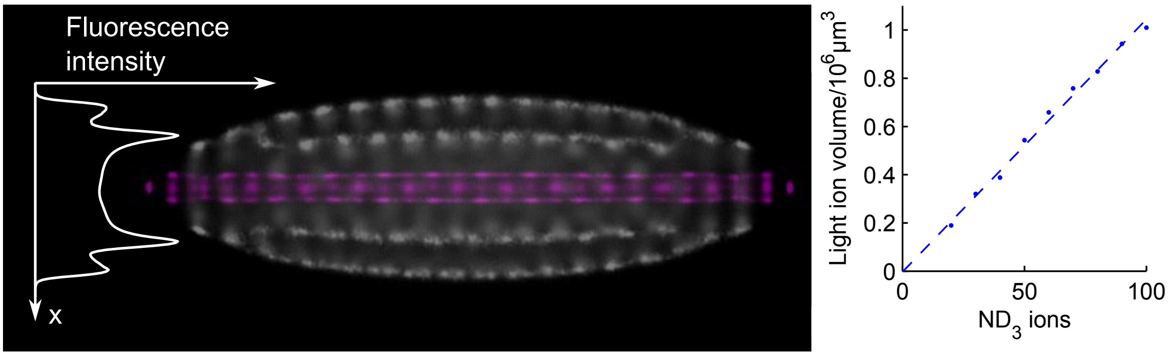

Figure 4.5: Simulated fluorescence profile of a 300 Ca^+, 50 ND_3^+ crystal (centre) and summed fluorescence intensity for each radial displacement in the focal plane (left). Plot of dark core volumes as determined by method in text compared to number of ND_3^+ ions in simulations of crystals containing 300 Ca^+ and a variable number of ND_3^+ (right).

ation pressure on the Ca^+ component to cause an axial asymmetry in the crystal, it is still possible to measure the volume of the dark core by measuring the diameter of the core at several points along the length of the crystal. Once measured, a spline can be fitted to these points which can give a core volume when rotated around the symmetry axis.

When the video output is analysed, the core volume growth can be evaluated which can then be used to determine the reaction rate. The frequency of volume data points is dependent on the frame acquisition rate of the CCD camera, and reduced somewhat by the need to average several (typically 8) frames to reduce noise in the image. However, a suitable image can still be gained every couple of seconds, so sufficient data points are acquired.

4.5.1 Modelling of reaction rates

Determination of rate constants for the reaction of ND_3 with Xe^+ is complicated due to the lack of knowledge regarding the initial number of reactant ions. When reactions involve the fluorescing ion as the reactant, the reaction progress can be easily determined and rates determined from the diminishing volume of the fluorescing part. However, when dark ions are used as a reactant, there is uncertainty in both the number of reactant ions formed and the number of other heavy ions that are formed, either through ionisation simultaneously with the ion of interest, or by reaction with that ion to form something that will not subsequently react. It is thus necessary to determine reaction rate constants from the rate of light ion formation.

In the reaction of ND_3 with Xe^+, assuming no background reactions take place involving either Xe^+ or Ca^+,

$$\frac{\mathrm{d}\left[\mathrm{ND}_3^+\right]}{\mathrm{d}t} = -\frac{\mathrm{d}\left[\mathrm{Xe}^+\right]}{\mathrm{d}t} \tag{4.2}$$

thus, loss of the reactant ion can be directly modelled by formation of the product ion. Since, if assuming a constant density of ND_3, this reaction is a pseudo-first order reaction, the loss of Xe^+ can thus be shown as

$$\left[\mathrm{Xe}^+\right]_t = \left[\mathrm{Xe}^+\right]_0 e^{-k_1 t} \tag{4.3}$$

where $\left[\mathrm{Xe}^+\right]_0$ is the number of Xe^+ at $t = 0$ and k_1 is the pseudo-first order rate. It can thus be assumed that

$$\left[\mathrm{ND}_3^+\right]_t = \left[\mathrm{Xe}^+\right]_0 \left(1 - e^{-k_1 t}\right). \tag{4.4}$$

When $k_1 t \gg 1$, $\left[\mathrm{ND}_3^+\right]_t$ will asymptotically approach $\left[\mathrm{Xe}^+\right]_0$. Thus, if reaction of a sufficient proportion of Xe^+ is observed, then a curve can be fitted to the data, which leads to a value for the initial number of xenon ions and for the charge-transfer rate constant.

For a pulsed beam source, the ND_3 number density must be averaged over the time between consecutive pulses – in this case, with a 10 Hz repetition rate.

However, the rate constant obtained from reaction of Xe^+ with ND_3 must be adjusted to take background reactions into account. In this case, the background rate constant must also be determined. This can be achieved in a similar fashion to the reaction of Xe^+ with ND_3,

$$\frac{\mathrm{d}\left[\mathrm{L}^+\right]}{\mathrm{d}t} = -\frac{\mathrm{d}\left[\mathrm{Xe}^+\right]}{\mathrm{d}t} \tag{4.5}$$

where $\left[\mathrm{L}^+\right]$ is the number of light ions formed from background reaction. Once again assuming a pseudo-first order reaction with respect to Xe^+, the formation of light ions can be modelled as

$$\left[\mathrm{L}^+\right]_t = \left[\mathrm{Xe}^+\right]_0 \left(1 - e^{-k_\mathrm{L} t}\right) \tag{4.6}$$

where k_L is the pseudo-first order rate constant of background reaction of Xe^+. Assuming that k_L is the same in both the presence and absence of ND_3, we can use this background rate constant to adjust the determined reaction rate constant between ND_3 and Xe^+.

The combination of reactions of Xe^+ with ND_3 and with background species will happen simultaneously such that, when ammonia is present in the chamber, the total rate, k_tot, shall be

$$k_\mathrm{tot} = k_1 + k_\mathrm{L}. \tag{4.7}$$

Since k_tot and k_L can be obtained experimentally, a value for k_1 can thus be obtained.

An example of the growth of the light core during the course of a reaction is shown in figure 4.6. A curve of the form shown in equation 4.4 is subsequently fitted to the core volumes both in the presence and absence of ND_3, which is achieved by opening the shutter or keeping it closed. Although there is the possibility of some transfer of ND_3 from the decelerator to the trap chamber while the shutter remains closed, there is no apparent difference in the background reaction rate when the shutter is closed whether the ammonia beam is running or not.

Although the complete charge transfer from all Xe^+ does not occur over the time

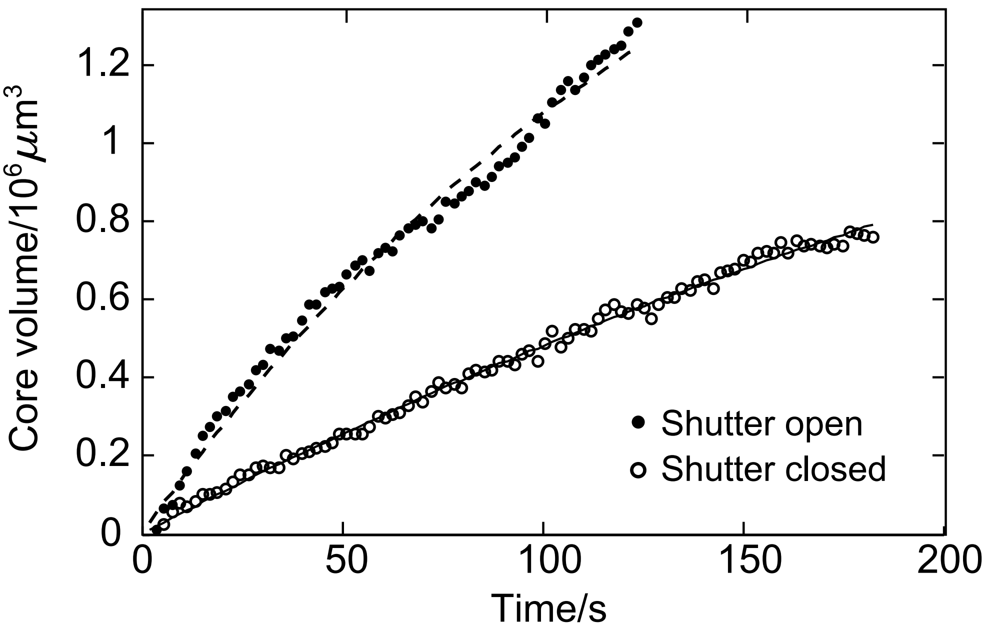

Figure 4.6: Growth of the light core volume during reaction of ND_3 with Xe^+. Growth while the shutter is closed is equivalent to the background reaction rate.

	k/s^{-1}
Shutter open	0.014(6)
Shutter closed	0.0040(7)
ND_3	0.010(6)

Table 4.1: Pseudo-first-order rate constants obtained from fitting crystal volumes according to equation 4.4 with the shutter open and closed, allowing and restricting reaction with ND_3 respectively.

studied, there is still sufficient detail in the data obtained to fit a curve of the required form and determine the rate constant for a particular crystal and set of experimental conditions. The rate constants obtained from these fitted curves are shown in table 4.1.

To obtain the bimolecular reaction rate constant, the density of ammonia at the crystal is also required. Although it is challenging to obtain a reliable value, an estimate can be made with some assumptions. Ions are assumed to be detected with unit efficiency in a cylindrical ionisation volume with a length of 1 cm and a diameter equal to the laser width at the centre of the trap of 100 μm; the transition appears to be

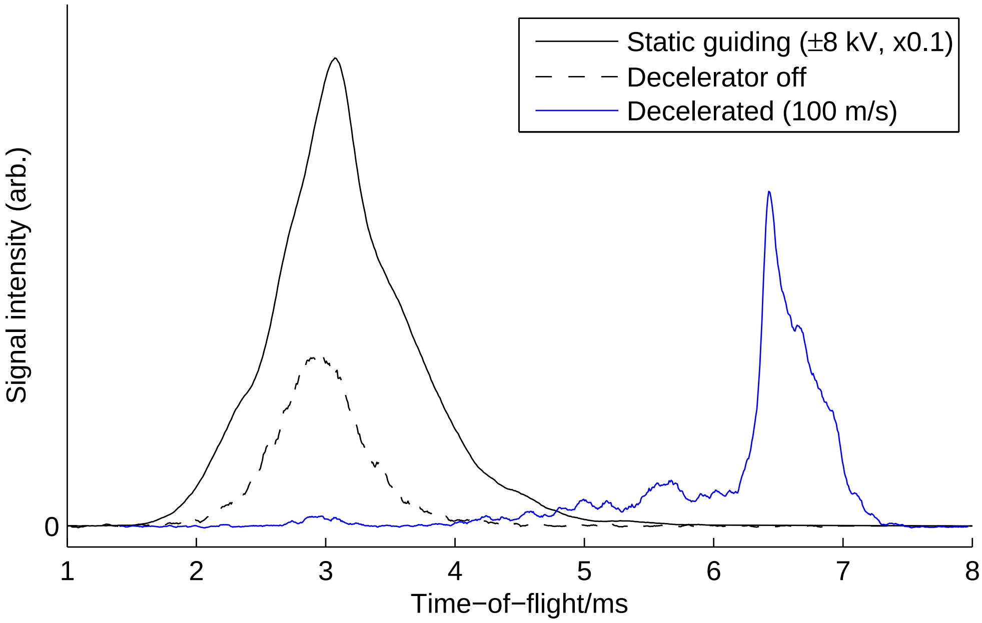

Figure 4.7: Comparison of signal intensities for decelerated and guided molecular beams.

saturated when using the peak available laser power of 15 mJ/pulse, so it can be further assumed that all molecules in the laser volume are ionised. It is also assumed that the density is constant throughout the ionisation volume since the hexapoles are charged at all times, so that molecules are guided through the hexapole without a significant focussing effect. From the individual time-of-flight scans, it is estimated that there is an average intensity of $30(12) \times 10^3$ ions/pulse, which corresponds to average density during the gas pulse of $40(16) \times 10^7$ cm^{-3}; assuming the pulse has a duration of 2 ms and a repetition rate of 10 Hz, this gives an average ND_3 density of $8(3) \times 10^6$ cm^{-3}. When combined with the pseudo-first order rate constant $k_1 = 0.010(6)$ s^{-1}, this leads to a bimolecular rate constant of $k = 1.3(9) \times 10^{-9}$ cm^3 s^{-1}. This is higher than the room temperature rate constant of Alge and co-workers of 8.3×10^{-10} cm^3 s^{-1} [190], although lower than the expected ADO rate of 2.2×10^{-9} cm^3 s^{-1} at the collision energy of 13 meV in this experiment.

One consideration that must be taken into account when wishing to study reactions with decelerated molecules is the reduction in flux when changing from a guided beam to a decelerated beam. For a beam that is decelerated to 100 m/s, there is approximately a factor of 25 reduction in flux, as can be seen in figure 4.7, although this factor could be reduced by optimisation of hexapole charge times. This means the background reaction rate, which is comparable to the guided ND_3 reaction rate, will instead overwhelm any reaction rate from decelerated ammonia. Hence although the background reaction can be removed from the total reaction rate for guided ND_3 without a detrimental effect on the uncertainty in the guided rate, there will be a large uncertainty for decelerated ND_3. The background rate must thus be reduced before investigating reactions with decelerated ND_3.

4.5.2 Background reactions and future reduction

The background rate observed in these experiments is obviously high and subject to improvements. It is theorised that most background reactions are due to charge-transfer between Xe^+ and hydrocarbons present in the trap chamber. The presence of these hydrocarbons is due to contamination of the trap chamber by pump oil vapours. It is, unfortunately, very difficult to remove this contamination, due to the low vapour pressure of the hydrocarbons. In addition, baking of the chamber will not remove these hydrocarbons, which is in contrast to desorption of water from the chamber walls.

One strategy that can be used to reduce the effect of chamber contaminants on the overall rate of reaction of Xe^+ is to use a so-called ‘cold finger’. This cold finger consists of a length of tubing located near the top of the chamber, through which liquid nitrogen is passed, which reduces the temperature of the tubing. Subsequent contact of hydrocarbons with the cold finger will result in adsorption of the hydrocarbon on the tubing; the substantially lower temperature of the tubing relative to the hydrocarbon will mean that a tiny proportion of the hydrocarbons shall desorb again while the tubing is cooled. Since the surface area of the tubing is far greater than that of the crystal, any hydrocarbon vapours present will most likely condense on the tubing before there is a chance to react with the crystal. This cold finger technique shall be used for future experiments on this chamber.

4.6 Conclusions

This chapter has shown the feasibility of studying ion-molecule reactions when using the decelerator as a source of reactant molecules, subject to resolution of two difficulties encountered during these experiments: the difficulties with achieving crystallisation when the decelerator is operating in deceleration mode, and the high background reaction rate. If both of these difficulties can be ameliorated, the reaction of Xe^+ with decelerated ammonia should be achievable. However, as with the majority of ion-molecule reactions investigated with Coulomb crystals, it is still difficult to gather much information about the nature of the ions in the crystal other than their approximate mass ratio with respect to Ca^+. The following chapter describes efforts to solve this problem.

Chapter 5

Ion identification and mass spectrometric methods

The defining challenge of reaction studies involving Coulomb crystals is the difficulty in distinguishing between ions of different mass. This is particularly true where several different ionic products could be formed, for example reaction of trapped NH_3^+ with ND_3 can lead to a range of products including NH_3D^+ or ND_3^+ or ND_3H^+ or NH_2^+. As described previously, the simplest method to monitor progression of a reaction is to note the change in the shape and size of the fluorescence profile, from which the volume of the various crystal components can be determined. This method is only suitable in two circumstances. Firstly, when the reaction of interest involves the laser cooled ion itself, for example the reaction of Ca^+ with methyl halides [15] or the reaction of Mg^+ with hydrogen [86]. In this case the volume of the fluorescing ion component changes proportionally to the reaction rate. Secondly the fluorescence profile will change if a sympathetically-cooled reactant ion heavier (lighter) than the laser cooled species reacts to form a lighter (heavier) ion[1]. In this case the fluorescing volume does not change, but a reaction can be inferred from the change in shape of the fluorescence

---

[1] This assumes only singly-charged ions are present–for multiply charged ions, the mass-to-charge ratio is required instead.

profile. Examples of this were observed in chapter 4, and in the reaction of H_3^+ with O_2 in a Be^+ crystal [192]. However, if multiple products are formed, they cannot be identified and differentiated by these methods.

There is also some impact on the errors that can be placed on a given reaction rate. During the course of a reaction, detunings of the cooling lasers may drift, and the cooling efficiency may change depending on the number of sympathetically cooled ions present, with an increasing SC ratio warming the entire crystal. Both of these factors can change the average Doppler shift experienced by the laser cooled species. Thus, different fluorescence intensities may be possible for a particular crystal. If the edge of the laser cooled volume is defined by the outermost pixels in the fluorescence profile that exceed a certain intensity when determining the laser cooled volume, an inconsistency can be introduced if the fluorescence intensities change.

The range of observable reactions can be increased by changing the laser cooled species. However, since reactive experiments with Coulomb crystals have only used group II cations as the laser cooled species, a great number of reactions of interest will have a change in ion mass that do not cross the possible mass-to-charge ratios of the laser cooled species. Reaction rates cannot therefore be determined from changes in crystal fluorescence profiles alone. This chapter aims to discuss methods that can be used to identify ion masses during, or at the end of, a reaction study. Together, these methods are a means towards quantitative ion identification number measurement of a crystal throughout a reaction scan.

5.1 Axial ion excitation

Multiple mass spectrometric techniques involving modulation of the axial forces upon the ions are possible. These can be generally split into two classes: resonant excitation and pulsed excitation, which are both considered below.

5.1.1 Resonant excitation

As discussed in section 2.1, the axial trapping voltages create an approximately harmonic axial potential in the trap at small axial displacements. Ions thus placed in this potential will have a characteristic axial frequency, dependent on the ion mass-to-charge ratio and trapping voltages. The value of this frequency is considered first for a single ion, and then for multiple ions.

A single ion experiences no Coulomb interaction, since there are no other ions present. The axial potential is thus completely described by the axial trapping potential

$$V(z) = \frac{q\kappa V_{\text{end}}}{z_0^2} z^2 \tag{5.1}$$

where κ and z_0 are defined in section 2.1. This leads to a trap frequency of

$$\omega_z = \sqrt{\frac{2q\kappa V_{\text{end}}}{m z_0^2}}. \tag{5.2}$$

For a $^{40}\text{Ca}^+$ ion with $V_{\text{end}} = 4.8$ V and with other experimental parameters as in table 2.1, $\omega_z/2\pi \approx 85$ kHz. Addition of an oscillating voltage to the trapping voltages already present on one set of endcap electrodes, as shown in figure 5.1, imparts motion onto the ions. This voltage, V_{drive}, is expressed $V_{\text{drive}} = V_{\text{drive},0}\cos(\omega_{\text{drive}} t)$, where $V_{\text{drive},0}$ and ω_{drive} are the amplitude and frequency respectively of the oscillating voltage. If the frequency of this driving force is significantly different to the resonant frequency of the ion, the average change in the velocity of the ion will rapidly reduce over time to zero[2]. Since $V_{\text{drive},0}$ is typically on the order of 10s of mV, any transient heating will be negligible. However, if the frequency of the driving force approaches that of the resonant frequency, the motion imparted can build over several oscillations, and shall thus increase the translational energy of the ion. This leads to two observations. Firstly, as the ion has more energy it moves over a greater axial distance, and so a

---

[2] An analogy can be made such that $\int_0^{\pi} \sin(nx)\sin(mx)\mathrm{d}x \neq 0$ only when $n = m$.

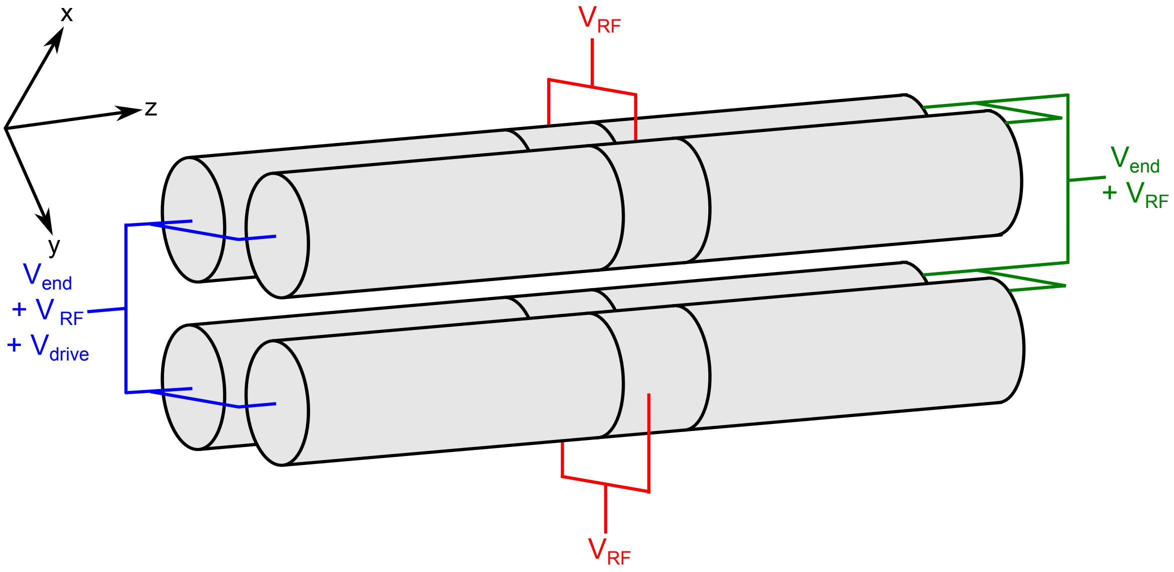

Figure 5.1: Schematic of the ion trap with driving voltages.

fluorescence image of the ion will be ‘smeared out’ axially. Secondly, the integrated fluorescence intensity will change since the effective laser detuning experienced by the ion will differ [193]. If the kinetic energy of the ion becomes sufficiently large, the ion will be Doppler-shifted from the laser cooling transition entirely, such that the ion fluorescence disappears [15]. If the resonant frequency of the ion is unknown, the frequency of the driving voltage is scanned over a particular region, and the resonant frequency measured when the fluorescence intensity is minimised.

Any time-dependent method of altering the axial force experienced by the ion can also induce this behaviour. Although this is conventionally achieved by adding a driving voltage, it is also possible by modulation of a cooling laser, which in turn modulates the resultant radiation pressure on the ion. The magnitude of the driving force is small in comparison to the trapping forces required, with $V_{\mathrm{drive},0}$ of 30 mV used in previous experiments [85].

This resonant excitation is also possible when multiple ions are present in the trap, although now a range of excitations are possible due to excitation of relative motional states of the ions. If the trapped ions are all of the same identity, the lowest motional frequency will equal the frequency for a single ion. This centre-of-mass mode has all ions in fixed positions relative to each other as they oscillate, and thus there is no change in the Coulomb repulsion between ions. Higher-order motional modes will have ions moving relative to each other in addition to oscillations in the trap. These modes have been best defined for ion strings and are described in Ref. [194]. The modes can be characterised by the overall symmetry of the relative ion motion, with a string of N ions having $N/2$ symmetric and $N/2$ antisymmetric modes for even N, and $(N+1)/2$ symmetric and $(N-1)/2$ antisymmetric modes for odd N.

When there are ions with different identities present, the frequencies of the normal modes will be dependent on the ion masses. The mode frequencies of many ion strings in comparison to that of a single ion can only be written analytically for strings of 2 or sometimes 3 ions. For a string of 2 ions, the mode frequencies are given as [193]

$$\nu_{+/-}^2 = \left[(1+\mu) \pm \sqrt{1-\mu+\mu^2}\right] \nu_1^2 \tag{5.3}$$

where ν_- and ν_+ are the centre-of-mass and breathing modes for the two-ion string, ν_1 is the mode for a single ion of mass m_1 and μ is the mass ratio of the two ions, $\mu = m_1/m_2$. In addition to determining masses of individual ions, this process can also be used to monitor processes occurring in one of the ions, for example sequential photodissociation events on the aniline ion and successor ions [195].

Oftentimes only the centre-of-mass mode will be seen when exciting an ion string. When axial trapping is approximated as a harmonic potential, symmetric modes in a string of identical ions are forbidden since a change in the curvature of the potential is required[3]. The efficiency of excitation of other higher modes is also reduced due to a uniform force being applied to all ions and a fairly shallow potential compared to the Coulomb potential between ions.

---

[3] A minor change in curvature is present, due to application of V_{drive} on one end-cap only, but there is less than 1% difference so no significant peak is seen. Splitting the driving voltage between the two endcaps can eliminate even this change.

Two strategies are used to determine the mode frequencies based on the fluorescence intensities. When using the optimal laser detunings to maximise cooling efficiency while no driving voltages are being applied, there will necessarily be a reduction in the ion fluorescence when the driving frequency is near resonance and exciting the ions. The mode frequency can be obtained by noting the frequency at which the fluorescence reaches its minimum intensity. The frequency range over which there is a reduced fluorescence increases in breadth as more ions are present. In contrast, applying large detunings to the cooling lasers will give a low fluorescence intensity in the absence of driving voltages, which can subsequently increase as the ions are excited and experience greater cooling [196]. Using this technique can reduce overheating and loss of ions that would otherwise be Doppler-shifted from the cooling transition.

This method can be further refined by recording the fluorescence only at certain phases in the driving cycle while scanning the excitation frequency, to obtain a 'gated excitation profile'. Upon passing through the resonance frequency, a π phase transition occurs so that the ions' observed positions are now the other side of their equilibrium positions. By monitoring the frequency at which the ion position passes the equilibrium position when in the absence of any driving voltage, a more precise determination of the resonance frequency is possible, with a potential mass resolution of 10^{-4} u. This is sufficient in a number of cases to distinguish between molecular ion isotopologues, *eg* ^{40}Ca^{18}O^{+} and ^{42}Ca^{16}O^{+} [193].

For ion strings that contain more than two ions, where it is no longer possible to analytically determine ion masses from mode frequencies, molecular dynamics simulations can be useful to determine mode frequencies of a particular ion string, and thus determine ion identities in an experimental string. These simulations are performed in much the same way as those described for simulations of Coulomb crystals in section 2.6, but in addition to the force model from equation 2.25 that was used in Coulomb crystal simulations, there must be a force to account for axial excitation of the ions, which is denoted $\boldsymbol{F}_{\text{drive}}$. The overall force model for resonant excitation simulations is thus written as

$$\boldsymbol{F}_{\text{tot}} = \boldsymbol{F}_{\text{trap}} + \boldsymbol{F}_{\text{ion}} + \boldsymbol{F}_{\text{cool}} + \boldsymbol{F}_{\text{heat}} + \boldsymbol{F}_{\text{drive}}, \tag{5.4}$$

where the first four forces on the RHS are as defined in section 2.6. In common with axial excitation experiments, $\boldsymbol{F}_{\text{drive}}$ is of the form

$$\boldsymbol{F}_{\text{drive}} = \alpha V_{\text{drive}} \cos\left(\Omega_{\text{drive}} t\right) \tag{5.5}$$

where Ω_{drive} is the drive frequency, and α is a proportionality constant to approximate the magnitude of ion oscillation due to the distance of the exciting electrodes. When performing an axial excitation simulation, the ions are allowed to cool and reach their equilibrium positions before the application of $\boldsymbol{F}_{\text{drive}}$.

If the resonant frequency of the ions is unknown, a scan of Ω_{drive} must be performed to determine the value of Ω_{drive} at which the resonant frequency occurs. The resonant frequency is determined in simulations by noting the frequency that the ions obtain their maximum kinetic energy, in common with the ‘smearing’ of ions seen experimentally, or if monitoring the ion position at a particular point in the drive cycle, analogous to an experimental gated excitation profile, when the ion crosses its equilibrium position.

When a linear scan of Ω_{drive} is required for a simulation, the frequency at time t in the simulation can be determined by the formula

$$\Omega_{\text{drive}} = \Omega_s + \frac{\left(\Omega_e - \Omega_s\right) t}{2\Delta t} \tag{5.6}$$

where Ω_s and Ω_e are the initial and final excitation frequencies respectively, and Δt is the time in the simulation that the drive voltage is applied for. A factor of 1/2 is required to maintain the correct slew rate.

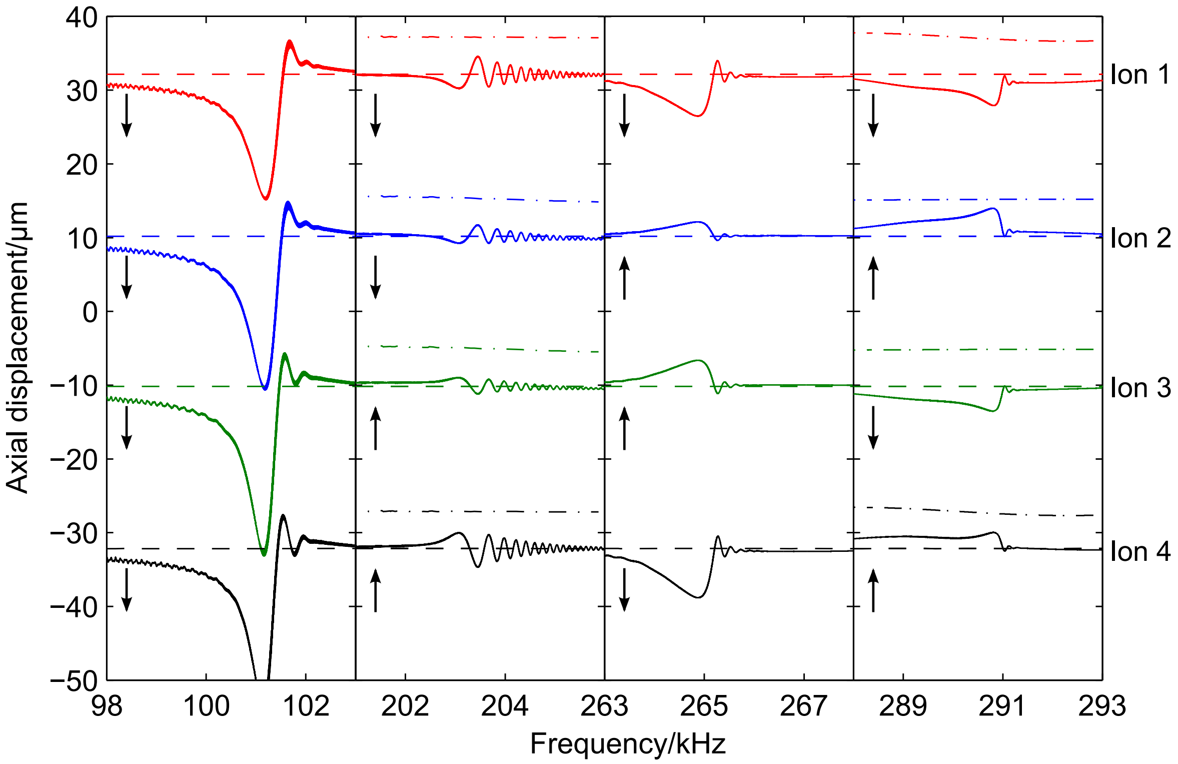

Figure 5.2: Simulated gated excitation profiles for an asymmetric four-ion string of NH_3D^+–$^{40}Ca^+$–$^{40}Ca^+$–NHD_3^+ in the regions surrounding the normal modes (solid) compared to equilibrium positions in absence of excitation (dashed). $V_{\mathrm{drive}} = 30$ mV for symmetric modes and 300 mV for antisymmetric modes. Excitation profiles for a symmetric string of ND_3^+–$^{40}Ca^+$–$^{40}Ca^+$–ND_3^+ are shown for antisymmetric modes (dot-dashed, shifted 5 μm for clarity); for this string, no excitation is observed.

Due to limits of computational resources, the timescale of the simulation is several orders of magnitude shorter than the duration of an experimental scan. A greater damping force is required to recool the ions, which can obtain a large amount of energy during the excitation process, within a timeframe that does not make the duration of the simulation prohibitively long. This can change the shape of the gated fluorescence profiles as exemplified in figure 5.2, but data regarding the mode frequencies can still be obtained by noting the frequency at which the profiles first cross the ions' equilibrium positions.

Use of excitation simulations demonstrate there is the possibility that, for crystals of two or more ions, any non-centre-of-mass motion present can also be seen using the technique of gated excitation profiles. This is shown in figure 5.2 for a string of four ions, NH_3D^+–$^{40}Ca^+$–$^{40}Ca^+$–NHD_3^+, which are denoted in the figure as ions 1-4 respectively. The gated profiles are shown in the frequency regions surrounding the mode frequencies, with the relative motion of the ions at each frequency denoted by arrows. The frequency of each mode is determined by the first frequency at which the ion positions cross their equilibrium positions; subsequent crossings are due to the strong cooling scheme applied in simulations.

Measurement of all the mode frequencies of a given string could particularly be used to distinguish between strings that have virtually identical average ion weights, for example a string that initially contains 2 Ca^+ and 2 ND_3^+. If this crystal has mirror symmetry, symmetric modes cannot be excited – however, reaction of ND_3^+ with NH_3 or ND_3 can lead to ion strings which have a near equal average ion mass (*eg* 2 $ND_3^+ \rightarrow NH_3D^+ + NHD_3^+$) or identical average ion mass (*eg* 2 $ND_3^+ \rightarrow ND_2^+ + ND_4^+$) to the original string. While the centre-of-mass mode frequency would not change perceptibly, the symmetric modes can now be excited, and so a reaction can be deduced, as seen in figure 5.2. Of course, if only one ion has reacted then a change in mass can be observed by a change in the centre-of-mass mode frequency.

Several analogies can be made between the resonant fluorescence spectroscopy of trapped ions and vibrational spectroscopy of linear polyatomic molecules. This is particularly evident when studying strings of ions. In this case, normal modes of progressively higher energy will have more nodes in the motion of the ions. One notable addition compared to vibrational spectroscopy is the presence of the centre-of-mass mode for the trapped ions.

Further increasing the ion number causes a change from a one-dimensional string to a two- or three-dimensional structure. Radial interactions must now be considered, which are particularly important in multicomponent ensembles. Since the ions of different mass in multicomponent crystals are essentially segregated the individual components can somewhat be considered in isolation, at least as far as concerns the resonance frequencies for each component. Examples of this fact can be seen in, for example, work by Willitsch *et al* [197]. In this case, excitation of a sympathetically cooled species will indirectly heat the laser cooled species, such that a drop in fluorescence can be observed at the frequency of the SC mode.

In general, observation of scanned fluorescence spectra is simpler when dealing with a few ion system. In this respect, care must be taken to prevent over-excitation of a particular component in a large multicomponent crystal since mixing of the ions can occur. If one component is moved too far from its equilibrium position, the sub-ensembles can both change shape due to modification of the ion-crystal Coulomb potential, which can destroy the stability of the crystal.

5.1.2 Pulsed voltage excitation

As shown above, ions are easily excited when coupling an oscillating force that matches the motional frequency of the ions, whereas they are unaffected if a continuously applied driving force is of sufficiently different frequency to the motional frequency of the ions. However, a small force applied for a sufficiently short time by an axial voltage pulse will displace the ions from their original equilibrium positions, inducing motion upon the ions regardless of their motional frequency.

The overall ion displacement is dependent on the duration and magnitude of the pulsed voltage. Application of the pulsed voltage will, to a first approximation, maintain the axial potential, but shift the minimum to a new position. Since the crystal, previously at equilibrium, is effectively displaced from the axial minimum when the voltage is applied, the crystal will move to restore its position in the potential minimum. Since the ions experience similar changes in the potential, the crystal will essentially move as a solid body, oscillating at the frequency of the crystal centre-of-mass mode; no separate peaks are seen for different masses. The maximum displacement

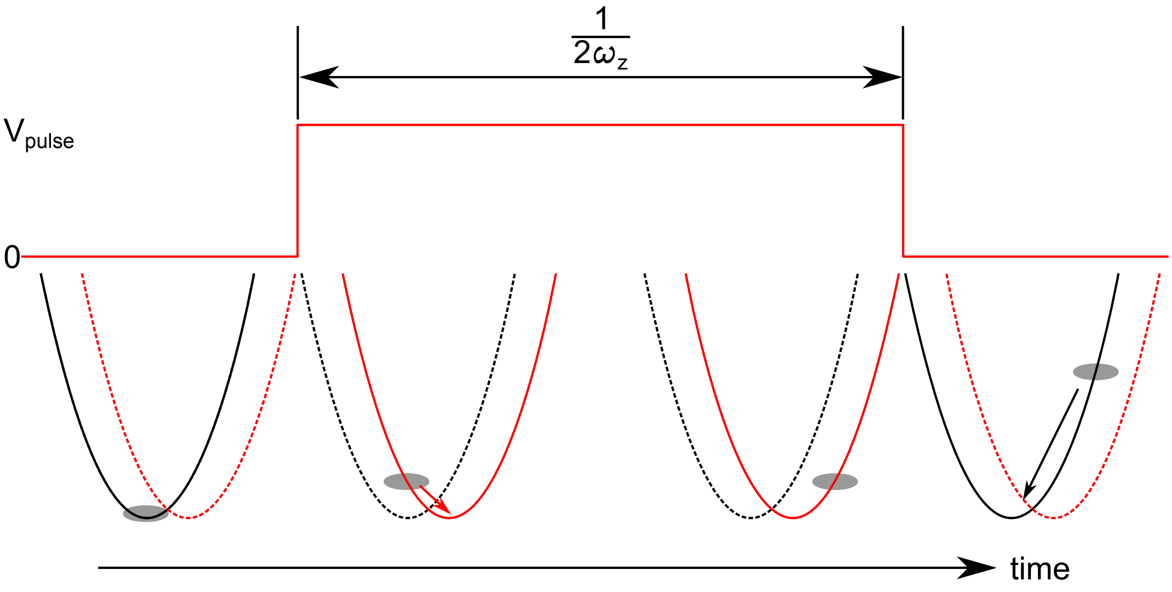

Figure 5.3: Motion of a crystal during an excitation pulse. The red and black curves represent the potential experienced when the pulse is switched on and off respectively. Maximum displacement of the crystal is achieved when the duration of the voltage pulse is equal to half the centre-of-mass oscillation.

occurs when the pulse duration is half that of the centre-of-mass oscillation, as shown in figure 5.3. As is the case with the resonant excitation method, only modest driving forces are required to induce this motion, with V_{pulse} typically between 30 and 100 mV.

After the voltage pulse, the axial minimum returns to its original position, with the crystal now displaced again. The crystal now oscillates again at the centre-of-mass frequency around the axial minimum. Although the magnitude of the oscillation is small, and no effect can be seen from fluorescence images of the crystal, this motion may be inferred by monitoring the time-dependent fluorescence intensity from the crystal. When the crystal moves in the opposite direction to the laser propagation, the effective laser wavelengths, and detunings from the atomic transitions are decreased. This increases the rate of photon absorption, and thus the emission rate and the subsequent fluorescence intensity obtained. Conversely, when the crystal moves in the same direction as the laser propagation, the fluorescence intensity decreases. If one assumes that no cooling takes place, this oscillation in fluorescence intensity will

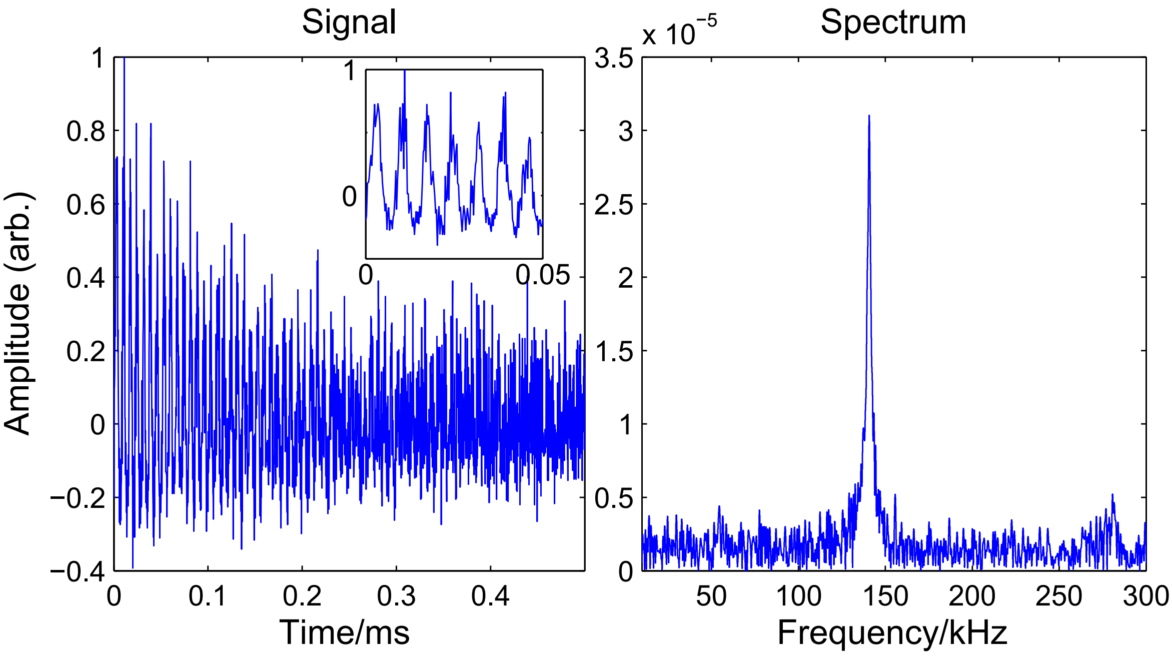

Figure 5.4: Fluorescence free induction decay (left) and Fourier transformed oscillation frequency spectrum (right) of a Ca^+ crystal that has undergone pulsed excitation. Modulation of the ion fluorescence can clearly be seen in the inset. An overtone can also be observed at $\sim$ 280 kHz.

correspond exactly to the axial oscillation, thus allowing the centre-of-mass frequency to deduced.

In addition to the motional frequency, it is also reasonable to expect that the initial amplitude of the oscillation is dependent on V_{end}. An excitation pulse with a fixed V_{pulse} results in a greater shift in the axial minimum for lower V_{end}. The duration of the pulse has an effect in this case as well, since the voltage pulse will now be present for a different fraction of an ion oscillation due to a change in ω_z. For example, an increase of V_{end} by a factor of four doubles the oscillation frequency; a pulse that is optimised to maximise crystal oscillation for the original V_{end} will thus last a whole oscillation at the higher V_{end}, returning the crystal to the true axial minimum when the pulse has finished. This results in no modulation of ion fluorescence after the excitation.

Although the ions are now oscillating in the trap, they are still being continuously cooled, as evidenced by the fluorescence intensity obtained, an example of which is seen in figure 5.4. Due to this fact the obtained fluorescence modulation about the equilibrium level is of the form expected of a damped oscillator. The damping rate is principally governed by the laser cooling parameters, since the optimal cooling conditions will evidently remove the motion imparted by the pulsed voltage most rapidly.

There are some advantages in using a pulsed excitation scheme as opposed to a resonant excitation scheme. Firstly, the repetition rate is significantly higher, with the ultimate repetition rate limited by the length that the free induction decay (FID) persists and the recording speed of the detecting electronics. A duty cycle of 400-1000 Hz is typical. The potential signal-noise ratio also increases upon acquisition of several FIDs by a factor of the square root of the number of spectra taken, assuming any noise present is random. The rapid repetition rate also proves to be useful for reactions that occur relatively quickly, since any changes in the average ion weight can be determined almost immediately, whereas continuously scanned spectra can take several minutes to acquire if performed over a broad frequency range, such that any temporal resolution will be significantly reduced.

Although it is principally expected that the centre-of-mass mode for the crystal shall be excited at the fundamental frequency, there is also the possibility of overtones of the centre-of-mass mode being excited, which will appear in the frequency spectrum as peaks at a multiple of the fundamental frequency. These overtones, an example of which is shown in figure 5.4, are particularly seen when large $V_{\text{drive},0}$ or small V_{end} are used.

Since the centre-of-mass frequency is solely considered for pulsed excitation, equation 5.2 can be modified such that the overall mass-to-charge ratio of the crystal is considered. If all ions in the crystal are singly charged, this modifies equation 5.2 to give

$$\omega_z = \sqrt{\frac{2q\kappa V_{\text{end}}}{z_0^2\langle m\rangle}} \tag{5.7}$$

where $\langle m \rangle$ denotes the mean ion weight. Since the impulse provided by the drive voltage is small, there is insufficient time and change in ion positions for the crystal to deform. Therefore, unlike the case of resonant excitation, a change in mass of some of the ions will lead to a shift in the axial frequency for the whole crystal without the appearance of an additional peak.

Experimentally, recording a pulsed excitation scheme was carried out in this work as follows. Following formation of a Coulomb crystal, a square-wave signal created from a function generator (Stanford Research Systems Inc, DS345), with pulse durations of 5-10 μs, and repetition rates of 400-1000 Hz, is sent to the trap voltage tuning box and incorporated with the other trapping voltages. The ion fluorescence is detected using a photomultiplier tube charged to 1700 V with the resulting signal put through a preamplifier (Stanford Research Systems Inc, SR445A). The resulting amplified signal is then summed into bins of 250 ns duration by a multiscaler card (Becker & Hickl GmbH, PMS-400A) to provide a temporal profile that can subsequently be fitted to the damped oscillator model.

A Fourier transform is taken of the damped oscillation to reveal the frequencies of the modes excited by the pulsed voltage. An appropriate laser detuning is required for this method – if the detuning is too small, the oscillation is dampened too quickly and the mode frequencies experience lifetime broadening. Conversely, if the detuning is too large, the photon flux can be insufficient to obtain a sufficiently intense oscillating signal against the background signal and so some resolution can be lost. With the bin size used, the sampling rate is 4×10^6 Hz and the associated Nyquist frequency is 2 MHz. Since the ion oscillation frequencies are of the order of 100 kHz there should thus be no additional peaks in the FT spectrum due to aliasing, and the bin widths are of a sufficient size for this technique. Sheridan and Keller have demonstrated this method by the alternative technique of autocorrelation of photon arrival times at a photomultiplier tube [198].

As seen from the example profile in figure 5.4 the initial oscillations are unbalanced relative to the stable background photon flux seen at the end of the scan. This can be attributed to the non-linear relationship between photon absorption and the cooling-laser detuning. With a pulsed voltage amplitude of 100 mV and duration of half an oscillation when $V_{\text{end}} = 4.8$ V, the ions can be expected to oscillate with an initial amplitude of ~ 20 μm. At a typical initial detuning of 30 fm from the 4p←4s transition, the range of effective detunings experienced through an oscillation cycle is from 8 to 52 fm. In this detuning range, and using the equations from section 2.2, the photon absorption rate changes from a minimum of 3.8×10^7 s^{-1} to a maximum of 5.3×10^7 s^{-1}.

Using this method should be particularly sensitive to investigating charge-transfer reactions in large crystals where the reactant and product ion masses are similar, for example in the reaction of $\text{ND}_3^+ + \text{ND}_3 \rightarrow \text{ND}_4^+ + \text{ND}_2$. In this case, a pure calcium Coulomb crystal is initially formed, and the motional frequency measured. This can then be used to calibrate subsequent spectra. Upon loading ND_3^+ ions into the crystal, the motional frequency will rise in accordance to that seen in equation 5.7. In the case where a Ca^+ crystal has a frequency of 100 kHz, loading of ND_3^+ ions until the crystal consists of 20% ND_3^+ and 80% Ca^+ gives a frequency of $\sim$ 105.41 kHz. Complete charge exchange leading to a core of ND_4^+ will result in a frequency of $\sim$ 104.82 kHz, a shift of $\sim$ 590 Hz.

An estimate for the statistical uncertainty present in spectrometric techniques of this type can be made by taking multiple measurements on a crystal of known average ion mass. The obvious candidate for this is a pure $^{40}\text{Ca}^+$ crystal. After initial formation of the crystal, the crystal is q-cleaned as described in section 4.3.2. The crystal is then maintained with trapping parameters such that $^{40}\text{Ca}^+$ remains trapped, on the edge of the Mathieu stability region, but any heavier ions formed will be immediately ejected. Using these trap parameters increases the loss rate of $^{40}\text{Ca}^+$ due to the significantly

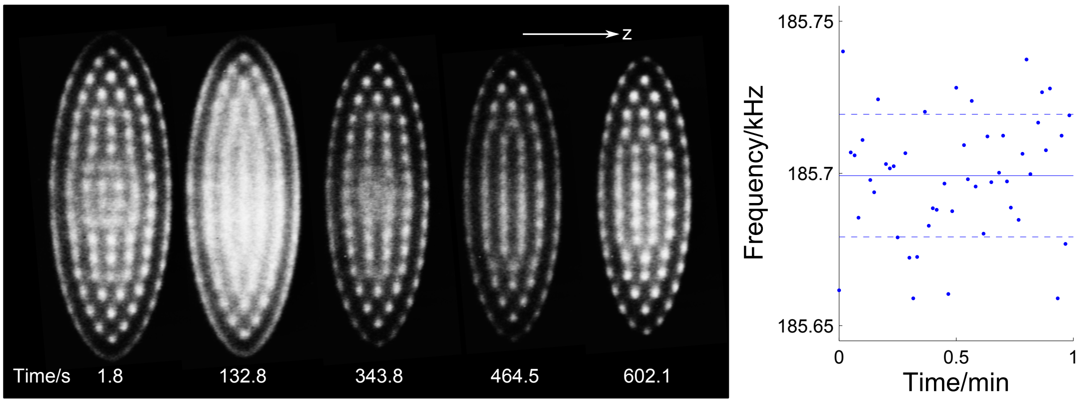

Figure 5.5: Fluorescence profiles of a highly oblate crystal, with $V_{\mathrm{RF}} = 90$ V and $V_{\mathrm{end}} = 8$ V (left). Oscillation frequencies from repeated pulsed excitation scans performed on a similar crystal (right). Solid and dashed lines refer to mean frequency, and one standard deviation from the mean frequency respectively.

reduced radial trapping depth, but loss of $^{40}\mathrm{Ca}^+$ does not change the average ion mass. The oblate nature of the resulting crystal means that any lighter ions formed can be easily observed. In this experiment none were observed over the duration of the pulsed excitations.

With trapping conditions of $V_{\mathrm{RF}} = 90$ V and $V_{\mathrm{end}} = 8$ V, the crystal has a $1/e$ lifetime of approximately 20 minutes; fluorescence images obtained are shown in figure 5.5. Although it is not possible to acquire both fluorescence images and fluorescence FIDs simultaneously when using the current setup, by keeping the loading and trapping conditions constant, it is reasonable to assume that duplicate crystals shall have the same properties. One can thus compare fluorescence images with corresponding FIDs. Under these trapping conditions, an axial frequency of 185.699(20) kHz is observed; the magnitude of the uncertainty is equal to the standard deviation of repeated measurements of the crystal frequency, as shown on the right of figure 5.5. Assuming this frequency corresponds to a pure crystal of $^{40}\mathrm{Ca}^+$ ions, with average weight of 39.96 u, a change in the average weight of 0.06 u can be detected. If this is applied to the case of a similar two-ion crystal to those used by Drewsen and co-workers, this provides a mass resolution, $m/\Delta m$, for the unknown ion of ~ 333. In the above case of a 100 ion crystal consisting of 20% ND_3^+ and 80% Ca^+, reaction of one ND_3^+ to form ND_4^+ will change the axial frequency by 23 Hz, at the limit of the resolution of this technique.

The autocorrelation method used by Sheridan and Keller mentioned earlier has shown that this method is also applicable for small crystals (up to 20 ions), and can detect charge exchange events with unit efficiency [198]. For small strings in which there is no migration within the string, it is possible to determine the absolute configuration of a string containing one ion of different mass.

This method, compared to crystal volume analysis, is also less sensitive to variations of cooling laser frequencies when determining reaction rates as the fluorescence modulation is monitored as opposed to the overall fluorescence intensity. This shall be particularly useful for reactions that require a crystal to be interrogated over several minutes during which time laser fluctuations may change the average fluorescence intensity.

5.1.3 Probing crystal changes with pulsed-voltage spectrometry

Two examples of the utility of this technique with evolving crystals are discussed in this section: the first, the reaction of a Ca^+ crystal with methyl fluoride, and the second, the loading of ND_3^+ into a crystal.

The reaction of methyl fluoride with low-temperature calcium ions has been investigated previously with reaction rates determined by fluorescence volume analysis; resonant excitation could be observed in strings and small crystals [49, 85, 197], although it was not used as a method of rate determination. However, when using pulsed-voltage excitation, the resolution of the axial peak is sufficient to determine a rate of reaction without requiring fluorescence volume analysis. It is thus required to show that there is agreement in reaction rates when using pulsed-voltage excitation.

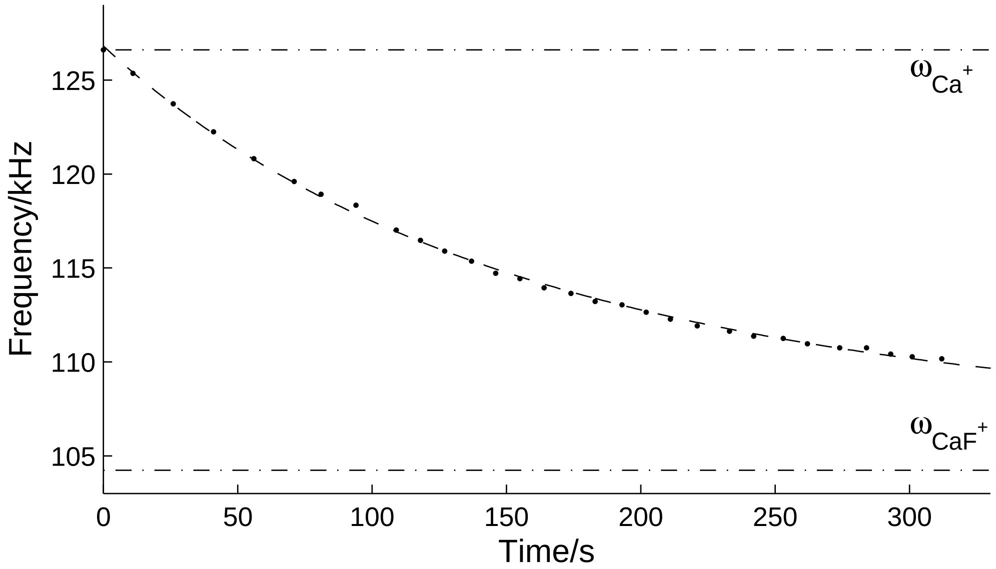

Figure 5.6: Progression of the centre-of-mass frequency during reaction of a Ca^+ crystal with methyl fluoride, $p_{\mathrm{CH_3F}} = 3 \times 10^{-10}$ mbar. Dot-dashed lines correspond to oscillation frequencies for pure calcium and calcium fluoride crystals.

After loading a crystal of sufficient size, methyl fluoride was leaked into the ion trap chamber through a leak valve. CH_3F partial pressures as measured on the ion gauge ranged from 5×10^{-10} to 3×10^{-9} mbar; a calibration factor was then applied to measured pressures to account for the ion gauge sensitivity [85]. An example progression of the frequency for the most intense peak present during a reaction cycle is shown in figure 5.6. From the oscillation frequencies of the pure Ca^+ crystal and of the crystal at time t, and from equation 5.7, we can state that

$$\frac{\omega_t}{\omega_{\mathrm{Ca}}} = \sqrt{\frac{m_{\mathrm{Ca}}}{\langle m_t \rangle}} \tag{5.8}$$

which must then be rearranged to determine the evolution of the average ion mass, so giving

$$\langle m_t \rangle = \left(\frac{\omega_{\mathrm{Ca}}}{\omega_t} \right)^2 m_{\mathrm{Ca}}. \tag{5.9}$$

Once the average ion mass has been obtained, the fraction of ions that have re-

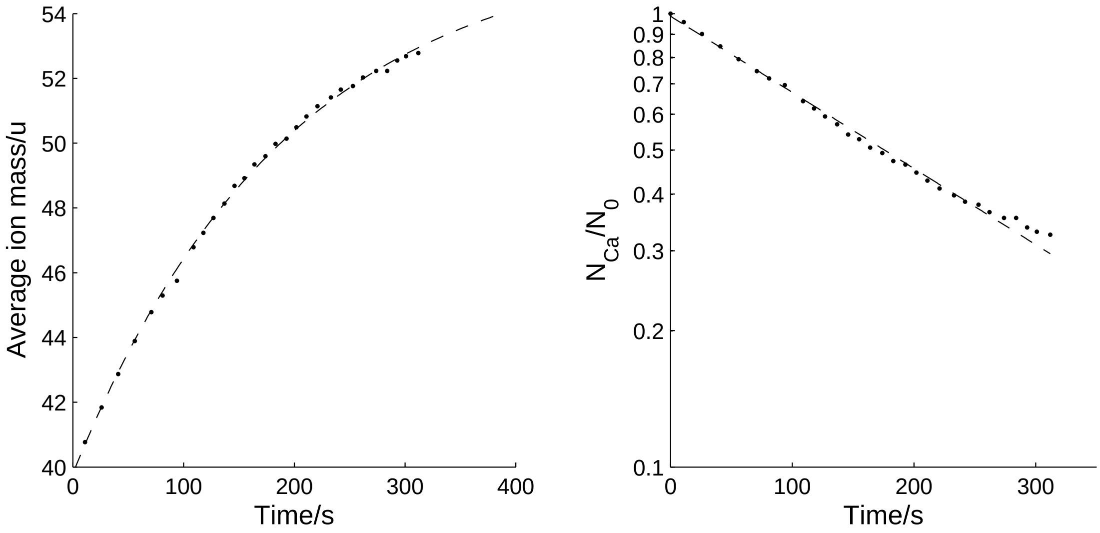

Figure 5.7: Progression of the average ion mass through a reaction cycle (left), from which the remaining proportion of unreacted Ca^+ can be deduced (right).

acted can be determined, which is shown in figure 5.7. This analysis assumes that no background losses of Ca^+ occur, which is reasonable with a sufficiently fast reaction of Ca^+ with CH_3F. If the rate of reaction is slow, a background scan is necessary to determine background loss rate of Ca^+. This information combined with the average ion mass could again lead to observing the reaction rate of interest.

The reaction of Ca^+ with CH_3F can be described as a pseudo-first order reaction with

$$\frac{\mathrm{d}[\mathrm{Ca}^+]}{\mathrm{d}t} = -k_1[\mathrm{Ca}^+] \tag{5.10}$$

where $k_1 = k[\mathrm{CH_3F}]$, which is observed in the reactions studied by this method, shown in figure 5.7. k_1 is measured at several CH_3F pressures by an exponential fit to the remaining Ca^+ fraction in a reacting crystal, shown in the right of figure 5.7. k_1 is equivalent to the negative gradient of the fitted line. The bimolecular rate constant is then obtained from the fit from the obtained k_1, as depicted in figure 5.8; fitting these points assuming a linear relationship to $[\mathrm{CH_3F}]$ gives a value of $k = 5.6(5) \times 10^{-10}$ cm^3 s^{-1}.

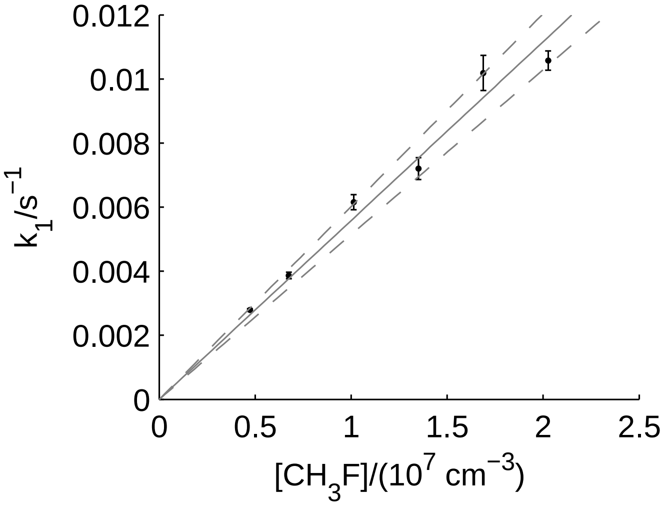

Figure 5.8: Plot of k_1 measured at various CH_3F densities and line of fit to determine the bimolecular rate constant k.

Comparison of the bimolecular rate constant obtained in this work with that of Ref. [16] shows that the rate constant acquired here is between the rate constants obtained for the ground ($^2S_{1/2}$) and excited ($^2P_{1/2}$ and $^2D_{3/2}$) electronic states of Ca^+ (4.2×10^{-10} and 1.1×10^{-9} cm^3 s^{-1} respectively). The excited state proportion can thus be established from these prior state-selective measurements by determination of the relative contributions for the ground and excited states that are consistent with the bimolecular rate constant measured here; this comparison suggests that 21(7)% of the Ca^+ ions are in an excited state. This is in agreement with the proportion expected from solution of the optical Bloch equations as described in Ref. [85] for the laser detunings used in these experiments, which give an excited state population of 24%.

In addition to monitoring reaction rates, ion loading rates can also be observed if loading an ion of different mass to $^{40}Ca^+$. This is exemplified in the loading of ND_3^+ into a crystal of Ca^+. In this case, the ion loading rate determined by the pulsed-voltage spectra can be compared to fluorescence images of ND_3^+ loading under similar conditions. Since ND_3^+ is a light ion it accumulates in the crystal core, and an ion number can be deduced from analysis of the dimensions of the dark core.

Since the number of Ca^+ is constant during the ionisation period, the ion loading rate can be deduced from knowledge of the light ion-Ca^+ ratio. Assuming a constant loading rate, k_L, of ND_3^+ into an initially pure $^{40}\mathrm{Ca}^+$ crystal that contains N_{Ca} ions,

$$\frac{\mathrm{d}[\mathrm{ND}_3^+]}{\mathrm{d}t} = k_L, \tag{5.11}$$

$$\Rightarrow N_{\mathrm{total},t} = N_{\mathrm{Ca}} + k_L t \tag{5.12}$$

where $N_{\mathrm{total},t}$ is the total number ions after t seconds of loading. The total and average crystal mass, $m_{\mathrm{total},t}$ and $\langle m_i \rangle_t$ respectively, can thus be determined,

$$\begin{aligned} m_{\mathrm{total},t} &= N_{\mathrm{Ca}} m_{\mathrm{Ca}} + k_L t m_{\mathrm{ND3}}, && (5.13)\\ \langle m_i \rangle_t &= \frac{m_{\mathrm{total},t}}{N_{\mathrm{total},t}} && (5.14)\\ &= \frac{N_{\mathrm{Ca}} m_{\mathrm{Ca}} + k_L t m_{\mathrm{ND3}}}{N_{\mathrm{Ca}} + k_L t} && (5.15)\\ &= m_{\mathrm{ND3}} + \frac{m_{\mathrm{Ca}} - m_{\mathrm{ND3}}}{1 + k_L t / N_{\mathrm{Ca}}}. && (5.16) \end{aligned}$$

The average mass thus changes from the initial mass of a calcium atom, steadily decreasing to the ammonia mass asymptote; an example of this is shown in figure 5.9. The speed of this change is determined by the initial number of Ca^+ and the loading rate as expected. Since the oscillation frequency is proportional to the inverse square root of the average mass, the oscillation frequency will thus be

$$\omega_{z,t} = \sqrt{\frac{2q\kappa V_{\mathrm{end}} \left(N_{\mathrm{Ca}} + k_L t\right)}{z_0^2 \left(N_{\mathrm{Ca}} m_{\mathrm{Ca}} + k_L t m_{\mathrm{ND3}}\right)}}. \tag{5.17}$$

Although the sensitivity for detection of ammonia loading decreases as the proportion of ammonia ions increases, there will be an increase in sensitivity to conversion of ND_3^+ to ND_4^+ – for example, from an initial pure Ca^+ crystal with an oscillation

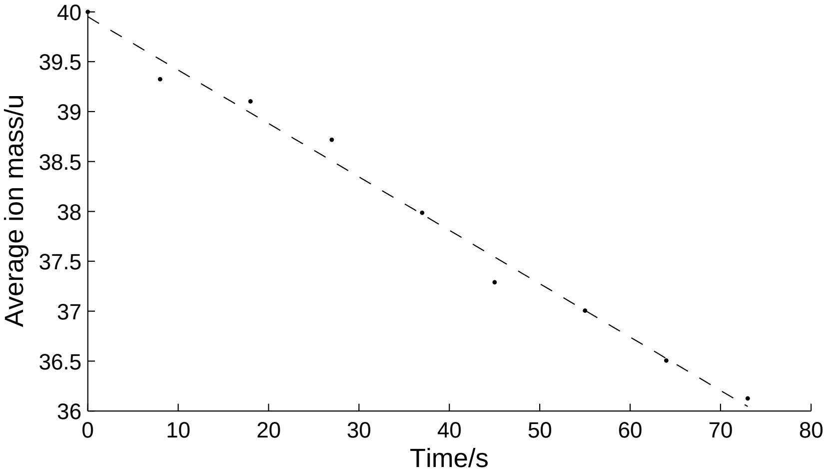

Figure 5.9: Change in the average mass of an initial pure ^{40}Ca$^+$ crystal upon loading of ND_3^+.

frequency of 100 kHz, there will be a shift of 5.41 kHz if sufficient ND_3^+ is loaded to comprise of 20% of the crystal. If the same number of ND_3^+ are loaded again, a further shift of 4.13 kHz occurs, with ND_3^+ now consisting of a third of the ion number. However, in the first case, complete conversion of ND_3^+ to ND_4^+ will result in a shift of 0.59 kHz, whereas in the second, a shift of 1.08 kHz will be seen. It should be noted that if the light ion core becomes too large, the calcium ions are pushed out of the cooling laser beam and so the intensity of the modulation and the stability of the signal, and of the crystal, shall decrease.

The speed at which spectra can be obtained raises interesting prospects for the identification of individual reaction events. This is particularly the case if there is a large change in mass upon reaction, such as the charge-transfer between Xe$^+$ and ND_3. Assuming standard trapping voltages of 150 V and 4 V for V_{RF} and V_{end} respectively, a crystal with 800 Ca$^+$ and 200 Xe$^+$ that undergoes a single charge transfer event will experience a frequency shift of 75 Hz. When half of the Xe$^+$ have exchanged, a further charge transfer will give a shift of 103 Hz. In this event, there is an increasing sensitivity as the reaction progresses, since changes in the average ion weight have a greater effect when the average weight is lower. The setup used makes it difficult to determine the number of ND_3^+ loaded since the calcium crystal cannot be observed directly and the size can only be estimated. However, use of a beamsplitter so that fluorescence could be detected by the camera and the PMT simultaneously would counter this problem.

5.2 Photodissociation of molecular ions

For certain molecular ions, electronic transitions are known in sufficient detail to probe molecular identities and gain information on internal rovibrational states of the ion. This technique has been used by Drewsen and co-workers to conclusively show the reaction of Mg^+ ions with H_2 to form MgH^+ [199]. Subsequent resonant photodissociation of the MgH^+ product forms Mg and H^+ in a 2-photon process, which are both lost from the trap. The reduction in crystal volume thus determines the proportion of MgH^+ in the crystal. When using a narrow-band laser, the spectral width of the laser will be smaller than adjacent rotational transitions [98], and thus populations of individual rotational states are also measured.

This method is also used by Schiller and co-workers as a way of obtaining highly-accurate frequencies of vibrational transitions in HD^+ that are sympathetically cooled in a $^9Be^+$ crystal. A combination of two-colour resonance-enhanced multiphoton dissociation of HD^+ with resonant excitation of the motion of the remaining HD^+ monitors the progression of ion loss as the wavelength of the vibrational-transition laser is varied [27].

5.3 Radial excitation

The above discussion of axial modes in strings implicitly assumes a one dimensional potential. However, as there is a trapping potential in the radial directions, there

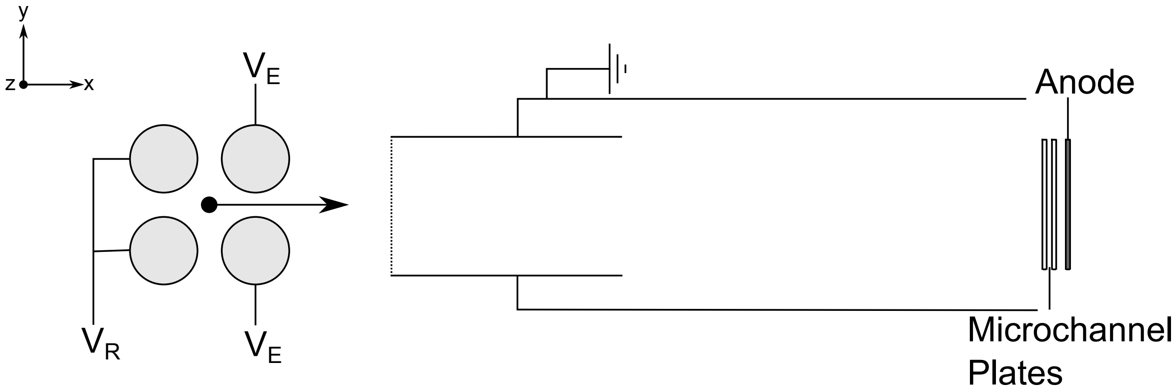

Figure 5.10: Schematic of the time-of-flight apparatus. Typical values are defined in table 5.1.

will also be corresponding oscillations for a single ion[4]. This can be used in a similar fashion to axial excitation. Schiller and co-workers have demonstrated this in many systems, including a bicomponent crystal of Be^+ and He^+ [200].

5.4 An ion-trap based Wiley-McLaren spectrometer

An alternative to *in situ* RF mass spectrometry is to eject the ions into a mass spectrometer at a specified time in the reaction. A time-of-flight spectrometer is best suited for this type of experiment. The contributions of Wiley and McLaren to the field of time-of-flight mass spectrometry [201], combined with laser ionisation of atoms and molecules, have facilitated a great deal of work with non-magnetic mass spectrometers. Adaptation of the three electrode spectrometer design has led to subsequent developments in ion velocity mapped imaging, with exquisite details of product distributions now possible [202, 203]. The improved mass resolution possible when using a Wiley-McLaren (WM) based spectrometer was significant even with the first designs, and is ideally suited for combination with the ion trap in a limited volume.

---

[4] Note that this is different to the RF frequency, instead referring to the radial frequency as seen in the pseudopotential model in equation 2.29.

Repeller voltage	200 V
Ionisation region	$7.5 \cdot \sqrt{2}$ mm (≈ 10.6 mm)
Extractor voltage	160-170 V
Acceleration region	50 mm
Free-flight region	120 mm

Table 5.1: Dimensions and typical voltages of the ion time-of-flight apparatus.

The basic design of a WM spectrometer is well-known. Ions are initially formed between two charged electrodes, a higher voltage applied to one of the electrodes to direct the ions towards a detector. After passing the second charged plate, they experience a further acceleration towards a grounded electrode followed by transit through a field-free region. By careful matching of the distances between the electrodes and voltages applied to the charged electrodes, a superior mass resolution is obtained in the time-of-flight mass spectrum.

Flat electrodes, extending radially much further than the ionisation volume, are traditionally used as the ion optic elements since the electric fields formed between the electrodes are thus uniform. However, non-planar electrodes may be used, although there is typically a corresponding decrease in the mass resolution of the spectrometer. In the spectrometer used in these experiments, the trap electrodes act as the first two stages of the spectrometer, as seen in figure 5.10. The potential experienced by the ions is plotted in figure 5.11. The principal difference between flat electrodes and the trap electrodes is seen in the region between the extracting electrodes. Since there is a significant region where the ions pass close to the extracting electrodes, the electric field is not homogeneous and reduces for several millimetres in a region between a pair of electrodes. Moreover, the length of the region of reduced electric field is dependent on the position of the ions relative to the electrodes (*ie* the vertical direction in figure 5.11). Ions passing equidistant from the electrodes will experience a minimised flattening.

The principal effect of this position-dependent flattening is a reduction in the mass

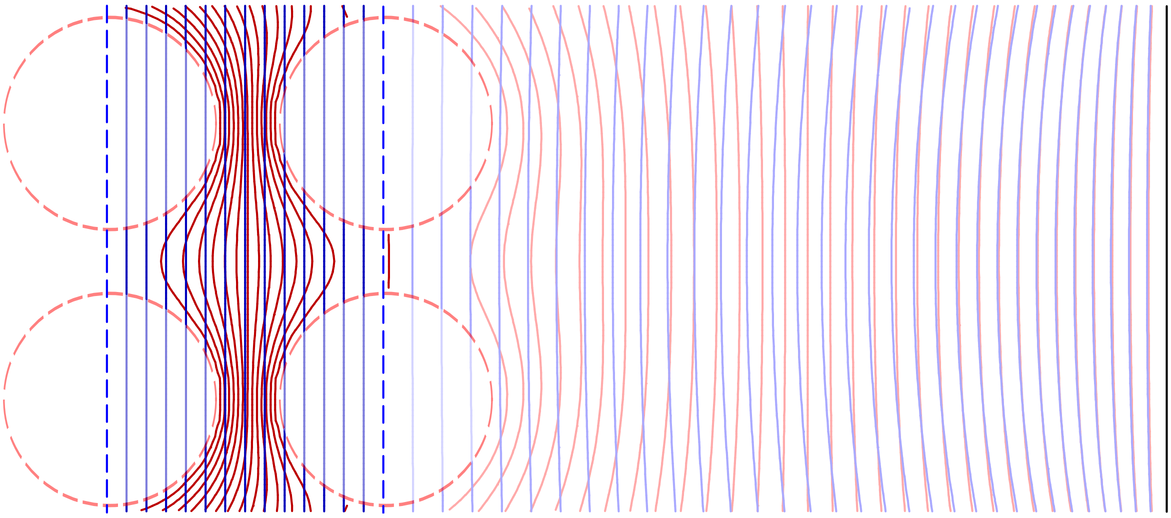

Figure 5.11: Potentials in the ion trap time-of-flight spectrometer (red) with corresponding flat plane electrodes (blue). Between the charged electrodes, potential contours are drawn every 2.5 V, between the extractor electrode and grounded plate, contours are drawn every 5 V. Dashed lines denote the cylindrical and flat electrodes.

resolution of the spectrometer, which can be observed in simulated time-of-flight spectra in figure 5.12. This problem is not considered significant in these studies since the ion identities are already known and resolution of peaks better than Δm of 1.0 is rarely required; of more importance is the integrated intensity of the recorded peaks to ensure it genuinely reflects the relative numbers of ions of different mass present. Simulations of the spectrometer compared to a similar spectrometer setup with flat electrodes replacing the cylindrical trap electrodes indicate a decrease in mass resolution from $m/\Delta m \sim 118$ to $m/\Delta m \sim 95$, assuming no recovery time for the detecting electronics.

The electrodes are charged using two power supplies built in-house – the voltage from each power supply is split six-ways such that each electrode segment in both the repeller and extraction electrodes, as in figure 5.10, holds the same voltage. The same vacuum chamber feedthrough is used to connect the trap with the external power supplies as it is when using trapping voltages; changing the trap from a trapping configuration to an ejection configuration and vice versa is thus quite facile.

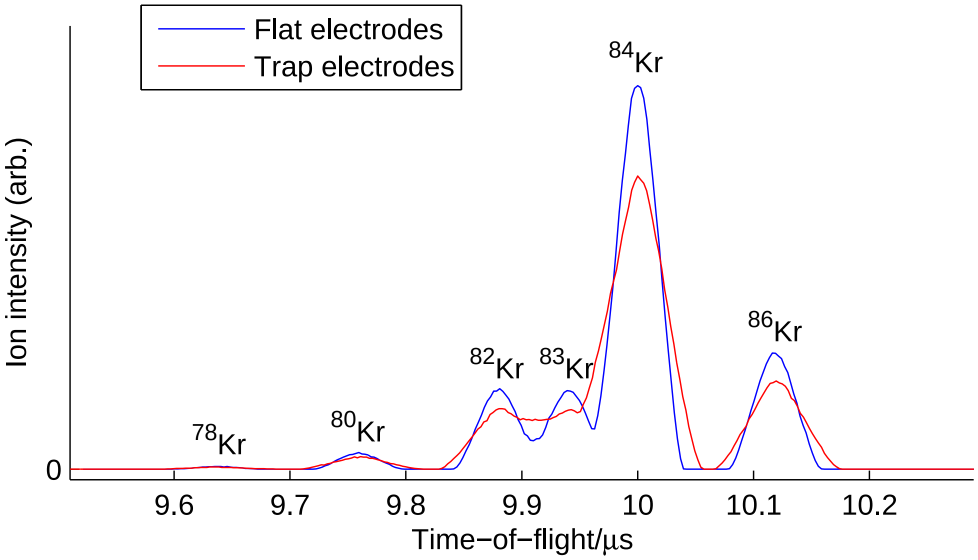

Figure 5.12: Comparison of simulated time-of-flight spectra for naturally abundant krypton isotopes when repeller and extractor elements are flat (blue) and cylindrical (red). $V_R = 150$V for both cases, with V_E varied for optimal mass resolution. Spectra are adjusted so that peak intensity is at 10 μs to aid comparison.

The grounded flight tube used in this experiment was built in-house and consists of two hollow cylinders. The narrower cylinder has an outer diameter of 2.5 cm, and is designed so that it can get close to the ion trap while avoiding contact with the recessed section of the vacuum chamber lid. A mesh with 85% transmission covers the tube end closest to the ion trap and prevents stray electric fields entering the tube. This is held in place with a ring which screws down against the cylinder. The wider cylinder has an outer diameter of 4 cm, and is capped on one end, with the exception of a hole where the narrow tube can be fit into. Use of the wider cylinder now allows the ions to continue travelling in free-flight while reducing the possibility of loss-causing collisions which could occur if only using the narrow tube. The narrow tube can be moved after the position of the wider cylinder has been fixed such that the lengths of the acceleration and free-flight regions can be changed while keeping the tube in the correct orientation.

Ions are detected using a pair of microchannel plates (MCPs) in a chevron configuration. A grounded mesh is located immediately before the MCPs to minimise stray electric fields in the free-flight volume. The electron shower released from the MCPs upon ion impact hits an anode behind the MCPs; the resulting voltage change on the anode is amplified and visualised on an oscilloscope.

5.4.1 Characterisation of time-of-flight apparatus

The time-of-flight apparatus needs to be characterised by determination of the mass resolution of the apparatus. This is achieved by studying the profiles of the signals obtained by ionisation of krypton, xenon and calcium. Due to the ease of ionisation and high natural abundance for ^{40}Ca, calcium is a useful tool for studying peak widths of a single mass. Optimisation and characterisation of the time-of-flight apparatus was performed through ionisation of calcium atoms from the oven; time-of-flight profiles are shown in figure 5.13. Greatest resolution is observed when V_E is approximately 85% of V_R; under these conditions, ions that are initially closer to the repeller electrode experience a potential sufficiently higher than ions in the centre of the trap. They subsequently reach a greater final velocity after acceleration and 'catch-up' with the other ions at the MCPs to minimise the peak width. At higher V_E, arrival times are later due to the increased time spent between the repeller and extractor electrodes, with the smaller electric field providing a smaller acceleration. Peak intensities decrease at lower V_E; this is accounted for by stray electric fields between the extractor and grounded electrodes, which leads to collisions of the ions with the grounded flight tube, so reducing the transmission of ions to the MCP detectors.

Characteristics of the spectrometer are investigated using SIMION 8.0, a charged particle optics simulation program [123]. Comparisons of the time-of-flight spectra obtained experimentally with ionised calcium are shown in figure 5.14. These are performed at a range of repeller and extractor voltages to seek the optimal voltages for ion spectrometry. Arrival times are similar for specific voltages for both experiment

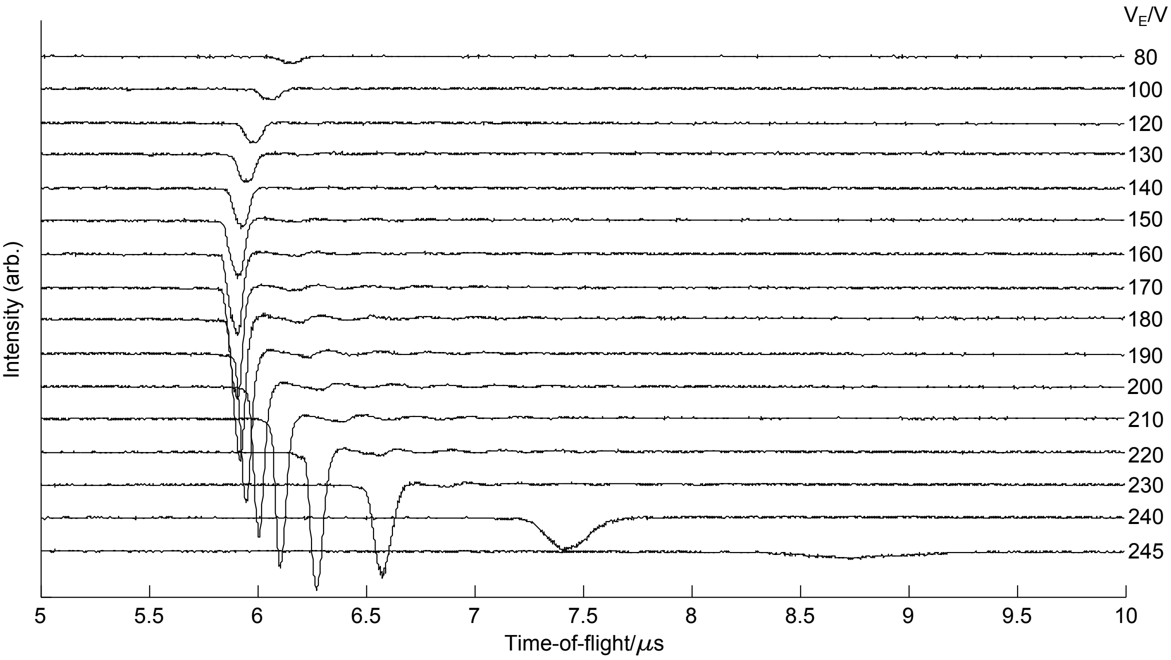

Figure 5.13: Time-of-flight spectra for calcium ionised in the trap centre at various extractor voltages, $V_R = 250$ V.

and simulation. At higher extractor voltages, the FWHM of the peak is noticeably larger experimentally, indicating Coulomb repulsion between the ions that could not be fully taken into account during simulations. At lower extractor voltages, the total experimental signal is less than that expected from simulations, presumably due to stray electric fields.

Compared to simulations, a decrease in mass resolution, to approximately $m/\Delta m \sim 70$, is observed in the experimental spectra using optimised $V_R : V_E$ ratios. This can also be seen for ionisation of krypton isotopes in figure 5.15. The reduction in resolution can potentially be explained by stray electric fields from the wires connected to the trap electrodes, from the low chamber top, which is grounded, or from Coulomb repulsion between the ions. Mass resolution of the time-of-flight apparatus can also be studied by ionisation of krypton or xenon atoms, either leaked into the trap chamber, or as part of a molecular beam packet travelling down the decelerator. Both species are suitable due to the range of isotopes that are naturally abundant.

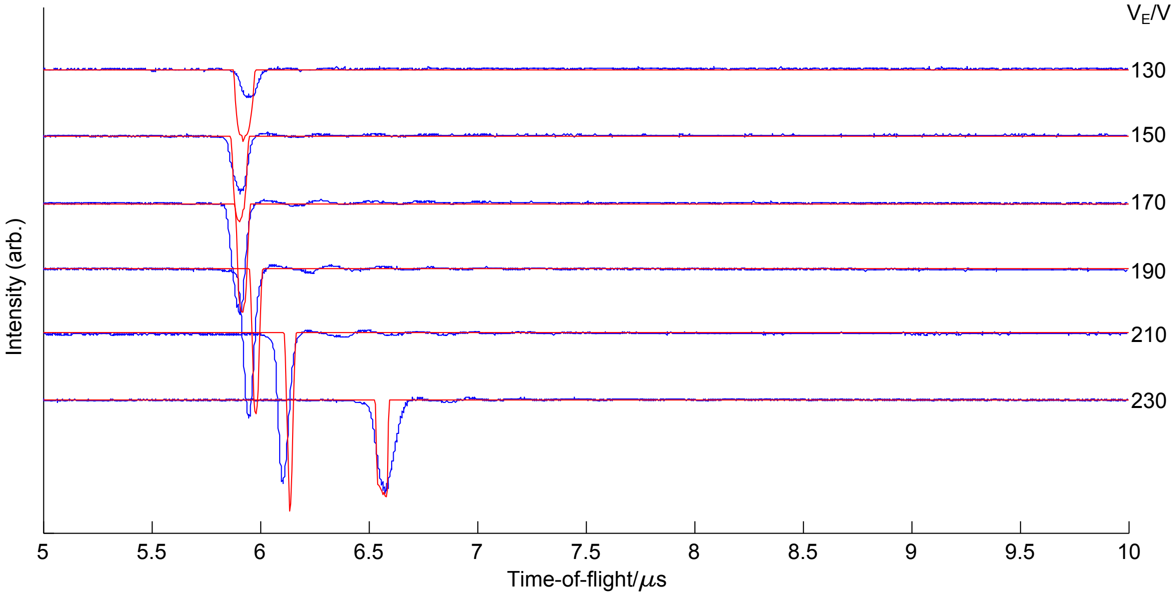

Figure 5.14: Comparison of experimental (blue) and simulated (red) time-of-flight spectra for calcium, with $V_R = 250$ V.

Also notable is the improved resolution when using a gas sample from the molecular beam. This is expected since the atoms in the beam will have negligible transverse velocities and similar longitudinal velocities, while ionisation of a background thermal sample will have a broad distribution of both. Simulations show that of these two factors, the spread in transverse velocities is more significant in increasing the peak breadth, as the ion cloud will spread further by the time the ions are passing the extraction electrodes. The cloud thus experiences a greater range of potential gradients.

Use of the time-of-flight mass spectrometer in a fashion similar to these examples is useful in optimising conditions for ionisation of various species that would be challenging and time-consuming if the ionisation rate is being monitored by the loading rate of ions into a crystal. This is particularly notable when using REMPI processes to form sympathetically-cooled ions; use of the mass spectrometer allows for immediate feedback of the ion formation rate for a particular laser wavelength. In contrast to this, loading into the crystal would require a crystal to cool down after ionisation,

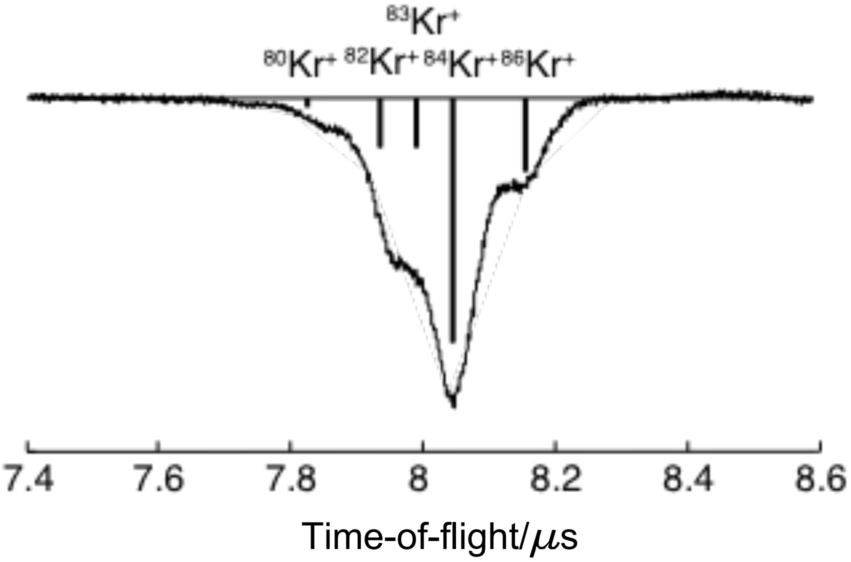

Figure 5.15: Experimental time-of-flight spectrum for krypton ionisation, $V_R = 200$ V and $V_E = 170$ V; mass resolution has significantly declined relative to the simulated spectrum in 5.12.

followed by analysis of the fluorescence profiles. Optimisation by this technique would also require loading of multiple crystals, with inevitable small changes between each crystal.

5.5 Ejection and detection of trapped ions

The time-of-flight apparatus as described above uses static voltages for instantaneous ejection of ions created in the ion trap. However, the ultimate aim is for a Coulomb crystal to be ejected and the absolute number of ions determined, which would allow additional confidence in the data obtained from reaction experiments by other means. This would additionally enable analysis of complex processes in which multiple ions may be formed.

The RF voltage applied for radial ion trapping is based upon a resonant circuit, which decays on the order of several hundred microseconds. Although ions can still

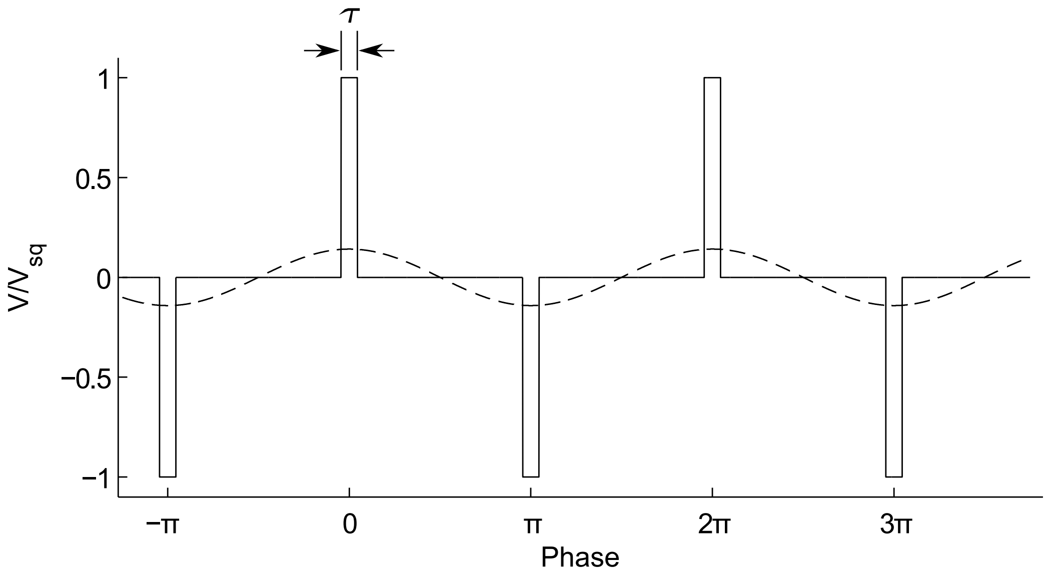

Figure 5.16: Radial voltages used in a square-wave trapping scheme, in which $\tau = 0.05/\Omega_{\mathrm{RF}}$. An RF potential with equal forces over a half-RF cycle is provided for comparison.

be ejected from the trap by applying a large voltage to the rear electrodes, their final trajectories will be heavily influenced by the RF voltages as they pass between the trapping electrodes, and the phase at which they leave the trap. Work by Schowalter *et al* showed consecutive trapping and ejecting of ions when trapping with an RF circuit, but with ejection voltages far higher than possible with the Oxford ion trap [204].

Due to these issues, it is beneficial to devise an alternate trapping and subsequent ejection scheme. This scheme will ideally have trapping voltages turned off throughout the entirety of ion ejection. This is realised most simply when using a square wave trapping potential instead of a sinusoidal potential. Experiments by Kjærgaard and Drewsen have shown a number of possible structures when using this potential, including a typical ion array and a 'string of discs' where discs of ions are axially separated [205]. Simulations of stable square wave trapping and subsequent ejection are shown here for future experiments.

Ion trapping with a square wave potential is conceptually very similar to trapping with RF potentials as discussed in section 2.1. The overall trapping forces experienced by the ions are

$$U_{\text{trap}}(x, y, z, t) = \phi_{\text{sq}}(x, y, t) + \phi_{end}(x, y, z). \tag{5.18}$$

In common with RF trapping, the harmonic end-cap potential is as given in equation 2.4, *ie*

$$\phi_{\text{end}}(x, y, z) = \frac{\kappa V_{\text{end}}}{z_0^2}\left(z^2 - \frac{x^2 + y^2}{2}\right). \tag{5.19}$$

The time-dependent potential arising from the square-wave voltages is, following the convention of Kjærgaard and Drewsen,

$$\phi_{\text{sq}}(x, y, t) = \frac{U_{\text{sq}}(t)}{2r_0^2}\left(x^2 - y^2\right) \tag{5.20}$$

with

$$U_{\text{sq}}(t) = \begin{cases} V_{\text{sq}} & \text{if } -\theta_{\text{sq}} < \theta < \theta_{\text{sq}} \\ -V_{\text{sq}} & \text{if } -\theta_{\text{sq}} < \theta + \pi < \theta_{\text{sq}} \\ 0 & \text{otherwise} \end{cases} \tag{5.21}$$

where θ is the phase of the square-wave cycle, and $\theta_{\text{sq}} = \tau/2\Omega_{\text{sq}}$ where τ is the length of the square-wave pulse, and Ω_{sq} is the repetition rate of the square-wave; an example is shown in figure 5.16. The square-wave generator built for future experiments has limitations such that $\Omega_{\text{sq}} < 1$ MHz and $V_{\text{sq}} < 120$ V; subsequent simulations will concentrate on using physical parameters in consideration of these limits.

In common with RF trapping, square wave trapping leads to a time-averaged attractive radial potential for certain trapping conditions. Although the depth of the RF pseudopotential is determined, for an ion with a given mass-to-charge ratio, by the frequency and amplitude of the RF voltage, the depth of the SW pseudopotential is additionally affected by τ. The reduced depth of the pseudopotential, particularly with the technical constraints noted above show a much lower axial voltage is required to allow trapping.

5.5.1 Stability in a square-wave potential

For short τ, the product of τ and V_{sq} can be used, since the adiabatic model takes no account of the duration of the impulse provided by the SW, just the magnitude. This can be useful in formulating stability diagrams for square-wave trapping. Similar to the simulated stability diagram for the Oxford ion trap as obtained by Alex Gingell [85], SIMION is used to determine whether an ion trajectory is stable over the course of 1 ms. If this is seen then trap voltages are considered stable for trapping. Stability regions observed from these trajectory simulations can be seen in figure 5.17. The stability regions have a similar shape to that seen in figure 2.2 when using RF voltages instead of SW voltages. Of note is the dependence on τ, an appropriate value for this needs to be chosen to ensure that crystals remain stable over the range of voltages that are to be used. In particular, using a large value of τ could mean that ions are ejected at high values of V_{sq}.

5.5.2 Ejection of trapped ions

ProtoMol, a molecular dynamics program [120] used in previous crystal simulations, is used to study expected time-of-flight spectra after ejection of ion ensembles, with forces from surrounding ions treated explicitly. While electrodes have trapping voltages applied, the force model matches that described in section 2.6 with an SW potential added. When electrodes have ejection voltages applied, a sixth-order polynomial is fitted to the SIMION-derived electric fields along the ejection axis through the centre of the trap. For individual ions, trajectories of individual ejected ions can be determined from both SIMION and ProtoMol and can be compared.

Simulations of the ejection process show that ion arrival times are strongly dependent on the phase at which the ions are ejected for a large crystal. For a lone hot

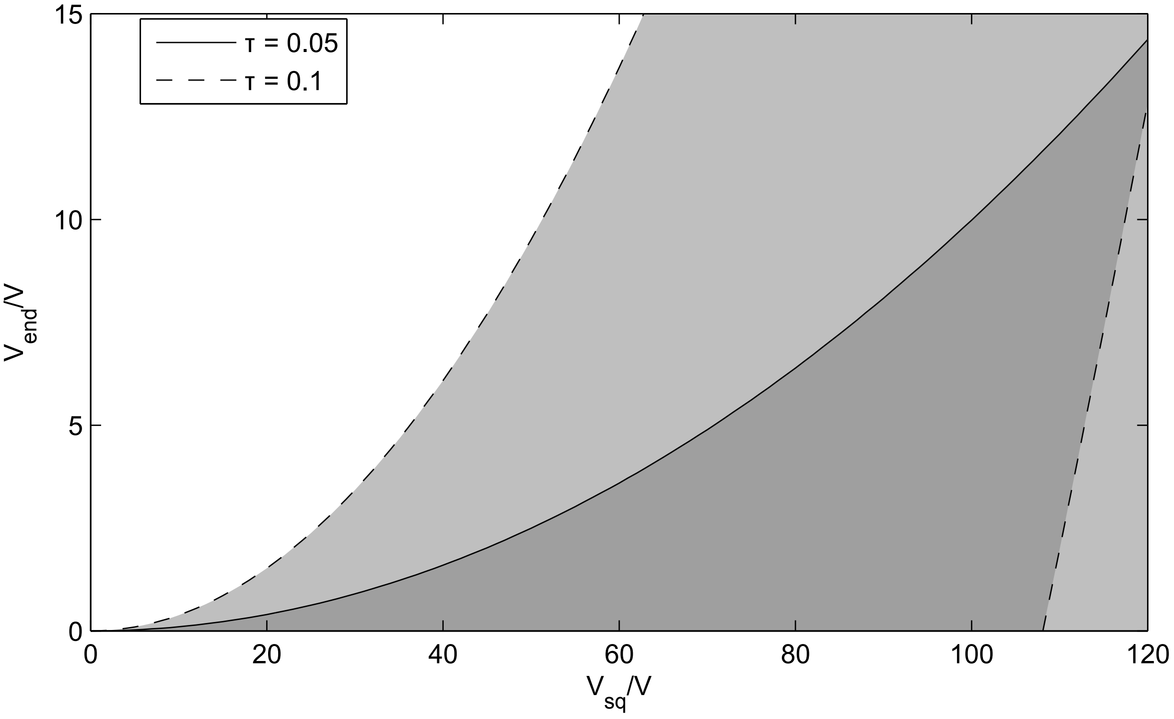

Figure 5.17: Stability plots for a square-wave trapping potential, with $\Omega_{\mathrm{sq}} = 1$ MHz. Stable regions are shaded for $\tau = 0.05$ (region edges marked by solid lines) and $\tau = 0.1$ (dashed).

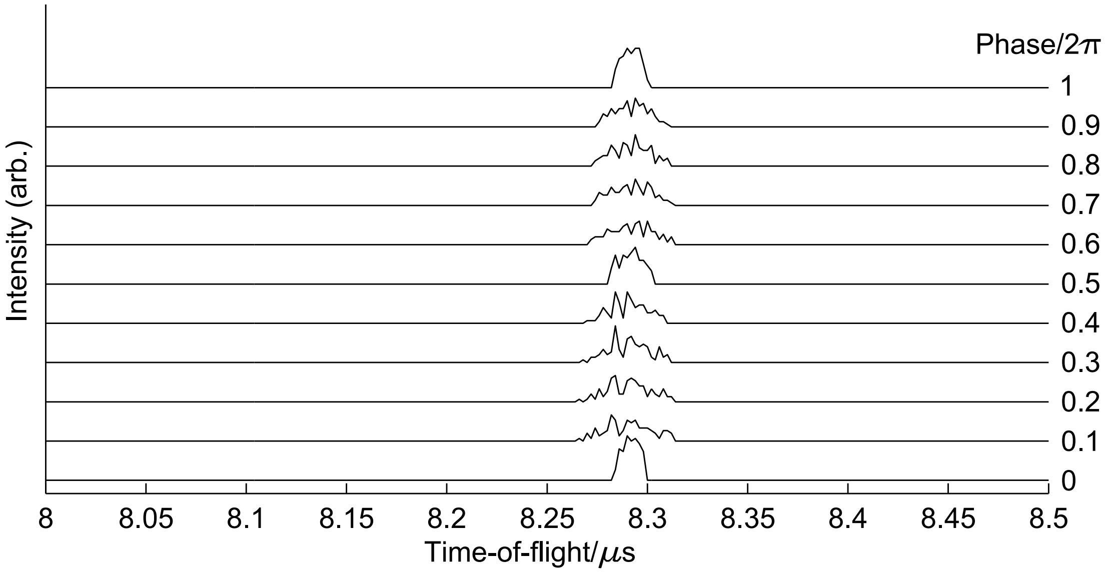

Figure 5.18: Simulated time-of-flight profiles for an ejected 500 Ca^+ crystal, with ejection forces implemented at various phases in the trapping cycle of figure 5.16.

ion the position in the trap will be of greatest importance, with the velocity of the ion broadly determined by the position. For a large crystal, the significant transverse motion that can be imparted on the ions prior to ejection has a more significant effect since Coulomb repulsion must be taken into account. This takes particular significance since the variable electric field gradients between the repeller electrodes will amplify any spatial differences. This means the phase of the cycle at which ions are ejected will be of some importance, which can be seen in figure 5.18. The shapes of the peaks obtained can effectively be thought of as a one-dimensional projection along the time-of-flight axis of the ion positions within the crystal when the ejection voltages are switched on.

5.6 Conclusions

A variety of techniques have been described in this chapter to provide vital information on the chemical events that occur in a crystal. Each technique provides a different dataset that can be combined to give a more complete description of a reaction cycle. These methods, both destructive and non-destructive, could be used in combination on the same crystal to obtain information during the reaction cycle whilst obtaining a quantitative description of the crystal when it is ejected.

The majority of non-destructive methods monitor changes in the crystal via a change in fluorescence intensities. In common with developments in NMR spectroscopy in the 1960s and microwave spectroscopy more recently [206], acquisition speed can be significantly enhanced when using a broadband excitation pulse followed by detection of a free induction decay. There is evidence to suggest that multiple species can be detected when using a continuous frequency scan – although this is most readily observed for small crystals. However, use of an average ionic weight, as determined by pulsed voltage excitation, with a quantitative measurement of the crystal contents at the end of a reaction will be able to elucidate both sequential reaction events and complicated reaction schemes. This combination of both non-destructive interrogation throughout the reaction cycle and quantitative identification at the end of a reaction holds the most promise for future studies of ion-molecule reactions using this apparatus.

Chapter 6

Conclusions

The previous chapters have discussed how cold ions and molecules can be formed, how they react and how they can be detected with the aim of increasing knowledge about ion-molecule reactions at low temperatures. The progress displayed means a diverse range of reactions could be examined subject to some modification of the experimental apparatus. The new techniques that have been demonstrated in this thesis have shown results consistent with previous studies: in the case of the $Xe^+ + ND_3$ reaction, rate constants are consistent with flow tube studies when assuming a ND_3 density similar to Meijer and co-workers; for pulsed axial excitation, rate constants for $Ca^+ + MeF$ are consistent with previous volume measurements from this group.

There are many aspects of progression from the work presented here. Further synergy of the component parts of the reaction apparatus is required in order to study a broader variety of reactions. Notably, there must be sufficient shielding placed between the decelerator and the ion trap to ensure that the molecular beam can be fully decelerated without disrupting the stability of the ion crystal. A simpler method of replacing the fast-opening shutter may also be beneficial. Combined with this, a method of reducing the flux of background contaminants is required; by using a cold finger, species that desorb from the chamber walls shall have a less significant effect on measured rate constants.

When these issues are resolved, there are powerful techniques available to analyse the reaction progress of a crystal. The ability to investigate the contents of a crystal both during and at the end of a reaction cycle will be critical in determining processes that employ more than one step in large crystals. The promise of this is great, with a substantial improvement from the statistical determination of reaction rates that is only possible when using two-ion crystals.

Determination of the collision energy distributions in a reaction is important in extracting temperature-dependent reaction rates. Although control of the collision energy will be principally performed by choice of the decelerator phase angle, and thus the final velocity of the decelerated molecules, the thermal properties of the trapped ions must also be considered – the wider energy distribution for ions will typically dictate that the crystal thermal properties will determine the uncertainty in collision energies for reactions studied. Smaller prolate crystals, having a lower range of energy distributions, are evidently also most beneficial in reaching the lowest collision energies possible for a given speed of decelerated molecules. However, the extreme case of using a string for reactions is not necessarily suitable if using sympathetically cooled ions as a reactant, since there can be no change in the fluorescence profile as there would be for a 3D crystal. In this case, mass spectrometric methods as described in chapter 5 would be necessary to determine reaction events.

The suitability of the decelerator, particularly when the buncher is used in a velocity narrowing configuration, is well-suited to reaction studies if crystals with narrow energy profiles are used. Even with larger crystals, the collision energies are sufficiently low to permit studies of reactions that are astrochemically relevant.

There are many future directions that this work can take. The viability of fluoromethane deceleration has previously been explored [147] and, if the experimental restrictions that prevented further examination of the Xe^+ + ND_3 reaction are resolved, this will permit further studies of the Ca^+ + CH_3F reaction. In contrast to previous studies, there will be far fewer rotational states in the flux that reaches the crystal, which can allow determination of the relative importance of rotational and translational kinetic energies in determining rate constants. This investigation can be further enhanced by studying this reaction with the recently constructed buffer-gas-cooled bent electrostatic quadrupole.

Also of great interest is the ability to use molecular ions that can be rotationally cooled. Although there is still only a limited number of ions for which cooling schemes have been devised, even for these species there would be much of interest in exploring reactions involving these ions. The possibility of studying reactions between ammonia molecules and ammonia ions, with the numerous pathways that can be followed, is also of considerable interest.

References

[1] R. Sahai and L.-Å. Nyman. “The Boomerang Nebula: The coldest region of the Universe?” In: *Astrophys. J.* 487 (1997), p. L155.

[2] A. G. Suits. “Titan: A strangely familiar world”. In: *J. Phys. Chem. A* 113 (2009), p. 11097.

[3] S. Chu, L. Hollberg, J. E. Bjorkholm, A. Cable, and A. Ashkin. “Three-dimensional viscous confinement and cooling of atoms by resonance radiation pressure”. In: *Phys. Rev. Lett.* 55 (1985), p. 48.

[4] C. C. Bradley, C. A. Sackett, J. J. Tollett, and R. G. Hulet. “Evidence of Bose-Einstein condensation in an atomic gas with attractive interactions”. In: *Phys. Rev. Lett.* 75 (1995), p. 1687.

[5] K. B. Davis, M.-O. Mewes, M. R. Andrews, N. J. van Druten, D. S. Durfee, D. M. Kurn, and W. Ketterle. “Bose-Einstein condensation in a gas of sodium atoms”. In: *Phys. Rev. Lett.* 75 (1995), p. 3969.

[6] M. H. Anderson, J. R. Ensher, M. R. Matthews, C. E. Wieman, and E. A. Cornell. “Observation of Bose-Einstein condensation in a dilute atomic vapor”. In: *Science* 269 (1995), p. 198.

[7] M. T. Bell and T. P. Softley. “Ultracold molecules and ultracold chemistry”. In: *Mol. Phys.* 107 (2009), p. 99.

[8] E. P. Wigner. “On the behavior of cross sections near thresholds”. In: *Phys. Rev.* 73 (1948), p. 1002.

[9] M. T. Cvitaš, P. Soldán, J. M. Hutson, P. Honvault, and J.-M. Launay. “Ultracold collisions involving heteronuclear alkali metal dimers”. In: *Phys. Rev. Lett.* 94 (2005), p. 200402.

[10] G. Quéméner and P. S. Julienne. “Ultracold molecules under control!” In: *Chem. Rev.* 112 (2012), p. 4949.

[11] A. O. G. Wallis and J. M. Hutson. “Production of ultracold NH molecules by sympathetic cooling with Mg”. In: *Phys. Rev. Lett.* 103 (2009), p. 183201.

[12] L. P. Parazzoli, N. J. Fitch, P. S. Żuchowski, J. M. Hutson, and H. J. Lewandowski. “Large effects of electric fields on atom-molecule collisions at millikelvin temperatures”. In: *Phys. Rev. Lett.* 106 (2011), p. 193201.

[13] J. Herbig, T. Kraemer, M. Mark, T. Weber, C. Chin, H.-C. Nägerl, and R. Grimm. “Preparation of a pure molecular quantum gas”. In: *Science* 301 (2003), p. 1510.

[14] D. C. Clary, T. S. Stoecklin, and A. G. Wickham. “Rate constants for chemical reactions of radicals at low temperatures”. In: *J. Chem. Soc. Faraday Trans.* 89 (1993), p. 2185.

[15] S. Willitsch, M. T. Bell, A. D. Gingell, S. R. Procter, and T. P. Softley. “Cold reactive collisions between laser-cooled ions and velocity-selected neutral molecules”. In: *Phys. Rev. Lett.* 100 (2008), p. 043203.

[16] A. D. Gingell, M. T. Bell, J. M. Oldham, T. P. Softley, and J. N. Harvey. “Cold chemistry with electronically excited Ca^+ Coulomb crystals”. In: *J. Chem. Phys.* 133 (2010), p. 194302.

[17] J. Liu, B. Van Devener, and S. L. Anderson. “Reaction of formaldehyde cation with methane: Effects of collision energy and H_2CO^+ and methane vibrations”. In: *J. Chem. Phys.* 119 (2003), p. 200.

[18] I. R. Sims, I. W. M. Smith, D. C. Clary, P. Bocherel, and B. R. Rowe. “Ultra-low temperature kinetics of neutral-neutral reactions: New experimental and theoretical results for OH+HBr between 295 and 23 K”. In: *J. Chem. Phys.* 101 (1994), p. 1748.

[19] F. Leonori, R. Petrucci, E. Segoloni, A. Bergeat, K. M. Hickson, N. Balucani, and P. Casavecchia. “Unraveling the dynamics of the $C(^3P,^1D) + C_2H_2$ reactions by the crossed molecular beam scattering technique”. In: *J. Phys. Chem. A* 112 (2008), p. 1363.

[20] S. T. Pratt, J. L. Dehmer, P. M. Dehmer, and W. A. Chupka. “Reactions of Rydberg states of molecular hydrogen”. In: *J. Chem. Phys.* 101 (1994), p. 882.

[21] T. P. Softley. “Applications of molecular Rydberg states in chemical dynamics and spectroscopy”. In: *Int. Rev. Phys. Chem.* 23 (2004), p. 1.

[22] S. Bize, P. Laurent, M. Abgrall, H. Marion, I. Maksimovic, L. Cacciapuoti, J. Grünert, C. Vian, F. Pereira dos Santos, P. Rosenbusch, P. Lemonde, G. Santarelli, P. Wolf, A. Clarion, A. Luiten, M. Tobar, and C. Salomon. “Cold atom clocks and applications”. In: *J. Phys. B* 38 (2005), S449.

[23] H. L. Bethlem, M. Kajita, B. Sartakov, G. Meijer, and W. Ubachs. “Prospects for precision measurements on ammonia molecules in a fountain”. In: *Eur. Phys. J. Special Topics* 163 (2008), p. 55.

[24] J. Baron, W. C. Campbell, D. DeMille, J. M. Doyle, G. Gabrielse, Y. V. Gurevich, P. W. Hess, N. R. Hutzler, E. Kirilov, I. Kozyryev, B. R. O’Leary, C. D. Panda, M. F. Parsons, E. S. Petric, B. Spaun, A. C. Vutha, and A. D. West. “Order of magnitude smaller limit on the electric dipole moment of the electron”. In: *Science* 343 (2014), p. 269.

[25] M. R. Tarbutt, B. E. Sauer, J. J. Hudson, and E. A. Hinds. “Design for a fountain of YbF molecules to measure the electron’s electric dipole moment”. In: *New J. Phys.* 15 (2013), p. 053034.

[26] J. J. Hudson, D. M. Kara, I. J. Smallman, B. E. Sauer, M. R. Tarbutt, and E. A. Hinds. “Improved measurement of the shape of the electron”. In: *Nature* 473 (2011), p. 493.

[27] J. C. J. Joelemeij, B. Roth, A. Wicht, I. Ernsting, and S. Schiller. “Vibrational spectroscopy of HD^+ with 2-ppb accuracy”. In: *Phys. Rev. Lett.* 98 (2007), p. 173002.

[28] J. D. Jost, J. P. Horne, J. M. Amini, D. Hanneke, R. Ozeri, C. Langer, J. J. Bollinger, D. Leibfriend, and D. J. Wineland. “Entangled mechanical oscillators”. In: *Nature* 459 (2009), p. 683.

[29] C. W. Chou, D. B. Hume, J. C. J. Koelemeij, D. J. Wineland, and T. Rosenband. “Frequency comparison of two high-accuracy Al^+ optical clocks”. In: *Phys. Rev. Lett.* 104 (2010), p. 070802.

[30] J. M. Raimond, M. Brune, and S. Haroche. “Manipulating quantum entanglement with atoms and photons in a cavity”. In: *Rev. Mod. Phys.* 73 (2001), p. 565.

[31] S. Gleyzed, S. Kuhr, C. Guerlin, J. Bernu, S. Deléglise, U. B. Hoff, M. Brune, J-M. Raimond, and S. Haroche. “Quantum jumps of light recording the birth and death of a photon in a cavity”. In: *Nature* 446 (2007), p. 297.

[32] Q. Chen, J. Stajic, S. Tan, and K. Levin. “BCS–BEC crossover: From high temperature superconductors to ultracold superfluids”. In: *Phys. Rep.* 412 (2005), p. 1.

[33] T. Bourdel, L. Khaykovich, J. Cubizolles, J. Zhang, F. Chevy, M. Teichmann, L. Tarruell, S. J. J. M. F. Kokkelmans, and C. Salomon. “Experimental study of the BEC-BCS crossover region in lithium 6”. In: *Phys. Rev. Lett.* 93 (2004), p. 050401.

[34] M. Greiner, C. A. Regal, and D. S. Jin. “Emergence of a molecular Bose-Einstein condensate from a Fermi gas”. In: *Nature* 426 (2003), p. 537.

[35] P. D. Lett, K. Helmerson, W. D. Phillips, L. P. Ratliff, S. L. Rolston, and M. E. Wagshul. “Spectroscopy of Na_2 by photoassociation of laser-cooled Na”. In: *Phys. Rev. Lett.* 71 (1993), p. 2200.

[36] J. D. Miller, R. A. Cline, and D. J. Heinzen. “Photoassociation spectrum of ultracold Rb atoms”. In: *Phys. Rev. Lett.* 71 (1993), p. 2204.

[37] J. M. Sage, S. Sainis, T. Bergeman, and D. DeMille. “Optical production of ultracold polar molecules”. In: *Phys. Rev. Lett.* 94 (2005), p. 203001.

[38] E. A. Donley, N. R. Claussen, S. T. Thompson, and C. E. Wieman. “Atom-molecule coherence in a Bose-Einstein condensate”. In: *Nature* 417 (2002), p. 529.

[39] G. Thalhammer, K. Winkler, F. Lang, S. Schmid, R. Grimm, and J. Hecker Denschlag. “Long-lived Feshbach molecules in a three-dimensional optical lattice”. In: *Phys. Rev. Lett.* 96 (2006), p. 050402.

[40] N. V. Vitanov, T. Halfmann, B. W. Shore, and K. Bergmann. “Laser-induced population transfer by adiabatic passage techniques”. In: *Annu. Rev. Phys. Chem.* 52 (2001), p. 763.

[41] F. Lang, K. Winkler, C. Strauss, R. Grimm, and J. Hecker Denschlag. “Ultracold triplet molecules in the rovibrational ground state”. In: *Phys. Rev. Lett.* 101 (2008), p. 133005.

[42] K.-K. Ni, S. Ospelkaus, M. H. G. de Miranda, A. Pe’er, B. Neyenhuis, J. J. Zirbel, S. Kotochigova, P. S. Julienne, D. S. Jin, and J. Ye. “A high phase-space-density gas of polar molecules”. In: *Science* 322 (2008), p. 231.

[43] S. Ospelkaus, K.-K. Ni, D. Wang, M. H. G. de Miranda, B. Neyenhuis, G. Quéméner, P. S. Julienne, J. L. Bohn, D. S. Jin, and J. Ye. “Quantum-state controlled chemical reactions of ultracold potassium-rubidium molecules”. In: *Science* 327 (2010), p. 853.

[44] T. Kraemer, M. Mark, P. Waldburger, J. G. Danzl, C. Chin, B. Engeser, A. D. Lange, K. Pilch, A. Jaakkola, H.-C. Nägerl, and R. Grimm. “Evidence for Efimov quantum states in an ultracold gas of caesium atoms”. In: *Nature* 440 (2006), p. 315.

[45] V. Efimov. “Energy levels arising from resonant two-body forces in a three-body system”. In: *Phys. Lett. B* 33 (1970), p. 563.

[46] M. H. G. de Miranda, A. Chotia, B. Neyenhuis, D. Wang, G. Quéméner, S. Ospelkaus, J. L. Bohn, J. Ye, and D. S. Jin. “Controlling the quantum stereodynamics of ultracold bimolecular reactions”. In: *Nature Phys.* 7 (2011), p. 502.

[47] S. A. Rangwala, T. Junglen, T. Rieger, P. W. H. Pinkse, and G. Rempe. “Continuous source of translationally cold dipolar molecules”. In: *Phys. Rev. A* 67 (2003), p. 043406.

[48] M. Motsch, M. Schenk, L. D. van Buuren, M. Zeppenfeld, P. W. H. Pinkse, and G. Rempe. “Internal-state thermometry by depletion spectroscopy in a cold guided beam of formaldehyde”. In: *Phys. Rev. A* 76 (2007), p. 061402.

[49] M. T. Bell, A. D. Gingell, J. M. Oldham, T. P. Softley, and S. Willitsch. “Ion-molecule chemistry at very low temperatures: cold chemical reactions between Coulomb-crystallized ions and velocity-selected neutral molecules”. In: *Faraday Discuss.* 142 (2009), p. 73.

[50] H. L. Bethlem, G. Berden, and G. Meijer. “Decelerating neutral dipolar molecules”. In: *Phys. Rev. Lett.* 83 (1999), p. 1558.

[51] N. Vanhaecke, U. Meier, M. Andrist, B. H. Meier, and F. Merkt. “Multistage Zeeman deceleration of hydrogen atoms”. In: *Phys. Rev. A* 75 (2007), p. 031402.

[52] R. Fulton, A. I. Bishop, and P. F. Barker. “Optical Stark decelerator for molecules”. In: *Phys. Rev. Lett.* 93 (2004), p. 243004.

[53] S. Merz, C. Brieger, N. Vanhaecke, G. Meijer, and M. Schnell. “Manipulating the motion of polar molecules with microwave radiation”. In: *Mol. Phys.* 111 (2013), p. 1855.

[54] M. S. Elioff, J. J. Valentini, and D. W. Chandler. “Subkelvin cooling NO molecules via “billiard-like” collisions with argon”. In: *Science* 302 (2003), p. 1940.

[55] J. J. Kay, S. Y. T. van de Meerakker, K. E. Strecker, and D. W. Chandler. “Production of cold ND_3 by kinematic cooling”. In: *Faraday Discuss.* 142 (2009), p. 143.

[56] A. Trottier, D. Carty, and E. Wrede. “Photostop: Production of zero-velocity molecules by photodissociation in a molecular beam”. In: *Mol. Phys.* 109 (2011), p. 725.

[57] W. G. Doherty, M. T. Bell, T. P. Softley, A. Rowland, E. Wrede, and D. Carty. “Production of cold bromine atoms at zero mean velocity by photodissociation”. In: *Phys. Chem. Chem. Phys.* 13 (2011), p. 8441.

[58] W. C. Cambell and J. M. Doyle. “Cooling, trap loading and beam production using a cryogenic helium buffer gas”. In: *Cold Molecules: Theory, Experiment, Applications.* Ed. by R. V. Krems, W. C. Stwalley, and B. Friedrich. CRC Press, 2009.

[59] S. E. Maxwell, N. Brahms, R. deCarvalho, D. R. Glenn, J. S. Helton, S. V. Nguyen, D. Patterson, J. Petricka, D. DeMille, and J. M. Doyle. “High-flux beam source for cold, slow atoms or molecules”. In: *Phys. Rev. Lett.* 95 (2005), p. 173201.

[60] P. B. Armentrout, A. Gabriel, and R. M. Moision. “An experimental and theoretical study of alkali metal cation/methionine interations”. In: *Int. J. Mass Spectrom.* 283 (2009), p. 56.

[61] D. Gerlich and G. Borodi. “Buffer gas cooling of polyatomic ions in RF multi-electrode traps”. In: *Faraday Discuss.* 142 (2009), p. 57.

[62] L. D. van Buuren, C. Sommer, M. Motsch, S. Pohle, M. Schenk, J. Bayerl, P. W. H. Pinkse, and G. Rempe. “Electrostatic extraction of cold molecules from a cryogenic reservoir”. In: *Phys. Rev. Lett.* 102 (2009), p. 033001.

[63] M. Hartmann, R. E. Miller, J. P. Toennies, and A. F. Vilesov. “High-resolution molecular spectroscopy of van der Waals clusters in Liquid Helium Droplets”. In: *Science* 272 (1996), p. 1631.

[64] B. G. Sartakov, J. P. Toennies, and A. F. Vilesov. “Infrared spectroscopy of carbonyl sulfide inside a pure ^{3}He droplet”. In: *J. Chem. Phys.* 136 (2012), p. 134316.

[65] E. Lugovoj, J. P. Toennies, and A. Vilesov. “Manipulating and enhancing chemical reactions in helium droplets”. In: *J. Chem. Phys.* 112 (2000), p. 8217.

[66] J. Nagl, G. Auböck, A. W. Hauser, O. Allard, C. Callegari, and W. E. Ernst. “High-spin alkali trimers on helium nanodroplets: Spectral separation and analysis”. In: *J. Chem. Phys.* 128 (2008), p. 154320.

[67] L. An der Lan, P. Bartl, C. Leidlmair, H. Schöbel, R. Jochum, S. Denifl, T. D. Märk, A. M. Ellis, and P. Scheier. “The submersion of sodium clusters in helium nanodroplets: Identification of the surface → interior transition”. In: *J. Chem. Phys.* 135 (2011), p. 044309.

[68] B. R. Rowe, G. Dupeyrat, J. B. Marquette, and P. Gaucherel. “Study of the reactions $N_2^+ + 2N_2 \rightarrow N_4^+ + N_2$ and $O_2^+ + 2O_2 \rightarrow O_4^+ + O_2$ from 20 to 160 K by the CRESU technique”. In: *J. Chem. Phys.* 80 (1984), p. 4915.

[69] I. R. Sims, J. L. Queffelec, A. Defrance, C. Rebrion-Rowe, D. Travers, B. R. Rowe, and I. W. M. Smith. “Ultra-low temperature kinetics of neutral-neutral reactions: The reaction $CN+O_2$ down to 26 K”. In: *J. Chem. Phys.* 97 (1992), p. 8798.

[70] C. Berteloite, M. Lara, A. Bergeat, S. D. Le Picard, F. Dayou, K. M. Hickson, A. Canosa, C. Naulin, J.-M. Launay, I. R. Sims, and M. Costes. “Kinetics and dynamics of the $S(^1D_2) + H_2 \rightarrow SH + H$ reaction at very low temperatures and collision energies”. In: *Phys. Rev. Lett.* 105 (2010), p. 203201.

[71] D. B. Atkinson and M. A. Smith. “Design and characterization of pulsed uniform supersonic expansions for chemical applications”. In: *Rev. Sci. Instrum.* 66 (1995), p. 4434.

[72] D. Patterson, M. Schnell, and J. M. Doyle. “Enantiomer-specific detection of chiral molecules via microwave spectroscopy”. In: *Nature* 497 (2013), p. 475.

[73] S. Earnshaw. “On the nature of the molecular forces which regulate the constitution of the luminferous ether”. In: *Trans. Camb. Phil. Soc.* 7 (1842), p. 97.

[74] H. G. Dehmelt and F. L. Walls. ““Bolometric” technique for the RF spectroscopy of stored ions”. In: *Phys. Rev. Lett.* 21 (1968), p. 127.

[75] L. S. Brown and G. Gabrielse. “Geonium theory: Physics of a single electron or ion in a Penning trap”. In: *Rev. Mod. Phys.* 58 (1986), p. 233.

[76] W. Paul and H. Steinwedel. “Ein neues Massenspektrometer ohne Magnetfield”. In: *Zeitschrift für Naturforschung A* 8 (1953), p. 448.

[77] D. J. Berkeland, J. D. Miller, J. C. Bergquist, W. M. Itano, and D. J. Wineland. “Minimization of ion micromotion in a Paul trap”. In: *J. Appl. Phys.* 83 (1998), p. 5025.

[78] D. Gerlich. “Inhomogeneous RF Fields: A versatile tool for the study of processes with slow ions”. In: *Adv. Chem. Phys.* 82 (1992), p. 1.

[79] P. K. Ghosh. *Ion Traps.* Clarendon Press, Oxford, 1995.

[80] H. J. Metcalf and P. van der Straten. *Laser cooling and trapping.* Springer-Verlag, 1999.

[81] D. F. V. James. “Quantum dynamics of cold trapped ions with application to quantum computation”. In: *Appl. Phys. B* 66 (1998), p. 181.

[82] P. Blythe, B. Roth, U. Fröhlich, H. Wenz, and S. Schiller. “Production of ultracold trapped molecular hydrogen ions”. In: *Phys. Rev. Lett.* 95 (2005), p. 183002.

[83] M. Drewsen, C. Brodersen, L. Hornekær, and J. S. Hangst. “Large ion crystals in a linear Paul trap”. In: *Phys. Rev. Lett.* 81 (1998), p. 2878.

[84] G. Poulsen, Y. Miroshnychenko, and M. Drewsen. “Efficient ground-state cooling of an ion in a large room-temperature linear Paul trap with a sub-Hertz heating rate”. In: *Phys. Rev. A* 86 (2012), p. 051402.

[85] A. D. Gingell. “Applications of Coulomb crystals in cold chemistry”. DPhil Thesis. University of Oxford, 2010.

[86] K. Mølhave and M. Drewsen. “Formation of translationally cold MgH^+ and MgD^+ molecules in an ion trap”. In: *Phys. Rev. A* 62 (2000), p. 011401.

[87] F. Diedrich, J. C. Bergquist, W. M. Itano, and D. J. Wineland. “Laser cooling to the zero-point energy of motion”. In: *Phys. Rev. Lett.* 62 (1989), p. 403.

[88] R. J. Hendricks, J. L. Sørensen, C. Champenois, M. Knoop, and M. Drewsen. “Doppler cooling of calcium ions using a dipole-forbidden transition”. In: *Phys. Rev. A* 2007 (2008), p. 021401.

[89] E. S. Shuman, J. F. Barry, and D. DeMille. “Laser cooling of a diatomic molecule”. In: *Nature* 467 (2010), p. 820.

[90] M. D. Di Rosa. “Laser-cooling molecules - Concept, candidates and supporting hyperfine-resolved measurements of rotational lines in the A-X(0,0) band of CaH”. In: *Eur. Phys. J. D* 31 (2004), p. 395.

[91] J. H. V. Nguyen, C. R. Viteri, E. G. Hohenstein, C. D. Sherrill, K. R. Brown, and B. Odom. “Challenges of laser-cooling molecular ions”. In: *New J. Phys.* 13 (2011), p. 063023.

[92] L. R. Hunter, S. K. Peck, A. S. Greenspon, S. Saad Alam, and D. DeMille. “Prospects for laser cooling TlF”. In: *Phys. Rev. A* 85 (2012), p. 012511.

[93] B. L. Lev, A. Vukics, E. R. Hudson, B. C. Sawyer, P. Domokos, H. Ritsch, and J. Ye. “Prospects for the cavity-assisted laser cooling of molecules”. In: *Phys. Rev. A* 77 (2008), p. 023402.

[94] P. F. Staanum, K. Højbjerre, P. S. Skyt, A. K. Hansen, and M. Drewsen. “Rotational laser cooling of vibrationally and translationally cold molecular ions”. In: *Nature Phys.* 6 (2010), p. 271.

[95] I. Manai, R. Horchani, H. Lignier, P. Pillet, D. Comparat, A. Fioretti, and M. Allegrini. “Rovibrational cooling of molecules by optical pumping”. In: *Phys. Rev. Lett.* 109 (2012), p. 183001.

[96] S. Schiller and C. Lämmerzahl. “Molecular dynamics simulation of sympathetic crystallization of molecular ions”. In: *Phys. Rev. A* 68 (2003), p. 053406.

[97] Y. Kai, K. Toyoda, M. Watanabe, and S. Urabe. “Motional resonances of sympathetically cooled $^{44}Ca^+$, Zn^+ or Ga^+ ions in a linear Paul trap”. In: *Jpn. J. Appl. Phys.* 40 (2001), p. 5136.

[98] A. Bertelsen, S. Jørgensen, and M. Drewsen. “The rotational temperature of polar molecular ions in Coulomb crystals”. In: *J. Phys. B* 39 (2006), p. L83.

[99] A. Bertelsen. “The rotational temperature of translational sympathetically cooled $^{24}MgH^+$ investigated by photo-dissociation”. MA thesis. University of Aarhus, 2005.

[100] I. S. Vogelius, L. B. Madsen, and M. Drewsen. “Rotational cooling of molecular ions through laser-induced coupling to the collective modes of a two-ion Coulomb crystal”. In: *J. Phys. B* 39 (2006), S1267.

[101] N. Deb, B. R. Heazlewood, M. T. Bell, and T. P. Softley. “Blackbody-mediated rotational laser cooling schemes in MgH^+, DCl^+, HCl^+, LiH and CsH”. In: *Phys. Chem. Chem. Phys.* 15 (2013), p. 14270.

[102] T. Schneider, B. Roth, H. Duncker, I. Ernsting, and S. Schiller. “All-optical preparation of molecular ions in the rovibrational ground state”. In: *Nature Phys.* 6 (2010), p. 275.

[103] M. Lara, J. L. Bohn, D. Potter, P. Soldán, and J. M. Hutson. “Ultracold Rb-OH collisions and prospects for sympathetic cooling”. In: *Phys. Rev. Lett.* 97 (2006), p. 183201.

[104] W. G. Rellergert, S. T. Sullivan, S. J. Schowalter, S. Kotochigova, K. Chen, and E. R. Hudson. “Evidence for sympathetic vibrational cooling of translationally cold molecules”. In: *Nature* 495 (2013), p. 490.

[105] I. E. Dayton, F. C. Shoemaker, and R. F. Mozley. “The measurement of two-dimensional fields. Part II: Study of a quadrupole magnet”. In: *Rev. Sci. Instrum.* 25 (1954), p. 485.

[106] D. R. Denison. “Operating parameters of a quadrupole in a grounded cylindrical housing”. In: *J. Vac. Sci. Technol.* 8 (1971), p. 266.

[107] L. Hornekær. “Single- and multi-species Coulomb ion crystals: Structures, dynamics and sympathetic cooling”. PhD thesis. University of Aarhus, 2000.

[108] A. Mortensen, J. J. T. Lindballe, I. S. Jensen, P. Staanum, D. Voigt, and M. Drewsen. “Isotope shifts of the $4s^{21}S_0 \Rightarrow 4s5p^1P_1$ transition and hyperfine splitting of the $4s5p^1P_1$ state in calcium”. In: *Phys. Rev. Lett.* 69 (2004), p. 042502.

[109] P. Staanum. “Quantum optics with trapped calcium ions”. PhD thesis. University of Aarhus, 2004.

[110] J. P. Hansen. “Statistical mechanics of dense ionized matter. I. Equilibrium properties of the classical one-component plasma”. In: *Phys. Rev. A* 8 (1973), p. 3096.

[111] E. L. Pollock and J. P. Hansen. “Statistical mechanics of dense ionized matter. II. Equilibrium properties and melting transition of the crystallized one-component plasma”. In: *Phys. Rev. A* 8 (1973), p. 3110.

[112] A. Mortensen, E. Nielsen, T. Matthey, and M. Drewsen. “Observation of three-dimensional long-range order in small ion Coulomb crystals in an rf trap”. In: *Phys. Rev. Lett.* 96 (2006), p. 103001.

[113] T. Matthey, J. P. Hansen, and M. Drewsen. “Coulomb bicrystals of species with identical charge-to-mass ratios”. In: *Phys. Rev. Lett.* 91 (2003), p. 165001.

[114] D. J. Larson, J. C. Bergquist, J. J. Bollinger, W. M. Itano, and D. J. Wineland. “Sympathetic cooling of trapped ions: A laser-cooled Two-Species nonneutral ion plasma”. In: *Phys. Rev. Lett.* 57 (1986), p. 70.

[115] D. Offenberg, Ch. Wellers, C. B. Zhang, B. Roth, and S. Schiller. “Measurement of small photodestruction of rates of cold, charged biomolecules in an ion trap”. In: *J. Phys. B* 42 (2009), p. 035101.

[116] D. J. Wineland. “Ion traps for large storage capacity”. In: *Proc. of the Cooling, Condensation and Storage of Hydrogen Cluster Ions Workshop.* 1987.

[117] L. Hornekær, N. Kjærgaard, A. M. Thommesen, and M. Drewsen. “Structural Properties of Two-Component Coulomb Crystals in Linear Paul Traps”. In: *Phys. Rev. Lett.* 86 (2001), p. 1994.

[118] C. B. Zhang, D. Offenberg, B. Roth, M. A. Wilson, and S. Schiller. “Molecular-dynamics simulations of cold single-species and multispecies ion ensembles in a linear Paul trap”. In: *Phys. Rev. A* 76 (2007), p. 012719.

[119] T. Matthey. “Framework design, parallelization and force computation in molecular dynamics”. PhD thesis. University of Bergen, 2002.

[120] T. Matthey, T. Cickovski, S. Hampton, A. Ko, Q. Ma, M. Nyerges, T. Raeder, T. Slabach, and J. A. Izaguirre. “ProtoMol, an object-oriented framework for prototyping novel algorithms for molecular dynamics”. In: *ACM Trans. Math. Soft.* 30 (2004), p. 237.

[121] A. Mortensen, E. Nielsen, T. Matthey, and M. Drewsen. “Radio frequency field-induced persistent long-range ordered structures in two-species ion Coulomb crystals”. In: *J. Phys. B* 40 (2007), F223.

[122] W. C. Swope, H. C. Andersen, P. H. Berens, and K. R. Wilson. “A computer simulation method for the calculation of equilibrium constants for the formation of physical clusters of molecules: Application to small water clusters”. In: *J. Chem. Phys.* 76 (1982), p. 637.

[123] D. Manura and D. Dahl. *SIMION, industry standard charged particle optics simulation software.* URL: `http://simion.com`.

[124] J. P. Schiffer, M. Drewsen, J. S. Hangst, and L. Hornekær. “Temperature, ordering and equilibrium with time-dependent confining forces”. In: *Proc. Natl. Acad. Sci. USA* 97 (2000), p. 10697.

[125] L. Hornekær and M. Drewsen. “Formation process of large ion Coulomb crystals in linear Paul traps”. In: *Phys. Rev. A* 66 (2002), p. 013412.

[126] H. J. C. Berensen, J. P. M. Postma, W. F. van Gunsteren, A. DiNola, and J. R. Haak. “Molecular dynamics with coupling to an external bath”. In: *J. Chem. Phys.* 81 (1984), p. 3684.

[127] W. Humphrey, A. Dalke, and K. Schulten. “VMD - Visual Molecular Dynamics”. In: *J. Molec. Graphics* 14 (1996), p. 33.

[128] G. Borodi, A. Luca, and D. Gerlich. “Reactions of CO_2^+ with H, H_2 and deuterated analogues”. In: *Int. J. Mass Spectrom.* 280 (2009), p. 218.

[129] K. Okada, K. Yasuda, T. Takayanagi, M. Wada, H. A. Schuessler, and S. Ohtani. “Crystallization of Ca^+ ions in a linear rf octupole ion trap”. In: *Phys. Rev. A* 75 (2007), p. 033409.

[130] G. Scoles, ed. *Atomic and molecular beam methods: Volume 1.* Oxford University Press, 1988.

[131] A. B. Henson, S. Gersten, Y. Shagam, J. Narevicius, and E. Narevicius. “Observation of resonances in Penning ionization reactions at sub-Kelvin temperatures in merged beams”. In: *Science* 338 (2012), p. 234.

[132] L. Sheffield, M. S. Hickey, V. Krasovitskiy, K. D. D. Rathnayaka, I. F. Lyuksyutov, and D. R. Herschbach. “Pulsed rotating supersonic source for merged molecular beams”. In: *Rev. Sci. Instrum.* 83 (2012), p. 064102.

[133] H. L. Bethlem, G. Berden, F. M. H. Crompvoets, R. T. Jongma, A. J. A. van Roij, and G. Meijer. “Electrostatic trapping of ammonia molecules”. In: *Nature* 406 (2000), p. 491.

[134] S. K. Tokunaga, J. M. Dyne, E. A. Hinds, and M. R. Tarbutt. “Stark deceleration of lithium hydride molecules”. In: *New J. Phys.* 11 (2009), p. 055038.

[135] E. R. Hudson, C. Ticknor, B. C. Sawyer, C. A. Taatjes, H. J. Lewandowski, J. R. Bochinski, J. L. Bohn, and J. Ye. “Production of cold formaldehde molecules for study and control of chemical reaction dynamics with hydroxyl radicals”. In: *Phys. Rev. A* 73 (2006), p. 063404.

[136] J. R. Bochinski, E. R. Hudson, H. J. Lewandowski, G. Meijer, and J. Ye. “Phase space manipulation of cold free radical OH molecules”. In: *Phys. Rev. Lett.* 91 (2003), p. 243001.

[137] S. Y. T. van de Meerakker, I. Labazan, S. Hoekstra, J. Küpper, and G. Meijer. “Production and deceleration of a pulsed beam of metastable NH ($a^1\Delta$) radicals”. In: *J. Phys. B* 39 (2006), S1077.

[138] O. Bucicov, M. Nowak, S. Jung, G. Meijer, E. Tiemann, and C. Lisdat. “Cold SO_2 molecules by Stark deceleration”. In: *Eur. Phys. J. D* 46 (2008), p. 463.

[139] N. E. Bulleid, R. J. Hendricks, E. A. Hinds, S. A. Meek, G. Meijer, A. Osterwalder, and M. R. Tarbutt. “Traveling-wave deceleration of heavy polar molecules in low-field-seeking states”. In: *Phys. Rev. A* 86 (2012), p. 021404.

[140] W. Gerlach and O. Stern. “Das magnetische Moment des Silberatoms”. In: *Zeitschrift für Physik* 9 (1922), p. 353.

[141] M. Lemeshko, R. V. Krems, J. M. Doyle, and S. Kais. “Manipulation of molecules with electromagnetic fields”. In: *Mol. Phys.* 111 (2013), p. 1648.

[142] D. Auerbach, E. E. A. Bromberg, and L. Wharton. “Alternate-gradient focusing of molecular beams”. In: *J. Chem. Phys.* 45 (1966), p. 2160.

[143] J. H. Glownia, S. J. Riley, S. D. Colson, and G. C. Nieman. “MPI spectroscopy of expansion cooled ammonia: Structure and dynamics at 50 K”. In: *J. Chem. Phys.* 72 (1980), p. 5998.

[144] S. R. Langford, A. J. Orr-Ewing, R. A. Morgan, C. M. Western, M. N. R. Ashfold, A. Rijkenberg, C. R. Scheper, W. J. Buma, and C. A. de Lange. “The spectroscopy of high Rydberg states of ammonia”. In: *J. Chem. Phys.* 108 (1998), p. 6667.

[145] J. M. Hollas. *High Resolution Spectroscopy.* John Wiley and Sons, New York, 1998.

[146] C. M. Western. *PGOPHER, a program for simulating rotational structure.* URL: `http://pgopher.chm.bris.ac.uk`.

[147] M. T. Bell. “Cold chemistry in the gas phase using velocity selection and molecular deceleration”. DPhil Thesis. University of Oxford, 2009.

[148] N. J. Fitch, D. A. Esteves, M. I. Fabrikant, T. C. Briles, Y. Shyur, L. P. Parazzoli, and H. J. Lewandowski. “State purity of decelerated molecular beams”. In: *J. Mol. Spectrosc.* 278 (2012), p. 1.

[149] H. L. Bethlem. “Deceleration and trapping of polar molecules using time-varying electric fields”. PhD thesis. University of Nijmegen, 2002.

[150] S. Y. T. van de Meerakker. “Deceleration and electrostatic trapping of OH radicals”. PhD thesis. University of Nijmegen, 2006.

[151] S.-Y. Lee. *Accelerator Physics.* World Scientific Publishing, 2005.

[152] L. P. Parazzoli, N. Fitch, D. S. Lobser, and H. J. Lewandowski. “High-energy-resolution molecular beams for cold collision studies”. In: *New J. Phys.* 11 (2009), p. 055031.

[153] A. Osterwalder, S. A. Meek, G. Hammer, H. Haak, and G. Meijer. “Deceleration of neutral molecules in macroscopic travelling traps”. In: *Phys. Rev. A* 81 (2010), p. 051401.

[154] A. I. González Flórez, S. A. Meek, H. Haak, H. Conrad, G. Santambrogio, and G. Meijer. “An electrostatic elliptical mirror for neutral polar molecules”. In: *Phys. Chem. Chem. Phys.* 13 (2011), p. 18830.

[155] S. Y. T. van de Meerakker, N. Vanhaecke, H. L. Bethlem, and G. Meijer. “Higher-order resonances in a Stark decelerator”. In: *Phys. Rev. A* 71 (2005), p. 053409.

[156] D. Irimia, D. Dobrikov, R. Korekaas, H. Voet, D. A. van den Ende, W. A. Groen, and M. H. M. Janssen. “A short pulse (7 μs FWHM) and high repetition rate (dc-5 kHz) cantilever piezovalve for pulsed atomic and molecular beams”. In: *Rev. Sci. Instrum.* 80 (2009), p. 113303.

[157] M. T. Bell. Private communication. 2012.

[158] H. L. Bethlem, G. Berden, A. J. A. van Roij, F. M. H. Crompvoets, and G. Meijer. “Trapping neutral molecules in a traveling potential well”. In: *Phys. Rev. Lett.* 84 (2000), p. 5744.

[159] S. A. Schulz, H. L. Bethlem, J. van Veldhoven, J. Küpper, H. Conrad, and G. Meijer. “Microstructured switchable mirror for polar molecules”. In: *Phys. Rev. Lett.* 93 (2004), p. 020406.

[160] T. Junglen. “Guiding and trapping of cold dipolar molecules”. PhD thesis. Technical University of Munich, 2005.

[161] C. E. Heiner. “A molecular synchrotron”. PhD thesis. University of Nijmegen, 2009.

[162] S. Y. T. van de Meerakker, H. L Bethlem, and G. Meijer. “Slowing, trapping, and storing of polar molecules by means of electric fields”. In: *Cold molecules: Theory, experiment, applications*. Ed. by R. V. Krems, W. C. Stwalley, and B. Friedrich. CRC Press, 2009.

[163] C. E. Heiner, H. L. Bethlem, and G. Meijer. “Molecular beams with a tunable velocity”. In: *Phys. Chem. Chem. Phys.* 8 (2006), p. 2666.

[164] S. A. Meek, M. F. Parsons, G. Heyne, V. Platschkowski, H. Haak, G. Meijer, and A. Osterwalder. “A traveling wave decelerator for neutral polar molecules”. In: *Rev. Sci. Instrum.* 82 (2011), p. 093108.

[165] H. L. Bethlem, M. R. Tarbutt, J. Küpper, D. Carty, K. Wohlfart, E. A. Hinds, and G. Meijer. “Alternating gradient focusing and deceleration of polar molecules”. In: *J. Phys. B* 39 (2006), R263.

[166] H. L. Bethlem, A. J. A. van Roij, R. T. Jongma, and G. Meijer. “Alternate gradient focusing and deceleration of a molecular beam”. In: *Phys. Rev. Lett.* 88 (2002), p. 133003.

[167] E. Narevicius, A. Libson, C. G. Parthey, I. Chavez, J. Narevicius, U. Even, and M. G. Raizen. “Stopping supersonic beams with a series of pulsed electromagnetic Coils: An Atomic coilgun”. In: *Phys. Rev. Lett.* 100 (2008), p. 093003.

[168] S. D. Hogan, D. Sprecher, M. Andrist, N. Vanhaecke, and F. Merkt. “Zeeman deceleration of H and D”. In: *Phys. Rev. A* 76 (2007), p. 023412.

[169] S. H. Autler and C. H. Townes. “Stark effect in rapidly varying fields”. In: *Phys. Rev.* 100 (1955), p. 703.

[170] H. Stapelfeldt, H. Sakai, E. Constant, and P. B. Corkum. “Deflection of neutral molecules using the noneresonant dipole force”. In: *Phys. Rev. Lett.* 79 (1997), p. 2787.

[171] R. Fulton, A. I. Bishop, M. N. Shneider, and P. F. Barker. “Controlling the motion of cold molecules with deep periodic optical potentials”. In: *Nature Phys.* 2 (2006), p. 465.

[172] S. Merz, N. Vanhaecke, W. Jäger, M. Schnell, and G. Meijer. “Decelerating molecules with microwave fields”. In: *Phys. Rev. A* 85 (2012), p. 063411.

[173] H. Odashima, S. Merz, K. Enomoto, M. Schnell, and G. Meijer. “Microwave lens for polar molecules”. In: *Phys. Rev. Lett.* 104 (2010), p. 253001.

[174] E. Herbst. “The chemistry of interstellar space”. In: *Chem. Soc. Rev.* 30 (2001), p. 168.

[175] J. J. Thomson. “Further experiments on positive rays”. In: *Philos. Mag.* 24 (1912), p. 209.

[176] E. Herbst. “The astrochemistry of H_3^+”. In: *Phil. Trans. R. Soc. Lond. A* 358 (2000), p. 2523.

[177] D. C. Clary. “Reactions of strongly polar ions with molecules”. In: *Chem. Phys. Lett.* 232 (1995), p. 267.

[178] T. Su and M. Bowers. “Ion-polar molecule collisions: The effect of ion size on ion-polar molecule rate constants; the parameterization of the Average-Dipole-Orientation theory”. In: *Int. J. Mass Spectrom.* 12 (1973), p. 347.

[179] T. Su and M. T. Bowers. “Ion-polar molecule collisions. Proton transfer reactions of H_3^+ and CH_5^+ to the geometric isomers of difluoroethylene, dichloroethylene and difluorobenzene”. In: *J. Am. Chem. Soc.* 95 (1973), p. 1370.

[180] T. Su and M. T. Bowers. “Theory of ion–polar molecule collisions. Comparison with experimental charge transfer reactions of rare gas ions to geometric isomers of difluorobenzene and dichloroethylene”. In: *J. Chem. Phys.* 58 (1973), p. 3027.

[181] Ch. Wellers, A. Borodin, S. Vasilyev, D. Offenberg, and S. Schiller. “Resonant IR multi-photon dissociation spectroscopy of a trapped and sympathetically cooled biomolecular ion species”. In: *Phys. Chem. Chem. Phys.* 13 (2011), p. 18799.

[182] A. Kramida, Yu. Ralchenk, J. Reader, and NIST ASD Team (2012). *NIST Atomic Spectra Database (ver. 5.0).* National Institute of Standards and Technology, Gaithersburg, MD. Aug. 2013. URL: `http://physics.nist.gov/asd`.

[183] S. G. Lias, J. E. Bartmess, J. F. Liebman, J. L. Holmes, R. D. Levin, and W. G. Mallard. *"Ion energetics data" in NIST Chemistry WebBook, NIST Standard Reference Database Number 69.* Ed. by P. J. Linstrom and W. G. Mallard. National Institute of Standards and Technology, Gaithersburg, MD. Aug. 2013. URL: `http://webbook.nist.gov`.

[184] S. J. Bajic, R. N. Compton, X. Tang, and P. Lambropoulos. “Resonantly enhanced multiphoton-ionization photoelectron spectroscopy of krypton and xenon: Experiment and theory”. In: *Phys. Rev. A* 44 (1991), p. 2102.

[185] S. Jullien, J. Lemaire, S. Fenistein, M. Heninger, G. Mauclaire, and R. Marx. "Radiative lifetimes of Xe^+ and Kr^+ in their $^2P_{1/2}$ spin-orbit states". In: *Chem. Phys. Lett.* 212 (1993), p. 340.

[186] O. Camino, M. Alonso, D. Gestal, J. de Bruin, P. Rathsman, J. Kugelberg, P. Bodin, S. Ricken, R. Blake, P. P. Voss, and L. Stagnaro. "SMART-1 operations experience and lessons learnt". In: *Acta Astronaut.* 61 (2007), p. 203.

[187] E. Canuto and L. Massotti. "All-propulsion design of the drag-free and attitude control of European satellite GOCE". In: *Acta Astronaut.* 64 (2009), p. 325.

[188] J. Brophy. "The Dawn ion propulsion system". In: *Space. Sci. Rev.* 163 (2011), p. 251.

[189] D. J. Levandier and Y.-H. Chiu. "A guided-ion beam study of the reactions of $Xe^+$and Xe^{2+} with NH_3at hyperthermal collision energies". In: *J. Chem. Phys.* 133 (2010), p. 154304.

[190] N. G. Adams, D. Smith, and E. Alge. "Reactions of the $^2P_{3/2}$ and $^2P_{1/2}$ doublet ground states of Kr^+ and Xe^+ at 300 K". In: *J. Phys. B* 13 (1980), p. 3235.

[191] X. Tong, A. H. Winney, and S. Willitsch. "Sympathetic cooling of molecular ions in selected rotational and vibrational states produced by threshold photoionization". In: *Phys. Rev. Lett.* 105 (2010), p. 143001.

[192] B. Roth, P. Blythe, H. Wenz, H. Daerr, and S. Schiller. "Ion-neutral chemical reactions between ultracold localized ions and neutral molecules with single-particle resolution". In: *Phys. Rev. A* 73 (2006), p. 042712.

[193] M. Drewsen, A. Mortensen, R. Martinussen, P. Staanum, and J. L. Sørensen. "Nondestructive identification of cold and extremely localized single molecular ions". In: *Phys. Rev. Lett.* 93 (2004), p. 243201.

[194] D. Kielpinski, B. E. King, C. J. Myatt, C. A. Sackett, Q. A Turchette, W. M. Itano, C. Monroe, D. J. Wineland, and W. H. Zurek. "Sympathetic cooling of trapped ions for quantum logic". In: *Phys. Rev. A* 61 (2000), p. 032310.

[195] K. Hølbjerre, D. Offenberg, C. Z. Bisgaard, H. Stapelfeldt, P. F. Staanum, A. Mortensen, and M. Drewsen. "Consecutive photodissociation of a single complex molecular ion". In: *Phys. Rev. A* 77 (2008), p. 030702.

[196] B. Roth, J. C. J. Koelemeij, H. Daerr, and S. Schiller. "Rovibrational spectroscopy of trapped molecular hydrogen ions at millikelvin temperatures". In: *Phys. Rev. A* 74 (2006), p. 040501.

[197] S. Willitsch, M. T. Bell, A. D. Gingell, and T. P. Softley. "Chemical applications of laser- and sympathetically-cooled ions in ion traps". In: *Phys. Chem. Chem. Phys.* 10 (2008), p. 7200.

[198] K. Sheridan and M. Keller. "Weighing of trapped ion crystals and its applications". In: *New J. Phys.* 13 (2011), p. 123002.

[199] A. Bertelsen, I. S. Vogelius, S. Jørgensen, R. Kosloff, and M. Drewsen. "Photodissociation of cold MgH^+ ions - towards rotational temperature measurements and controlled dissociation". In: *Eur. Phys. J. D* 31 (2004), p. 403.

[200] B. Roth, P. Blythe, and S. Schiller. “Motional resonance coupling in cold multispecies Coulomb crystals”. In: *Phys. Rev. A* 75 (2007), p. 023402.

[201] W. C. Wiley and I. H. McLaren. “Time-of-flight mass spectrometer with improved resolution”. In: *Rev. Sci. Instrum.* 26 (1955), p. 1150.

[202] A. T. J. B. Eppink and D. H. Parker. “Velocity map imagine of ions and electrons using electrostatic lenses: Application in photoelectron and photofragment ion imaging of molecular oxygen”. In: *Rev. Sci. Instrum.* 68 (1997), p. 3477.

[203] D. Townsend, M. P. Minitti, and A. G. Suits. “Direct current slice imaging”. In: *Rev. Sci. Instrum.* 74 (2003), p. 2530.

[204] S. J. Showalter, K. Chen, W. G. Rellergert, S. T. Sullivan, and E. R. Hudson. “An integrated ion trap and time-of-flight mass spectrometer for chemical and photo-raction dynamics studies”. In: *Rev. Sci. Instrum.* 83 (2012), p. 043103.

[205] N. Kjærgaard and M. Drewsen. “Observation of a structural transition for Coulomb crystals in a linear Paul trap”. In: *Phys. Rev. Lett.* 91 (2003), p. 095002.

[206] G. C. Brown, B. C. Dian, K. O. Douglass, S. M. Geyer, S. T. Shipman, and B. H. Pate. “A broadband Fourier transform microwave spectrometer based on chirped pulse excitation”. In: *Rev. Sci. Instrum.* 79 (2008), p. 053103.